

Design and Development of Spectrophotometric Systems for Fast Detection and Quantification of Analytes

By

NEETHU EMMANUEL

20EE18J39008

A thesis submitted to the
Academy of Scientific and Innovative Research
for the award of the degree of

DOCTOR OF PHILOSOPHY

in

ENGINEERING

Under the supervision of

Dr. K. YOOSAF & Dr. NARAYANAN UNNI K. N.



**CSIR-National Institute for Interdisciplinary
Science and Technology (CSIR-NIIST),
Thiruvananthapuram - 695 019**

AcSIR

Academy of Scientific and Innovative Research
AcSIR Headquarters, CSIR-HRDC campus
Sector 19, Kamla Nehru Nagar,
Ghaziabad, U.P. - 201 002, India

June 2021

This thesis is dedicated to my loving parents and
my dear husband.



**NATIONAL INSTITUTE FOR INTERDISCIPLINARY SCIENCE AND
TECHNOLOGY**

**Council of Scientific & Industrial Research
Industrial Estate P. O., Thiruvananthapuram – 695 019, Kerala, INDIA**

22nd June 2021

CERTIFICATE

This is to certify that the work incorporated in this Ph.D. thesis entitled '*Design and Development of Spectrophotometric Systems for Fast Detection and Quantification of Analytes*' submitted by Ms. Neethu Emmanuel to Academy of Scientific and Innovative Research (AcSIR) in fulfilment of the requirements for the award of the Degree of Doctor of Philosophy in Engineering Sciences, embodies original research work under our supervision/guidance. We further certify that this work has not been submitted to any other University or Institution in part or full for the award of any degree or diploma. Research material obtained from other sources has been duly acknowledged in the thesis. Any text, diagrams, data etc., used in the thesis from other sources, have been duly cited and acknowledged. It is also certified that this work done by the student, under our supervision, is plagiarism free.

XHP
22/6/2021

Neethu Emmanuel

K. Y.
22/6/21

**Dr. K. Yoosaf
(Supervisor)**

U. K. N.
22/06/21

**Dr. Narayanan Unni. K. N.
(Co-Supervisor)**

STATEMENTS OF ACADEMIC INTEGRITY

I Neethu Emmanuel, a Ph.D. student of the Academy of Scientific and Innovative Research (AcSIR) with Registration No. 20EE18J39008 hereby undertake that, the thesis entitled ‘**Design and Development of Spectrophotometric Systems for Fast Detection and Quantification of Analytes**’ has been prepared by me and that the document reports original work carried out by me and is free of any plagiarism in compliance with the UGC Regulations on “*Promotion of Academic Integrity and Prevention of Plagiarism in Higher Educational Institutions (2018)*” and the CSIR Guidelines for “*Ethics in Research and in Governance (2020)*”.

KHP
22/6/2021

Neethu Emmanuel

22nd June 2021
Thiruvananthapuram

It is hereby certified that the work done by the student, under my/our supervision, is plagiarism-free in accordance with the UGC Regulations on “*Promotion of Academic Integrity and Prevention of Plagiarism in Higher Educational Institutions (2018)*” and the CSIR Guidelines for “*Ethics in Research and in Governance (2020)*”.

K. Yoosaf
22/6/21

Dr. K. Yoosaf
(Supervisor)

Narayanan Unni K. N.
22/6/21

Dr. Narayanan Unni K. N.
(Co-Supervisor)

22nd June 2021
Thiruvananthapuram

22nd June 2021
Thiruvananthapuram

DECLARATION

I hereby declare that the matter embodied in the thesis entitled: ‘Design and Development of Spectrophotometric Systems for Fast Detection and Quantification of Analytes’ is the result of the investigations carried out by me at the Photosciences and Photonics Section, Chemical Sciences and Technology Division, CSIR-National Institute for Interdisciplinary Science and Technology (CSIR-NIIST), Thiruvananthapuram, under the supervision of Dr. K. Yoosaf and Dr. Narayanan Unni K. N., and the same has not been submitted elsewhere for any other degree.

In keeping with the general practice of reporting scientific observations, due acknowledgement has been made wherever the work described is based on the findings of other investigators.

KHP
22/6/2021

Neethu Emmanuel

22nd June 2021
Thiruvananthapuram

ACKNOWLEDGEMENTS

I have great pleasure in expressing my deep sense of gratitude to Dr. K. Yoosaf and Dr. Narayanan Unni K. N. my thesis supervisor and co-supervisor for suggesting the research problem, for their valuable guidance, support and encouragement, providing scientific freedom of thought and action leading to the successful completion of this work.

I thank Dr. A. Ajayaghosh, Director of the CSIR-National Institute for Interdisciplinary Science and Technology (NIIST), Thiruvananthapuram, for providing the necessary facilities for carrying out this work.

I would like to express my sincere thanks to Prof. K. P. Sudheer and Dr. Suresh Das, present and former Executive Vice President, Kerala State Council for Science Technology and Environment (KSCSTE), Dr. S. Pradeep Kumar, former director of KSCSTE for providing all the support for the Partnering Academic Industrial Research (PAIR) program and evaluating the progress of the work.

I am particularly grateful to the industry partner of the PAIR program M/s Vinvish Technologies Pvt. Ltd, Technopark, Thiruvananthapuram for the financial and technical assistance.

My sincere thanks are also due to:

- ❖ *Dr. V. Karunakaran, Dr. C. H. Suresh and Dr. R. Laxmi Varma; present and former AcSIR co-ordinators for the timely conduction of all AcSIR course work.*
- ❖ *Dr. Sujatha Devi P., Head, Chemical Sciences and Technology Division for her support.*
- ❖ *Dr. Manoj Raama Varma, Dr. Kaustabh Kumar Maiti, and Dr. Saju Pillai; Doctoral Advisory Committee (DAC) members for their insightful comments and encouragement and assistance in keeping my progress on schedule.*
- ❖ *Prof. Chandrabas Narayana, Prof. G. M. Nair, Dr. K. G. Gopchandran, Mr. Pius Varghese, and Mr. Ignatious; PAIR Advisory Committee members for giving immense support and valuable suggestions which inspired me to widen my research from various perspectives.*
- ❖ *Dr. Elizabeth Jacob, Computational Modelling group for her valuable guidance and generously spent precious time in giving the suggestion and comments on*

the signal analysis part.

- ❖ *Dr. K. R. Gopidas, Dr. Biswapriya Deb, Dr. Joshy Joseph, Dr. Vijayakumar C. Nair, Dr. Praveen V. K., Dr. Suraj Soman, Dr. Ishitha Neogi, Dr. Adersh Ashok, and Dr. Sreejith Sankar; scientists of the Photosciences and Photonics Section, Chemical Sciences and Technology Division (CSTD), for their help and support.*
- ❖ *I wish to acknowledge the help provided by Dr. Nisha. P. and Mr. Billu Abraham, Agroprocessing and Technology Division, with HPLC analysis.*
- ❖ *Mr. Robert Philip and Mr. Merin Santhosh for general help.*
- ❖ *Present and former group members: Ms. Raji B. Nair, Ms. Reethu Haridas, Ms. Bamisha Balan, Mr. Sanoop P., Ms. Bini Abraham, Mr. Nandu A., Mr. Sarath J. S., Ms. Liya Elsa Varghese, Mr. Arun M., Dr. Sajitha Manikantan, Dr. Arun Gopi, Mr. Listo Varghese, Mr. Renjith, Mr. Sreenandu, Ms. Gangothri, Ms. Anasooya, and Mr. Akhil.*
- ❖ *Graduate students: Mr. Raoof, Mr. Hazan, Ms. Harshita, Mr. Safwan, Ms. Amrutha, Ms. Ambili, Ms. Sreekala, and Ms. Kavya for their help and cooperation.*
- ❖ *All other members of the Photosciences and Photonics section, and friends at CSIR-NIIST.*
- ❖ *My special thanks are extended to Mr. Jijo V. I., Mr. Jishnu, and all other colleagues from Vinvish technologies. Pvt. Ltd.*
- ❖ *All my classmates, friends and teachers for their love and inspiration.*
- ❖ *Kerala State Council for Science Technology and Environment (KSCSTE) for financial assistance.*

I am deeply grateful to my parents, my husband (Jyothish) and my sisters (Anu, Anju) for their constant source of love, support, understanding and encouragement which have been a great inspiration for these efforts. Finally, I thank Almighty for all His blessings.

Neethu Emmanuel

CONTENTS

	Title	Page
	Certificate	i
	Statements of academic integrity	ii
	Declaration	iii
	Acknowledgements	iv
	Contents	vi
	List of figures	x
	List of tables	xviii
	List of abbreviations	xx
	Preface	xxv
Chapter 1	An overview of recent developments in portable spectroscopic devices for chemical analysis	1-26
1.1	Abstract	1
1.2	Introduction	2
1.2.1	Counterfeit drugs	4
1.2.2	Heavy metal toxicity	6
1.2.3	Spectroscopy for onsite analysis	7
1.3	Raman spectroscopy	8
1.3.1	Instrumentation of Raman spectroscopy	9
1.3.2	Advantages and limitations of Raman spectroscopy	11
1.3.3	Noises in Raman spectroscopy	13
1.3.4	Raman Spectroscopy in pharmaceutical analysis	14
1.3.5	Chemometric analysis	15
1.4	Smartphone spectroscopy	16
1.4.1	Colour detection	17
1.5	Objectives of the thesis	18
1.6	References	19
Chapter 2	Building an optical bench configuration of Raman spectrometer and characterization of its components.	27-51
2.1	Abstract	27
2.2	Introduction	28
2.3	Experimental section	30
2.3.1	Optical configuration	30

2.3.2	Assembling the components	30
2.3.3	Chemicals and instruments used	31
2.4	Results and discussion	32
2.4.1	Tabletop Raman spectrometer	32
2.4.2	Characterization of components	34
2.4.3	Raman shift calibration of the spectrometer	41
2.4.4	Performance evaluation of tabletop RS	43
2.4.5	Scope for SNR improvement	46
2.5	Summary	48
2.6.	References	49
Chapter 3	Design and development of a portable Raman spectrometer and its performance evaluation	52-76
3.1	Abstract	52
3.2	Introduction	53
3.3	Experimental section	55
3.3.1	Optical configuration	55
3.3.2	Instruments used	56
3.4	Results and discussion	57
3.4.1	Design of mechanical mounts	57
3.4.2	Integrating portable Raman spectrometer	60
3.4.3	Performance comparison with the tabletop version	63
3.4.4	Performance comparison with a commercial device	63
3.4.5	Quantitative analysis	66
3.4.6	Onsite analysis	68
3.4.7	Scope for improvement	71
3.5	Summary	73
3.6	References	73
Chapter 4	Spectral processing and library matching tools for onsite analysis	77-111
4.1	Abstract	77
4.2	Introduction	78
4.3	Experimental section	84
4.3.1	Portable Raman spectrometer	84
4.3.2	Generation of synthetic Raman spectrum	85
4.3.3	Baseline correction algorithms	87
4.3.4	High-frequency noise removal	89
4.3.5	Software development	89

4.4	Results and discussion	90
4.4.1	Processing of simulated spectra	90
4.4.2	Processing of experimental spectrum	97
4.4.3	Raman spectral library creation	99
4.4.4	Standalone application development	103
4.5	Summary and future scope	105
4.6	References	106
Chapter 5	Application of Raman spectroscopy for quantification of aceclofenac from combinational tablets using chemometric methods	112-142
5.1	Abstract	112
5.2	Introduction	113
5.3	Experimental section	114
5.3.1	Materials and methods	114
5.3.2	Raman spectral measurements	115
5.3.3	Data pre-processing	116
5.3.4	Chemometric analysis	116
5.3.5	Application development	118
5.3.6	HPLC analysis	120
5.4	Results and discussion	121
5.4.1	Raman spectral analysis	121
5.4.2	Qualitative analysis	124
5.4.3	Quantitative analysis	126
5.4.4	Prediction accuracy of quantitative models	130
5.4.5	Evaluation of the model in classifying genuine and fake samples	131
5.4.6	Software development for quality testing	134
5.5	Summary and future scope	138
5.6	References	139
Chapter 6	Development of a smartphone spectrometer system for colourimetric detection of heavy metal ions	143-172
6.1	Abstract	143
6.2	Introduction	144
6.3	Experimental section	146
6.3.1	Materials and methods	146
6.3.2	Synthesis of silver nanoparticles (AgNPs)	147
6.3.3	Interaction of AgNPs with metal ions	147
6.3.4	Mobile application development	148
6.4	Results and discussion	148

6.4.1	Characterization of AgNPs	148
6.4.2	Interaction of silver nanoparticles with Hg ²⁺ ions	150
6.4.3	Interaction of silver nanoparticles with Pb ²⁺ ions	155
6.4.4	Interaction of silver nanoparticles with other metal ions	157
6.4.5	Colourimetric analysis through photographs	158
6.4.6	Android smartphone application development	163
6.4.7	Real sample analysis	167
6.5	Summary and future scope	168
6.6	References	169
Abstract		173
List of publications		174
List of posters and oral presentations at conferences		175

LIST OF FIGURES

Figure No.	Title	Page
Figure 1.1	Photographs illustrating examples for different portable spectroscopic devices for onsite analysis (A) pulse oximeter, (B) handheld Raman spectrometer from Metrohm, (C) GoSpectro handheld spectrometer from GoyaLab, (D) Scio pocket-size NIR spectrometer, (E) A2 Technologies's FTIR spectrometer for soil analysis, (F) Cloud AI handheld Raman spectrometer, (G) smartphone colourimetric analyser for food adulterant detection and (H) X-ray fluorescence spectrometer from Lanscientific.	3
Figure 1.2	(A) Types of counterfeit drugs, (B) image showing the package and tablet of genuine and counterfeit artesunate antimalarial tablets, and (C-G) different portable detection techniques for pharmaceutical analysis (C) TrueTag Micro tag tablets, (D) US FDA's CD3 detector, (E) Paper analytical device, (F) GPHF Minilab TLC test kit, and (G) Thermofisher Truescan Raman spectrometer for pharmaceutical raw material analysis.	5
Figure 1.3	Principle and applications of Raman spectroscopy	8
Figure 1.4	Different light sources (A) mercury arc lamp, (B) bulky gas lasers (e.g. He-Ne), and (C) small footprint laser diodes, used in the previous and current generation Raman spectrometers	9
Figure 1.5	Different probe optics configurations of Raman spectrometers (A) transmission, (B) spatially offset, (C) 90 degree, and (D) backscattering.	10
Figure 1.6	Different detector systems (A) spectrometer used by C.V Raman for recording the first Raman spectra, (B) rotating grating and single point detector-based spectrometer, and (C) linear array CCD spectrometer.	11
Figure 1.7	Pictures showing examples of various smartphone based sensing devices. (A) Bisphenol detection using an immersion probe, (B) 8 channel spectrometer for multiplex detection, (C) Zika virus detection through fluorescence measurement, and (D) colourimetric pH sensor.	16
Figure 1.8	Principle of colour detection (A) absorption spectra of human visual pigments in eye, (B) spectra showing the light absorbed by chlorophyll pigment in green coloured leaf and the RGB colour values of its image, ⁷⁸ and (C) principle of colour detection in a digital camera.	18
Figure 2.1	Schematic layout of the Raman spectrometer configuration adopted	32
Figure 2.2	Photograph showing the organization of components for Raman spectrometer on an optical table; (1) laser pointer, (2) soldered wire for powering laser diode through USB powering, (3) variable optical attenuator to adjust laser power, (4) band-pass filter to block 808 nm, (5) beam splitter, (6) focusing convex lens with focal length 50 mm, (7) sample holder with the sample placed inside a glass vial, (8) focusing convex lens with focal length 50 mm, (9) 550 nm cut off long-pass filter, (10) XYZ fibre holder (inset shows the top view of the fibre holder showing Z-axis movement), (11) 500 μ m optical fibre, and (12) Science surplus detector	33
Figure 2.3	(A) Photograph of the JD-851 laser pointer and (B) graph showing the spectral profile of the laser emission measured using a spectrometer	35

	having ~0.3 nm resolution	
Figure 2.4	Graph showing the wavelength-dependent transmission of the band-pass filter used for blocking the 808 nm, inset showing the photograph of the filter	35
Figure 2.5	Graphs showing the laser's emission spectral profile measured in the (A) absence and (B) presence of band-pass filter	36
Figure 2.6	Schematic representation of the adopted probe optics arrangement	36
Figure 2.7	Graph showing the wavelength-dependent transmission of the long-pass filter with cut off at 550 nm (Newport CGA-550)	37
Figure 2.8	Graphs showing the obtained emission profile of rhodamine B in the (A) absence of any long-pass filter, (B) presence of one 550 nm long-pass filter (optical density at 532 nm = 3) installed in between beam splitter and focusing lens L2; the reduced interference from the laser is marked with the red arrow, and (C) presence of two numbers of 550 nm long-pass filters (each having optical density 3 at 532 nm) installed in between beam splitter and focusing lens. All the spectra were taken with 0.5 s integration time	38
Figure 2.9	Graphs showing the improvement in signal intensity during fine alignment of the probe optics using the XYZ translational stage. All spectra were taken from diluted rhodamine B solution with 100 ms integration time	39
Figure 2.10	Photograph of spectrometer's optical bench configuration and the position of component	40
Figure 2.11	(A) CCD dark spectrum showing the hot pixels (B) dark spectrum measured at three different integration time, i.e. 100 ms, 1000 ms, and 3000 ms and (C) after dark spectrum subtraction	40
Figure 2.12	Reference spectra of CFL lamp	41
Figure 2.13	The spectrum of fluorescent lamp collected using the spectrometer represented in terms of (A) pixel number vs intensity, (B) pixel number vs reported wavelength, and (C) calibrated spectrum represented in wavelengths	42
Figure 2.14	Raman spectrum of cyclohexane, benzonitrile, PDMS, and acetone acquired using the tabletop setup (shown in Figure 2.2) with laser power 55 mW, integration time 5 s, and no. of average = 1	43
Figure 2.15	(A) Raman spectrum of benzonitrile taken with varying excitation laser power (integration time = 5 s, number of averages = 1) and (B) plot showing the variation in intensity of peak at 2243 cm^{-1} as a function of excitation laser power. Optical power adjustment was achieved using variable optical attenuator placed in between the laser source and the beam splitter	45
Figure 2.16	Variation in signal and background noise with increment in laser power	46
Figure 2.17	Raman spectra of benzonitrile taken with collection optics having L1 lens with focal length respectively as 15 mm, 30 mm, and 50 mm. All spectra were taken with 5 s integration time and an average 1	47
Figure 2.18	Schematic representation of (A) focusing a laser of beam diameter 'D', to a spot size 'd' using a lens of focal length 'f', (B) measuring the laser	47

	spot size, and CCD image of the focused laser spot with focal length (C) 50 mm (D) 30 mm (E) 15 mm	
Figure 2.19	Raman spectra of cyclohexane collected under identical conditions and varying the mode of detector coupling with the probe optics	48
Figure 3.1	Different instrumental configurations of Raman spectrometers (A) high end (Renishaw inVia Raman microscope), (B) modular (BW-Tek Fiber optic Raman system) and (C) portable (Metrohm Mira handheld)	53
Figure 3.2	Schematic representation of the optical configuration adopted for portable Raman spectrometer	56
Figure 3.3	3D design and photographs of the mounts for (A) and (B) laser pointer (C) and (D) Band-pass filter to block 808 nm. Red arrow marks show the mounting screws to the chassis	57
Figure 3.4	3D design and photograph of mount for (A,B) beam splitter, (C,D) sample holder. Red arrow marks show the mounting screws to the chassis	58
Figure 3.5	(A) 3D design and (B) photograph of the lens mount. The arrow marks indicate the provision provided for 5 mm movement freedom along the X and Y-axis	59
Figure 3.6	3D design showing the spectrometer mounted on the chassis using the four screws (arrow marks) with parts marked as 1. optical bench, 2. electronics board, and 3. base of the chassis	60
Figure 3.7	3D drawing of the Raman spectrometer showing the internal components 1. laser diode mount, 2. laser diode, 3. bandpass filter, 4. beam splitter, 5. focusing lens, L1, 6. glass vial holder, 7. long pass filter, 8. focusing lens L2 on XY translating mount, 9. spectrometer, 10. charging port, 11. external switch to control the laser ON/OFF, and 12. RS232 to USB converter to communicate with a windows tablet, and (B) photograph of the assembled system	61
Figure 3.8	Photographs showing the interfaces on the sidewall of the chassis, marked as 1. powering port, 2. switch for laser control, and 3. RS232 port to communicate with the tablet PC	61
Figure 3.9	Mount for the tablet PC (A) exploded view and the assembled view. Arrow marks indicate the slot for 1: accessing the microUSB port 2: power switch of the tablet PC	62
Figure 3.10	Photographs showing the different stages of the assembled system	62
Figure 3.11	(A) 3D design of the Raman spectrometer and (B) photograph of the assembled system	62
Figure 3.12	Raman spectra of (A) cyclohexane and (B) benzonitrile took using the portable Raman spectrometer (red) and tabletop version (black), all spectra were taken with 5 s integration time	63
Figure 3.13	Raman spectra of (A) benzonitrile (B) cyclohexane (C) PDMS and (D) toluene obtained using the confocal Raman microscope (laser power 25 mW) (green) and fabricated portable system microscope (laser power 10 mW) (red). All spectra were taken with 5 s integration time	64
Figure 3.14	Raman spectra of cyclohexane-toluene mixtures of varying compositions collected using the fabricated portable device with acquisition parameters: integration time 3 s, no. of averages 5, laser power 10 mW measured at sample point	67

Figure 3.15	(A) Raman spectra of cyclohexane-toluene mixtures in the range 2700 to 3100 cm^{-1} (B) variation in peak intensity at 2858 cm^{-1} and 3055 cm^{-1} with respect to cyclohexane concentration	68
Figure 3.16	Variation in peak intensity in the range 2830 cm^{-1} to 2880 cm^{-1} vs cyclohexane concentration	68
Figure 3.17	Raman spectra of ethanol collected using the fabricated portable device	69
Figure 3.18	Raman spectra of ethanol-water mixtures of varying compositions collected using the fabricated portable device with acquisition parameters: integration time 5 s, no of averages 5, laser power 10 mW measured at the sample point	69
Figure 3.19	(A) Raman spectra in the range 2700- 3700 cm^{-1} of ethanol-water mixtures of varying compositions collected using the device with 10 mW laser power and 5 s integration time and (B) plot showing the variation in integrated peak intensity in the range 2800-3000 cm^{-1} vs ethanol concentration	70
Figure 3.20	Raman spectrum of an alcoholic drink containing 42.86 alcohol V/V %, inset shows the photograph of the sample under analysis	71
Figure 4.1	Raman spectrum of toluene taken using the portable Raman spectrometer developed in chapter 3 (red), and its decomposed components: high-frequency noise (black), low-frequency baseline (green), and the denoised Raman spectrum (blue).	79
Figure 4.2	Raw Raman spectrum of cyclohexane taken at (A) 3 s, (B) 0.5 s integration time using the upgraded version of portable Raman spectrometer at laser power \sim 5 mW (Figure 4.5).	80
Figure 4.3	Principle of baseline estimation by (A) single polynomial fitting and (B) Mod-Poly algorithm	82
Figure 4.4	Pictorial representation of RCF algorithm	84
Figure 4.5	Photograph of the upgraded portable Raman spectrometer	85
Figure 4.6	Simulated spectrum with 10 Lorentzian peaks on a null baseline	86
Figure 4.7	Mathematically generated (A) random noise and (B) baseline following a Gaussian distribution (black), sigmoidal curve (blue), and exponential shape (red)	87
Figure 4.8	Mathematically simulated Raman spectrum added with random noise and three baseline types (A) exponential baseline, (B) Gaussian distribution and (C) sigmoidal baseline.	87
Figure 4.9	Pictorial representation of RIA algorithm showing Raman spectrum added with Gaussian peaks on extrapolated ends, and the estimated background after each iteration.	88
Figure 4.10	(left) Simulated noisy raw data (black) and estimated baseline (red) and (right) extracted Raman spectra (blue) and originally added spectra (wine red); (top) sigmoidal background, (middle) exponential baseline (underestimated baseline is marked in green) and (bottom) Gaussian background using the RIA algorithm.	91
Figure 4.11	(left) Simulated noisy raw data (black) and estimated baseline (red) and (right) extracted Raman spectra (blue) and originally added spectra (wine red); (top) sigmoidal background, (middle) exponential baseline (underestimated baseline is marked in green) and (bottom) Gaussian background using the SCARF algorithm with $(n,r,s)=(1,30,40)$.	92

Figure 4.12	SCARF estimated baseline on the simulated spectrum with Gaussian baseline obtained by varying (A) r values and (B) s values at r = 30.	93
Figure 4.13	SCARF estimated baseline on the simulated spectrum with Gaussian baseline for different values of n	94
Figure 4.14	Extracted Raman spectrum with a single pass (black), double pass (red) SCARF along with the original spectrum (red).	95
Figure 4.15	Extracted Raman spectrum using I-Mod-Poly algorithm n = 3 (blue), n = 5 (green), and n=7 (red), along with the originally added Raman spectra to the Gaussian baseline.	96
Figure 4.16	(left) Simulated noisy raw data (black) and estimated baseline (red) and (right) extracted Raman spectra (blue) and originally added spectra (wine red); (top) sigmoidal background, (middle) exponential baseline (underestimated baseline is marked in green) and (bottom) Gaussian background using the I-Mod-Poly algorithm.	96
Figure 4.17	(A) Dark spectrum taken at 5 s integration time; raw spectra (blue), blank subtracted spectra (red) and S-Golay filtered spectra (green overlaid) of (B) cyclohexane and (C) paracetamol tablet taken with 5 s integration time. Baseline corrected spectrum (brown) of paracetamol is also shown.	98
Figure 4.18	Raman spectra of the chemicals after noise removal saved into the database.	101
Figure 4.19	Algorithm for the developed software	104
Figure 4.20	Snapshot of the GUI of the developed application showing the ‘ Set parameters’ tab.	105
Figure 4.21	Snapshot of the GUI of the developed application showing the ‘Acquisition’ tab with user interfaces marked as 1. button to acquire bank spectra, 2. button to enable/disable blank subtraction,3. button to enable/disable baseline correction, 4. button to save the acquired sample spectra in ‘.txt’ form, 5. prediction results based on library search and 6. the acquired spectra after processing.	105
Figure 5.1	Application flowchart	118
Figure 5.2	Chromatogram of a solution containing 1 mg aceclofenac in 1 mL acetonitrile	119
Figure 5.3	Chromatogram of a solution containing 1 mg paracetamol in 1 mL acetonitrile	119
Figure 5.4	Calibration graphs showing area under the curve against the concentration of (A) paracetamol and (B) aceclofenac	120
Figure 5.5	(A) Raw and (B) processed Raman spectra of the pharmaceutical tablets under study	121
Figure 5.6	Raw and processed Raman spectra of the pharmaceutical tablets under study	123
Figure 5.7	Raman spectrum of TiO ₂	123
Figure 5.8	(A) Explained variance by the first ten principal components, and (B) PCA score plot showing the clustering of tablets based on their ingredients	124

Figure 5.9	PCA loading vectors of (A) 1st (B) 2nd and (C) 3rd components	124
Figure 5.10	Classification of test data using the PCA model, the points marked in star shape corresponds to the test data, and the round shape corresponds to the training data	125
Figure 5.11	Raman spectra of laboratory prepared 0-100 % w/w mixtures of ACE. Data were baseline corrected, trimmed to 810-1750 cm^{-1} , and intensity normalised	126
Figure 5.12	(A) PCA score plot and (B) explained variance of the first 10 principal components	126
Figure 5.13	(A) PC1 and (B) PC2 loading vectors of the PCA model performed on the quantification calibration model	126
Figure 5.14	Plot showing the relation between PC1 values against the concentration predicted by the multiple linear equations	127
Figure 5.15	Plot showing the relation between PC1 values against API concentration, the red line showing the non-linear fit	128
Figure 5.16	Relation between PC1+PC2 values against API concentration	129
Figure 5.17	ROC plot for the three quantification models at nine different threshold levels	132
Figure 5.18	Snap-shot showing GUI of the standalone application	134
Figure 5.19	Computational algorithm of the developed standalone application for pharmaceutical quality estimation	135
Figure 5.20	The predicted API concentration from the laboratory prepared mixture containing 23.5% ACE	137
Figure 5.21	HPLC Chromatogram of the laboratory prepared mixture containing 23.5% ACE	137
Figure 6.1	(A) Colour photograph and (B) absorption spectra of the AgNP synthesized by addition of 10 mM DHCA to 0.74 mM AgNO_3 in the presence of 0.15M NaOH	149
Figure 6.2	(A) DLS curve and (B) TEM image, showing the size distribution of synthesized AgNPs	149
Figure 6.3	FTIR spectrum of the DHCA capped AgNPs	150
Figure 6.4	Photographs illustrating the colour changes induced to AgNPs by the presence of Hg^{2+} ions at 0 ppm, 0.8 ppm, 1.6 ppm, 2.2 ppm, 3.3 ppm, 6.1 ppm, and 7.6 ppm	151
Figure 6.5	(A) Changes in absorption spectra of AgNPs by the presence of varying concentrations of Hg^{2+} ions, and (B) plot of the area under the absorption curve in the range 320-500 nm as a function of Hg^{2+} concentration	151
Figure 6.6	Absorption spectra of AgNP solution in the presence of (A) 0-33 ppm cadmium(II) chloride (B) 9 ppm mercury(II) acetate	153
Figure 6.7	(A) DLS curve, and (B) TEM image, showing the size distribution of AgNPs in the presence of Hg^{2+} ions	153
Figure 6.8	Energy dispersive spectrum(EDS) showing the presence of Hg atoms on the surface of AgNPs	154
Figure 6.9	Schematic representation of electrochemical displacement of Ag atoms by Hg^{2+} ions and its adsorption onto the nanoparticle surface.	154

Figure 6.10	Photographs illustrating the colour changes induced to AgNPs by the presence of Pb^{2+} ions (from left to right $[Hg^{2+}] = 0$ ppm, 1.45 ppm, 2.9 ppm, 4.35 ppm, 5.8 ppm, and 8.7 ppm)	155
Figure 6.11	(A) Changes in absorption spectra of AgNPs by the presence of varying concentrations of Pb^{2+} ions, and (B) plot of the area under the absorption curve in the range 500-700 nm as a function of Pb^{2+} concentration	155
Figure 6.12	(A) TEM image, and (B) DLS data showing the size distribution of AgNPs in the presence of Pb^{2+} ions	156
Figure 6.13	Schematic representation of the aggregate formation of AgNP induced by Pb^{2+} ions	157
Figure 6.14	Absorption spectra of AgNP solution in presence of (A) 0-12 ppm calcium(II) perchlorate, (B) 0-17 ppm nickel(II) acetate, (C) 0-19 ppm zinc(II) sulphate, (D) 0-33 ppm Cadmium(II) chloride and (E) 0-7 ppm magnesium(II) sulphate and (F) selectivity plot showing the absorbance difference at 400 nm between AgNPs in the absence and presence of different metal ions	158
Figure 6.15	chematic representation illustrating the basic principle of colour photographing using a mobile phone camera. The Graphical user interface (GUI) of the developed application for metal ion sensing is also shown	159
Figure 6.16	Variation in R, G, and B values in nanoparticle's photograph in the presence of varying concentrations of Hg^{2+}	160
Figure 6.17	Plots showing variation in (A) S value and (B) B value of nanoparticle's photograph in the presence of varying concentrations of Hg^{2+} ions.	161
Figure 6.18	Variation in R, G, and B values in nanoparticle's photograph in the presence of varying concentrations of Pb^{2+}	162
Figure 6.19	(A) Linear variation in H value, and (B) linear variation of R+G value, in nanoparticle's photograph in the presence of varying concentrations of Pb^{2+}	163
Figure 6.20	Schematic representation of the algorithm developed for metal ion distinction and quantification.	164
Figure 6.21	Snapshot of the developed android application's GUI showing the user controls marked as 1. colour of the reference sample i.e. pure AgNP already in the database, 2. button for updating the reference, 3.button for loading a new data for analysis 4. colour of the recently selected ROI, 5. panel showing the colour chart based on the concentration for easy interpretation of the results, and 6. panel showing the predicted results.	165
Figure 6.22	Developed android application screen (i) step 1: loading the reference sample (pure AgNP) data, (ii) step 2: select the ROI from the reference sample's photograph, (iii) step 3: saving the reference sample image into the database, (iv) step 4: updated the reference sample details and load a new sample, (v) step 5: select the ROI, and (vi) step 6: determined and quantified the metal ion present in the sample as lead and quantified as < 3 ppm.	166
Figure 6.23	Predicted vs actual concentration of (a) Pb^{2+} ions and (b) Hg^{2+} ions using colour values from ImageJ, using the mobile app and from absorbance curve.	167
Figure 6.24	Details of calibration data used for quantifying Hg^{2+} ions from tap water (A) colour photograph of the AgNP solutions in the presence of varying	168

concentrations of Hg^{2+} ions (from left to right $[\text{Hg}^{2+}] = 0, 2, 26, 35$ and 42 ppm) and corresponding variations in (B) area under the curve 320-500 nm, (C) B values, and (D) absorption spectra of AgNP solutions in the absence and presence tap water spiked with 15 ppm Hg^{2+} ions. Inset shows the corresponding photographs of AgNP solutions.

LIST OF TABLES

Table No.	Title	Page
Table 2.1	Component list with price details	33
Table 2.2	Peak positions of CFL lamp emission spectrum	42
Table 2.3	Comparison of the observed and reported Raman peaks of analyzed chemicals	44
Table 3.1	Comparison between the optical components used in tabletop and portable version	56
Table 3.2	Specifications of the commercial device and the fabricated system	64
Table 3.3	Comparison of the peak positions observed from the confocal microscope, the developed portable device and reported values	65
Table 3.4	Prepared and predicted ethanol concentration in laboratory prepared mixtures	70
Table 3.5	Component list of fabricated portable Raman spectrometer with price details	72
Table 4.1	Lorentzian function parameters utilized to create the synthetic Raman spectrum	86
Table 4.2	R^2 value and recovered peak intensities of the extracted spectra with RIA	91
Table 4.3	R^2 value and recovered peak intensities of the extracted spectra from Figure 4.12 A with different r values in SCARF	93
Table 4.4	R^2 value of the extracted spectra of data with different n values in SCARF and (r,s)=(30,40).	94
Table 4.5	R^2 value and recovered peak intensities of the extracted spectra with single-pass and double-pass SCARF.	95
Table 4.6	R^2 value and recovered peak intensities of the extracted spectra with I-Mod-Poly background removal.	97
Table 4.7	SNR of experimental spectra before and after noise removal.	98
Table 4.8	List of chemicals selected for spectral database creation.	99
Table 4.9	The calculated correlation coefficient for paracetamol sample with library database. The highest correlation coefficient marked in red	102
Table 5.1	List of pharmaceutical tablets used for the study	115
Table 5.2	Important vibrational frequencies of ACE And PARA	123
Table 5.3	Actual and predicted concentration of API from test data using PCR, Mod-PCR1 and Mod-PCR2 models	130
Table 5.4	Comparison of RMSE and R^2 value of the quantification models	131
Table 5.5	Actual and predicted concentration of API for genuine and fake equivalent samples	132
Table 5.6	Confusion matrix for three different methods at a selected threshold	133

Table 5.7	Calculated TPR and FPR at different threshold levels	133
Table 5.8	Comparison of results obtained from HPLC and the developed standalone application	137
Table 6.1	Important vibrational frequencies of the DHCA capped AgNPs	150
Table 6.2	Variation in RGB and HSV values of photographs of AgNP solutions containing different Hg ²⁺ ion concentrations	160
Table 6.3	Variation in RGB and HSV values of photographs of AgNP solutions containing different amounts of Pb ²⁺ ions	162

LIST OF ABBREVIATIONS

2D	Two dimensional
3D	Three dimensional
a.u.	Arbitrary unit
ABS	Acrylonitrile Butadiene Styrene
ABV	Alcohol by volume
ACE	Aceclofenac
AgNO ₃	Silver nitrate
AgNP	Silver nanoparticle
AI	Artificial intelligence
APD	Avalanche photodiode
API	Active pharmaceutical ingredient
Ar ⁺	Argon ion
AUC	Area under the curve
B	Blue
B _{ref}	Blue reference
CARS	Coherent anti-Stokes Raman scattering
CC	Correlation coefficient
CCD	Charge-coupled device
CdCl ₂	Cadmium chloride
cm	Centi meter
CMOS	Complementary metal-oxide semiconductor
DC	Direct current
DHCA	3,4-dihydroxyhydrocinnamic acid
DLS	Dynamic light scattering
DPSS	Diode pumped solid state laser
EDAX	Energy dispersive x-ray analysis
EDS	Energy dispersive spectrum
EM	Electromagnetic

Eu	Europium
FDA	Food and drug administration
FL	Focal length
FN	False negative
FP	False positive
FPR	False positive rate
FT	Fourier transform
FTIR	Fourier transform infrared spectroscopy
FWHM	Full width half maximum
G	Green
GC	Gas chromatography
GPHF	Global pharma health fund
G _{ref}	Green reference
GUI	Graphical user interface
He-Ne	Helium-neon
Hg	Mercury
HgCl ₂	Mercury(II) chloride
HPLC	High-performance liquid chromatography
HSV	Hue saturation value
I-Mod-Poly	Improved modified polynomial fitting
IR	Infrared
KBr	Potassium bromide
Kg	Kilo gram
KTP	Potassium titanyl phosphate
Kv	Kilo volt
LASER	Light amplification by stimulated emission of radiation
LDA	Linear discriminant analysis
L-DOPA	Levodopa
LFIA	Lateral flow immunoassay
LOD	Limit of detection
M	Molar

M6	6 mm metric
MEMS	Microelectromechanical system
mg	Milli gram
min	Minute
mL	Milli litre
mm	Milli meter
mM	Milli molar
MPA	Moving point averaging
Mod-Poly	Modified polynomial fitting
Mod-PCR1	Modified pcr regression with 1 component
Mod-PCR2	Modified pcr regression with 2 components
ms	Milli second
mW	Mill watt
NA	Numerical aperture
NaOH	Sodium hydroxide
ND	Neutral density
Nd:YAG	Neodymium-doped yttrium aluminium garnet
NIR	Near-infrared radiation
nm	Nano meter
NMR	Nuclear magnetic resonance
ORS	Orbital raster scan
OS	Operating system
PAD	Paper analytical devices
PARA	Paracetamol
Pb	Lead
$\text{Pb}(\text{ClO}_4)_2 \cdot 3\text{H}_2\text{O}$	Lead(II) perchlorate trihydrate
PC	Personal computer
PCA	Principal component analysis
PCR	Principal component regression
PDMS	Polydimethylsiloxane
pH	Potential of hydrogen

PLA	Polylactic acid
PLSR	Partial least square regression
PMT	Photomultiplier tube
POC device	Point of care device
PPM	Parts per million
PTFE	Polytetrafluoroethylene
R	Red
RIA	Range Independent background subtraction algorithm
RMSE	Root mean square error
ROC	Receiver operating characteristic
ROI	Region of interest
Rref	Red reference
RS	Raman spectroscopy
RS232	Recommended standard 232
s	Second
SBR	Signal to baseline ratio
SCARF	Savitzky–Golay coupled advanced rolling circle filter
SDK	Software development kit
SERS	Surface-enhanced Raman spectroscopy
S-Golay	Savitzky–Golay filter
SNR	Signal to noise ratio
SNV	Standard normal variate
SVM	Support vector machine
Tb	Terbium
TEC	Thermoelectric cooler
TEM	Transmission electron microscope
TiO ₂	Titanium dioxide
TLC	Thin-layer chromatography
TN	True negative
TP	True positive
TPR	True positive rate

USB	Universal serial bus
USD	Us dollar
UV	Ultra violet
WHO	World health organization
WiRE	Windows®-based Raman Environment
"	Inch
%	Percentage
% W/W	Weight percentage
°	Degree
°C	Degree celsius
μL	Micro litre
μm	Micrometre
Φ_{em}	Fluorescence emission quantum yield
$\Delta\nu$	Frequency shift
λ	Wavelength
λ_{exc}	Wavelength of the excitation laser
λ_{Raman}	Wavelength of Raman scattered light

PREFACE

Spectroscopy has become an important aspect of many modern devices and form the heart of many sensors, such as for material composition analysis and disease diagnostics. The latest technological advances have brought a lot of progress in this area leading to the introduction of several portable spectroscopic devices for point of care applications. A dramatic increase in counterfeit drugs has been observed in the past few decades posing threat to public health. The challenge for public health safety officers is to identify and discard the poor quality medicines available on the market. However, the availability of easy and robust quality testing methods for determining counterfeit drug is an unmet need. The use of specialized inks and packaging materials has been used for simple visual and quality inspections and served authentication tools in the past. Increased counterfeiting sophistication techniques in packaging and labelling imitations are becoming nearly perfect, making it extremely difficult to distinguish from genuine drugs through simple analysis, which necessitated the need for detailed chemical analysis of the drugs for the identity of APIs and composition estimation. Drug content analysis is done through analytical equipment like GC, HPLC, which is bulky and costly and unsuitable for onsite analysis. Similarly, environmental pollution is one of the serious issues faced by the entire globe. The most important one is the pollution of aquatic bodies. Mercury and lead are the two heavy metals considered to be the most toxic that pollute aquatic systems and pose a life-threatening danger to living beings. Presently, their estimation also requires sophisticated analytical instruments such as mass, atomic absorption and emission spectroscopies. Therefore, there is an unmet global need to develop portable and cost-effective devices and methodologies that are easy to perform, have fast response, high sensitivity, and selectivity. The current thesis focuses on developing spectrophotometric methodologies for fast quality analysis of pharmaceutical product as well as drinking water.

Over the years, Raman spectroscopy has evolved as a molecular fingerprinting and non-destructive technique. Presently, Raman spectrometers are available in handheld versions opening new possibilities for point of care and testing applications. However, this requires gaining in-depth knowledge through extensive fundamental studies on the various factors contributing to the observed Raman signal and

developing the know-how to use spectral information for a specific application. Similarly, smartphones have become an inevitable part of human life. Most of them have capabilities to be used as minicomputers, enabling advanced technologies like artificial intelligence and machine learning to pocket-size devices. Smartphone usually comes with sensitive cameras, and incorporating image processing techniques opens up possibilities for low-cost photometric and colourimetric measurement systems for a broad range of chemical analysis.

The first part of the thesis focuses on developing a model Raman system, a comparative study of various signal processing methods, Raman spectral studies of an identified class of pharmaceuticals, develop data processing methods for qualitative and quantitative estimations. In the second part of the thesis, the potential of a silver nanoparticle-based system for colourimetric sensing of two toxic metal ions from water is investigated. Further, the feasibility of using the smartphone as a spectrochemical device for aiding their automated colourimetric detection and quantification was also studied.

Chapter 1 gives an overview of the existing spectroscopic techniques used for onsite analysis with emphasis on Raman spectroscopy and smartphone spectroscopy. A literature review of the applications of spectroscopic technique for quality analysis in the pharmaceutical industry and water quality analysis in environmental studies is also included.

In chapter 2, we describe the feasibility of setting up a Raman spectrometer on an optical benchtop. Different properties of each of the optical components and how they influence the quality of the spectra has been discussed. For the setting up of the model system the following components were used, (i) green laser pointer (JD-851) as the excitation source, (ii) probe optics with backscattering configuration and a compact spectrometer (Science surplus) having ~450-700 nm spectral range and ~1 nm spectral resolution. It was equipped with 1800 g/mm plane ruled reflection grating, 50 μ m slit, and sony ILX linear CCD detector.

In chapter 3, the translation of the tabletop Raman spectrometer into a portable device is described. To evaluate its performance, various standard samples were analyzed and were compared with a commercial Raman spectrometer system. In general, for all the compounds investigated, we found a good agreement between the results obtained from the commercial device and the fabricated system. The potential of the fabricated system for quantitative analysis of alcoholic beverages was also

investigated.

The development of software tools for the portable Raman spectrometer enabling automatic spectral processing and library matching is described in chapter 4. Raman effect being weak, the spectroscopic data out of it has low SNR, and it is essential to evolve apt signal processing methodologies to extract any meaningful information. The main identified contributions to noises are (i) low-frequency fluorescence background, (ii) high-frequency electronic noises like dark current and readout noise, (iii) photon flux dependent noise and (iv) stray light. The effect of dark current, readout noise and stray light has been removed by subtracting the blank spectrum from the acquired sample spectrum. The efficacy of different methods like digital filtering, polynomial based fitting and moving point average based methods for low-frequency background removal has studied. Further to automate molecule identification, a library matching algorithm was employed, and its prediction accuracy was studied. A Raman spectral library of 24 different chemicals was generated using the spectrum collected from the fabricated system, and the automatic identification ability of the developed algorithm was demonstrated.

In chapter 5, we have attempted to combine the versatility of Raman spectroscopy with chemometrics for pharmaceutical product quality analysis. The work involves determining the active ingredients in commercially available tablets. The study was conducted on a model system of Aceclofenac-Paracetamol mixture. A new quantification model was developed using MATLAB programming environment with PCA (Principle component analysis) combined with polynomial regression. This modified method was compared with traditional PCR using statistical parameters like ROC, RMSE, correlation coefficient etc. Results showed that the modified algorithm is having better quantification accuracy than other methods. Using the developed algorithm, a standalone application was built, which could be incorporated into portable Raman spectrometers.

In chapter 6, a novel method for the identification of heavy metal ion from aqueous media using a smartphone as a spectroscopic device has been discussed. We explored a silver nanoparticle (AgNP) based system exhibiting high selectivity and distinct spectrophotometric behaviour towards lead and mercury ions in the aqueous medium. Our studies revealed that most of the metal ions did not influence the characteristic plasmon spectral profile of AgNPs. On the contrary, mercury caused the disappearance of absorbance at ~400 nm. Consequently, the yellow solution became

colourless at around 7.6 ppm of Hg^{2+} ions. While the presence of Pb^{2+} ions induced a decrease in the initial plasmon intensity with the concomitant emergence of a new red-shifted band above 500 nm. As a result, the colour of the solution turned from yellow to red. These colour changes are found to fall well within the spectral responses of R, G and B filters of the digital camera. By making use of this, an android mobile application was developed for digitizing the colour values and for doing further quantitative analysis. The observed linearity in the absorbance spectral changes of nanoparticle solutions and the RGB values of their photographs opened up possibilities for quantitative estimation of Hg^{2+} and Pb^{2+} ions.

References

1. **Emmanuel, N.;** Nair, R. B.; Abraham, B.; Yoosaf, K., Fabricating a low-cost Raman Spectrometer to introduce students to spectroscopy basics and applied instrument design. *J. Chem. Educ.* 2021, 98(6), 2109-2116.
2. **Emmanuel, N.;** Haridas, R.; Chelakkara, S.; Nair, R. B.; Gopi, A.; Sajitha, M.; Yoosaf, K., Smartphone assisted colourimetric detection and quantification of Pb^{2+} and Hg^{2+} ions using Ag nanoparticles from aqueous medium. *IEEE Sens. J.* 2020, 20 (15), 8512-8519.

An Overview of Recent Developments in Portable Spectroscopic Devices for Chemical Analysis



1.1. Abstract

Spectroscopy, the study of interaction of light with materials, has emerged as an analytical technique and forms the heart of many sensors for composition analysis of samples and diagnosis. Advancements in electronics, optics, and artificial intelligence have introduced several portable technologies like Raman spectrometers, smartphone spectrometer, X-ray fluorescence spectrometers for point of care applications. The use of these kinds of portable devices helped to improve the quality of services in various areas, especially in the health care and environmental sectors. Recent years have witnessed a dramatic increase in counterfeit drugs posing threat to public health. The availability of accessible and robust quality testing methods for determining counterfeit drugs is an unmet need. Environmental pollution is yet another severe

issue faced by humankind ever since civilisation. Ensuring water quality is essential for sustaining the good health of humans and other life forms. Presently, these two issues are addressed through sophisticated analytical instruments that are not suitable for onsite analysis. Therefore, there is an unmet global need to develop portable and cost-effective devices and methodologies that are easy to perform, having fast response, high sensitivity, and selectivity. The present chapter gives an insight into spectroscopy-based onsite analytical instruments, with special emphasis on Raman spectroscopy and smartphone spectroscopy.

1.2. Introduction

Spectroscopy denotes the techniques utilising electromagnetic (EM) radiation to obtain information on matter's structural and functional properties. Over the years, spectroscopy has evolved as a valuable tool to solve various analytical problems. In general, EM radiation interacts with matter, resulting in various processes like absorption, emission, scattering, etc. Different spectroscopic techniques exist today for chemical analysis depending on the species under study (atom/molecule), the energy of EM radiation, and the type of monitored interaction. However, the ultimate principle shared by all these techniques is shining a beam of EM radiation onto the sample, measure their response, and use this information to understand the analyte. From an instrument point of view, these devices consist of a light source to provide energy into matter, an optical unit and a detector to collect and measure the generated photons from the sample, and a signal processing unit to display the response in the form of spectra.¹

The conventional spectroscopic techniques rely on sophisticated laboratory equipment operating under controlled condition. For testing, the sample needs to be carried to the laboratory, where a trained professional will perform the sample

analysis, providing accurate results depending upon the device's resolution and the technician's proficiency. Along with these, the struggle in making informed decisions on the spot has forced to introduce the concept of 'moving laboratory to the point of need'. The recent efforts in this direction led to the development of handheld or portable devices which are easy to handle even by a layperson.² Figure 1.1 represents some examples of the current generation spectroscopic devices for onsite analysis like a simple pulse oximeter routinely used in clinical settings,³ vibrational spectroscopic instruments like Raman spectrometer⁴ and IR spectrometer for molecular analysis, X-ray fluorescence spectrometer for elemental analysis, etc. In the last decade, several smartphone integrated devices have been introduced. These include a tiny pocket-size Scio NIR spectrometer developed by M/s Consumer Physics for food analysis,⁵ Artificial intelligence (AI) integrated smart Raman spectrometer from M/s CloudMinds,⁶ M/s Goyalab's Gospectro multipurpose smartphone spectrometer,⁷ smartphone integrated colourimetric devices for analyte detection,^{8,9} etc. These



Figure 1.1. Photographs illustrating examples for different portable spectroscopic devices for onsite analysis (A) pulse oximeter, (B) handheld Raman spectrometer from Metrohm, (C) GoSpectro handheld spectrometer from GoyaLab, (D) Scio pocket-size NIR spectrometer, (E) A2 Technologies's FTIR spectrometer for soil analysis, (F) Cloud AI handheld Raman spectrometer, (G) smartphone colourimetric analyser for food adulterant detection and (H) X-ray fluorescence spectrometer from Lanscientific.

technologies have proven their usage in various areas like environmental analysis,¹⁰ agricultural fields,¹¹ biomedical science,¹² pharmaceutical industry,¹³ etc.

1.2.1. Counterfeit Drugs

In the pharmaceutical industry, checking the quality and authenticity of medicines is essential. Recent years have witnessed a dramatic increase in counterfeit drugs, posing a threat to public health and the economy. According to the World Health Organization (WHO), 'A counterfeit drug¹⁴ is deliberately and fraudulently mislabeled for identity and/or source'. Counterfeit products may include the following variants; (i) drug having very little or no active pharmaceutical ingredient (API); in this case, the patient does not get harmed directly but gets affected indirectly through prolonged sickness due to delayed treatment. Also, antibiotic resistance may be wrongly diagnosed as a result of the ineffectiveness of the counterfeit drug.¹⁵ (ii) Drugs having the wrong API; this scenario would be similar to the patient taking another drug instead of the prescribed one without knowing it. (iii) Drugs having all necessary APIs but in the wrong quantities. (iv) Drugs having no API but harmful ingredients; here, the patient may develop unexpected adverse drug reactions leading to even death. India is the third-largest drug manufacturer around the globe, with an annual turnover worth Rs. 1,29,000 crore in 2018. With such a huge market, there are tremendous possibilities for counterfeiters.

According to a study conducted by WHO in 2002, around 20% of the drug in the Indian market are counterfeit.¹⁶ In a random survey conducted on drugs, 5% in Chennai and 12% in Delhi failed the quality test.¹⁷ Based on research conducted by the European Commission, around 75% of the reported counterfeit cases in the global market originated from India. In 2001, ~1000 Kg of fake raw materials and ~660 Kg of counterfeit medicines with the logo of a reputable pharmaceutical company were

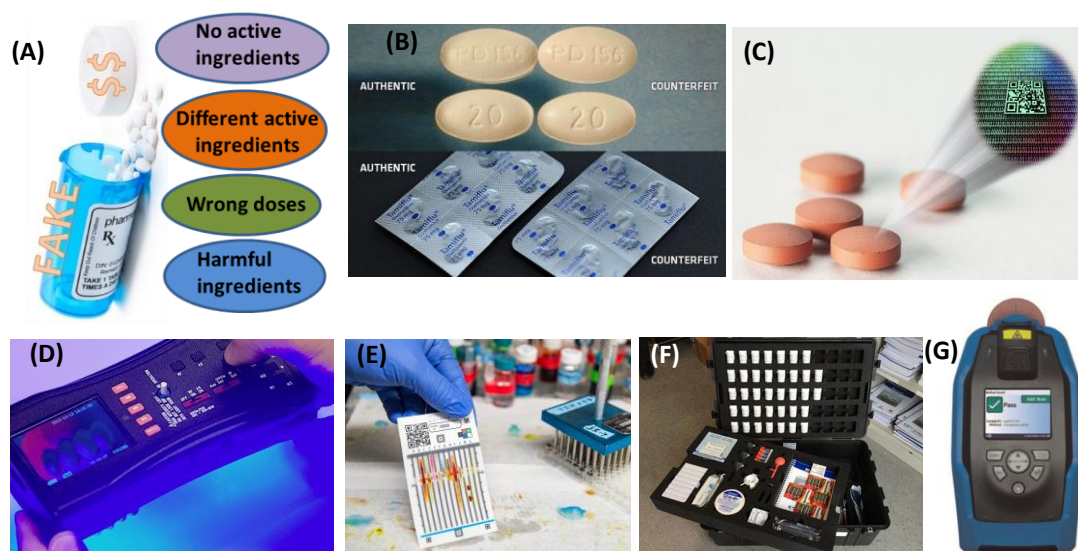


Figure 1.2. (A) Types of counterfeit drugs, (B) image showing the package and tablet of genuine and counterfeit artesunate antimalarial tablets, and (C-G) different portable detection techniques for pharmaceutical analysis (C) TrueTag Micro tag tablets, (D) US FDA's CD3 detector, (E) Paper analytical device, (F) GPHF Minilab TLC test kit, and (G) Thermofisher Truescan Raman spectrometer for pharmaceutical raw material analysis.

ceased by police from a factory in India.¹⁴ The challenges for the health department are the timely identification and clearance of the fake medicines available on the market. However, easily accessible and robust quality testing devices for determining counterfeit drugs are an unmet need. Specialised inks and packaging materials have served as simple authentication tools in the past. However, sophisticated counterfeiting techniques have made fairly close imitations of packaging and labels, making it extremely difficult to distinguish them from genuine drugs through simple analysis. This necessitates the need for detailed chemical analysis for the content and composition. Analytical equipment like GC, HPLC are perfect for material identification and composition estimation. However, the bottleneck for onsite analysis is their bulkiness, high cost, and elaborate process. Although a few portable technologies are available, each of them has its limitations. For analysing fluorescence from the authentic packages, a portable device was developed by USA's FDA agency¹⁸ where the analysis occurs only at packaging levels, thus unable to find fake

drug hidden under the legitimate package. Colourimetric paper analytical devices (PAD)¹⁹ developed by USA researchers for API identification are cost-effective, but they are not suitable for all class of drugs. Moreover, this is a destructive technique. Product tracking through edible imprinted codes like nanotags (developed by M/s TrueTag Technologies),²⁰ is a promising technique, however, it requires modification in the existing manufacturing process. A briefcase type counterfeit drug detection kit, GPHF Minilab, was developed by the Global Pharma Health Fund, which performs the drug content analysis mainly by TLC along with other physical tests like visual inspection, weight verification, and disintegration test.²¹ This technique is slow, destructive and requires specific chemicals and reagents for different types of drugs. Ideally, the detection method needs to be non-destructive, aiding large volume medicine analysis in a short duration.

1.2.2. Heavy Metal Toxicity

In environmental science, ensuring water quality is essential for sustaining the good health of humans and the existence of other life forms. Mercury and lead are the two heavy metals considered to be the most toxic that pollute aquatic systems and pose a life-threatening danger to living beings. The sources of water contamination are both from humans as well as from natural interventions. For example, lead is one of the components in many consumer products like batteries, paints, pigments, electronics, plastics, cable sheathing, ceramics, etc. Through their unwise disposal and consequent leaching, lead ions reach water bodies.²² Due to the vast global abundance and distribution, natural forces like volcanoes and forest fires also accelerate lead ions flow into water bodies.²³ Similarly, apart from the innate degassing of the earth's surface, human activities like gold mining, solid waste incineration, coal-burning power plants, etc., are the foremost sources of mercury pollution. The complications

arising from the intake of polluted water include malfunctioning of organs like kidneys, reproductive systems, central nervous system, and gastrointestinal tract.^{24,25} Mercury consumption also contributes to physiological stress, hypertension^{26,27} and affects biological processes like haemoglobin synthesis. Exposure to heavy metals at higher doses by pregnant women may even damage the fetus. Presently, their estimation requires sophisticated analytical instruments such as mass, atomic absorption, and emission spectroscopies, which suffer from various limitations like high cost, complex sample preparation, need of trained professionals etc. Alternatively, emerging technologies like chemical and optical nanosensors²⁸ can detect toxic heavy metals, which work based on colourimetric detection. These methodologies are relatively inexpensive and the detection is easy even with the naked eye.²⁹ To make this technology suitable for field applications and fully automated, integrating the same with a smartphone is a feasible option.³⁰

1.2.3. Spectroscopy for Onsite Analysis

In this regard, the present thesis describes the development of two distinct spectroscopic methodologies based on Raman scattering and smartphone technology for onsite analysis of pharmaceutical products and drinking water. The first part of the thesis focuses on developing a model Raman spectrometer, a comparative study of various signal processing methods, Raman spectral studies of an identified class of pharmaceuticals, and developing data processing methods for qualitative and quantitative estimations. In the second part of the thesis, the potential of a silver nanoparticle-based system for colourimetric sensing of two toxic metal ions from water is investigated. Further, we studied the feasibility of utilising the smartphone as an analytical device for aiding their automated colourimetric detection and quantification.

1.3. Raman Spectroscopy

Raman spectroscopy (RS) is a type of vibrational spectroscopic technique capable of providing a structural fingerprint of molecules non-destructively. It is based on the concept of inelastic scattering invented by C.V. Raman,³¹ who received the Nobel prize in Physics in 1930. When photons interact with molecules in a solid, liquid, or gas, most photons get scattered without any change in energy of incident photons and this type of scattering is known as the Rayleigh scattering or elastic scattering. A small proportion of the incident photons, i.e. around 1 in 10 million photons, gets scattered with a shifted frequency/energy compared to that of the incident photon. This phenomenon is known as the Raman effect or inelastic scattering. The difference in energy is termed the Raman shift. The interacting photon causes a change in the vibrational energy levels of materials. If incident radiation causes a transition into

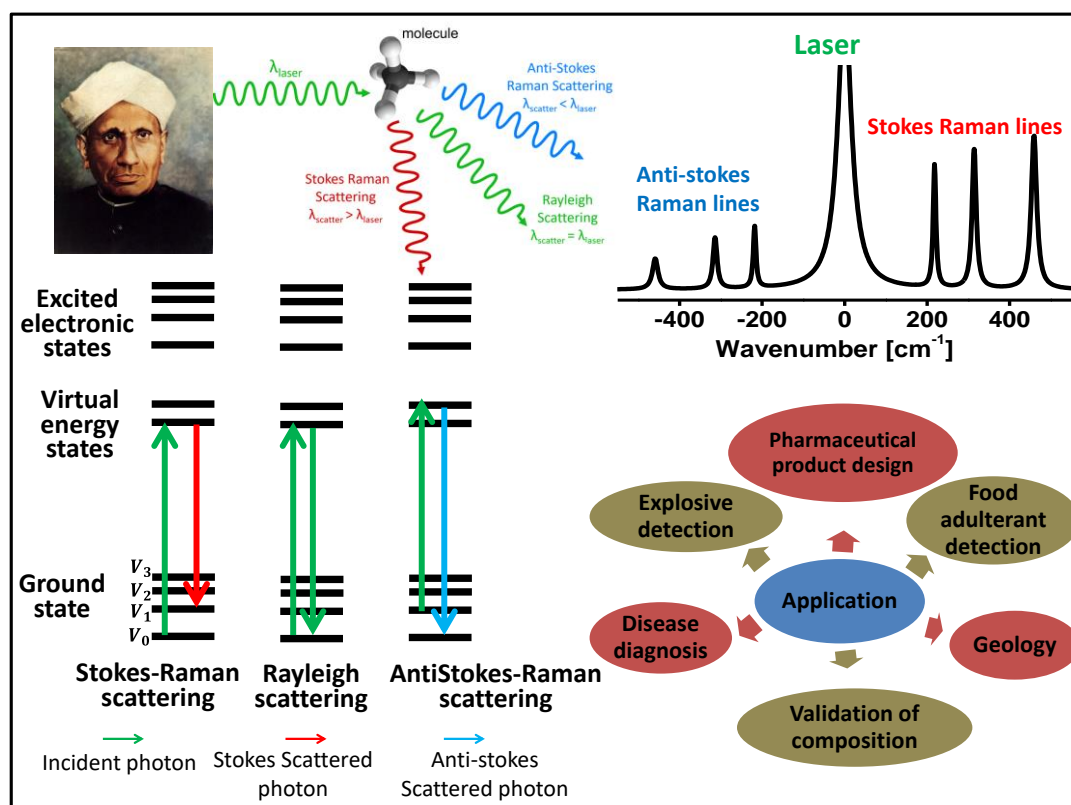


Figure 1.3. Principle and applications of Raman spectroscopy.

higher energy levels of materials, the scattered photons will have reduced energy/frequency which is called a Stokes shift. If the molecular transitions are to a lower level, the scattered photons will have higher energy/frequency and are known as anti-Stokes shift. Therefore, the difference in energy or the Raman shift corresponds to molecular vibrational transitions, and hence RS allows collecting molecule's vibrational signature.

1.3.1. Instrumentation of Raman Spectroscopy

Depending on how the scattered photons are measured, two types of Raman spectrometer configuration are available (i) Fourier Transform (FT) and (ii) dispersive Raman spectrometer. Dispersive spectrometers have diffraction grating or prism for splitting the collected radiation into its frequency components and measure individual frequencies using a photo-sensitive element. FT based spectrometer (originally developed for IR spectroscopy) employs a moving mirror-based interferometer and an IR detector to measure the scattered light's frequency. FT-Raman spectroscopy was introduced in 1986, and it is now available as a bolt-on to many IR spectrometers³² and it generally uses a 1064 nm laser.³³ The viability of FT Raman spectrometer with a visible laser was recently demonstrated by Dzsaber, S. et al.³⁴ On the other hand, dispersive spectrometers are available in diverse configurations and works with visible and NIR lasers. Also, it has got the distinct advantage of a few orders higher

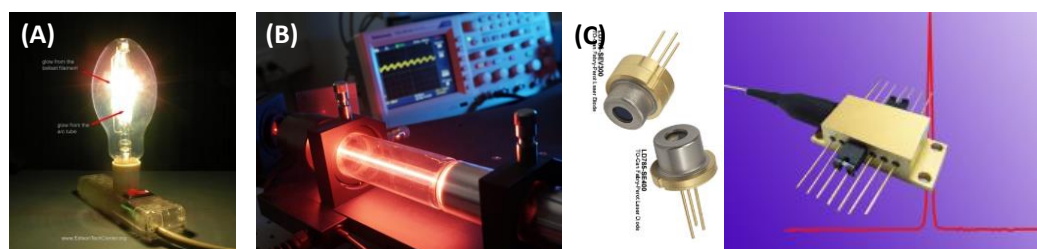


Figure 1.4. Different light sources (A) mercury arc lamp, (B) bulky gas lasers (e.g. He-Ne), and (C) small footprint laser diodes, used in the previous and current generation Raman spectrometers.

sensitivity compared to the FT systems.

The components of a dispersive Raman spectrometer are an excitation light source, probe optics, and a detector. Figure 1.4 represents the various generations of light sources used in the Raman spectrometer. In the beginning, exploring the full capabilities of RS was restricted by the unavailability of apt light sources; the mostly used ones being mercury arc lamps. Later in the 1970s, a highly intense, monochromatic, and coherent light source, i.e. LASER, was introduced and revolutionised RS. Initially developed gas lasers (e.g. Argon ion laser and He-Ne lasers) were mostly bulky; however, nowadays small footprint tiny laser diodes offer help in realising miniaturised devices. Raman probe consists of optics for focusing the laser into the sample and collecting the scattered light from the sample. Additional filters are used to separate the weak Raman scattered photons from intense Rayleigh scattered signal. Raman scattered radiation occurs in all directions, giving freedom in designing the probe optics. Based on the relative orientation of the excitation beam and scattered light collection path, different probe optics configurations for RS exist and are generally classified into four types (Figure 1.5). These are (i) transmission probe optics, where the excitation laser and detector unit are on the opposite sides of the sample, (ii) spatially offset RS, where the scattered light is collected from a spatially offset point from the excitation laser, (iii) 90-degree probe optics, as the name indicates here the excitation and collection paths are at an angle of 90 degrees, and (iv) backscattering probe optics, where the same optics is used for both excitation

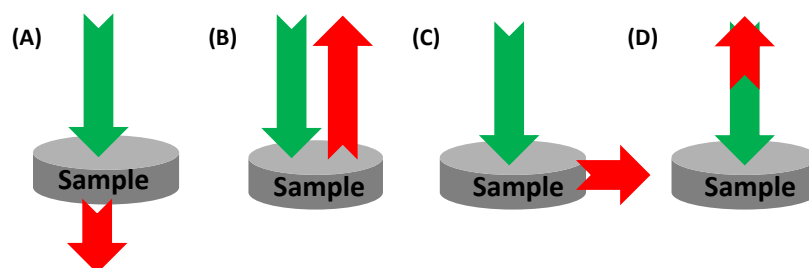


Figure 1.5. Different probe optics configurations of Raman spectrometers (A) transmission, (B) spatially offset, (C) 90 degree, and (D) backscattering.

and collection. Finally, a spectrometer measures this signal. Figure 1.6 represents the evolution of the Raman detector unit. The spectrometers used by C. V. Raman for measuring the first spectra composed of a prism as the dispersive element and a photographic plate as the detector. Next-generation devices were equipped with single-point sensors like photomultiplier tubes (PMT) or later avalanche photodiodes (APD) and rotating prism/grating. The latest generation detector mainly consists of CCDs in combination with the diffraction grating.

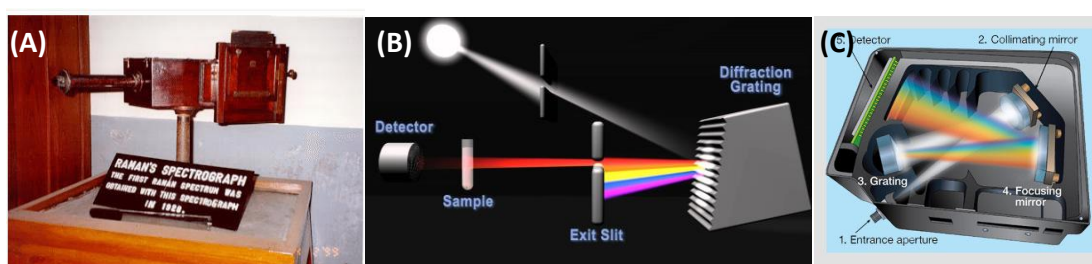


Figure 1.6. Different detector systems (A) spectrometer used by C.V Raman for recording the first Raman spectra, (B) rotating grating and single point detector-based spectrometer, and (C) linear array CCD spectrometer.

1.3.2. Advantages and Limitations of Raman Spectroscopy

The frequency of bond vibrations depends on the interatomic binding energy. This in turn depends on the bond strength, bond length, mass of the interacting atoms, the angle between the bond etc.³⁵ Consequently, molecular vibrations provide unique structural fingerprint information about materials, facilitating material identification. Raman and IR are the two spectroscopic techniques that exclusively probe molecular vibrations. They differ mainly in their operational principle; Raman measures the scattered photons while IR examines the absorbed radiation. These vibrational spectroscopic techniques offer many advantages over other spectroscopic methods. For example, X-ray crystallography provides absolute determination of structure however, it is quite expensive and often limited to small compounds that can crystallize; mass spectroscopy can identify the empirical formula but the

determination of functional groups is arbitrarily dependent on how the molecule fragments; nuclear magnetic resonance spectroscopy (NMR), is limited to the type of samples having nuclei that will give useful spectra. While vibrational spectroscopy can identify the structure and functional groups and is suitable to any compound having a covalent bond whether organic or inorganic without any constraints on the physical state (liquid, solid, crystal, powder, gas) of the sample, unlike others. Additionally, it is cost-effective and analysis is less time-consuming thus they are best suited for the initial examination of a completely unknown material.³⁶ Therefore, Raman and IR have been widely used in both research and industry for chemical analysis.

In contrast with absorption-based IR spectroscopy, RS relies on scattering, offering considerable flexibility to instrumental designs and sample handling. IR spectroscopy requires unique sample preparation protocols to be followed; mainly, the sample needs to be analysed in powdered form by mixing it with non-interfering materials like KBr. The solution state analysis requires sample holders made of specific materials. In contrast, the Raman spectrum can be acquired directly from liquid, gases, and solids and in some cases without opening bottles and packages. With the advent of new generation lasers and optical components, Raman spectra can currently be acquired even with handheld and battery-operatable systems, which have elevated their potential for onsite and point of care applications.

A significant limitation of RS is its inherently weak signal intensity due to the inadequate scattering cross-section; however, this was solved by signal enhancement techniques like Resonance Raman spectroscopy, Surface-enhanced Raman spectroscopy (SERS),³⁷ Coherent anti-Stokes Raman scattering (CARS)³⁸ etc. Another issue is extracting weak Raman scattered signal from intense fluorescence signal, especially with lower excitation wavelengths. Employing an excitation laser at

a higher wavelength (785 nm/1064 nm) helps to reduce this issue. However, the signal intensity is then compromised. Fortunately, numerous methods for minimising fluorescence noise have been proposed based on either hardware modifications or computational algorithms.

1.3.3. Noises in Raman Spectroscopy

Noise is a collective term for undesired signals other than Raman spectra, and it is grouped into two categories based on their frequency, (i) low-frequency background, and (ii) high-frequency noises.³⁹

The major sources of high-frequency noises are shot noise, dark noise, cosmic rays, and readout noises.⁴⁰ Photon shot noise is caused by the random nature of photons incident on the detector.⁴¹ The shot noise follows a Poisson distribution, i.e. directly related to the square root of the incident photon flux.⁴² A photodetector exhibits a small output even when no incident light is present, known as the dark noise which is due to the thermally generated charged particles and the same increases with the ambient temperature. Like shot noise, dark noise also follows a Poisson distribution; thus, dark noise is proportional to the square root of the dark current.⁴³ Readout noise is caused by electronic noise in the detector circuitry and it largely dictates the spectrometer's detection limit.

Low-frequency noises, often known as the baseline, are mostly caused by fluorescence. Simple optical filters cannot separate between fluorescence and Stokes Raman signals since they are in the same wavelength range. Fortunately, the characteristics of these signals differ in a variety of ways, and a range of fluorescence removal techniques for Raman measurements have been developed.

Time-domain: Scattering is an instantaneous process (on the order of picoseconds), while the fluorescence emission lifetime is much longer (a few nanoseconds). This

principle helps in separating fluorescence from Raman scattering through various time-domain methods⁴⁴ like excitation using pulsed lasers and polarisation-based studies.^{45,46}

Wavelength domain: With the change in excitation wavelength, the Raman scattered signal wavelength changes, whereas the fluorescence is independent of excitation wavelength. This property has led to various wavelength domain methods such as shifted excitation Raman difference spectroscopy.⁴⁷

SERS: The fluorescence signal will be quenched to a great extent when a molecule comes in direct contact with the metal surface, while the Raman signal will be intensely improved.⁴⁸

Even though the above methods effectively separate fluorescence signal from Raman scattering signal, they have got the following demerits. The time-domain methods need ultrafast lasers and time-gated electronics for spectrum collection. The wavelength domain methods require lasers with additional wavelengths for shifted excitation. Thus, these additional hardware modifications increase the complexity and cost of the device. In SERS technology, the samples are measured in the presence of plasmonic nanoparticles or substrates, thus compromising the non-destructive functionality of RS. On the contrary, software algorithms work based on the fact that Raman peaks are much narrower in bandwidth than fluorescence peaks. These are relatively simple and user-friendly. In chapter 4, we go through the computational-based noise reduction approaches in greater depth.

1.3.4. Raman Spectroscopy in Pharmaceutical Analysis

RS is currently being employed in the pharmaceutical industry for various quality testing purposes. FT-Raman spectroscopy has been utilised to study various solid-state forms of drugs,⁴⁹ quantifications of polymorphs,⁵⁰ and degree of crystallinity in pharmaceuticals.⁵¹

S. Sasic et al. combined RS with imaging to determine the spatial distributions of low-content (less than 1% weight concentration) API in commercial tablets.⁵² The content uniformity analysis of tablets⁵³ for in-line monitoring shows the capability of RS in quality control. Conventional backscattering RS has limitations in the bulk analysis of pharmaceuticals, as the data is mainly acquired from the surface. Recent studies show that configuring RS to transmission mode enables bulk analysis of capsules and tablets.⁵⁴⁻⁵⁶ Apart from content, analysis of packaging of pharmaceutical drugs has been carried out through RS. This helps identify the authentic package while the drug is packed in an aluminium packet where analysis without removing the package is impossible.⁵⁷

RS has also been applied for the quantification of API from various drugs. Quantitative information is gathered either by directly measuring the intensity of a specific peak⁵⁸ from the spectra or through multivariate regression analysis.^{59,60} More detailed information are provided in chapter 5.

1.3.5. Chemometric Analysis

Chemometrics is the area in science that extracts information present in chemical systems by developing mathematical or statistical methods. This helps to analyse vast and highly complex data sets to determine the properties of substances which is often very difficult to measure directly. Raman spectroscopic studies of closely related species are usually accompanied by chemometric analysis for efficient classification. These techniques essentially transform the complex multivariate data set into a new space with a minimum number of significant variables. The multivariate analysis used for the discrimination of dataset includes Principal Component Analysis (PCA),⁶¹ Support Vector Machine (SVM),^{62,63} Linear Discriminant Analysis (LDA),⁶⁴ etc. Quantification of components is often performed by applying various regression models⁶⁵ like Principal Component Regression (PCR), Partial Least Square Regression (PLSR), etc.

1.4. SmartPhone Spectroscopy

Smartphone-based technologies are gaining popularity in research and science for the last 10 years. This was possible due to their data capture and processing capability and wide availability at a low cost. Moreover, they contain various onboard sensors, like cameras, fingerprint sensors, gyroscopes, proximity sensors, gravity sensors, magnetic compass, ambient light sensors, etc. They can also be interfaced with external hardware for data acquisition. The imaging capability of the smartphone camera has been explored in multiple ways for spectroscopic applications, and some examples are presented in Figure 1.7. One way is to use optical components like a diffraction grating or prism or G-Fresnel for splitting the incoming light into its wavelength components and image it with the smartphone camera. The obtained information can be converted to spectral data through proper calibration of pixels against wavelength.⁶⁶ This principle has been demonstrated for easy detection of various analytes like haemoglobin in the blood,⁶⁷ proteins,⁶⁸ bisphenol from water,⁶⁹ etc.

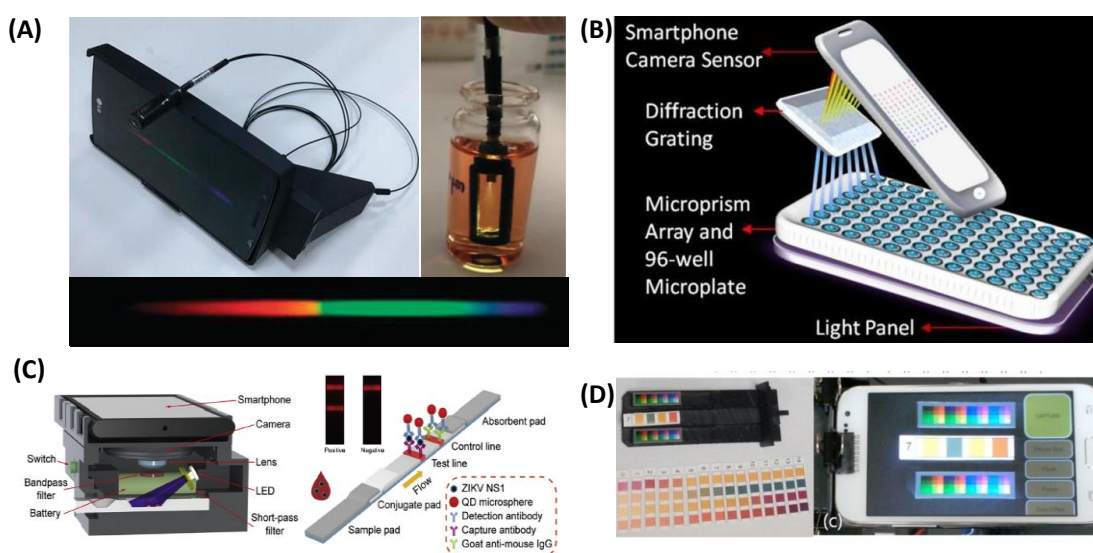


Figure 1.7. Pictures showing examples of various smartphone based sensing devices. (A) Bisphenol detection using an immersion probe, (B) 8 channel spectrometer for multiplex detection, (C) Zika virus detection through fluorescence measurement, and (D) colourimetric pH sensor.

Another key class of smartphone spectrometers is non-grating-based devices exploited for colourimetric detection. Herein, the colour of the light falling on the camera is directly measured. This concept has been explored mainly for fluorescence applications for detecting Zika virus,⁷⁰ pH,⁷¹ aerosol pollutants,⁷² metal ions,³⁰ etc. Alternatively, smartphones can be coupled with an external spectrometer having its own detection unit. In such cases, smartphones serve the purposes of data processing and displaying. Some of the examples are wirelessly connected ultra-compact device for non-destructive monitoring of fruit ripeness,^{73,74} MEMS (microelectromechanical system) architectures based spectrometers,⁷⁵ and tiny smartphone integrated Raman spectrometer with cloud computing.⁷⁶

1.4.1. Colour Detection

Colours are an interpretation of the human brain based on the limited spectral information received by the eyes. An object appears as coloured when it either transmits or reflects light of a particular wavelength region. The eye perceives the reflected light with the help of the cone cells having absorption in the visible range, as shown in Figure 1.8 A.

A digital camera consists of a 2D array of photosensory elements called pixels. Each pixel is equipped with a combination of red (R), green (G) and blue (B) filters which selectively pass a band of wavelengths in the visible range matching with the absorption characteristics of cone cells of the human eye. R, G, and B filters have transmission wavelength ranges of 700-600 nm, 600-500 nm, and 500-400 nm, respectively. The intensities of each of these primary colours are represented on an absolute scale of 0-255. Alternatively, colours are also digitally represented using various mathematical spaces called colour spaces, like CMYK, CIE, HSV etc.⁷⁷ For example, in the HSV colour code, each colour has a specific Hue (H) value varying from 0-360 degree, and a Saturation (S)

value ranging from 0-100 depending on the extent of the colour or its saturation, and Value (V) varies from 0-100 with the lighting conditions.

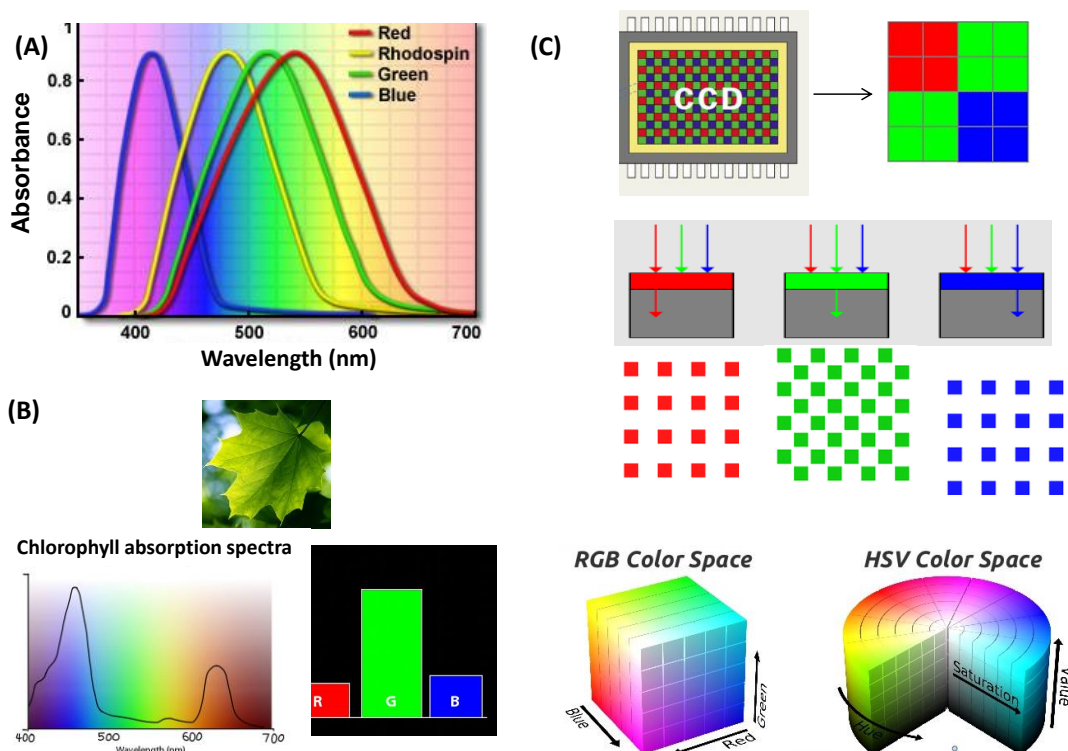


Figure 1.8. Principle of colour detection (A) absorption spectra of human visual pigments in eye, (B) spectra showing the light absorbed by chlorophyll pigment in green coloured leaf and the RGB colour values of its image,⁷⁸ and (C) principle of colour detection in a digital camera.

1.5. Objectives of the Thesis

The overall focus of the present thesis is to (i) conduct detailed studies on various factors contributing to the observed Raman signal and develop a portable prototype system, (ii) understand how to use spectral information for a specific application and develop suitable software methodologies for spectrum processing, (iii) conduct Raman spectral studies of an identified class of pharmaceuticals, develop data processing methods for qualitative and quantitative estimations. (iv) study the feasibility of employing a smartphone as a spectrophotometric device for water quality analysis. The second and third chapter deals with building a proof of concept of Raman

spectrometer with a component cost of less than 1000 USD and its performance evaluation. Different approaches for extracting the Raman spectrum from noisy background and algorithm for automatic identification of chemicals are described in the fourth chapter. In the fifth chapter, the application of RS for pharmaceutical analysis is explained. The work involves determining and quantifying the active ingredient from commercial tablets. The study was conducted on a model system of Aceclofenac-Paracetamol mixture. Finally, in the last chapter, the potential of a silver nanoparticle-based system for colourimetric sensing of two toxic metal ions from water is investigated. A smartphone application was developed for aiding their automated colourimetric detection and quantification.

1.6. References

1. Marczenko, Z.; Balcerzak, M., Chapter 2 - Principles of Spectrophotometry. In *Analytical Spectroscopy Library*, Elsevier: 2000; Vol. 10, pp 26-38.
2. Sharples, R. M.; Allington-Smith, J. R.; Buscher, D. F.; Content, R.; Haynes, R.; Myers, R. M., Recent developments in spectroscopy. *New. Astron. Rev.* **2001**, *45* (1), 77-81.
3. Jubran, A., Pulse oximetry. *Crit. Care.* **2015**, *19* (272), 1-7.
4. Metrohm handheld Raman spectrometer. <https://www.metrohm.com/en-in/products/spectroscopy/mira-handheld-raman-spectrometer/> (accessed 22/04/2021).
5. Damian, G.; Dror, S. Low-cost spectrometry system for end-user food analysis. US9377396B2, 2016.
6. Lynn, C.; Bill, H.; Tao Tao, M. In *A smart handheld Raman spectrometer with cloud and AI deep learning algorithm for mixture analysis*, Proc. SPIE 2019.
7. Goyalab GoSpectro handheld spectrometer. <https://www.goyalab.com/product/handheld-spectrometer-gospectro/> (accessed 22/04/2021).
8. Chen, A.; Wang, R.; Bever, C. R.; Xing, S.; Hammock, B. D.; Pan, T., Smartphone-interfaced lab-on-a-chip devices for field-deployable enzyme-linked immunosorbent assay. *Biomicrofluidics.* **2014**, *8* (6), 1-11.

9. McGonigle, A. J. S.; Wilkes, T. C.; Pering, T. D.; Willmott, J. R.; Cook, J. M.; Mims, F. M.; Parisi, A. V., Smartphone Spectrometers. *Sensors (Basel)*. **2018**, *18* (1), 223.
10. Tanner, P. A., Application of spectroscopic methods to environmental problems. *Spectrosc. Lett.* **2005**, *38* (3), 211-212.
11. Yeong, T. J.; Pin Jern, K.; Yao, L. K.; Hannan, M. A.; Hoon, S. T. G., Applications of photonics in agriculture sector: a review. *Molecules*. **2019**, *24* (10), 2025(38).
12. Sahu, R. K.; Mordechai, S., Spectroscopic techniques in medicine: The future of diagnostics. *Appl. Spectrosc. Rev.* **2016**, *51* (6), 484-499.
13. Buckley, K.; Ryder, A. G., Applications of Raman spectroscopy in biopharmaceutical manufacturing: a short review. *Appl. Spectrosc.* **2017**, *71* (6), 1085-1116.
14. Deisingh, A. K., Pharmaceutical counterfeiting. *Analyst*. **2005**, *130* (3), 271-279.
15. Roper, C.; Pearce, R.; Nair, S.; Sharp, B.; Nosten, F.; Anderson, T., Intercontinental spread of pyrimethamine-resistant malaria. *Science*. **2004**, *305* (5687), 1124.
16. Bate, R., Fatal pharmaceuticals: The Indian counterfeit drug market. *Georget. J. Int. Aff.* **2010**, *11* (1), 125-130.
17. Bate, R.; Tren, R.; Mooney, L.; Hess, K.; Mitra, B.; Debroy, B.; Attaran, A., Pilot study of essential drug quality in two major cities in India. *PLoS ONE*. **2009**, *4* (6), e6003 1-6.
18. Batson, J. S.; Bempong, D. K.; Lukulay, P. H.; Ranieri, N.; Satzger, R. D.; Verbois, L., Assessment of the effectiveness of the CD³⁺ tool to detect counterfeit and substandard anti-malarials. *Malar. J.* **2016**, *15*, 119-119.
19. Kumar, C. A.; Gurupadayya, B. M.; Sloka, N.; Chandan, R.; Thejaswini, J. C., Colorimetric determination of Cefadroxil and Ceftriazone in pharmaceutical dosage forms. *Trop. J. Pharm. Res.* **2011**, *10*, 81-88.
20. WXPRESS Fighting counterfeit medicines with TruTag Technologies. <https://wxpress.wuxiapptec.com/conversation-peter-wong-coo-trutag-technologies/> (accessed 04/03/2021).
21. Jähnke, R., Counterfeit medicines and the GPHF-Minilab for rapid drug quality verification. *Pharm Ind.* **2004**, *66*, 1187-1193.
22. Hanna-Attisha, M.; LaChance, J.; Sadler, R. C.; Champney Schnepf, A.,

- Elevated blood lead levels in children associated with the flint drinking water crisis: A spatial analysis of risk and public health response. *Am. J. Public Health* **2016**, *106* (2), 283-90.
23. Ignatavičius, G.; Sakalauskienė, G.; Oškinis, V., Influence of land fires on increase of heavy metal concentrations in river waters of Lithuania. *J. environ. eng. landsc. manag.* **2010**, *14*, 46-51.
 24. Hernberg, S., Lead poisoning in a historical perspective. *Am. J. Ind. Med.* **2000**, *38* (3), 244-254.
 25. Vassallo, D. V.; Simões, M. R.; Furieri, L. B.; Fioresi, M.; Fiorim, J.; Almeida, E. A. S.; Angeli, J. K.; Wiggers, G. A.; Peçanha, F. M.; Salaiques, M., Toxic effects of mercury, lead and gadolinium on vascular reactivity. *Braz. J. Med. Biol. Res.* **2011**, *44*, 939-946.
 26. Gonick, H. C.; Behari, J. R., Is lead exposure the principal cause of essential hypertension? *Med. Hypotheses.* **2002**, *59* (3), 239-246.
 27. Korrick, S. A.; Hunter, D. J.; Rotnitzky, A.; Hu, H.; Speizer, F. E., Lead and hypertension in a sample of middle-aged women. *Am. J. Public Health.* **1999**, *89* (3), 330-335.
 28. Buledi, J. A.; Amin, S.; Haider, S. I.; Bhangar, M. I.; Solangi, A. R., A review on detection of heavy metals from aqueous media using nanomaterial-based sensors. *Environ. Sci. Pollut. Res.* **2020**, *24* (30),1-9.
 29. Gumpu, M. B.; Sethuraman, S.; Krishnan, U. M.; Rayappan, J. B. B., A review on detection of heavy metal ions in water – An electrochemical approach. *Sens. Actuators B Chem.* **2015**, *213*, 515-533.
 30. Motalebizadeh, A.; Bagheri, H.; Asiaei, S.; Fekrat, N.; Afkhami, A., New portable smartphone-based PDMS microfluidic kit for the simultaneous colorimetric detection of arsenic and mercury. *RSC Adv.* **2018**, *8* (48), 27091-27100.
 31. Raman, C. V.; Krishnan, K. S., A new class of spectra due to secondary radiation. *Indian J. Phys.* **1928**, *2*, 379-396.
 32. Gilbert, A. S., *Encyclopedia of Spectroscopy and Spectrometry*. Elsevier: Oxford, 1999.
 33. Felipe, L. M.; Alexei, M. C. M.; Eduardo, P.; Sangram, K. S.; Ana, M. d. P.; Aloísio, M. G.; Ishan, B.; Jaqueline, S. S.; Marcelo, M., Raman spectroscopy with a 1064-nm wavelength laser as a potential molecular tool for prostate

- cancer diagnosis: a pilot study. *J. Biomed. Opt.* **2018**, *23* (12), 1-6.
34. Dzsaber, S.; Negyedi, M.; Bernáth, B.; Gyüre, B.; Fehér, T.; Kramberger, C.; Pichler, T.; Simon, F., A Fourier transform Raman spectrometer with visible laser excitation. *J. Raman Spectrosc.* **2015**, *46* (3), 327-332.
35. Introduction to Vibrations. <https://chem.libretexts.org/@go/page/77584>. (accessed 12/03/2021)
36. Gilbert, A. S., IR spectral group frequencies of organic compounds. In *Encyclopedia of Spectroscopy and Spectrometry*, Third ed.; Lindon, J. C., et al., Eds. Academic Press: Oxford, 2017; pp 408-418.
37. Wilson, R.; Bowden, S. A.; Parnell, J.; Cooper, J. M., Signal Enhancement of surface enhanced Raman scattering and surface enhanced resonance Raman scattering using in situ colloidal synthesis in microfluidics. *Anal. Chem.* **2010**, *82* (5), 2119-2123.
38. Li, S.; Li, Y.; Yi, R.; Liu, L.; Qu, J., Coherent anti-stokes Raman scattering microscopy and its applications. *Front. Phys.* **2020**, *8* (515).
39. Smulko, J.; Wróbel, M. S. In *Noise sources in Raman spectroscopy of biological objects*, Proc. SPIE, 2017.
40. Smulko, J.; Wróbel, M. S.; Barman, I. In *Noise in biological Raman spectroscopy*, 2015 International Conference on Noise and Fluctuations (ICNF), 2-6 June; 2015; pp 1-6.
41. Rabinowitz, J.; Rezaei, M.; Park, M.-S.; Leong Tan, C.; Ulmer, M.; Mohseni, H., When shot-noise-limited photodetectors disobey Poisson statistics. *Opt. Lett.* **2020**, *45* (11), 3009-3012.
42. Sinéad Barton, B. E. Methods for improving signal to noise ratio in Raman spectra. PhD Engineering, Maynooth University 2018.
43. D. W. Ball, *Field Guide to Spectroscopy*. SPIE Press: Bellingham, 2006.
44. Rojalín, T.; Kurki, L.; Laaksonen, T.; Viitala, T.; Kostamovaara, J.; Gordon, K. C.; Galvis, L.; Wachsmann-Hogiu, S.; Strachan, C. J.; Yliperttula, M., Fluorescence-suppressed time-resolved Raman spectroscopy of pharmaceuticals using complementary metal-oxide semiconductor (CMOS) single-photon avalanche diode (SPAD) detector. *Anal. Bioanal. Chem.* **2016**, *408* (3), 761-774.
45. Yaney, P. P., The pulsed laser and gated detection in Raman spectroscopy – A survey of the spectra of common substances including studies of adsorbed benzene. *J. Raman Spectrosc.* **1976**, *5* (3), 219-241.

46. Ruiz-Moreno, S.; López-Gil, A.; Gabaldón, A.; Sandalinas, C., Raman spectroscopy and UV pulsed laser: an excellent symbiosis. *J. Raman Spectrosc.* **2004**, *35*, 640–645.
47. Gebrekidan, M. T.; Knipfer, C.; Stelzle, F.; Popp, J.; Will, S.; Braeuer, A., A shifted-excitation Raman difference spectroscopy (SERDS) evaluation strategy for the efficient isolation of Raman spectra from extreme fluorescence interference. *J. Raman Spectrosc.* **2016**, *47* (2), 198-209.
48. Wahadoszamen, M.; Rahaman, A.; Hoque, N. M. R.; I Talukder, A.; Abedin, K. M.; Haider, A. F. M. Y., Laser Raman spectroscopy with different excitation sources and extension to Surface Enhanced Raman Spectroscopy. *J. Spectrosc.* **2015**, *2015*, 1-8.
49. Strachan, C. J.; Rades, T.; Gordon, K. C.; Rantanen, J., Raman spectroscopy for quantitative analysis of pharmaceutical solids. *J. Pharm. Pharmacol.* **2007**, *59* (2), 179-92.
50. Kachrimanis, K.; Braun, D. E.; Griesser, U. J., Quantitative analysis of paracetamol polymorphs in powder mixtures by FT-Raman spectroscopy and PLS regression. *J. Pharm. Biomed. Anal.* **2007**, *43* (2), 407-412.
51. Taylor, L. S.; Zografí, G., The quantitative analysis of crystallinity using FT-Raman spectroscopy. *Pharm. Res.* **1998**, *15* (5), 755-761.
52. Šašić, S., Raman mapping of low-content API pharmaceutical formulations. I. Mapping of Alprazolam in Alprazolam/Xanax tablets. *Pharm. Res.* **2007**, *24*, 58-65.
53. Ha Julie Ann, S. W.; Edward R, G.; Lynne S, T., On-line content uniformity determination of tablets using low-resolution Raman spectroscopy. *Appl. Spectrosc.* **2016**, *60* (6), 672-681.
54. Aina, A.; Hargreaves, M. D.; Matousek, P.; Burley, J. C., Transmission Raman spectroscopy as a tool for quantifying polymorphic content of pharmaceutical formulations. *Analyst.* **2010**, *135* (9), 2328-2333.
55. Buckley, K.; Matousek, P., Recent advances in the application of transmission Raman spectroscopy to pharmaceutical analysis. *J. Pharm. Biomed. Anal.* **2011**, *55* (4), 645-652.
56. Yi, L.; Benoît, I.; James K, D. I.; Carl A, A., Method development and validation for pharmaceutical tablets analysis using transmission Raman spectroscopy. *Int. J. Pharm.* **2016**, *498*, 318-325.

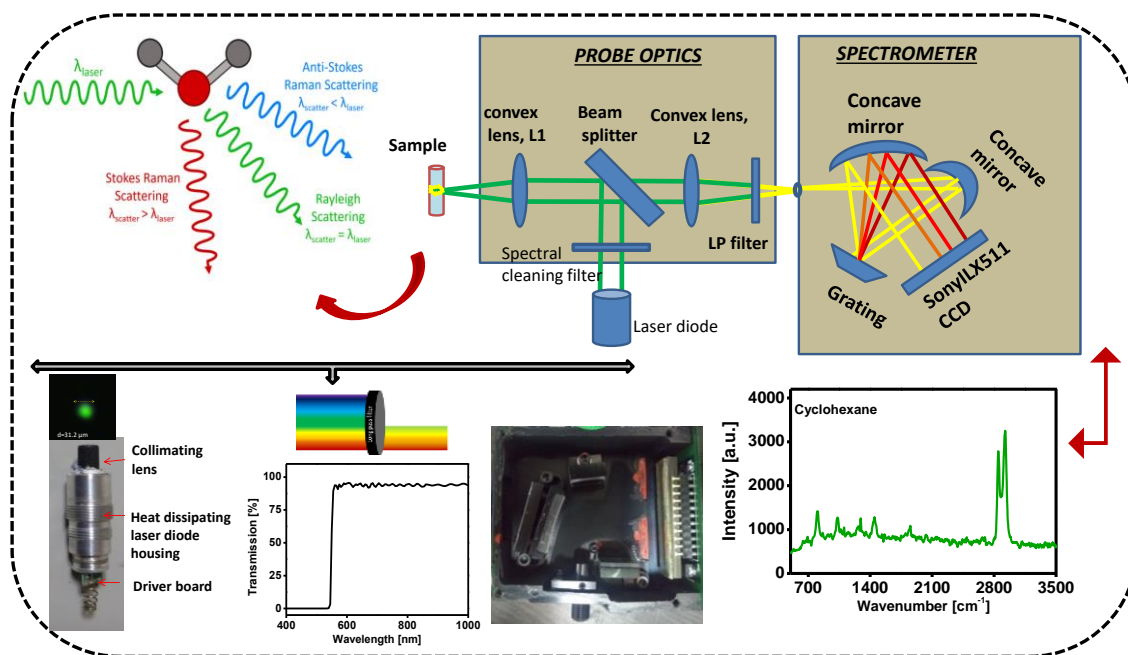
57. Dégardin, K.; Guillemain, A.; Klespe, P.; Hindelang, F.; Zurbach, R.; Roggo, Y., Packaging analysis of counterfeit medicines. *Forensic. Sci. Int.* **2018**, *291*, 144-157.
58. Lakhwani, G.; Sherikar, D. O.; Mehta, P., Nondestructive and rapid concurrent estimation of Paracetamol and Nimesulide in their combined dosage form using Raman spectroscopic technique. *Indian J. Pharm. Sci.* **2013**, *75*, 211-217.
59. Li., Y.; Guorong, D.; Wensheng, C.; Xueguang, S., Classification and quantitative analysis of Azithromycin tablets by Raman spectroscopy and chemometrics. *Am. J. Analyt. Chem.* **2011**, *2*, 135-141.
60. Makki, A. A.; Bonnier, F.; Respaud, R.; Chtara, F.; Tfayli, A.; Tauber, C.; Bertrand, D.; Byrne, H. J.; Mohammed, E.; Chourpa, I., Qualitative and quantitative analysis of therapeutic solutions using Raman and infrared spectroscopy. *Spectrochim. Acta A Mol. Biomol. Spectrosc.* **2019**, *218*, 97-108.
61. He, X.; Liu, Y.; Huang, S.; Liu, Y.; Pu, X.; Xu, T., Raman spectroscopy coupled with principal component analysis to quantitatively analyze four crystallographic phases of explosive CL-20. *RSC Adv.* **2018**, *8* (41), 23348-23352.
62. Ullah, R.; Khan, S.; Javaid, S.; Ali, H.; Bilal, M.; Saleem, M., Raman spectroscopy combined with a support vector machine for differentiating between feeding male and female infants mother's milk. *Biomed. Opt. Express.* **2018**, *9* (2), 844-851.
63. Sattlecker, M.; Bessant, C.; Smith, J.; Stone, N., Investigation of support vector machines and Raman spectroscopy for lymph node diagnostics. *Analyst.* **2010**, *135* (5), 895-901.
64. Liu, W.; Sun, Z.; Chen, J.; Jing, C., Raman spectroscopy in colorectal cancer diagnostics: comparison of PCA-LDA and PLS-DA models. *J. Spectrosc.* **2016**, *2016*, 1-6
65. Farkas, A.; Vajna, B.; Sóti, P. L.; Nagy, Z. K.; Pataki, H.; Van der Gucht, F.; Marosi, G., Comparison of multivariate linear regression methods in micro-Raman spectrometric quantitative characterization. *J. Raman Spectrosc.* **2015**, *46* (6), 566-576.
66. Zhang, C.; Cheng, G.; Edwards, P.; Zhou, M.-D.; Zheng, S.; Liu, Z., G-Fresnel smartphone spectrometer. *Lab Chip.* **2016**, *16* (2), 246-250.
67. Edwards, P.; Zhang, C.; Zhang, B.; Hong, X.; Nagarajan, V. K.; Yu, B.; Liu, Z.,

- Smartphone based optical spectrometer for diffusive reflectance spectroscopic measurement of hemoglobin. *Sci. Rep.* **2017**, *7* (1), 1-7.
68. Wang, L.-J.; Naudé, N.; Chang, Y.-C.; Crivaro, A.; Kamoun, M.; Wang, P.; Li, L., An ultra-low-cost smartphone octochannel spectrometer for mobile health diagnostics. *J. Biophotonics.* **2018**, *11* (8), 1-9.
69. Bayram, A.; Horzum, N.; Metin, A. U.; Kılıç, V.; Solmaz, M. E., Colorimetric Bisphenol-A detection with a portable smartphone-based spectrometer. *IEEE Sens. J.* **2018**, *18* (14), 5948-5955.
70. Rong, Z.; Wang, Q.; Sun, N.; Jia, X.; Wang, K.; Xiao, R.; Wang, S., Smartphone-based fluorescent lateral flow immunoassay platform for highly sensitive point-of-care detection of Zika virus nonstructural protein 1. *Anal. Chim. Acta.* **2019**, *1055*, 140-147.
71. Kim, S. D.; Koo, Y.; Yun, Y., A Smartphone-Based Automatic Measurement Method for Colorimetric pH Detection Using a Color Adaptation Algorithm. *Sensors.* **2017**, *17* (7), 1-17.
72. Igoe, D. P.; Parisi, A.; Carter, B., Smartphone-based android app for determining UVA aerosol optical depth and direct solar irradiances. *Photochem. Photobiol.* **2014**, *90* (1), 233-237.
73. Das, A. J.; Wahi, A.; Kothari, I.; Raskar, R., Ultra-portable, wireless smartphone spectrometer for rapid, non-destructive testing of fruit ripeness. *Sci. Rep.* **2016**, *6* (1), 32504.
74. Yu, X.; Lu, Q.; Gao, H.; Ding, H., Development of a handheld spectrometer based on a linear variable filter and a complementary metal-oxide-semiconductor detector for measuring the internal quality of fruit. *J. Near Infrared Spectrosc.* **2016**, *24* (1), 69-76.
75. Wolffenbuttel, R. F., MEMS-based optical mini- and microspectrometers for the visible and infrared spectral range. *J. Micromech. Microeng.* **2005**, *15* (7), S145-S152.
76. Mu, T.; Li, S.; Feng, H.; Zhang, C.; Wang, B.; Ma, X.; Guo, J.; Huang, B.; Zhu, L., High-Sensitive Smartphone-Based Raman System Based on Cloud Network Architecture. *IEEE J. Sel. Top. Quantum Electron.* **2019**, *25* (1), 1-6.
77. Color models and color spaces.
<https://programmingdesignsystems.com/color/color-models-and-color-spaces/index.html> (accessed 20/01/2021).

78. Simonds, B. Chlorophyll absorption spectra.

<https://bensimonds.com/2013/05/30/light-and-colour-perception-or-why-are-leaves-green/>(accessed 02/03/2021).

Building an Optical Bench Configuration of Raman Spectrometer and Characterization of its Components



2.1. Abstract

Raman spectroscopy has become a popular analytical tool because of its ability to probe non-destructively and provide fingerprint information about materials. Configuring a Raman spectrometer for onsite analysis requires knowledge about various factors contributing to the spectrum intensity, resolution, etc. Few low-cost components such as laser source, dispersive spectrometer, and filters were identified and in-depth characterization of the chosen components is carried out. The goal of this chapter is to describe the assembly of an inexpensive and simple Raman spectrometer on an optical benchtop using the chosen components. The spectrometer is built in a backscattering probe optics configuration. Later we present the spectra acquired with this system to

highlight the capabilities of the system and discuss possible ways to improve the quality of the spectra.

2.2. Introduction

Raman spectroscopy (RS), the inelastic scattering phenomenon invented by C.V. Raman,¹ provides fingerprint vibrational information and serves as a non-destructive technique for the reliable identification of substances. Nowadays, RS has evolved as one of the most important analytical tools and widely used in various fields. In contrast with absorption-based IR spectroscopy, RS relies on scattering, offering considerable flexibility to both instrumental design and sample handling. Due to minimal interference from water, RS is suitable for studying biological samples even in their native state. Thus, surpassing the limitations of other spectroscopic techniques, RS has evolved as a preferable analytical tool in numerous areas like medical diagnosis,^{2,3} pharmaceutical, and food industries,^{4,5} environmental quality testing,⁶ forensics,⁷ homeland security,⁸ anti-counterfeiting,⁹ archaeology,¹⁰ geology,¹¹ gemstone purity checking,^{12,13} etc. In general, RS techniques can be used for qualitative as well as quantitative purposes. Qualitative analysis is based on measuring the frequencies of scattered radiations and assigning them to specific structural features. In contrast, quantitative analysis requires accurate measurement of the intensity of corresponding vibrational transitions.

With the advent of new generation lasers and optical components, Raman spectra can currently be acquired even with handheld and battery-operatable systems, which have elevated their potential for onsite and point of care applications.¹⁴⁻¹⁶ The presently available commercial Raman Spectrometers differ mainly in their optical components and configurations. Raman spectrometer generally consists of three primary parts: an excitation source, probe optics, and a detector.

In Raman scattering, the interacting photon causes the excitation of matter to a higher energy virtual state. The instantaneous decay from this virtually excited state to different vibrational levels of the electronic ground state yields new photons of shifted energies. The energy difference between the incident photon and the scattered photon represented in wavenumber provides the Raman shift ($\Delta\nu = \frac{1}{\lambda_{exc}} - \frac{1}{\lambda_{Raman}}$). Where λ_{exc} represents the wavelength of the excitation laser and λ_{Raman} represents the wavelength of the scattered light respectively. Thus, if the excitation light contains photons of different energies, each of them inelastically interacts with matter yielding their own Raman scattered radiation. This causes undesirable peak broadening, and it is necessary to have monochromatic excitation radiation for obtaining a highly resolved Raman spectrum. In this context, lasers could be a better choice for an excitation source as they provide monochromatic and coherent light. Earlier days (before 1970),¹⁷ mercury arc lamp was used as the light source,^{18,19} and the full capabilities of RS have not been explored much until the invention of the laser. Modern Raman instrumentation primarily uses a laser as the excitation source and a dispersive spectrometer for the detector.²⁰

Similarly, earlier used detectors were single-point detectors like PMT, APD combined with rotating grating, and the spectrum is acquired by scanning intensity at each wavenumber.^{21,22} Considering the low scattering efficiency, this process requires an extended period for single spectral acquisitions. However, the invention of the diode array spectrometer has helped to solve this issue, and Raman spectrometer have become more compact.^{20,23}

Out of the different probe optics configuration, backscattering mode requires a minimum number of optical components, since the same optics is used for both excitation and collection.

This chapter outlines the functions of various components in a Raman spectrometer, identified low-cost laser source, dispersive spectrometer, and filters for building an affordable Raman spectrometer. We also describe the detailed characterization of the components and studied how each of these components affects the quality of the spectra.

2.3. Experimental Section

2.3.1. Optical Configuration

For building a Raman spectrometer, we used a JD-851 green laser pointer as the excitation source, probe optics with backscattering configuration, and a Science surplus spectrometer with 1800 lines/mm grating having ~450-700 nm spectral range and ~1 nm spectral resolution as the detector. Probe optics consists of two convex lenses, each having a focal length of 50 mm, a beam splitter with a 30:70 reflection transmission ratio, and a long-pass filter with a 550 nm cut-off wavelength (Newport, CGA-550) to block the Rayleigh scattered light.

2.3.2. Assembling the Components

For building a tabletop Raman spectrometer, alignment was done on an optical table having 1/4"-20 (M6) mounting holes on 1" (25 mm) centres. All the optical components were mounted on appropriate mounts and affixed to the optical table using relevant posts, M6 screws, and post holder. The battery was removed from the laser pointer, and the laser driver board was powered directly from the computer's USB port. To achieve this, two leads of the USB cable were connected to the ground and the positive terminals of the diode driver using alligator clips. Later, the laser pointer was mounted on a kinematic lens mount and post assembly, which allows control over the optical path of the laser. A variable optical attenuator placed in the

front of the laser diode allows the laser power adjustment. The beam splitter was mounted on a rectangular optics mount and aligned exactly 45° with the incident beam. The light reflected from the beam splitter was focused on the sample using a convex lens (L1) mounted on a kinematic lens mount. The back-reflected and scattered light is collected by L1 and focused onto the core of an optical fibre using a second convex lens (L2) mounted on a rigid lens mount. A long-pass filter with a cut-off at 550 nm was used to block the Rayleigh scattered light and kept between L2 and the detector.

The optical signal collected by the probe optics is fed into the detector unit through an optical fibre mounted on an XYZ translational stage. By precise adjusting the fibre position in a micrometre range, maximum coupling of the scattered signal into the detector unit is achieved.

2.3.3. Chemicals and Instruments Used

A dilute solution of rhodamine B (M/s Sigma Aldrich corporation) was used for aligning the probe optics. Standard chemicals like benzonitrile (M/s Sigma Aldrich corporation), cyclohexane (M/s Spectrochem Pvt. ltd), poly dimethyl siloxane (PDMS) (M/s Sigma Aldrich corporation), and acetone (M/s SD fine chemicals ltd.) were used for testing the aligned system.

The laser spectral profile was measured using a RI-series spectrometer (M/s Research India) having a resolution of 0.3 nm. An optical power meter (843-R with 818-UV/DB silicon detector, M/s Newport corporation) was used for measuring the laser power. Laser beam profile measurement was carried out using a CMOS colour camera (Model No: CS165CU, Thorlabs Inc.) with 1440 x 1080 dimensions with each pixel of size $3.45 \mu\text{m} \times 3.45 \mu\text{m}$. Special care was taken not to damage the detector by the high-intensity laser beam, which was managed by placing ND (neutral density)

filters in the beam path and operating the camera at a very low exposure time.

2.4. Results and Discussion

2.4.1. Tabletop Raman Spectrometer

Figure 2.1 displays the optical layout adopted for setting up the tabletop version of the Raman spectrometer. The chosen configuration is backscattering mode, and the output of the probe optics is coupled to the spectrometer's entrance with an optical fibre. Represented in Figure 2.2 is the photograph of the tabletop set up with all the optical components mounted using appropriate holding mechanisms. Table 2.1 shows the price of the optical components used.

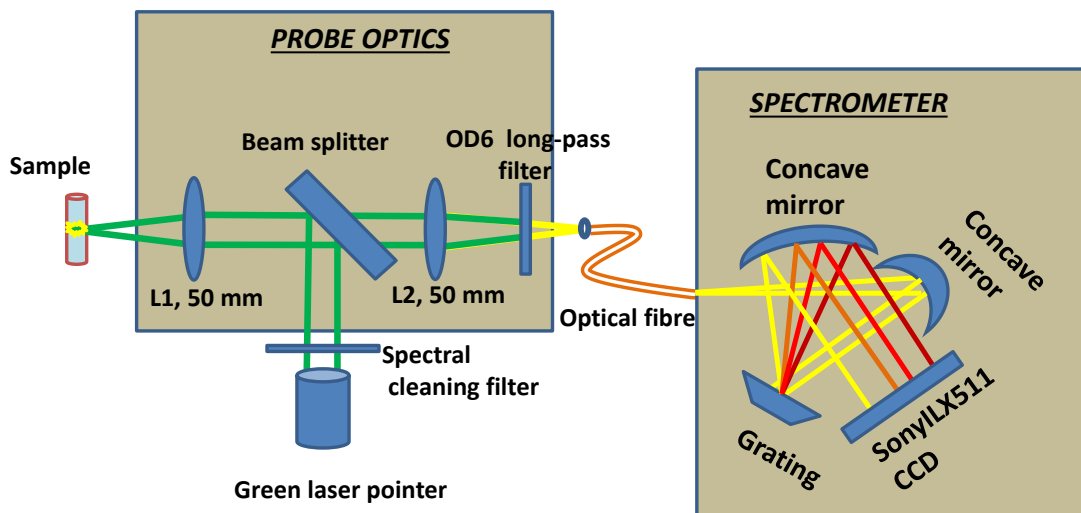


Figure 2.1. Schematic layout of the Raman spectrometer configuration adopted.

A dilute solution of strong fluorescing material, rhodamine B, was used to align the optical components. The selected dye's absorption maximum (520-560 nm) matches with the excitation laser wavelength, and the emission profile lies in the 550-650 nm spectral range, the region of our interest of Stokes Raman bands.

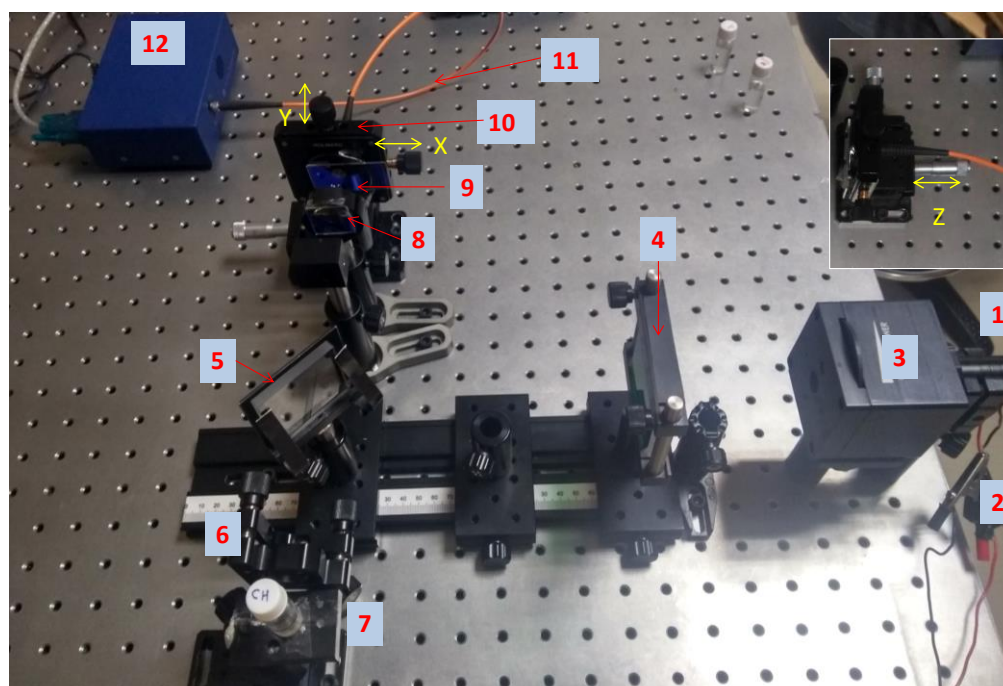


Figure 2.2. Photograph showing the organization of components of Raman spectrometer on an optical table; (1) laser pointer, (2) soldered wire for powering laser diode through USB powering, (3) variable optical attenuator to adjust laser power, (4) band-pass filter to block 808 nm, (5) beam splitter, (6) focusing convex lens with focal length 50 mm, (7) sample holder with the sample placed inside a glass vial, (8) focusing convex lens with focal length 50 mm, (9) 550 nm cut off long-pass filter, (10) XYZ fibre holder (inset shows the top view of the fibre holder showing Z-axis movement), (11) 500 μm optical fibre, and (12) Science surplus detector.

Table 2.1. Component list with price details

No	Component	Quantity	Make and model	Price (INR)
1	Green laser pointer	1	Huonje, JD851, 70 mW	1000
2	30:70 beamsplitter	1	Holmarc, HO-MPSBS-25	3550
3	Long-pass filter	1	Newport, 20CGA-550	8000
4	Biconvex lens, (FL-50 mm)	2	Holmarc, HO-BXL25-02	2300
5	Spectrometer	1	Science surplus	14000
6	Optical post	8	Holmarc, P-30	2000
7	Optical post holder	8	Holmarc, PH-50	3000
8	Kinematic lens mount	2	Holmarc, KMC-CS-T-25	5600
9	YZ lens mount with fibre holder	1	Holmarc, YZLM-25, FAD25MA	12000
10	Rigid lens mount	1	Holmarc, RLM-25	1200
11	Bar type adjustable lens mount	2	Holmarc, ALM-B-50	7000
12	Linear translational stage	1	Holmarc, TS-50	7000
Total cost				66650

2.4.2. Characterization of Components

Excitation source:

In a Raman spectrometer, the light source's primary role is to provide exciting photons that inelastically interact with the analyte and provide Raman scattered radiation. The excitation source's technical specifications, such as wavelength, line width (monochromaticity), optical power, etc., are crucial for obtaining good quality Raman spectra. The Raman scattering efficiency varies inversely to the fourth power of the excitation wavelength.¹⁸ Thus, lasers with lower excitation wavelength (UV and visible) produce better Raman signals than the IR light sources.

For the current work, we used a low-cost and readily available green (~532 nm) laser pointer JD-851, a Diode Pumped Solid State Laser (DPSS), as the excitation source. Figure 2.3 A represents the photograph of the laser pointer. The inbuilt Nd:YAG and KTP crystals convert the laser diode's primary emission wavelength, 808 nm, first to 1064 nm and then to 532 nm. Favourably, these laser pointers come with the necessary electronic driver circuit, passive heat dissipater, and collimator lens assembly, eliminating the need for additional components.

The measured laser beam diameter and optical output power are respectively ~1 mm and ~70 mW and are sufficient to produce an easily detectable amount of Raman scattered photons. The measured spectral profile (Figure 2.3 B) indicated that the central wavelength and FWHM are ~531.8 nm and ~0.32 nm, respectively. From this, the estimated minimum achievable Raman spectral resolution is in the range of 7-11 cm^{-1} . It is to be noted that any inaccuracies in measuring wavelength will lead to a considerable variation in Raman peak positions in the wavenumber domain. The deviation will be worse in the lower wavelength region than the higher wavelength region (a 0.4 nm inaccuracy for 532 nm excitation leads to a deviation of 13 cm^{-1} at lower wavenumbers). Typically, the Raman spectrum appears ~10-200 nm above

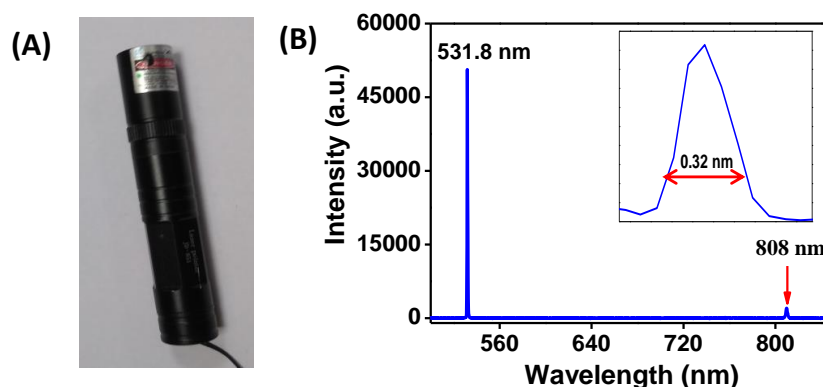


Figure 2.3. (A) Photograph of the JD-851 laser pointer and (B) graph showing the spectral profile of the laser emission measured using a spectrometer having ~ 0.3 nm resolution.

(Stokes) and below (anti-Stokes) the excitation wavelength. Corresponding to $300\text{--}3000\text{ cm}^{-1}$ Raman shift, the Stokes lines will fall in the range of $540\text{--}630$ nm, and typical silicon detectors exhibit the highest efficiency in this range.²⁴ All these factors contribute to the easy detection of Raman scattered photons using a silicon CCD detector. This eliminates the need for cooled detectors, which are bulky and costly. The only problem envisaged here could be the interference from background fluorescence for certain samples.

Spectral cleaning filter:

It is also noticed that the laser emission contains an additional diminished output at 808 nm. A band-pass filter with transmission characteristics shown in Figure 2.4 is

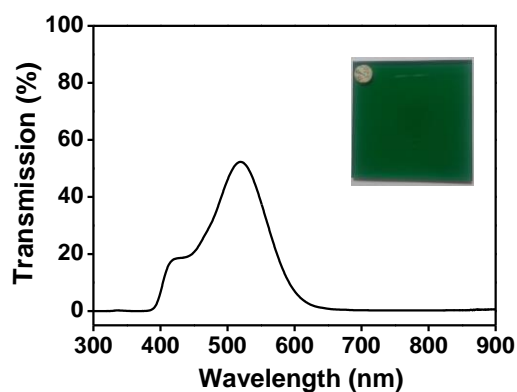


Figure 2.4. Graph showing the wavelength-dependent transmission of the band-pass filter used for blocking the 808 nm, inset showing the photograph of the filter

used to block 808 nm from the excitation radiation. The laser spectrum after the band-pass filter (Figure 2.5) shows that the laser peak intensity at 532 nm is reduced to 55%, in accordance with the transmission efficiency of the filter.

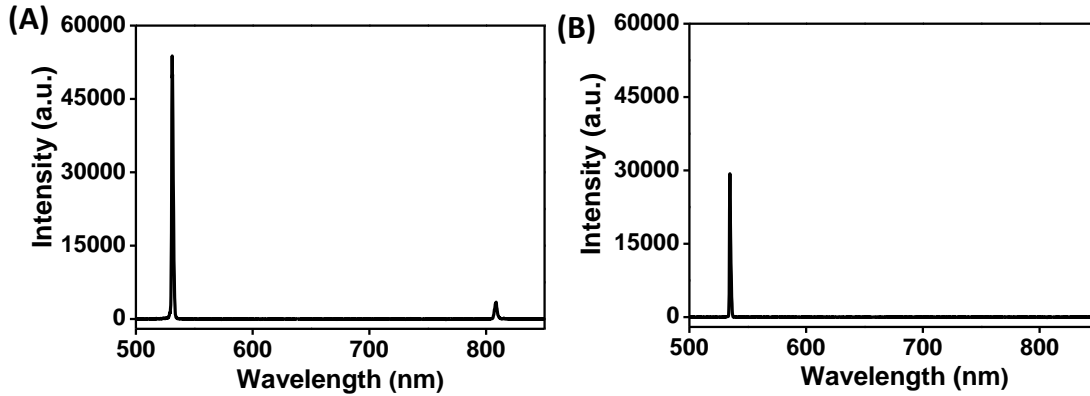


Figure 2.5. Graphs showing the laser's emission spectral profile measured in the (A) absence and (B) presence of band-pass filter.

Probe optics configuration:

The major preferred configurations for probe optics are transmission, 90° , backscattered, and spatially offset. The third is the simplest and is easy to set up with minimum components and alignment. Figure 2.6 shows the layout of the adopted backscattered probe optics configuration. The primary considerations while designing probe optics are to maximize the collection efficiency of the weak Raman radiation and block the intense Rayleigh radiation from entering into the detection unit.

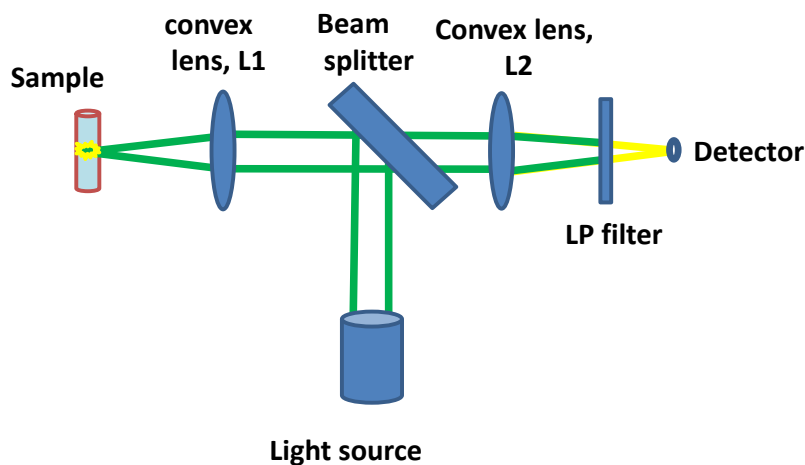


Figure 2.6. Schematic representation of the adopted probe optics arrangement.

These goals are achieved through focusing lenses, a beam splitter, and a long-pass filter. The collimated light from the laser diode is directed to the sample through a beam splitter and a focusing lens (L1). The backscattered radiation is collected by the same lens (L1), and a portion of this beam (70%) directly passes through the beam splitter and is focused onto the detector using a second focusing lens (L2). Rayleigh scattered light was blocked using a long-pass filter kept in between the beam splitter and L2 lens.

Long-pass filter:

The transmission spectral profile of the chosen long-pass filter with cut-off wavelength at 550 nm is shown in Figure 2.7. The filter has approximately 0% transmission below 550 nm (OD ~3), thus restricts the lower spectral limit to ~ 630 cm^{-1} .

To study how effectively the long-pass filter blocks the Rayleigh scattered signal entering the detection unit, rhodamine B solution's fluorescence was analyzed using the tabletop arrangement. In the absence of any long-pass filter, the back collected radiation exhibited mainly two components (i) a strong narrow peak at 532 nm arising from Rayleigh scattered and back-reflected laser light, and (ii) relatively weak fluorescence from the rhodamine B solution (~ 7740 counts). i.e., the highest

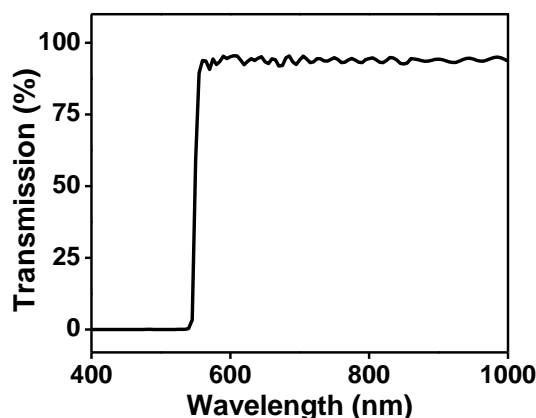


Figure 2.7. Graph showing the wavelength-dependent transmission of the long-pass filter with cut off at 550 nm (Newport CGA-550).

intensity is observed for laser line radiation (~ 62000 counts) irrespective of the strong fluorescing nature of rhodamine B, $\Phi_{em} = 31\%$ ²⁵ (Figure 2.8.A). In a typical Raman spectral acquisition, the strong Rayleigh scattered signal's intensity can saturate the detector, and observation of the weak Raman scattered signal is a challenging task. We overcame this issue by installing the long-pass filter, which blocks Rayleigh scattered radiation from entering the detection unit. Figure 2.8 B represents the emission spectrum collected in the presence of the long-pass filter (optical density of 3 at 532 nm) between lens L2 and the beam splitter. For optimal filter arrangement, two similar filters were cascaded together, yielding a total optical density of 6, and the fluorescent spectra were evaluated (Figure 2.8 C). The fluorescence intensity reduces by 12% (count: 6750) of the initial value (count: 7740) after placing a single filter, and

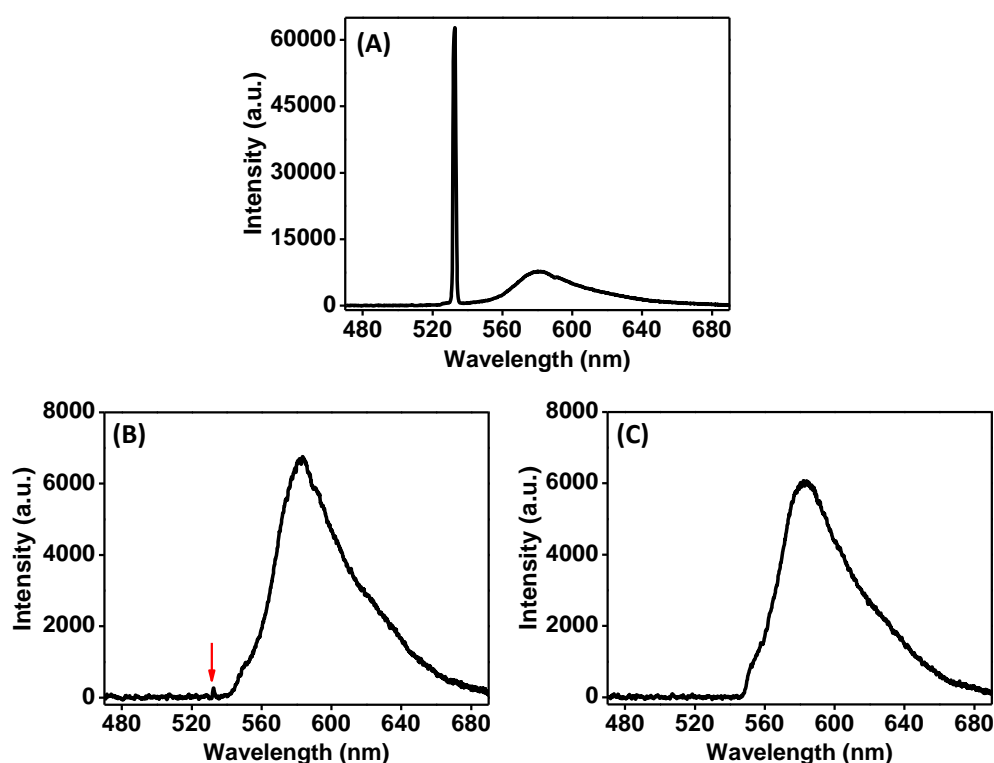


Figure 2.8. Graphs showing the obtained emission profile of rhodamine B in the (A) absence of long-pass filter, (B) presence of one 550 nm long-pass filter (optical density at 532 nm = 3) installed in between beam splitter and focusing lens L2; the reduced interference from the laser is marked with the red arrow, and (C) presence of two numbers of 550 nm long-pass filters (each having optical density 3 at 532 nm) installed in between beam splitter and focusing lens. All the spectra were taken with 0.5 s integration time.

to 22% (count: 6040) with two filters, while the laser intensity reduces from the initially saturated 62000 counts to 270 with one filter, and to 80 with two filters (noise level: 90).

After placing two long pass filters, fine alignment of the probe optics was done by adjusting the fibre position using the XYZ translational stage (marked as 10 in Figure 2.2). When aligning the fibre core to the focus of L2 the detected fluorescence signal gradually increases as shown in Figure 2.9.

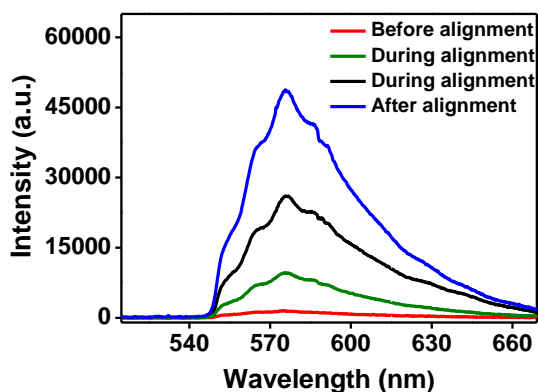


Figure 2.9. Graphs showing the improvement in signal intensity during fine alignment of the probe optics using the XYZ translational stage. All spectra were taken from diluted rhodamine B solution with 100 ms integration time.

Detector:

The detector used is Science surplus make having a spectral range of ~450-700 nm. The approximate cost for this spectrometer is Rs. 14000/-. The spectrometer essentially consists of a 50 μm entrance slit, concave mirrors for collimation and focusing with focal length respectively as ~38 mm and ~40 mm, an 1800 lines/mm diffraction grating, and a Sony ILX511 linear silicon CCD detector. Figure 2.10 shows the photographs of the optical bench inside the spectrometer. The current spectrometer has a spectral resolution of ~1 nm, restricting the maximum achievable Raman spectral resolution to ~33 cm^{-1} at 600 cm^{-1} and ~25 cm^{-1} at 3000 cm^{-1} for a 532 nm excitation.

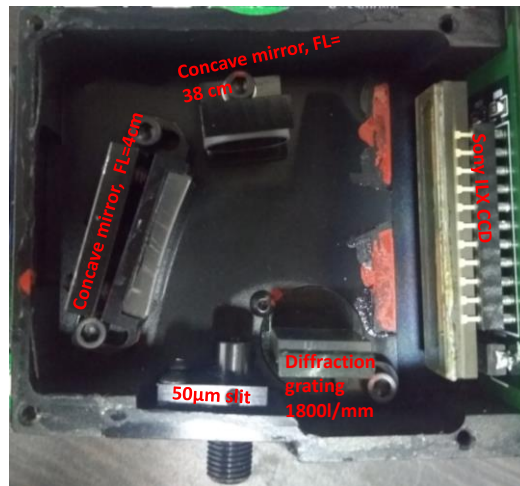


Figure 2.10. Photograph of spectrometer's optical bench configuration and the position of components.

One of the noted issues with the spectrometer was the presence of hot pixels. Hot pixels are certain pixels in the CCD detector having a much higher dark current than their neighbours (Figure 2.11 A). The effect of hot pixels is found to worsen with an increase in exposure time (Figure 2.11 B) and when the signal intensity is

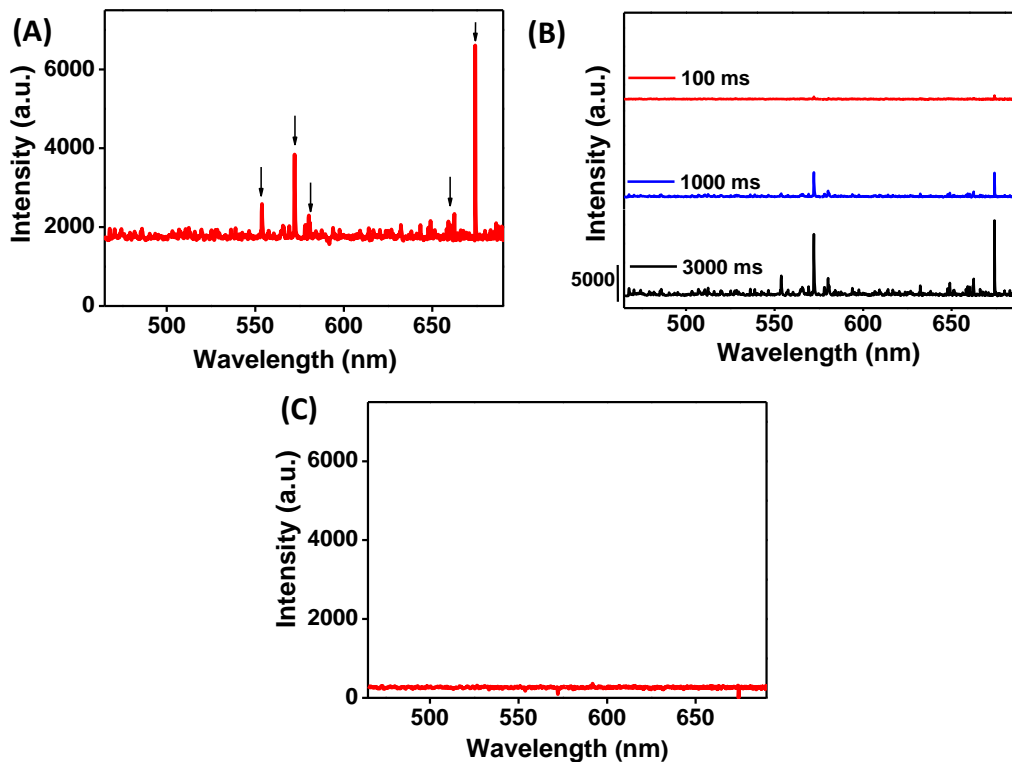


Figure 2.11. (A) CCD dark spectrum showing the hot pixels, (B) dark spectrum measured at three different integration time, i.e. 100 ms, 1000 ms, and 3000 ms and (C) after dark spectrum subtraction.

extremely low. Though this is not a problem for measuring highly intense and broad signals like fluorescence, hot pixels critically interfere with relatively weak and narrow Raman signals. To some extent, the hot pixels' effect can be nullified by subtracting samples spectrum with a blank spectrum recorded under identical conditions, see Figure 2.11.C.

2.4.3. Raman Shift Calibration of the Spectrometer

The raw information obtained from the CCD spectrometer is of the form light intensity (CCD counts) with respect to the pixel number. To perform Raman shift calibration of the device, we used the fluorescent lamp, which has highly distinguishable multiple sharp peaks in the entire visible range (refer table 2.2) and is emanating from Hg, Eu, and Tb ions. The fluorescent lamp spectrum was first collected using the spectrometer and did a one-to-one matching of the peak position with the reported wavelengths. The reference spectrum of the fluorescent lamp is shown in Figure 2.12.

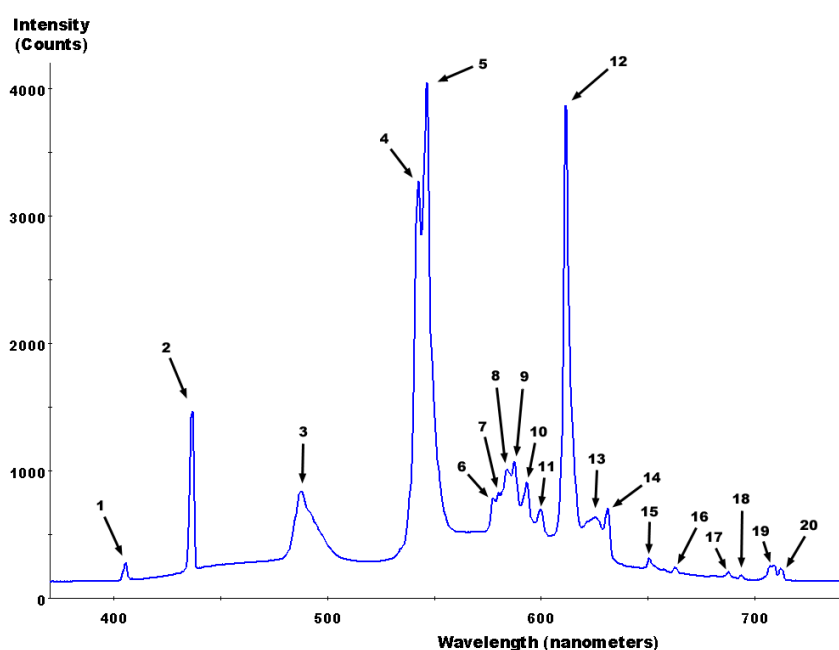


Figure 2.12. Reference spectra of CFL lamp²⁶

Table 2.2. Peak positions of CFL lamp emission spectrum

Peak No.	Wavelength of peak (nm)	Species producing peak
1	405.4	mercury
2	436.6	Mercury
3	487.7	terbium from Tb ³⁺
4	542.4	terbium from Tb ³⁺
5	546.5	Mercury
6	577.7	likely terbium from Tb ³⁺ or mercury
7	580.2	mercury or terbium from Tb ³⁺
8	584.0	terbium from Tb ³⁺
9	587.6	likely europium in Eu ⁺³ :Y ₂ O ₃
10	593.4	likely europium in Eu ⁺³ :Y ₂ O ₃
11	599.7	likely europium in Eu ⁺³ :Y ₂ O ₃
12	611.6	europium in Eu ⁺³ :Y ₂ O ₃
13	625.7	likely terbium from Tb ₃₊
14	631.1	likely europium in Eu ⁺³ :Y ₂ O ₃
15	650.8	likely europium in Eu ⁺³ :Y ₂ O ₃
16	662.6	likely europium in Eu ⁺³ :Y ₂ O ₃
17	687.7	likely europium in Eu ⁺³ :Y ₂ O ₃
18	693.7	likely europium in Eu ⁺³ :Y ₂ O ₃
19	707 & 709	likely europium in Eu ⁺³ :Y ₂ O ₃
20	712.3	likely europium in Eu ⁺³ :Y ₂ O ₃

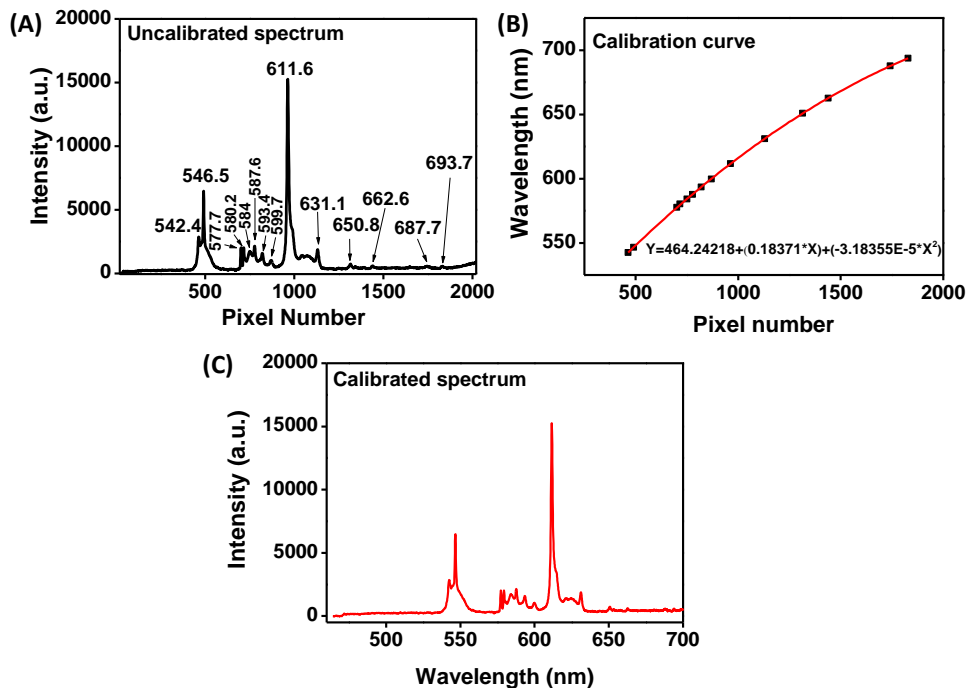


Figure 2.13. The spectrum of fluorescent lamp collected using the spectrometer represented in terms of (A) pixel number vs intensity, (B) pixel number vs reported wavelength, and (C) calibrated spectrum represented in wavelengths.

A plot of the wavelength against pixel number yielded a nonlinear curve that is best fitted with a quadratic equation of the form $y = Ax^2 + Bx + C$. The extracted values of the coefficients are used for the actual calibration of the device. Then, the spectrum was converted into the Raman shift values using the equation (Raman shift, $\Delta\nu = 1/\lambda_{\text{exc}} - 1/\lambda_{\text{Raman}}$). Where λ_{exc} is the emission wavelength of the excitation source (in the present case λ of the laser diode is 531.8 nm) and λ_{Raman} is the wavelength of the Raman scattered photons. Both λ_{exc} and λ_{Raman} are expressed in cm.

2.4.4. Performance Evaluation of Tabletop RS

(i). Standard chemical analysis

Figure 2.14 shows the Raman spectra of various common chemicals like PDMS, benzonitrile, cyclohexane, and acetone recorded using the built tabletop spectrometer system. Comparison of the reported and the observed peak values are tabulated in Table 2.3.

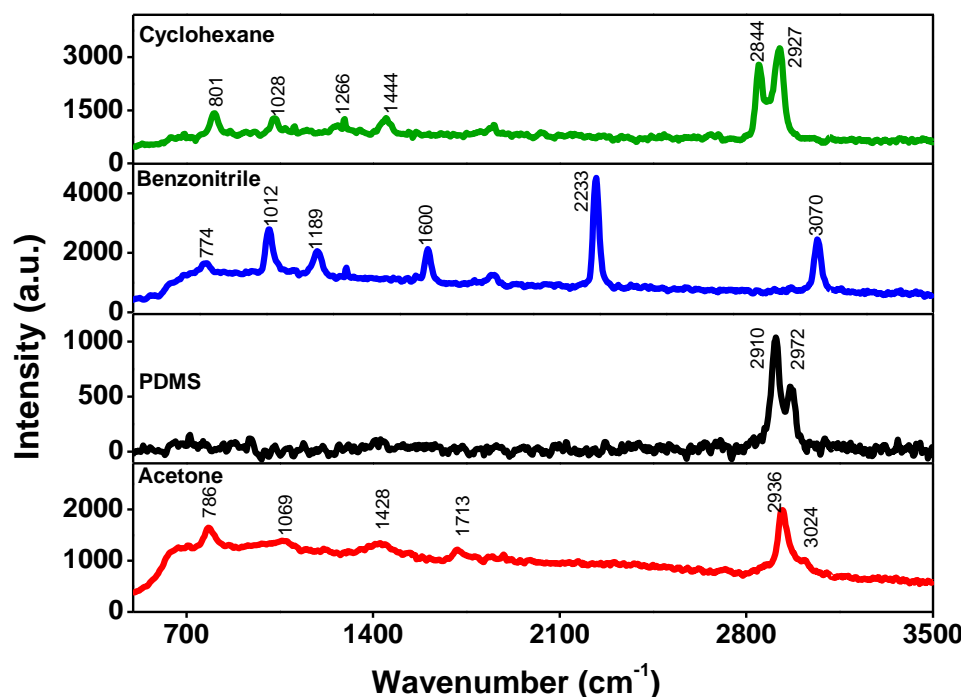


Figure 2.14. Raman spectrum of cyclohexane, benzonitrile, PDMS, and acetone acquired using the tabletop setup (shown in Figure 2.2) with laser power 55 mW, integration time 5 s, and no. of average = 1.

Table 2.3. Comparison of the observed and reported Raman peaks of analyzed chemicals

No.	Assigned bond vibration	Raman shift, $\Delta\nu$ (cm^{-1})		Deviation
		Reported	Observed	
Cyclohexane				
1	C-C str	802	801	-1
2	C-C str	1027	1028	1
3	CH ₂ twist	1266	1266	0
4	CH ₂ scis	1444	1444	0
5	CH ₂ s-str	2852	2848	-4
6	CH ₂ a-str	2923		
7	CH ₂ a-str	2938	2927	
Benzonitrile				
1	C-H bend	751.3		
2	C-H bend	767.1	774	
3	C-C stretch	1007		
4	C-C stretch	1026.6	1012	
5	C-CN stretch	1177.7		
6	C-CN stretch	1192.6	1189	
7	C=C stretch	1598.9	1600	1
8	C-N stretch	2229.4	2233	4
9	C-H stretch	3072.3	3070	-2
PDMS				
1	C-H stretch	2909	2910	1
2	C-H stretch	2971	2972	1
Acetone ²⁷				
1	C-C symm stretch	789	786	-3
2	CH ₃ rock	1068	1069	1
3	CH ₃ deformation	1427	1428	1
4	C=O stretch	1711	1713	2
5	C-H stretch	2940	2936	4
6	C-H stretch	3020	3024	4

(ii). Analyzing the effect of laser power

To identify the minimum excitation power requirements, the Raman spectrum of benzonitrile was acquired by continuously reducing the laser power from 55 mW to 5 mW and keeping all other acquisition parameters (like sample position, integration time, averaging, etc.) constant. Optical power adjustment was achieved using a variable optical attenuator (marked as 3 in Figure 2.2) placed in between the laser source and the beam splitter. From the data presented in Figure 2.15, the following observations can be made; in general, both the peak intensity and the noise are enhanced with laser power. However, the rate at which the Raman peak intensity increases is much higher than the increment in noise. For example, as shown in Figure 2.16, when the laser power increases from 5 mW to 55 mW, the peak intensity at 2243 cm^{-1} increases from 255 to 3928 (rate: 74), while noise increases only at a rate ~ 8 (30 to 431). Nevertheless, with the present configuration, the Raman signals were visible and distinguishable at powers as small as 5 mW. Thus these results indicate adaptability of the current design with Class 3A visible laser pointers or laser diodes or the lower end of Class 3B lasers (eg: Thorlabs DJ 532-10).

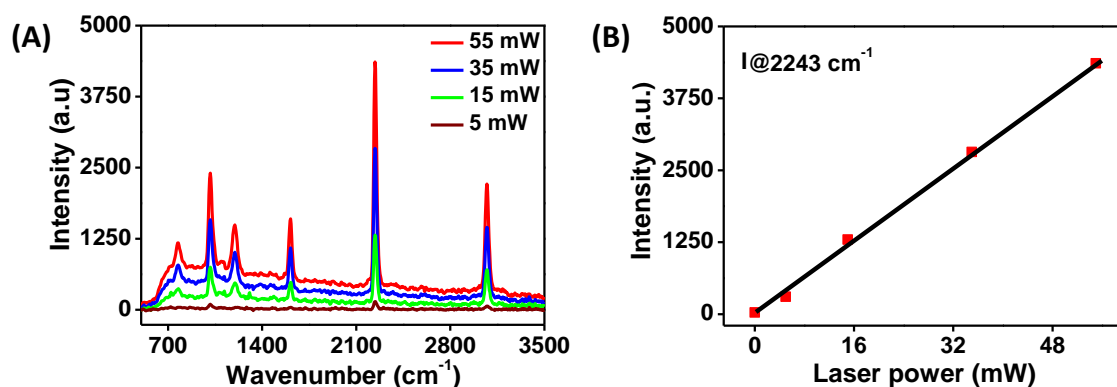


Figure 2.15. (A) Raman spectrum of benzonitrile taken with varying excitation laser power (integration time = 5 s, number of averages = 1) and (B) plot showing the variation in intensity of peak at 2243 cm^{-1} as a function of excitation laser power. Optical power adjustment was achieved using a variable optical attenuator placed in between the laser source and the beam splitter

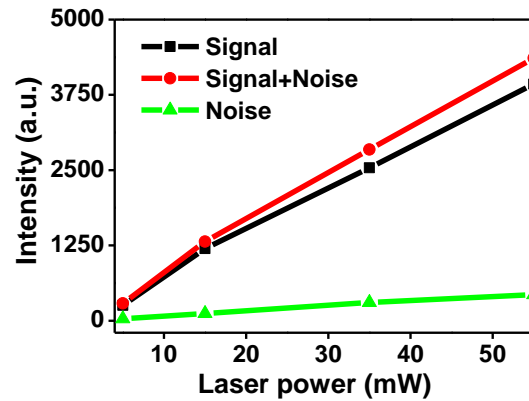


Figure 2.16. Variation in signal and background noise with increment in laser power.

2.4.5. Scope for SNR Improvement

Different ways could be adopted to improve the detected signal intensity without changing the laser source, detector, and probe optics configuration. To achieve this goal we tailored the numerical aperture (NA) of the collection optics and altered the probe optics-detector coupling mechanism. Details of signal to noise ratio (SNR) improvement are provided below.

(a). NA of collection optics

To study the effect of collection optics on the quality of Raman spectra, studies were conducted with different focal length lenses (15 mm, 30 mm, and 50 mm) for focusing the laser on the sample. Raman spectrum of benzonitrile collected with the selected lenses are shown in Figure 2.17. The signal intensity enhanced with the decrease in the focal length of the convex lenses. Around 2.5 times improvement in signal intensity was obtained with 15 mm lens and 1.9 times improvement in signal intensity was obtained with 30 mm lens with respect to the 50 mm lens.

To have a clear understanding of the reason for the signal improvement, the focused laser spot size was measured using a CMOS camera having a pixel dimension of 3.45 μm . The collimated laser was focused using this three different convex lenses

and the measured spot size is shown in Figure 2.18.

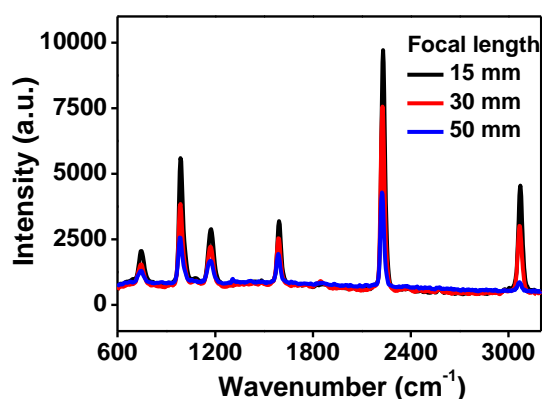


Figure 2.17. Raman spectra of benzonitrile taken with collection optics having L1 lens with focal length respectively as 15 mm, 30 mm, and 50 mm. All spectra were taken with 5 s integration time and an average 1.

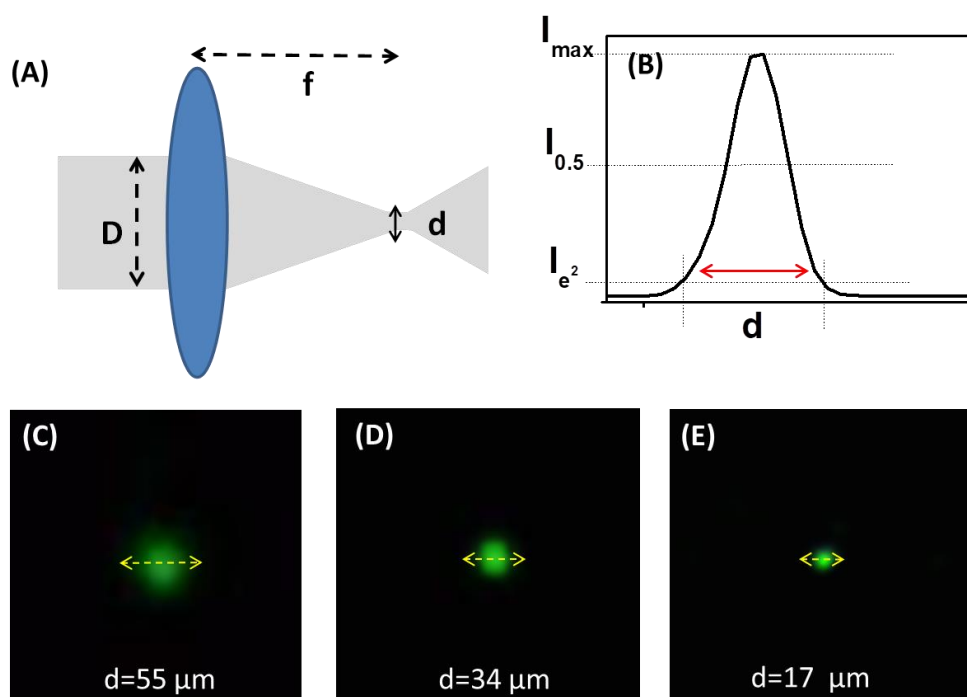


Figure 2.18. Schematic representation of (A) focusing a laser of beam diameter ' D ', to a spot size ' d ' using a lens of focal length ' f ', (B) measuring the laser spot size, and CCD image of the focused laser spot with focal length (C) 50 mm (D) 30 mm (E) 15 mm

The measured focused laser spot size was $\sim 17 \mu\text{m}$, $\sim 34 \mu\text{m}$, and $\sim 55 \mu\text{m}$ respectively for lenses with 15 mm, 30 mm, and 50 mm focal length. i.e. shorter the focal length tighter will be the laser spot size, thus this will allow higher laser power density at the sample. Since the Raman signal intensity is directly proportional to the

laser power density at the sample, a shorter focal length lens will provide higher signal intensity. With decreasing the focal length of the lenses it's effective NA also improves.

(b). Coupling mode to the detector

Most of the modular Raman spectrometers uses coupling of the probe optics to the detector via optical fibre. On the other hand, the free-space coupling of the output of the collection optics to the detector may avoid fibre coupling and transmission losses, allowing the detection of less intense signals yielding improved sensitivity. So instead of an optical fibre, we attempted direct coupling of the Raman signal to the spectrometer's entrance slit. The measured data showed an almost 3.7 times improvement in signal strength for the direct coupling approach than the fibre coupling with 500 μm fibre (Figure 2.19). The use of fibre with core size matching with the slit size will provide maximum coupling of the light to the detector.

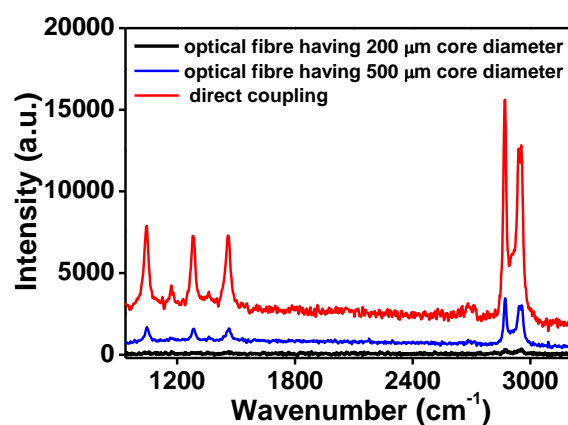


Figure 2.19. Raman spectra of cyclohexane collected under identical conditions and varying the mode of detector coupling with the probe optics

2.5. Summary

In this chapter, we identified cost-effective optical elements that can be used for the fabrication of a Raman spectrometer. Using these components a simple backscattering

probe optics based Raman spectrometer was built using excitation wavelength 532 nm, spectral range 650-4000 cm^{-1} , and spectral resolution of $\sim 25\text{-}33 \text{ cm}^{-1}$. The influence of each of the components on the quality of the Raman spectra has been studied in detail. Additionally, improvement in signal intensity was achieved with increasing laser power, focusing optics with shorter focal length, and higher numerical aperture, and direct coupling of the scattered into the detector, rather than through an optical fibre. The spectral resolution is mainly limited by the resolution of the detector unit. With the currently used laser pointer, spectral resolution can go up to 10 cm^{-1} by using a spectrometer of matching resolution.

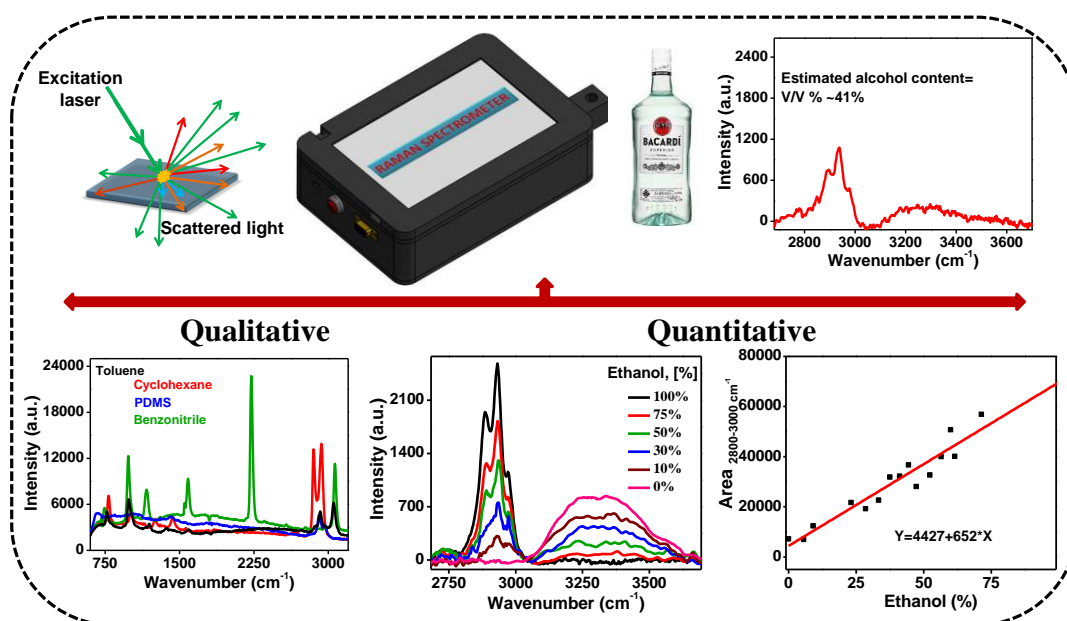
2.6. References

1. Raman, C. V.; Krishnan, K. S., A new class of spectra due to secondary radiation. *Indian J. Phys.* **1928**, *2*, 379-396.
2. Kong, K.; Kendall, C.; Stone, N.; Notingher, I., Raman spectroscopy for medical diagnostics From in-vitro biofluid assays to in-vivo cancer detection. *Adv. Drug Deliv. Rev.* **2015**, *89*, 121-134.
3. Synytsya, A.; Judexova, M.; Hoskovec, D.; Miskovicova, M.; Petruzalka, L., Raman spectroscopy at different excitation wavelengths (1064, 785 and 532 nm) as a tool for diagnosis of colon cancer. *J. Raman Spectrosc.* **2014**, *45* (10), 903-911.
4. Li, Y.; Igne, B.; Drennen, J. K.; Anderson, C. A., Method development and validation for pharmaceutical tablets analysis using transmission Raman spectroscopy. *Int. J. Pharm* **2016**, *498* (1-2), 318-325.
5. Herrero, A. M., Raman spectroscopy a promising technique for quality assessment of meat and fish: A review. *Food Chem.* **2008**, *107* (4), 1642-1651.
6. Ong, T. T. X.; Blanch, E. W.; Jones, O. A. H., Surface enhanced Raman spectroscopy in environmental analysis, monitoring and assessment. *Sci. Total Environ.* **2020**, *720*, 137601.
7. Izake, E. L.; Cletus, B.; Olds, W.; Sundarajoo, S.; Fredericks, P. M.; Jaatinen, E., Deep Raman spectroscopy for the non-invasive standoff detection of concealed chemical threat agents. *Talanta* **2012**, *94*, 342-349.

8. Izake, E. L., Forensic and homeland security applications of modern portable Raman spectroscopy. *Forensic Sci. Int.* **2010**, *202* (1-3), 1-8.
9. Cui, Y.; Phang, I. Y.; Lee, Y. H.; Lee, M. R.; Zhang, Q.; Ling, X. Y., Multiplex plasmonic anti-counterfeiting security labels based on surface-enhanced Raman scattering. *ChemComm* **2015**, *51* (25), 5363-5366.
10. Edwards, H. G. M., Chapter 5 - Raman Spectroscopy in art and archaeology: A new light on historical mysteries. In *Frontiers of Molecular Spectroscopy*, Laane, J., Ed. Elsevier: Amsterdam, 2009; pp 133-173.
11. Xi, S.; Zhang, X.; Du, Z.; Li, L.; Wang, B. Z.; Luan, Z.; Lian, C.; Yan, J. Y., Laser Raman detection of authigenic carbonates from cold seeps at the formosa ridge and east of the pear river mouth basin in the south China sea. *J. Asian Earth. Sci.* **2018**, *168*, 207-224.
12. O'Brien, L. C.; Kubicek, R. L.; O'Brien, J. J., Laser Raman spectroscopy of diamond. *J. Chem. Educ.* **1994**, *71* (9), 759-760.
13. Aponick, A.; Marchozzi, E.; Johnston, C. R.; Wigal, C. T., Determining the authenticity of gemstones using Raman spectroscopy. *J. Chem. Educ.* **1998**, *75* (4), 465-466.
14. Heuler, J.; He, S.; Ambardar, S.; Voronine, D. V., Point-of-care detection, characterization, and removal of chocolate bloom using a handheld Raman spectrometer. *Sci. Rep.* **2020**, *10* (1), 9833.
15. Owens, N. A.; Laurentius, L. B.; Porter, M. D.; Li, Q.; Wang, S.; Chatterjee, D., Handheld Raman spectrometer instrumentation for quantitative tuberculosis biomarker detection: A performance assessment for point-of-need infectious disease diagnostics. *Appl. Spectrosc.* **2018**, *72* (7), 1104-1115.
16. Tran, V.; Walkenfort, B.; König, M.; Salehi, M.; Schlücker, S., Rapid, quantitative, and ultrasensitive point-of-care testing: A portable SERS reader for lateral flow assays in clinical chemistry. *Angew. Chem* **2019**, *58* (2), 442-446.
17. Hecht, J., Short history of laser development. *Opt. Eng.* **2010**, *49* (9), 091002.
18. Shull, E. R., High-current mercury arc Raman source. *J. Opt. Soc. Am.* **1955**, *45* (8), 670_1-671.
19. Woodward, L. A.; Waters, D. N., A water-cooled mercury arc lamp for the excitation of Raman spectra. *J. Sci. Instrum.* **1957**, *34* (6), 222-224.
20. Adar, F.; Delhaye, M.; DaSilva, E., Evolution of instrumentation for detection of the Raman effect as driven by available technologies and by developing

- applications. *J. Chem. Educ.* **2007**, *84* (1), 50.
21. Lewis, E. N.; Treado, P. J.; Levin, I. W., A miniaturized, no-moving-parts Raman spectrometer. *Appl. Spectrosc.* **1993**, *47* (5), 539-543.
 22. Galloway, D. B.; Ciolkowski, E. L.; Dallinger, R. F., Raman spectroscopy for the undergraduate physical and analytical laboratories. *J. Chem. Educ.* **1992**, *69* (1), 79.
 23. Denson, S. C.; Pommier, C. J. S.; Denton, M. B., The Impact of array detectors on Raman spectroscopy. *J. Chem. Educ.* **2007**, *84* (1), 67.
 24. Spieler, H., Silicon Detectors Many different applications, but built on the same basic physics. In *IEEE 2012 Nuclear Science Symposium, Medical Imaging Conference*, Anaheim, California, 2012.
 25. Magde, D.; Rojas, G. E.; Seybold, P. G., Solvent dependence of the fluorescence lifetimes of xanthene dyes. *Photochem. Photobiol.* **1999**, *70* (5), 737-744.
 26. Fluorescent lighting spectrum peaks labelled.
https://commons.wikimedia.org/wiki/File:Fluorescent_lighting_spectrum_peaks_labelled.gif (accessed 03/04/2021).
 27. Acetone Raman spectrum-SpectraBase.
<https://spectrabase.com/spectrum/FK0qD5oM1fZ> (accessed 03-04-2021).

Design and Development of a Portable Raman Spectrometer and its Performance Evaluation



3.1. Abstract

Availability of Raman spectrometers in handheld and portable versions opens new possibilities for point of care diagnosis and testing applications. The Raman spectrometer model demonstrated in the previous chapter is a tabletop version and thus not suitable for onsite analysis. In this chapter, we focus on translating the tabletop Raman spectrometer arrangement to a fully integrated portable version with improved collection efficiency. The technical specifications of portable version is the same as the tabletop system; 532 nm excitation laser, spectral range 650-4000 cm^{-1} and spectral resolution of $\sim 25 \text{ cm}^{-1}$. The performance of the fabricated portable Raman spectrometer was compared with a state of the art commercial Raman spectrometer system. Furthermore, the device was used for onsite testing of alcoholic content from beverages.

3.2. Introduction

Commercial Raman spectrometers are available at different price ranges depending upon their functional capabilities. The high-end Raman spectrometers equipped with microimaging cost a minimum of 100k USD. These instruments have many more functional capabilities than the other two classes and are best suited for creating 2D/3D Raman spectral images, especially biological samples.¹ They have a larger footprint, high spatial and spectral resolution, hence apt for research applications. The second category is the modular Raman spectrometer with flexible instrumental design and costs around 30k to 50k USD. Instead of an integrated system, it uses a separate laser module, spectrometer unit, and fibre optics-based probe module. The third category is the portable/handheld versions cost around 10k to 30k USD. Out of these different configurations, portable versions are suitable for onsite testing applications because of their small footprint, compact design, and handiness. With device miniaturisation, Raman spectroscopy is currently being introduced to several applications that were not possible earlier using the conventionally used cumbersome instruments. The introduction of handheld or portable Raman spectrometers has eliminated the need to transfer samples to the laboratory for testing. Instead, the analysis could be done at the site, opening possibilities for point of care and onsite testing.²

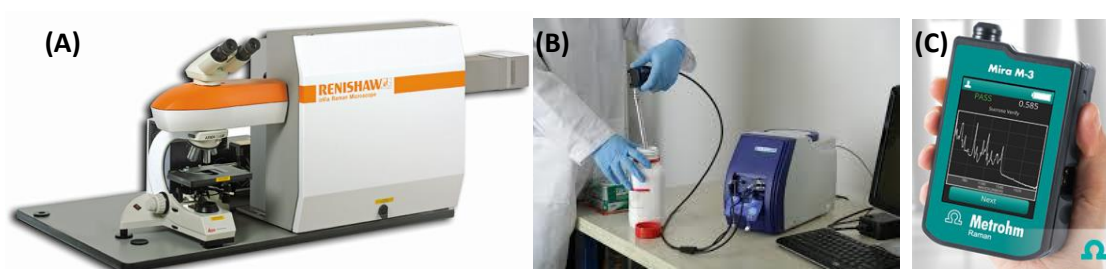


Figure 3.1. Different instrumental configurations of Raman spectrometers (A) high end (Renishaw inVia Raman microscope), (B) modular (BW-Tek Fiber optic Raman system) and (C) portable (Metrohm Mira handheld).

Several recent studies have unravelled RS's potential to applications like medical diagnosis,³ pharmaceutical, food⁴ and environmental quality assessment and monitoring,⁵ forensics, safety and security, archaeology, geology, and many others. Some illustrated diagnostic applications of RS include detecting various biomarkers of diseases like gout,⁶ kidney failure,⁷ tuberculosis,⁸ and cancer.^{9,10} Apart from disease diagnosis RS has been used in the production¹¹ and quality control^{4,12} of pharmaceutical products. In forensic science, it is being employed for the identification of illegal drugs, explosives,¹³ gunshot residue,¹⁴ and inks in counterfeit labelling.¹⁵ While in the food industry, identifying foreign substances and quality assessment of milk¹⁶ and milk products¹⁷, edible oil,¹⁸ fish and meat¹⁹, coffee bean,²⁰ etc. has been explored using Raman spectroscopy. Quantification of ethanol in alcoholic beverages,^{21,22} identification of illegal alcohols containing methanol content²³ using Raman spectrometer provided easy and rapid results.

Apart from the commercially available portable devices, there have been few efforts to provide cost-effective solutions for Raman spectroscopy. In 2008, D. Johnson et al. reported setting up a modular Raman spectrometer suitable for organic and inorganic solid samples using a combination of 532-nm diode-pumped YAG laser, fiber optics probe, notch filter and Ocean optic's HR2000 high-resolution spectrometer at a cost of 6.5k USD.²⁴ In a similar line, C. Mohr et al. assembled an inexpensive modular Raman spectrometer using a green laser pointer at a cost below 5k USD²⁵ and W. R. C. Somerville et al. succeeded in setting up of Raman spectrometer system in both backscattering as well as 90° configurations. In the later, authors used Ocean Optics HR4000, laser pointer (5 mW, 532 nm), Ar⁺ laser (514.5 nm), and HeNe (633 nm, 30 mW) lasers. Out of these, the 90° configuration had the advantage of visualizing both Stokes and anti Stokes lines with minimum optical components.²⁶ Feasibility of fabricating a portable Raman spectrometer using a digital

camera as the detector at a cost of 3k USD has also been demonstrated.²⁷ Most of these demonstrated configurations were modular, not completely portable, utilizes costly spectrometers and connected to the collection optics via fibre optics. On the other hand, a completely integrated and battery operable system will have the advantage of easily carrying to the point of requirements. To the best of our knowledge, there were no previous attempts in this direction, other than the commercial system, normally costing above 10k USD.

This chapter focuses on translating the tabletop version of the RS to a fully integrated portable Raman spectrometer and illustrates its application to a model onsite testing of quantifying ethanol from alcoholic beverages. Special considerations has been given to make the device more handy and easy to use. All the essential optical components are the same as used in tabletop design. The performance of the device was evaluated and compared with a commercial Raman spectrometer system.

3.3. Experimental Section

3.3.1. Optical Configuration

The optical components used for fabricating the portable Raman spectrometer are essentially the same as in the tabletop version. The comparison between the optical configuration of portable and the tabletop version is listed in Table 3.1. The entire optical layout of the portable Raman spectrometer is provided in Figure 3.2.

Modifications: A power bank (portable mobile charger) is used to supply power for both the laser diode and the detector, and an 8-inch tablet (Nuvision, TM800W610L) with Windows OS for spectral acquisition and display. The entire unit was powered using a 5V, 2A DC adapter. Chasis and mounts for optical components were designed in 3D designing software, Solidworks (M/s Dassault Systèmes), and fabricated in Aluminium with the support of M/s Vinvish Technologies Pvt. Ltd.

Table 3.1. Comparison between the optical components used in tabletop and portable version

Optical component	Tabletop design	Portable
Laser source	JD-851 Green laser pointer	JD-851 Green laser pointer
Probe optics configuration	Backscattering	Backscattering
Spectrometer	Science surplus	Science surplus
Beam splitter	30:70	50:50
Focusing lens, L1	Convex lens, focal length 50 mm	Convex lens, focal length 30 mm
Focusing lens, L2	Convex lens, focal length 50 mm	Convex lens, focal length 30 mm
Laser blocking filter	OD 6, long-pass filter, cut off at 550 nm	OD 6, long-pass filter, cut off at 550 nm
Probe optics coupling to the detector	via optical fibre	Direct coupling
Mechanical design	On an optical tabletop	Fully integrated Aluminium chassis

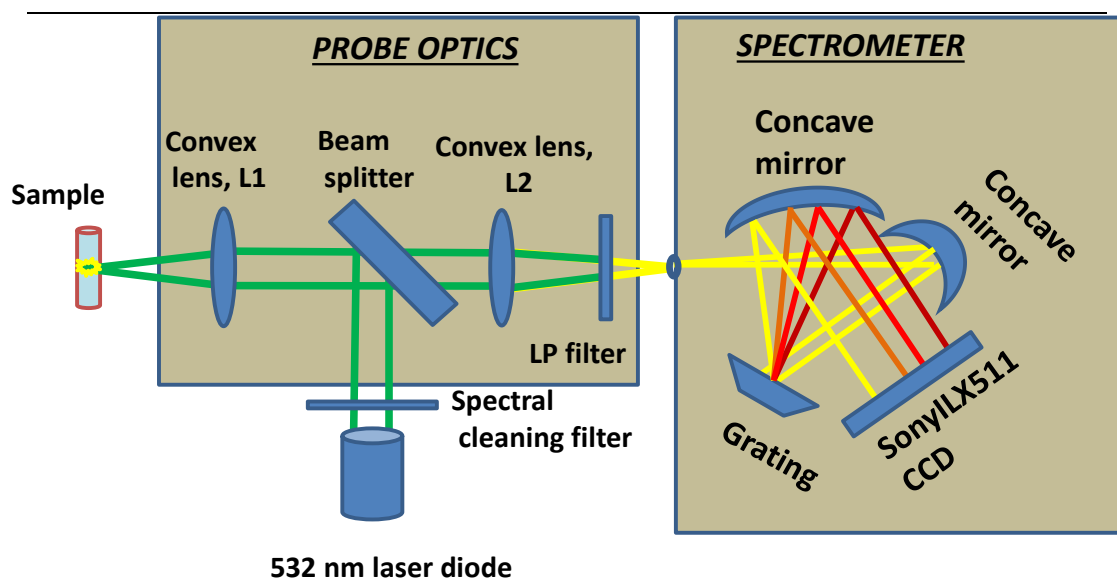


Figure 3.2. Schematic representation of the optical configuration adopted for portable Raman spectrometer.

3.3.2. Instruments Used

The performance of the fabricated system was compared with a commercial confocal Raman microscope with model number WITec Alpha300R (M/s WITec Inc Germany). This device was equipped with a 532 nm excitation laser, an inverted

microscope with a 10X objective lens, and ActonSpectraPro® SP2300, a cooled spectrograph from M/s Princeton instruments with 600 lines/mm, 180-3200 cm^{-1} spectral range, and $<3 \text{ cm}^{-1}$ spectral resolution.

3.4. Results and Discussion

3.4.1. Design of Mechanical Mounts

For translating the tabletop design to a compact and portable version, the major work was done on the mechanical design. To achieve proper mechanical sturdiness, firm optical mounts were designed for all components and mounted to the base of the chassis. The detailed mechanical design is provided below.

Laser source: A mechanical mount was designed to hold the laser pointer as shown in Figure 3.3 A. The holder was fixed to the base of the chassis through proper mounting screws. Figure 3.3 B shows the photographs of the laser diode mounted on the chassis.

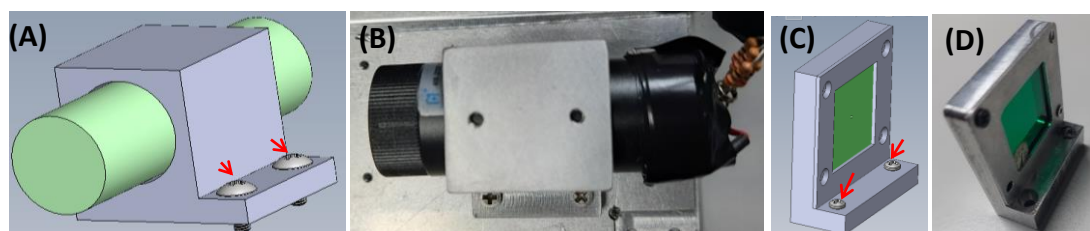


Figure 3.3. 3D design and photographs of the mounts for (A) and (B) laser pointer (C) and (D) band-pass filter to block 808 nm. Red arrow marks show the mounting screws to the chassis.

Laser spectral cleaning filter: The band-pass filter to block the 808 nm emission was cut to a size of 25 x 25 mm, and was mounted on an appropriately designed mount; the 3D design and the photograph are shown in Figure 3.3 C and D.

Beam splitter: For improving the signal collection efficiency, a beam splitter with a 50:50 transmission-reflection ratio was used. While comparing with the 30:70 beam splitter (used in tabletop arrangement in chapter 2), this allows more amount of laser

power to reach the sample. The beam splitter was cut to 2.5 cm x 2.5 cm square size and mounted on the designed mount as shown in Figure 3.4 A. Provision was provided to mount the beam splitter at 45° with the axis of the laser pointer and the sample, with a tolerance of $\pm 5^\circ$. This tolerance limit was defined by the length of the channel provided for mounting the screws as marked in yellow colour in Figure 3.4 B.

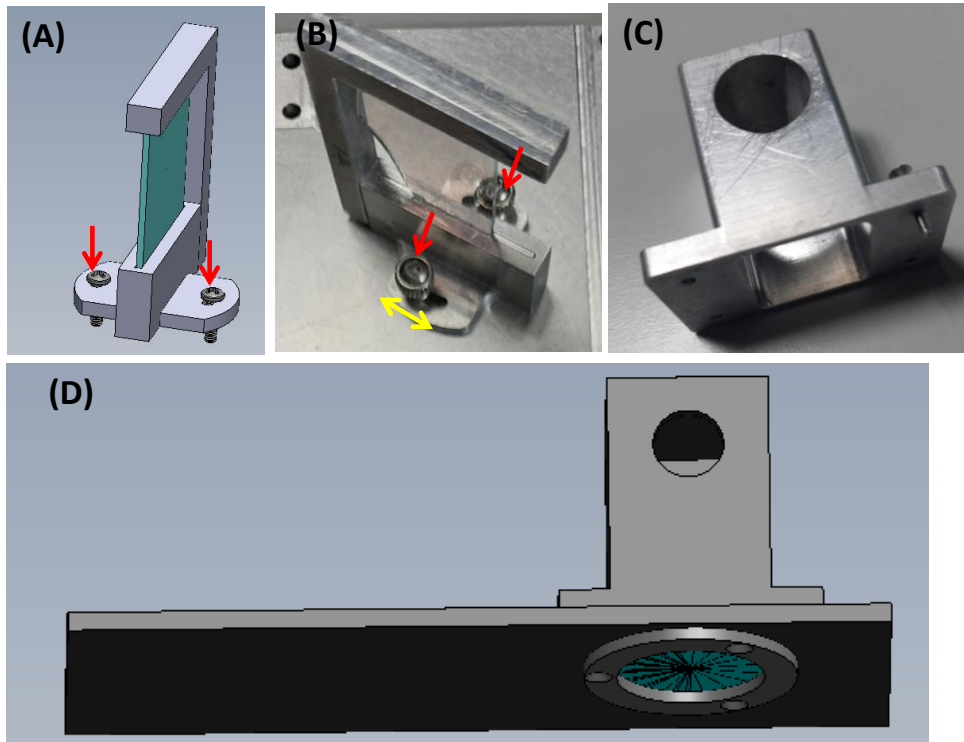


Figure 3.4. 3D design and photograph of mount for (A,B) beam splitter, (C,D) sample holder. Red arrow marks show the mounting screws to the chassis.

Focusing lens L1: Once the beam splitter was aligned at 45°, the convex lens L1 (aperture: 25 mm, FL: 30 mm) used to focus the laser onto the sample was mounted onto the wall of the chassis, as shown in Figure 3.4 D.

Sample holder: To improve the usability and safety aspect, a sample holder was designed (Figure 3.4 C) to hold glass vials of diameter up to 1 cm. This specifically designed sample holder confines the laser radiation inside and gets rid of unnecessary exposure to the personnel. It also avoids the need for manual focusing of the laser on the sample.

Focusing lens L2: The scattered light collected by the lens L1 is focused onto the detector unit using a second lens L2 (aperture: 25 mm diameter and 30 mm focal length). The lens was mounted on a holder placed at a distance of 30 mm from the entrance slit of the detector. In the tabletop version, for aligning the probe optics to the detector unit with micrometer precision, a facility was provided for the X, Y, and Z movement of the optical fibre using the translational stage. Conversely, in the portable version 5 mm movement freedom was provided for the lens L2 (Figure 3.5) in both X and Y axis. This helps in aligning the probe optics with the detector and thus achieve maximum signal coupling.

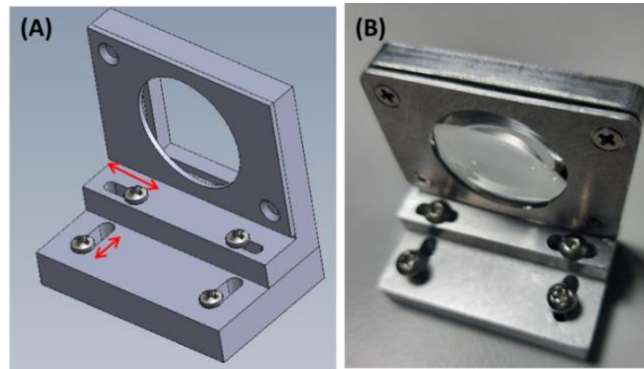


Figure 3.5. (A) 3D design and (B) photograph of the lens mount. The arrow marks indicate the provision provided for 5 mm movement freedom along the X and Y-axis.

Rayleigh blocking filter: To block the Rayleigh scattered light, two long-pass filters with cut off at 550 nm were cut into a size of 2.5 x 2.5 cm, and stacked together, and placed in between the beam splitter and the lens L2. Filters were affixed on the sheet having a hole that coincides with the optical axis of other components to avoid any stray light entering the detector.

Detector: To achieve maximum coupling of the light to the detector, direct coupling was adopted rather than fibre coupling. The case of the spectrometer was removed, and the entire unit was mounted on the chassis through 4 screws, as shown in Figure 3.6. The spectrometer was mounted in such a way that the entrance slit of the detector

was exactly aligned with the optical axis. Figure 3.6 shows the 3D design of the spectrometer unit mounted on the base of the chassis.

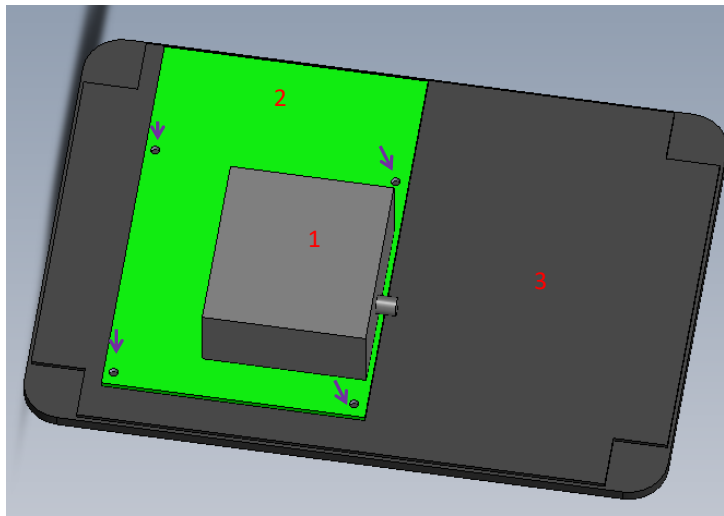


Figure 3.6. 3D design showing the spectrometer mounted on the chassis using the four screws (arrow marks) with parts marked as 1. optical bench, 2. electronics board, and 3. base of the chassis.

3.4.2. Integrating Portable Raman Spectrometer

Once all the components were mounted on the chassis, as shown in Figure 3.7, the necessary electrical connections were made. Three external interfaces were included onto the chassis sidewall, (i) a micro-USB connector for powering the device, (ii) an external switch, and (iii) a DB9 connector, as shown in Figure 3.8.

In comparison with the tabletop version, a single power supply was provided for both the laser diode and the spectrometer using a 5V DC adapter through a micro USB connector (marked as 1 in figure 3.8). The detector unit was powered directly from this input power supply. While the laser diode requires a voltage of 3.3V, the voltage supply was step down from 5V to 3.3 V by adding an extra resistor. To avoid unintentional laser exposure to the sample, an external mechanical switch (marked as 2 in Figure 3.8) was added to turn ON/OFF the laser without powering off the entire unit.

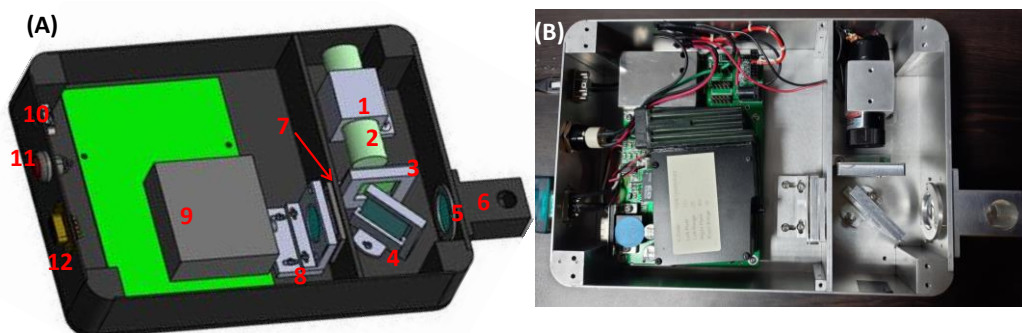


Figure 3.7. 3D drawing of the Raman spectrometer showing the internal components 1. laser diode mount, 2. laser diode, 3. band-pass filter, 4. beam splitter, 5. focusing lens, L1, 6. glass vial holder, 7. long-pass filter, 8. focusing lens L2 on XY translating mount, 9. spectrometer, 10. charging port, 11. external switch to control the laser ON/OFF, and 12. RS232 to USB converter to communicate with a windows tablet, and (B) photograph of the assembled system.



Figure 3.8. Photographs showing the interfaces on the sidewall of the chassis, marked as 1. powering port, 2. switch for laser control, and 3. RS232 port to communicate with the tablet PC.

For spectrum acquisition and displaying the results, a tablet PC with Windows OS was used. A mechanical mount was designed for the tablet, as shown in Figure 3.9, and integrated into the main chassis. The PC communicates with the spectrometer through RS232 using the DB9 connector marked as 3 in Figure 3.8. Figure 3.10 shows the different stages of integrating the device. An image of the fully integrated system is shown in Figure 3.11. Once all the integration was done, fine optical alignment was performed using a fluorescence sample.

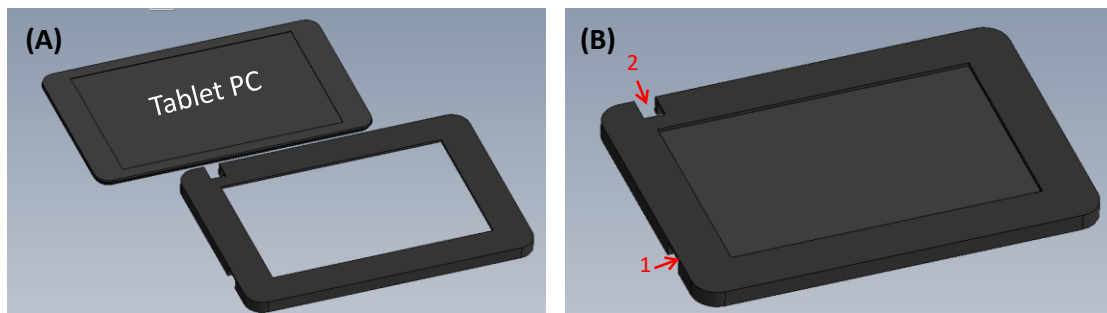


Figure 3.9. Mount for the tablet PC (A) exploded view and the assembled view. Arrow marks indicate the slot for 1: accessing the microUSB port 2: power switch of the tablet PC.

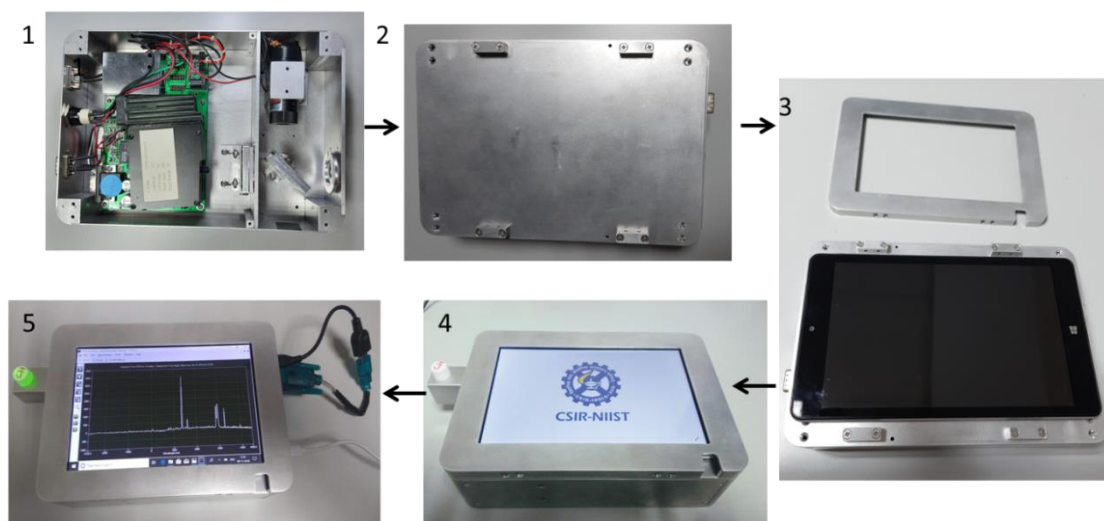


Figure 3.10. Photographs showing the different stages of the assembled system.

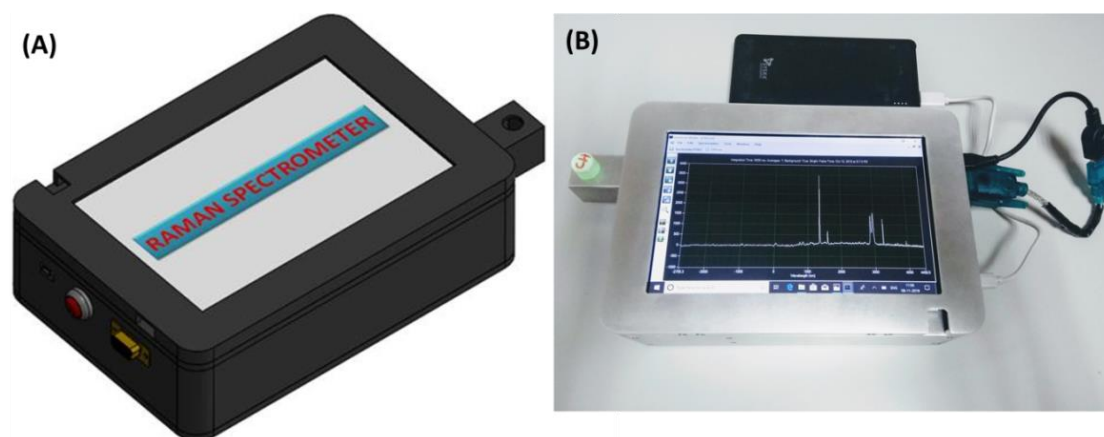


Figure 3.11. (A) 3D design of the Raman spectrometer and (B) photograph of the assembled system.

3.4.3. Performance Comparison with Tabletop Version

Figure 3.12 represents the Raman spectra of cyclohexane and benzonitrile taken using the fabricated and the tabletop system. For a meaningful comparison, both the spectra were taken using the same integration time (5 s) and no. of averages (1). As expected, better signal intensity is obtained for the fabricated system than the tabletop arrangement mainly due to the following reasons, (i) direct coupling of the probe optics provides better signal coupling to the detector than fibre optics coupling, (ii) lens L1 has a shorter focal length; thus laser spot at the sample ($\sim 34 \mu\text{m}$) is smaller, and hence higher laser power per unit area, (iii) the focal length of L2 is selected such that the focal spot size of L2 is not greater than the entrance slit of the detector i.e. $50 \mu\text{m}$, and (iv) use of 50:50 beam splitter. Around 5 to 6 times increment in signal intensity was obtained.

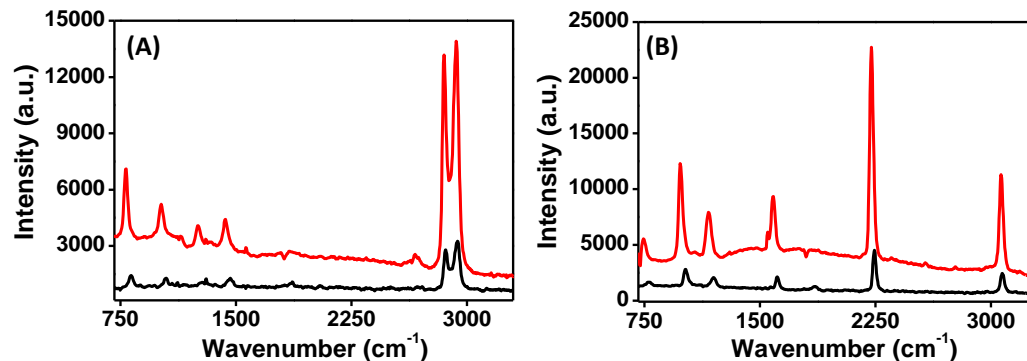


Figure 3.12. Raman spectra of (A) cyclohexane and (B) benzonitrile took using the portable Raman spectrometer (red) and tabletop version (black), all spectra were taken with 5 s integration time.

3.4.4. Performance Comparison with a Commercial Device

Validation of the fabricated device was carried out by analysing various standard samples and comparing the data with those recorded using a commercial confocal Raman microscope with model number WITec Alpha300R, M/s WITec Inc Germany. Table 3.2 compares the specifications of commercial and fabricated systems.

Table 3.2. Specifications of the commercial device and the fabricated system

Parameters	Portable RS	Confocal RS
Excitation laser	532 nm, 10 mW	532 nm, 25 mW
Detector	SonyILX511 Linear CCD	M/s Princeton instruments ActonSpectraPro® SP2300
Grating	1800 lines/mm	600 lines/mm
Collection optics	Convex lens 30 mm focal length	10X, 0.25 NA objective lens
Spectral range	700-4000 cm^{-1}	180-3200 cm^{-1}
Spectral resolution	25-28 cm^{-1}	$<3 \text{ cm}^{-1}$

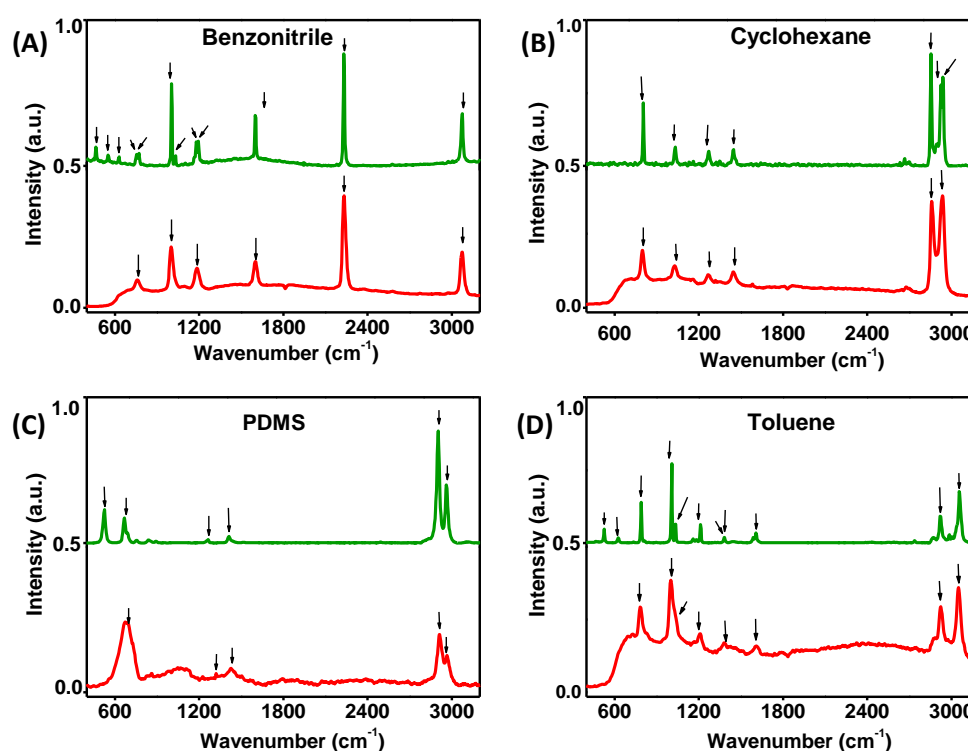


Figure 3.13. Raman spectra of (A) benzonitrile (B) cyclohexane (C) PDMS and (D) toluene obtained using the confocal Raman microscope (laser power 25 mW) (green) and fabricated portable system (laser power 10 mW) (red). All spectra were taken with 5 s integration time.

Figure 3.13 represents the Raman spectra of various chemicals such as benzonitrile, cyclohexane, polydimethylsiloxane (PDMS), and toluene measured using the fabricated system and the confocal Raman microscope. The observed peak positions are tabulated in Table 3.3 and were assigned to specific bond vibrations from literature references.²⁸⁻³¹

Table 3.3. Comparison of the peak positions observed from the confocal microscope, the developed portable device and reported values

Reported (a)	Raman Shift, $\Delta\bar{\nu}$ (cm^{-1})		Deviation (cm^{-1})		Assigned bond vibration
	Confocal Microscope (b)	Portable spectrometer (c)	Confocal Microscope (b-a)	Portable spectrometer (c-a)	
Benzonitrile					
460.9	464	-	3.1	-	Ring deformation
548.5	551	-	2.5	-	C \equiv N in-plane bending
751.3	753	757	1.7		C-H bend
767.1	771		3.9		C-H bend
1007	1003	1002	-4		C-C stretch
1026.6	1030		3.4		C-C stretch
1177.7	1179	1185	1.3		C-CN stretch
1192.6	1195		2.4		
1598.9	1601	1600	2.1	1.1	C=C stretch
2229.4	2232	2232	2.6	2.6	C-N stretch
3072.3	3074	3072	1.7	0.3	C-H stretch
Cyclohexane					
801.3	806	802	4.7	0.7	C-C stretch
1028.3	1032	1032	3.7	3.7	C-C stretch
1266.4	1269	1268	2.6	1.6	CH ₂ twist
1444.4	1447	1448	2.6	3.6	CH ₂ -scis
2852.9	2855	2854	2.1	1.1	CH ₂ stretch
2923.8	2927		3.2		CH ₂ -asym stretch
2938.3	2940	2926	1.7		CH ₂ -asym stretch
PDMS					
492	525	-	33		Si-O-Si stretch
688	667	689	-21	1	CH ₃ rock
1413	1411	1418	-2	5	CH ₃ asym bend
2906	2902	2911	-4	5	C-H stretch
2967	2963	2969	-4	2	C-H stretch
Toluene					
521.7	525	-	3.3	-	Ring deformation
786.5	788	789	1.5	0.5	Out of plane C- H bend
1003.6	1006		2.4		
1030.6	1033	1007	2.4		In-plane C-H bend

1211.4	1213	1212	1.6	0.6	Aromatic C-C stretch
1605.1	1608	1609	2.9	3.9	Aromatic C=C stretch
2919.5	2921	2922	1.5	2.5	C-H stretch
3057.1	3056	3056	-1.1	-1.1	Aromatic C-H stretch

In general, for all the compounds investigated, we found good agreements between data obtained from the fabricated device and commercial system in terms of spectral band position and relative intensities. For example, the dominant peaks observed with the fabricated spectrometer system for benzonitrile were 1002 cm^{-1} , 1600 cm^{-1} , 2232 cm^{-1} , and 3072 cm^{-1} arising from the C-C stretch/Ring breath, C=C stretch, C-N stretch, and C-H stretch vibrations, respectively. Our spectrometer's lower spectral acquisition limit is $\sim 620\text{ cm}^{-1}$ because we have employed a 550 nm long-pass filter. The other apparent difference was with the spectral resolution. Very close peaks (751.3 cm^{-1} and 767.1 cm^{-1} , 1007 cm^{-1} and 1026.6 cm^{-1} , 1177.7 cm^{-1} and 1192.6 cm^{-1}) whose separation was less than 30 cm^{-1} appeared as single peaks in the Raman spectrum acquired with the currently fabricated system. This is mainly limited by the FWHM of the laser, and the resolution of the spectrometer, which resulted in minor variation in the spectral band position with respect to the reported values, as noted in Table 3.2. The other factors contributing to this could be inaccuracies in determining the exact wavelength of the excitation source.

3.4.5. Quantitative Analysis

As the obtained Raman spectral intensities are functions of excitation power, scattering cross-section of the sample, and the concentration of the component in the sample, the technique can be used for quantitative analysis. In effect, the observed Raman spectrum will be the algebraic sum of the contributions of the individual components.

To illustrate the potential of the current system for mixture analysis, we studied a model system of cyclohexane-toluene mixture. Seven mixtures of toluene blended with cyclohexane at a concentration range 0-100 volume percentage was prepared. The raw spectra of the mixtures are represented in Figure 3.14.

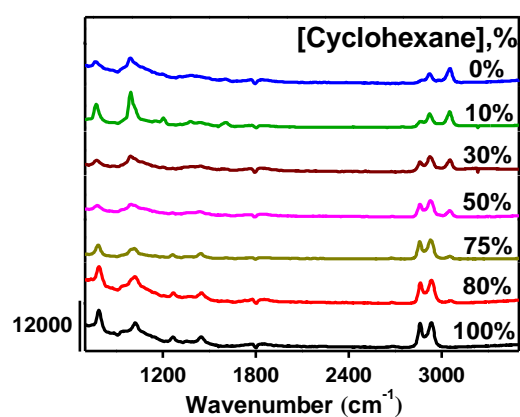


Figure 3.14. Raman spectra of cyclohexane-toluene mixtures of varying compositions collected using the fabricated portable device with acquisition parameters: integration time 3 s, no. of averages 5, laser power 10 mW measured at sample point.

Toluene and cyclohexane have characteristic peaks with high intensity in the range 2500-3100 cm^{-1} (Figure 3.15). Due to their non-overlapping nature, the peaks at 2858 cm^{-1} (CH_2 stretching) and 3055 cm^{-1} (aromatic C-H stretch) were selected as marker peaks for cyclohexane and toluene, respectively. The analysis of the data revealed a linear response for both the increase of peak intensity at 2858 cm^{-1} and the decrease of peak intensity at 3055 cm^{-1} with an increase in cyclohexane concentration. This could serve as the calibration curve for the quantitative analysis of samples of unknown concentrations. Instead of peak intensity, one could also employ the peak area for generating a calibration graph. A representative example of the calibration curve for quantifying cyclohexane using peak area under the range 2830-2880 cm^{-1} is shown in Figure 3.16.

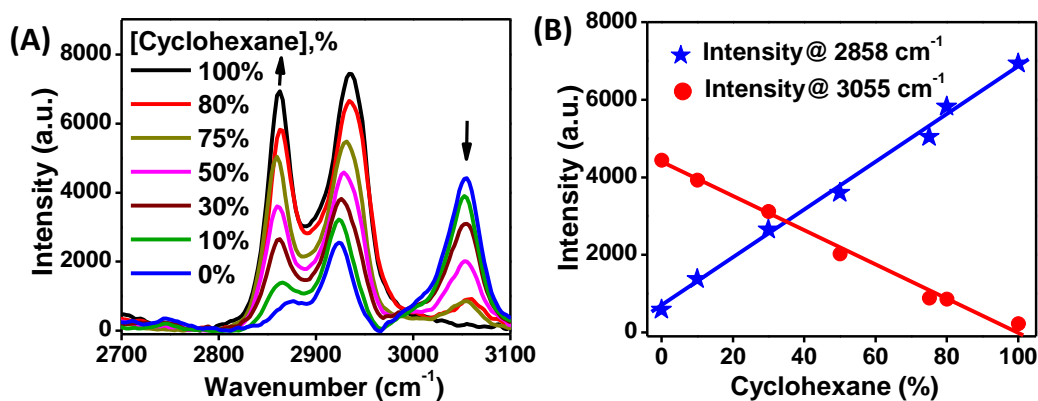


Figure 3.15. (A) Raman spectra of cyclohexane-toluene mixtures in the range 2700 to 3100 cm⁻¹ (B) variation in peak intensity at 2858 cm⁻¹ and 3055 cm⁻¹ with respect to cyclohexane concentration.

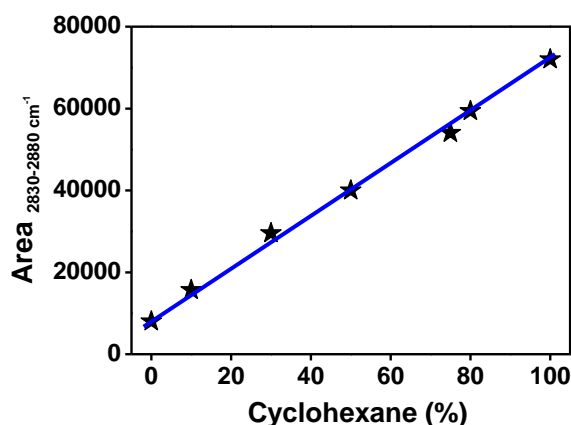


Figure 3.16. Variation in peak intensity in the range 2830 cm⁻¹ to 2880 cm⁻¹ vs cyclohexane concentration.

The plot of cyclohexane concentration against peak intensity at 2850 cm⁻¹ and peak area in the range 2830 cm⁻¹ to 2880 cm⁻¹ showed a correlation of 0.993 and 0.998, respectively. This shows that quantification prediction accuracy could be improved by peak area analysis than peak intensity.

3.4.6. Onsite Analysis

To study the possibility of onsite analysis using the fabricated portable Raman spectrometer, we considered a real-life scenario to predict alcohol content in beverages. Ethanol and water are the main components of most alcoholic beverages, and they vary by the alcohol by volume (ABV) content. For creating calibration data,

mixtures of ethanol and water were prepared in the concentration range 0-100 volume percentage of ethanol and analysed using the fabricated system. The characteristic Raman peaks for water due to OH stretching appeared in the range 3100-3600 cm^{-1} , while $\text{CH}_3\text{-CH}_2$ stretching of ethanol peaked in the range $\sim 2800\text{-}3000 \text{ cm}^{-1}$.²² The acquired spectra of the ethanol and the mixtures after baseline correction are presented in Figure 3.17 and 3.18.

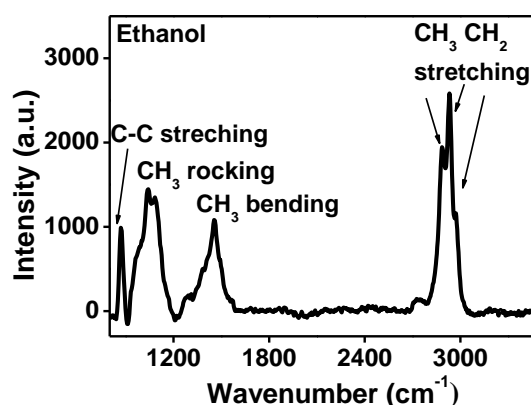


Figure 3.17. Raman spectra of ethanol collected using the fabricated portable device

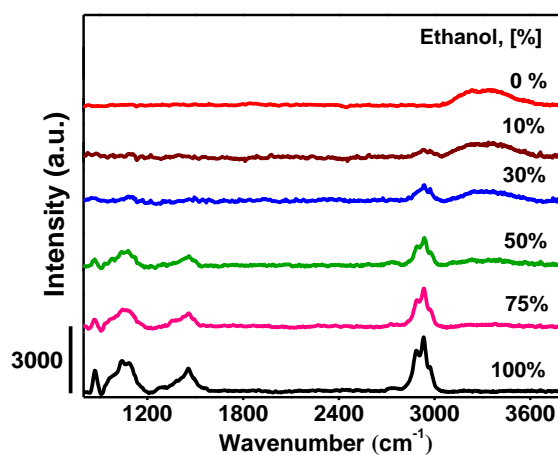


Figure 3.18. Raman spectra of ethanol-water mixtures of varying compositions collected using the fabricated portable device with acquisition parameters: integration time 5 s, no of averages 5, laser power 10 mW measured at the sample point.

The goal is to quantify the ethanol from the mixtures by analysing the spectral region 2800-3000 cm^{-1} . To achieve this a calibration curve was plotted with integrated peak intensities in this range against ethanol concentration and is shown in Figure 3.19.

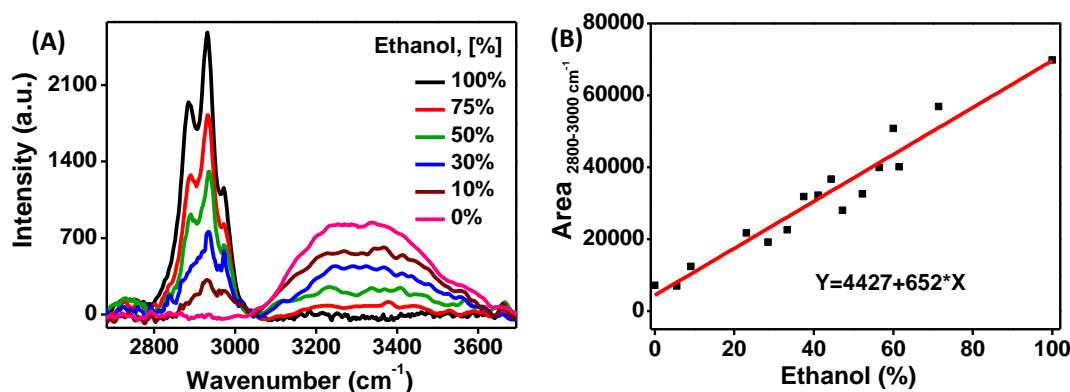


Figure 3.19. (A) Raman spectra in the range 2700- 3700 cm⁻¹ of ethanol-water mixtures of varying compositions collected using the device with 10 mW laser power and 5 s integration time and (B) plot showing the variation in integrated peak intensity in the range 2800-3000 cm⁻¹ vs ethanol concentration.

The linear fit ($Y = mX + C$) of this graph yielded a correlation coefficient R^2 value of 0.97. Using the calibration curve provided in Figure 3.19 B, ethanol was predicted from new samples, which were not used for calibration. The prepared and predicted ethanol concentration in new samples is tabulated in Table 3.4.

Table 3.4. Prepared and predicted ethanol concentration in laboratory prepared mixtures

Prepared ethanol conc. %	Predicted ethanol conc. %
5.6	3.88
23	26
41	42.5
56.5	54.45
100	100

Apart from the laboratory prepared samples, alcohol was also quantified from commercially available real alcoholic beverages. According to the package details provided by the manufacturer, the sample under analysis (white rum) containing alcohol V/V 42.86 %. The Raman spectrum of the sample collected using the fabricated spectrometer is given in Figure 3.19. Using the calibration curve provided

in Figure 3.18 B alcohol content was estimated as ~ 41%.

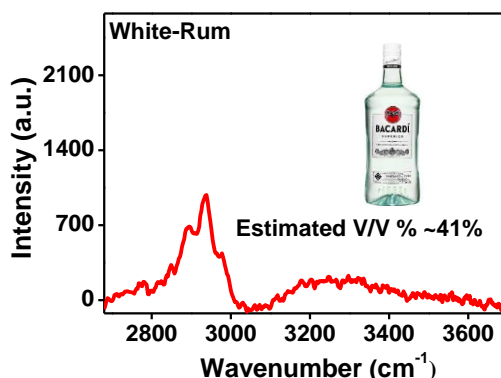


Figure 3.20. Raman spectrum of an alcoholic drink containing 42.86 alcohol V/V %, inset shows the photograph of the sample under analysis.

3.4.7. Scope for Improvement

Relevant parts and prices of the proposed Raman spectrometer are tabulated in Table

3.4.

Table 3.5. Component list of fabricated portable Raman spectrometer with price details

Sl No	Component	QTY	Make and model	Price(INR)
1	Green laser pointer	1	Huonje, JD851, 70 mW output power	1000
2	50-50 beam splitter	1	Banggood, 50R/50T Plate Beam Splitter Plate 80 x 80 x 1.1 mm	2000
3	Band-pass filter	1	BP520	
4	Long-pass filter (2x2 inch)	1	Newport , 20CGA-550	8000
5	Biconvex lens (FL-3cm)	2	Holmarc, HO-BXL25-1.2	3000
6	Spectrometer	1	Science Surplus1800 lies/mm,1 nm resolution, 500-700 nm range	14000
7	8 inch windows tablet	1	Nuvision, TM800W610L	14000
8	Power bank and USB cable (portable mobile charger)	1	Syska Power Pro2000	1000
9	Material cost for chasis fabrication	1	Aluminum	9000
Total cost				52000

From the data, it can be inferred that a good cost-effective, portable, and fully integrated Raman spectrometer, can be implemented at a material cost of around Rs. 52000/-. The design and machining cost for chassis fabrication was not included in the price calculation. The chassis could also be 3D printed using materials like PLA/ABS. Instead of a science surplus spectrometer, one could build an own low-cost spectrometer at a much lower cost compared to other commercially available spectrometers.

Current limitations and feasible improvements of the developed equipment are listed below.

(i). Fluctuation in the output optical power of the laser pointer mainly due to thermal variations. To maintain the operating temperature at a specific value (e.g. 25 °C) TEC cooling needs to be incorporated with the laser diode.

(ii). The spectral range is mainly limited by the cut-off wavelength (550 nm) of the long-pass filter. This could be overcome using a filter with a lower cut-off wavelength, for example, the band-pass filter, NF533-17 from Thorlabs, can provide a spectral range from 320 cm^{-1} .

(iii). The spectral resolution (25-30 cm^{-1}) is mainly limited by the resolution of the detector unit (~ 1 nm). This could be improved up to ~ 10 -17 cm^{-1} without replacing the laser source by using an alternated spectrometer with a better resolution (0.3-0.5 nm).

(iv). Improve the laser signal intensity at the sample using a dichroic beam splitter, rather than a 50-50 beam splitter. For example, dichroic beam splitter Di03-R532-t1-25x36, Semrock reflects almost 98% of the 532 nm wavelength to the sample and transmits >93% of all the wavelengths above 541 nm at an angle of incidence 45°.

The inclusion of these improvements would imply a considerable increment in the performance (spectral range: 300-4000 cm^{-1} , and spectral resolution: ~ 15 cm^{-1}) of

the proposed device, at an extra cost of approximately Rs. 1,50,000/-.

3.5. Summary

The results presented in this chapter demonstrate the feasibility of the implementation of a portable Raman spectrometer having the following specifications; excitation wavelength: 532 nm, spectral range: 650-4000 cm^{-1} , and spectral resolution $\sim 25 \text{ cm}^{-1}$. The fabricated system has many favourable qualities like affordable price, ease of construction, and reliability. Moreover, the design strategy provided offers the flexibility of configuring Raman systems with a different excitation wavelength, and the only modification to be implemented will be the choice of the long-pass filter with the right cut-off wavelength. The performance of the system was compared with the commercially available device and exhibited good matching with Raman shift values and relative peak intensity of the commercial system, which was confirmed by the obtained spectra of cyclohexane, benzonitrile, PDMS, and toluene. Quantitative analysis of components from mixtures was studied and utilised the device for quantifying alcohol from alcoholic beverages.

3.6. References

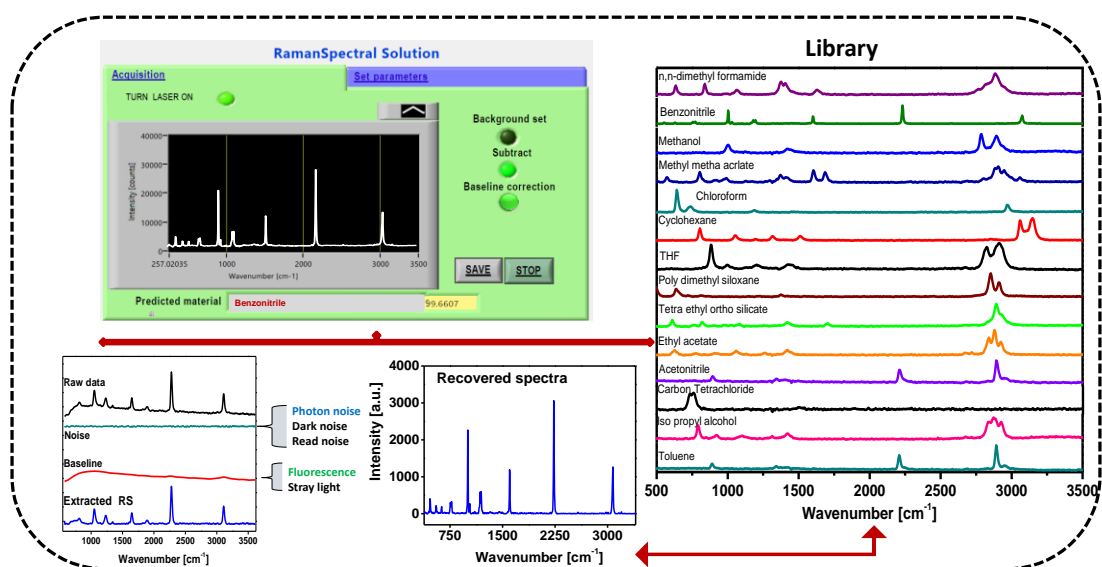
1. Giridhar, G.; Manepalli, R. R. K. N.; Apparao, G., Chapter 7 - Confocal Raman Spectroscopy. In *Spectroscopic Methods for Nanomaterials Characterization*, Thomas, S., et al., Eds. Elsevier: 2017; pp 141-161.
2. Zhu, X.; Xu, T.; Lin, Q.; Duan, Y., Technical development of Raman Spectroscopy: from instrumental to advanced combined technologies. *Appl. Spectrosc. Rev.* **2014**, *49* (1), 64-82.
3. Pence, I.; Mahadevan-Jansen, A., Clinical instrumentation and applications of Raman spectroscopy. *Chem. Soc. Rev.* **2016**, *45* (7), 1958-1979.
4. Li, Y.-S.; Church, J. S., Raman spectroscopy in the analysis of food and pharmaceutical nanomaterials. *J. Food Drug Anal.* **2014**, *22* (1), 29-48.

5. Tucker, S. C.; Honn, K. V.; Kast, R. E.; Auner, G. W., Agricultural and environmental management with Raman spectroscopy. *Spectroscopy* 2015, pp 47–53.
6. Li, B.; Singer, N. G.; Yeni, Y. N.; Haggins, D. G.; Barnboym, E.; Oravec, D.; Lewis, S.; Akkus, O., A point-of-care Raman Spectroscopy-based device for the diagnosis of gout and pseudogout: comparison with the clinical standard microscopy. *Arthritis Rheumatol.* **2016**, *68* (7), 1751-1757.
7. Senger, R. S.; Sullivan, M.; Gouldin, A.; Lundgren, S.; Merrifield, K.; Steen, C.; Baker, E.; Vu, T.; Agnor, B.; Martinez, G.; Coogan, H.; Carswell, W.; Kavuru, V.; Karageorge, L.; Dev, D.; Du, P.; Sklar, A.; Pirkle, J., Jr.; Guelich, S.; Orlando, G.; Robertson, J. L., Spectral characteristics of urine from patients with end-stage kidney disease analyzed using Raman Chemometric Urinalysis (Rametrix). *PLoS ONE* **2020**, *15* (1), e0227281.
8. Owens, N. A.; Laurentius, L. B.; Porter, M. D.; Li, Q.; Wang, S.; Chatterjee, D., Handheld Raman spectrometer instrumentation for quantitative tuberculosis biomarker detection: A performance assessment for point-of-need infectious disease diagnostics. *Appl. Spectrosc.* **2018**, *72* (7), 1104-1115.
9. Jin, H.; He, X.; Zhou, H.; Zhang, M.; Tang, Q.; Lin, L.; Hao, J.; Zeng, R., Efficacy of raman spectroscopy in the diagnosis of kidney cancer: A systematic review and meta-analysis. *Medicine* **2020**, *99* (27).
10. Kong, K.; Kendall, C.; Stone, N.; Notingher, I., Raman spectroscopy for medical diagnostics From in-vitro biofluid assays to in-vivo cancer detection. *Adv. Drug Deliv. Rev.* **2015**, *89*, 121-134.
11. Paudel, A.; Rajjada, D.; Rantanen, J., Raman spectroscopy in pharmaceutical product design. *Adv. Drug Deliv. Rev.* **2015**, *89*, 3-20.
12. Visser, B. J.; de Vries, S. G.; Bache, E. B.; Meerveld-Gerrits, J.; Kroon, D.; Boersma, J.; Agnandji, S. T.; van Vugt, M.; Grobusch, M. P., The diagnostic accuracy of the hand-held Raman spectrometer for the identification of anti-malarial drugs. *Malar. J.* **2016**, *15* (1), 160.
13. Gao, F.; Liu, W.; Meng, Z.; Su, P.; Li, Z.; Wang, M., A rapid and sensitive quantitative analysis method for TNT using Raman Spectroscopy. *Propellants Explos. Pyrotech* **2019**, *44* (3), 337-344.
14. Robert, T.; Bakeev, K. A., The use of portable and handheld Raman spectroscopy for forensic investigations. *Spectrosc.* **2014**, *29* (6).

15. Izake, E. L., Forensic and homeland security applications of modern portable Raman spectroscopy. *Forensic Sci. Int.* **2010**, *202* (1-3), 1-8.
16. Karacaglar, N. N. Y.; Bulat, T.; Boyaci, I. H.; Topcu, A., Raman spectroscopy coupled with chemometric methods for the discrimination of foreign fats and oils in cream and yogurt. *J. Food Drug Anal.* **2019**, *27* (1), 101-110.
17. Heuler, J.; He, S.; Ambardar, S.; Voronine, D. V., Point-of-care detection, characterization, and removal of chocolate bloom using a handheld Raman spectrometer. *Sci. Rep.* **2020**, *10* (1), 9833.
18. Zou, M.-Q.; Zhang, X.-F.; Qi, X.-H.; Ma, H.-L.; Dong, Y.; Liu, C.-W.; Guo, X.; Wang, H., Rapid authentication of olive oil adulteration by Raman spectrometry. *J. Agric. Food Chem* **2009**, *57*, 6001-6.
19. Herrero, A. M., Raman spectroscopy a promising technique for quality assessment of meat and fish: A review. *Food Chem.* **2008**, *107* (4), 1642-1651.
20. Keidel, A.; von Stetten, D.; Rodrigues, C.; Máguas, C.; Hildebrandt, P., Discrimination of green arabica and Robusta coffee beans by Raman spectroscopy. *J. Agric. Food Chem.* **2010**, *58* (21), 11187-92.
21. Sanford, C. L.; Mantooth, B. A.; Jones, B. T., Determination of ethanol in alcohol samples using a modular Raman SPECTROMETER. *J. Chem. Educ.* **2001**, *78* (9), 1221-1225.
22. Numata, Y.; Iida, Y.; Tanaka, H., Quantitative analysis of alcohol–water binary solutions using Raman spectroscopy. *J. Quant. Spectrosc. Radiat. Transf.* **2011**, *112* (6), 1043-1049.
23. Vaskova, H., Spectroscopic determination of methanol content in alcoholic drinks. *Int. J. Biol. Biomed. Eng.* **2014**, *8*, 27-34.
24. Debra Johnson, P. L.; Jerry Fluellen, Douglas Furton, Stephanie A. Schaertel, A modular Raman spectrometer for solids. *Chem. Educator.* **2008**, *13* (2), 82-86.
25. Mohr, C.; Spencer, C. L.; Hippler, M., Inexpensive Raman spectrometer for undergraduate and graduate experiments and research. *J. Chem. Educ.* **2010**, *87* (3), 326-330.
26. Somerville, W. R. C.; Ru, E. C. L.; Northcote, P. T.; Etchegoin, P. G., High performance Raman spectroscopy with simple optical components. *Am. J. Phys.* **2010**, *78* (7), 671-677.

27. Eduardo H. Montoya R, A. A. L., Oscar R. Baltuano E., A Homemade cost effective Raman spectrometer with high performance. *J. Lab. Chem. Educ.* **2015**, 3 (4), 67-75.
28. Borjanovic, V.; Bistričić, L.; Vlasov, I.; Furić, K.; Zamboni, I.; Jaksic, M.; Shenderova, O., Influence of proton irradiation on the structure and stability of poly(dimethylsiloxane) and poly(dimethylsiloxane)-nanodiamond composite. *J. Vac. Sci. Technol.* **2009**, 27 (6), 2396-2403.
29. Dengke, C.; Andreas, N.; Rüdiger, K.; Heise, H. M., Raman, mid-infrared, near-infrared and ultraviolet–visible spectroscopy of PDMS silicone rubber for characterization of polymer optical waveguide materials. *J. Mol. Struct.* **2010**, 976 (1), 274-281.
30. McCreery, R. L., *Raman spectroscopy for chemical analysis*. John Wiley & sons: Canada, 2000.
31. Yadav, R. A.; Singh, I. S., Vibrational spectra and normal coordinate analysis for substituted trifluoromethyl benzenes. *J. Chem. Sci.* **1985**, 95 (5), 471-487.

Spectral Processing and Library Matching Tools for Onsite Analysis



4.1. Abstract

The fingerprinting capability of Raman spectroscopy makes it a powerful tool for material identification. However, the low signal strength and interfering contribution from several noises necessitate post-acquisition spectral processing to extract useful information from the raw spectra. Incorporating spectral processing and analysis tool into the data acquisition software architecture elevates the potential of portable/handheld Raman spectrometer for onsite testing. Thus, the device provides rapid results, becomes more convenient to use, and assists in making informed decisions on the spot. Herein, we attempted to develop a software tool for spectral processing and library matching to integrate with the fabricated Raman spectrometer. The efficacy of several existing background removal techniques was investigated on mathematically simulated spectra. Blank subtraction and Savitsky-Golay filtering

were found to be effective in removing high-frequency noises. While, the I-Mod-Poly method could correct the baseline without the need for any user-defined parameters, regardless of the baseline shape. Thus, these methods could accurately retrieve Raman spectral information with minimum user intervention and hence chosen to construct spectral analysis software. The fabricated portable device was used to build a Raman spectral library comprising 24 distinct compounds. Together with a correlation coefficient-based library matching algorithm, this spectral database was incorporated into the software. The software was designed and built with a user-friendly and straightforward graphical user interface using LabVIEW.

4.2. Introduction

Raman spectroscopy has emerged as a valuable and promising tool in various material identification and sensing fields, including disease diagnosis,¹ food quality analysis,^{2,3} and environmental monitoring.⁴ Despite the fact that Raman spectroscopy is a powerful technology for spectral fingerprinting, there are a few hurdles to be solved for improving the end-user experience, especially in the context of onsite analysis. Raman scattering is intrinsically a weak phenomenon, with just one out of every 10^7 photons experiencing inelastic scattering.⁵ Due to technical restrictions, only a tiny portion of these scattered photons can be measured.⁶ As a result, the measured Raman scattered light is much weaker than the incident laser and is highly susceptible to interferences and noises.⁷ The challenge of transforming the raw spectral data into useful information is significant and requires a lot of spectrum processing. Thus, data acquisition, signal processing and analysis need to be entirely automated for an ideal POC device. There exist a few commercial software tools for post-acquisition Raman spectral processing like WiRE (M/s Renishaw, UK), WiTec Suite Five (M/s WITec, Germany), OPUS (M/s Bruker, USA), Unscrambler® X (M/s Camo Analytics,

Norway) and open-source tools like Vespucci,⁸ RamanProcessing,⁹ Rampy,¹⁰ RamanToolSet,^{11,12} SpecTool,¹³ etc. These software packages work stand alone and are not expandable or modifiable. This chapter explores different spectral processing methodologies and the development of fully integrated software for the portable Raman spectrometer, which offers easy onsite testing. The portable Raman spectrophotometer detailed in this chapter is an improved version of the device described in chapter 3.

In general, noises are of either high or low frequency in nature compared to the Raman spectrum.¹⁴ Shot noise, readout noise, dark noise are examples of the former, while fluorescence and stray light contribute to the latter. Figure 4.1 is an example of the raw Raman spectrum of toluene obtained with the portable Raman spectrometer (described in the previous chapter) and depicts contributions from noises and background. Ultimately, noises define the sensitivity and detection limit of the Raman spectrometer. In general, the sensitivity of a Raman spectrometer can be expressed in terms of signal-to-noise ratio (SNR)¹⁵. Figure 4.2 is an example of the Raman spectra of cyclohexane measured with two different integration times and illustrates the influence of integration time on noises. At a very low integration time (0.5 s), all the peaks except the high-intensity ones in the range 2700-3100 cm^{-1} are masked under

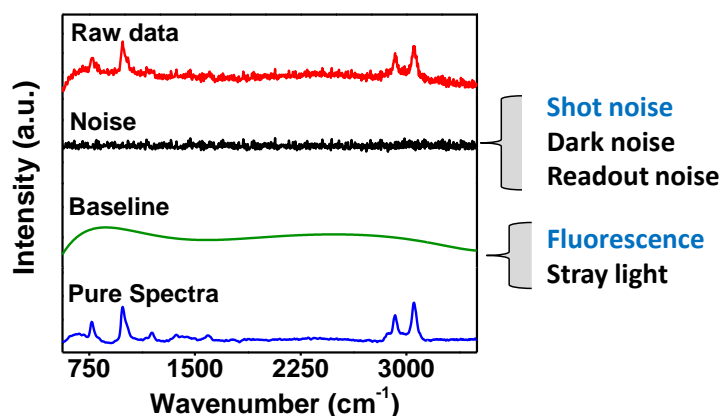


Figure 4.1. Raman spectrum of toluene taken using the portable Raman spectrometer developed in chapter 3 (red), and its decomposed components: high-frequency noise (black), low-frequency baseline (green), and the denoised Raman spectrum (blue).

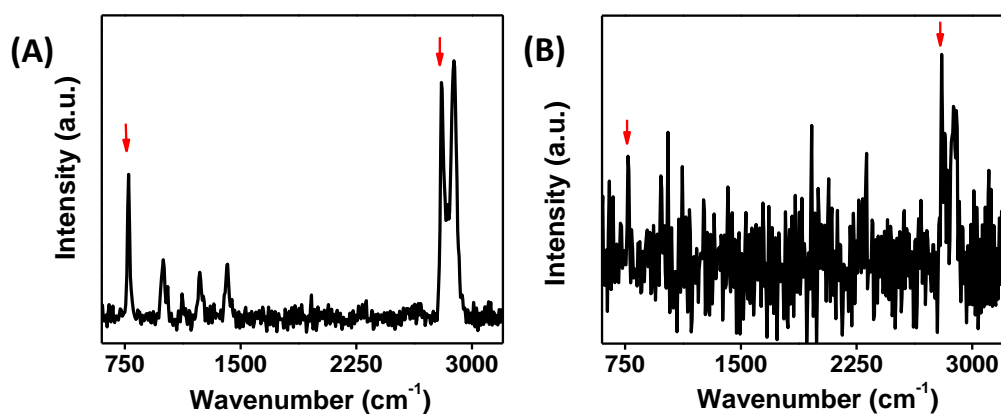


Figure 4.2. Raw Raman spectrum of cyclohexane taken at (A) 3 s, (B) 0.5 s integration time using the upgraded version of portable Raman spectrometer at laser power ~ 5 mW (Figure 4.5).

the noise and have $\text{SNR} \leq 2$. When the integration time is substantially increased to 3 s, the signal level got considerably increased, enhancing the $\text{SNR} \geq 5$. As a result, all the peaks became easily noticeable and distinguishable. Therefore, in instances of low SNR, it is necessary to adopt proper means to improve the SNR.

Various possibilities for increasing the SNR of Raman spectroscopic systems¹⁶ are: (i) Increase the number of scattered photons using higher laser power; however, this is often limited by the photodamage to the sample, especially in biological samples. (ii) Increase the acquisition time and thus collect more photons. But the prolonged exposure of the sample to the laser may result in photodamage. (iii) Collect more amount of scattered photons by optimising the hardware features (e.g. improving the numerical aperture).¹⁷ (iv) Reduce the noise by optimising the detector unit like using those with higher quantum efficiency, reduced readout noise and dark currents, and by operating at a lower temperature. This may require additional hardware changes increasing the cost and sophistication of the device. Denoising the acquired spectrum through software methods^{18,19} is another viable approach to improve the SNR, and could be implemented alone or together with the other techniques discussed above.

Similar to high-frequency noises, fluorescence from samples under consideration significantly impact the Raman spectral measurements. In most cases, fluorescence has several orders of magnitude higher quantum efficiency than the Raman scattering. Also, Stokes Raman bands appear in the same spectral region as that of fluorescence. This leads to engulfing of weak Raman signal inside the strong fluorescence spectrum. Instrumental and computational approaches have been explored to suppress or remove fluorescence from Raman spectral data.²⁰ Shifted excitation^{21,22} and time gating²³ are examples of instrumental techniques that require hardware modifications. SERS technology is another way in which the fluorescence of a sample can be suppressed. Herein, samples are analysed in the presence of plasmonic nanoparticles or substrates, compromising the non-destructive capability of RS. Whereas computational methods, aided by software algorithms, are relatively affordable and doesn't require any hardware modifications. Over the years, several mathematical approaches for fluorescence background removal have been established. These include frequency-domain filtering,^{24,25} wavelet transformation methods,²⁶⁻²⁹ least square methods,^{30,31} polynomial fitting,³²⁻³⁵ moving point average methods,³⁶⁻³⁸ etc. The critical requirements of noise and baseline correction algorithms for portable Raman spectrometer is that they should be automated with minimum user interaction and recover the Raman peaks with the most accuracy. In this context, we explored various available algorithms and details are discussed below.

Polynomial least square regression is a method first introduced by Gergonne in 1815 and has been used in various spectroscopic data for baseline estimation even before the invention of Raman spectroscopy.³⁹ The polynomial fitting method is simple and relatively faster, where an n^{th} order polynomial function mathematically models the low-frequency baseline. The value of n is selected to fit the shape of the baseline, thus vary from spectrum to spectrum. The single polynomial function not

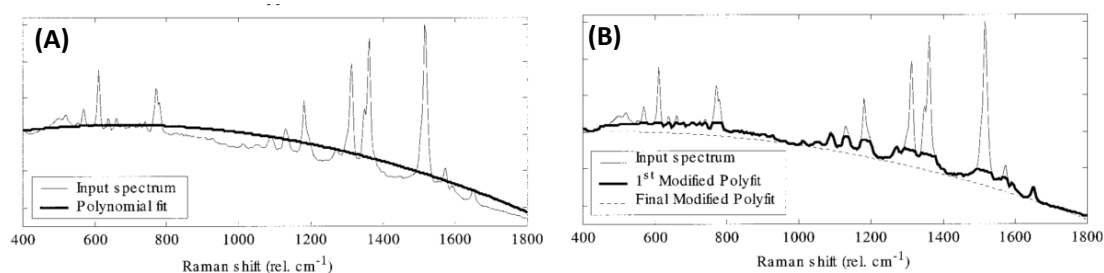


Figure 4.3.³⁴ Principle of baseline estimation by (A) single polynomial fitting and (B) Mod-Poly algorithm

only represents the low fluorescence background, but have contributions from Raman peaks as well. However, this type of fitting using the least square approach has a significant disadvantage, i.e. it does not adequately mimic the fluorescence background (Figure 4.3.A). This is because the curve fitting is based on minimising the error between the fitted curve and the observed spectrum. As a result, the polynomial fitting must be performed in spectral areas with just background fluorescence while ignoring spectral regions with Raman bands. Lieber suggested a modified multi polynomial fitting (Mod-Poly) based iterative approach to overcome the constraints of the single polynomial fitting.³⁴ Here, the raw spectrum is first fitted using a polynomial function, like the conventional least square method. The fitted polynomial ordinates and raw spectral intensity values are then compared at each wavenumber value. The lowest values for each wavenumber are selected for each subsequent cycle of polynomial fitting and then concatenated to construct a modified spectrum, which is then re-fitted. Figure 4.3 B shows the modified spectrum after 1st iteration and the finally estimated baseline. Later Mod-Poly method was further improved by Zhao et al.³⁵ by adding a peak trimming step in the first stage of Mod-Poly, which substantially reduces the computation time. According to reported studies, this improved modified polynomial algorithm (I-Mod-Poly) is an automated approach for baseline correction that requires less computing time and hence considered for the current study. More details of this algorithm are discussed in the

experimental section.

Another simple and popular way for extracting the baseline is to iteratively smooth the raw Raman spectra by averaging until the Raman peaks are stripped off. However, selecting an apt iteration stopping criterion is crucial in this approach. Depending on implemented stopping criterion, many smoothing-based baseline estimation algorithms were introduced in the past.^{37, 38, 40} For example, Krishna et al. have suggested a range independent background-subtraction algorithm and works based on the moving point average (MPA) smoothing.⁴⁰ The RIA algorithm repetitively smoothens the raw Raman spectrum to gradually reduce the high-frequency Raman peaks, finally resulting in the underlying wide baseline that can be subtracted from the raw spectrum to retrieve the actual Raman signal. The main benefit of this approach is that, unlike other approaches, it is not affected by the spectral region chosen for baseline correction, and it could find the spectral contour most accurately, especially in a shorter spectral region.

In another work, Mikhailyuk et al. proposed a rolling-circle spectral filter (RCF), a type of digital filtering.⁴¹ This method involves rolling a circle of radius ' r ' below data points on the spectra, and background is estimated at each point by comparing the actual intensity in the spectra and the vertical locus²⁴ (see Figure 4.4). The smallest of these two values is selected as the updated value. This procedure is repeated, and as the circle rolls under the entire spectrum, the fragments of the curve whose radius of curvature greater than the r is trimmed. At a certain value of r , the entire background can be effectively subtracted without disturbing the Raman peaks. However, at spectral regions with overlapping peaks having baseline width larger than $2r$, the propagating circle rolls into the peak, thus subtract more than the actual background. To overcome this limitation of RCF, a Savitzky-Golay (S-Golay) coupled advanced rolling circle filter (SCARF) has been proposed by James. T.N et.al.⁴²

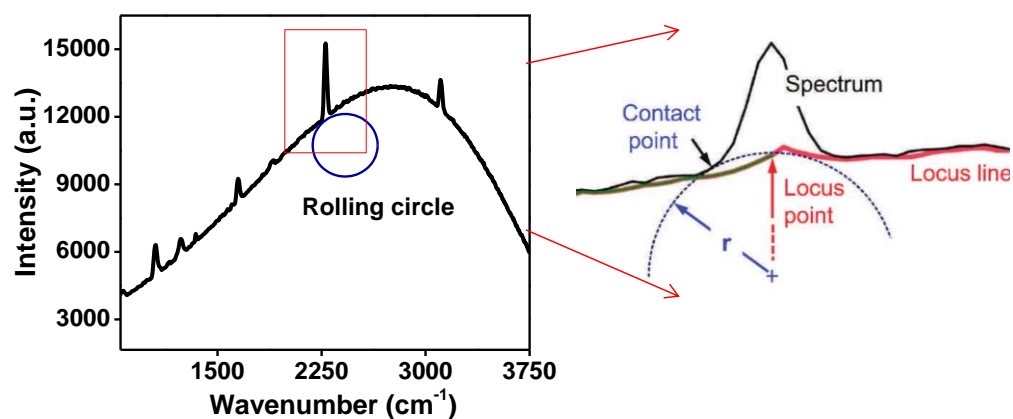


Figure 4.4. Pictorial representation of RCF algorithm.³⁵

In the present work, the above said three algorithms (I-Mod-Poly, RIA, and SCARF) have been selected for spectral processing and were validated using mathematically simulated spectra. The best-found approach was chosen to process the fabricated spectrometer acquired Raman spectra and develop the software. Further, a Raman spectral library of 24 distinct compounds is built from the denoised Raman spectra to aid in automated material identification. Among the several available spectral matching algorithms,^{43,44} the correlation approach is the most popular and hence chosen for library search. Finally, dedicated software comprising the functionalities for acquisition control, high-frequency noise reduction, baseline correction, and library search was made for the fabricated portable spectrometer.

4.3. Experimental Section

4.3.1. Portable Raman Spectrometer

The portable Raman spectrometer presented in the previous chapter was improved in terms of signal intensity, spectrum range, and spectral resolution. The upgraded fabricated system (Figure 4.5) consists of a 532 nm (Thorlabs, DJ532-40) laser diode with 40 mW output power and 0.3 nm FWHM. The temperature of the diode was maintained at 25 °C with TEC cooling; a dichroic mirror with edge wavelength at

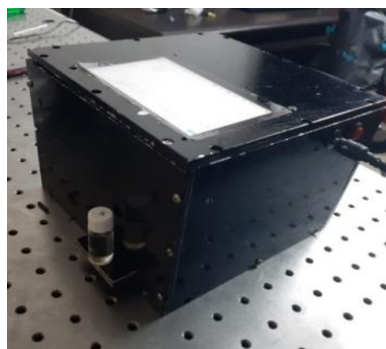


Figure 4.5. Photograph of the upgraded portable Raman spectrometer.

538.4 nm and $T_{\text{avg}} > 93\%$ above 541.6 nm (Semrock, Di03-R532 t125x36); a notch filter with centre wavelength at 533 nm and 17 nm FWHM to block the Rayleigh scattered signal (Thorlabs, NF533-17); Research India spectrometer consisting of a Toshiba linear CCD, spectral range 300-1100 nm and spectral resolution of 0.5 nm. The fabricated system has a spectral range and resolution of 330-3500 cm^{-1} and 11-17 cm^{-1} , respectively. Spectrum acquisition and analysis are controlled through a compute stick (Intel, STK1AW32SC) with windows OS installed, together with a 5-inch display.

4.3.2. Generation of Synthetic Raman Spectrum

A synthetic Raman spectrum was constructed using MATLAB® to compare the effectiveness of distinct baseline correction algorithms. Generally, the measured raw Raman spectrum can be expressed as a sum of Raman signal (y), baseline (B), and noise (N). The combination of a series of Lorentzian peaks on a null baseline is used to generate the simulated Raman peaks. The Lorentzian peaks were generated using equation 4.1.

$$y(x) = I * \left[\frac{w^2}{(x-x_0)^2 + w^2} \right] \quad (4.1)$$

Where I is the peak intensity, w is the peak width defined in terms of FWHM, and x_0 is the centre of the peak position along the wavenumber axis. The parameter values

used in constructing the 10 Raman peaks in the range of 300 to 3300 cm^{-1} are shown in Table 4.1, and Figure 4.6 represents the resulting spectrum.

Table 4.1. Lorentzian function parameters utilised to create the synthetic Raman spectrum.

Peak position (x_0)	Peak width (w)	Intensity (I)
700	10	1660
950	22	1636
1200	20	2376
1300	35	4189
1450	25	2900
1750	18	1686
1900	14	1115
2400	17	1643
2880	15	2444
2953	17	4611

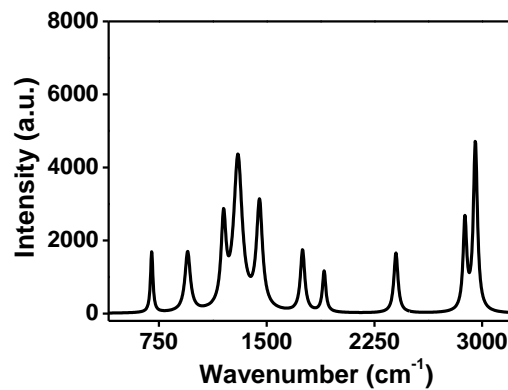


Figure 4.6. Simulated spectrum with 10 Lorentzian peaks on a null baseline.

The high-frequency random noise, N was then simulated using the MATLAB function *awgn()* and added to the Raman signal, resulting in a final SNR of 20 (see Figure 4.7 A). The shape of the low-frequency baseline is generally characterised by the detector's sensitivity and the fluorescence emission profile of the sample under observation.⁴⁵ Herein, three distinct types of baseline (i) Gaussian, (ii) exponential, and (iii) sigmoidal were designed for modelling the low-frequency fluorescence. This was accomplished by utilising inbuilt MATLAB functions: *gaussmf()*, *sigmf()*, and

$exp()$. Figure 4.7 B depicts the shape of the synthesised baselines, and Figure 4.8 shows the overall Raman spectra with white noise overlaid on the three baselines.

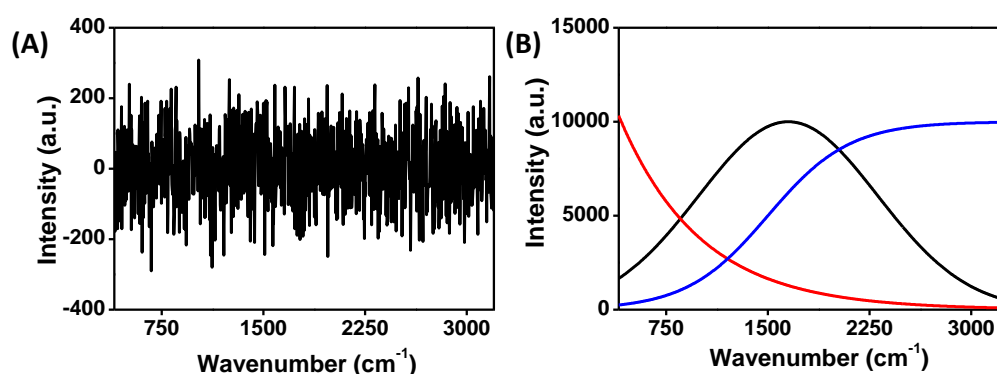


Figure 4.7. Mathematically generated (A) random noise and (B) baseline following a Gaussian distribution (black), sigmoidal curve (blue), and exponential shape (red).

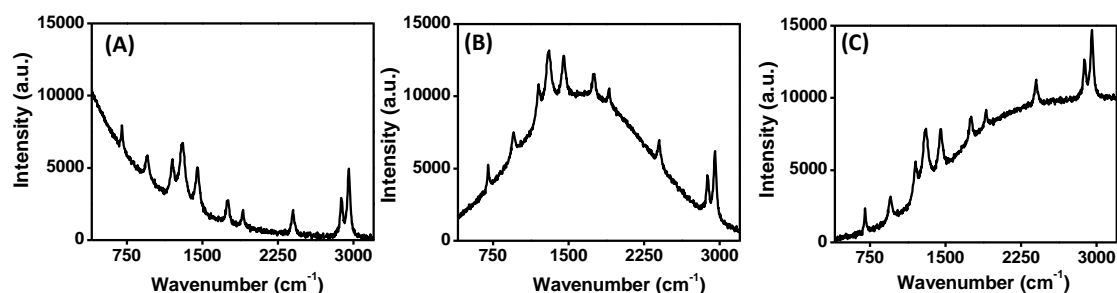


Figure 4.8. Mathematically simulated Raman spectrum added with random noise and three baseline types (A) exponential baseline, (B) Gaussian distribution, and (C) sigmoidal baseline.

4.3.3. Baseline Correction Algorithms

The I-Mod-Poly, RIA methods (both developed in MATLAB), and the SCARF (written in LabVIEW) were used to remove the low-frequency baseline from synthetic Raman spectra in the range 300-3300 cm^{-1} .

RIA Algorithm:⁴⁰ This algorithm trims the spectra to the desired wavenumber range and extrapolates the data to a straight line on both ends. To this extrapolated region, a Gaussian peak having similar height and width is added on both ends. This modified spectrum is repeatedly smoothed until the height of the added Gaussian peak is entirely restored. Figure 4.9 illustrates the concept of RIA. The width and position of

the Gaussian peaks were set at 50 cm^{-1} and 100 cm^{-1} , respectively, while the height (*'pheight'*) was selected between 900 and 2500.

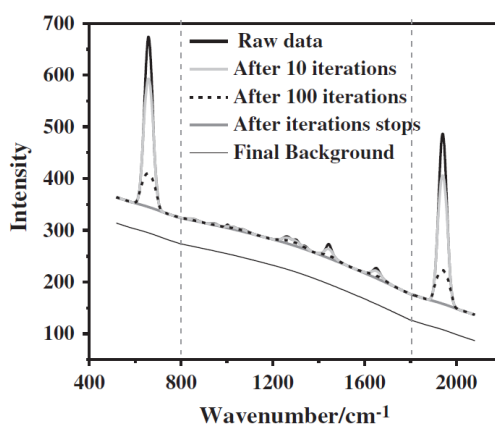


Figure 4.9. Pictorial representation of RIA algorithm showing Raman spectrum added with Gaussian peaks on extrapolated ends, and the estimated background after each iteration.⁴⁰

SCARF:⁴² As previously stated, SCARF is a more advanced form of rolling circle filtering in which the baseline formed by a single pass RCF is filtered via S-Golay. S-Golay is a digital filter for smoothing, that uses a lower degree polynomial to fit neighbouring data points. SCARF handles three parameters, '*r*' the rolling circle's radius, '*s*' the number of side points (half of S-Golay filter window size), and '*n*' the order of the polynomial function of the S-Golay filter. To capture details in the fluctuation of the baseline level, *r* should be smaller than the radii of curvature of the baseline and not less than the broadest Raman peak. For *r*, values between 10 and 60 were tested, and *s* was selected in such a way that $s \geq r$; optimised results were obtained at $(r,s) = (30,40)$. Different polynomial order ranging from 1 to 7 has been investigated for the S-Golay filter, and the best results were obtained with $n = 1$.

I-Mod-Poly Algorithm:³⁵ This fluorescence removal algorithm is based on modified multi-polynomial fitting with a peak-removal procedure during the first iteration. This is done by calculating the noise level in the spectra, and all the peaks above the noise

level are stripped off. Then, a polynomial of order ' n ' is used to fit this peak-stripped spectrum repeatedly. Data points in the fitted spectrum with intensities larger than their associated pixel values in the input spectrum are automatically reassigned to the original intensity after each iteration. Because additional iteration does not significantly remove any baseline, this iteration is continued until the difference in the standard deviation of the residual between two subsequent iterations is less than 5%. Various polynomial order ranging from $n = 1$ to 7 has been investigated, and the best baseline fitting was obtained with the highest order $n = 7$ and chosen for the present study. An increment in n beyond 7 doesn't bring a significant improvement in the estimated baseline.

4.3.4. High-Frequency Noise Removal

Dark noise, readout noise, and stray light contributions are considered fixed for a given integration time and temperature. Therefore, blank spectrum subtraction might eliminate them. The spectra taken with the same integration time in the absence of any sample is called blank spectra. After blank subtraction, a third-order S-Golay filter was employed to smooth the spectrum with a window size of 9. This reduces high-frequency fluctuations such as photon flux dependent shot noise while having no effect on Raman peaks and so boosting the SNR.

4.3.5. Software Development

The portable Raman spectrometer's software was developed entirely in National Instruments LabVIEW on a Windows PC. LabVIEW was preferred because it is simple to integrate data acquisition with the spectrum analysis tools. The system is built in the form of a straightforward and minimalistic graphical user interface (GUI). The integrated functions are divided into three stages: data acquisition, spectrum processing, and spectral database organisation. The acquisition module has the functions for setting laser power

and integration. The spectrum processing module includes functions such as blank subtraction, baseline correction, and high-frequency noise reduction. The baseline correction method, built in MATLAB, was imported into LabVIEW using the Mathscript module.⁴⁶ The library search and material prediction are added in the database management section. More details on the GUI are discussed in the later sections of this chapter. The developed LabVIEW project is compiled into a standalone application and installed in the Windows stick PC integrated into the portable Raman spectrometer.

4.4. Results and Discussion

4.4.1. Processing of Simulated Spectra

This section describes the findings of the baseline-correction algorithms on the simulated spectra. The performance of various baseline correction procedures is assessed using: (i) R^2 value of the fit between the originally added Raman spectra and the recovered spectra, (ii) comparison between the fitted baseline and the simulated baseline, and (iii) analysis of recovered peak intensities.

(i). RIA algorithm

Figure 4.10 depicts the baseline correction applied to the simulated spectra using the RIA algorithm. The estimated baseline is near the contour across the spectral range for spectra with sigmoidal and Gaussian background. Thus the recovered spectrum is almost identical to the originally added spectra ($R^2 \geq 0.95$) (Figure 4.10 A and E and Table 4.2). For exponential data, on the other hand, the calculated baseline is nearly optimal only in the central region ($500\text{-}2500\text{ cm}^{-1}$), and it is underestimated towards the edges (see green marking in Figure 4.10 C). This discrepancy leads to a corrupted recovered spectrum at the tail end with a low R^2 value of 0.32 (Table 4.2). Furthermore, the best *pheight* for each type of baseline must be determined

individually. The recovered spectra with the closest match to the original were obtained with *pheight* at 1270, 1000, and 2300, respectively, for sigmoidal, exponential, and Gaussian data. $\sim 95\%$ of the peak intensities from the original was recovered by applying these settings. Because of its dependency on the *pheight* value, the RIA method is inappropriate to use in a portable Raman spectrometer for automated applications.

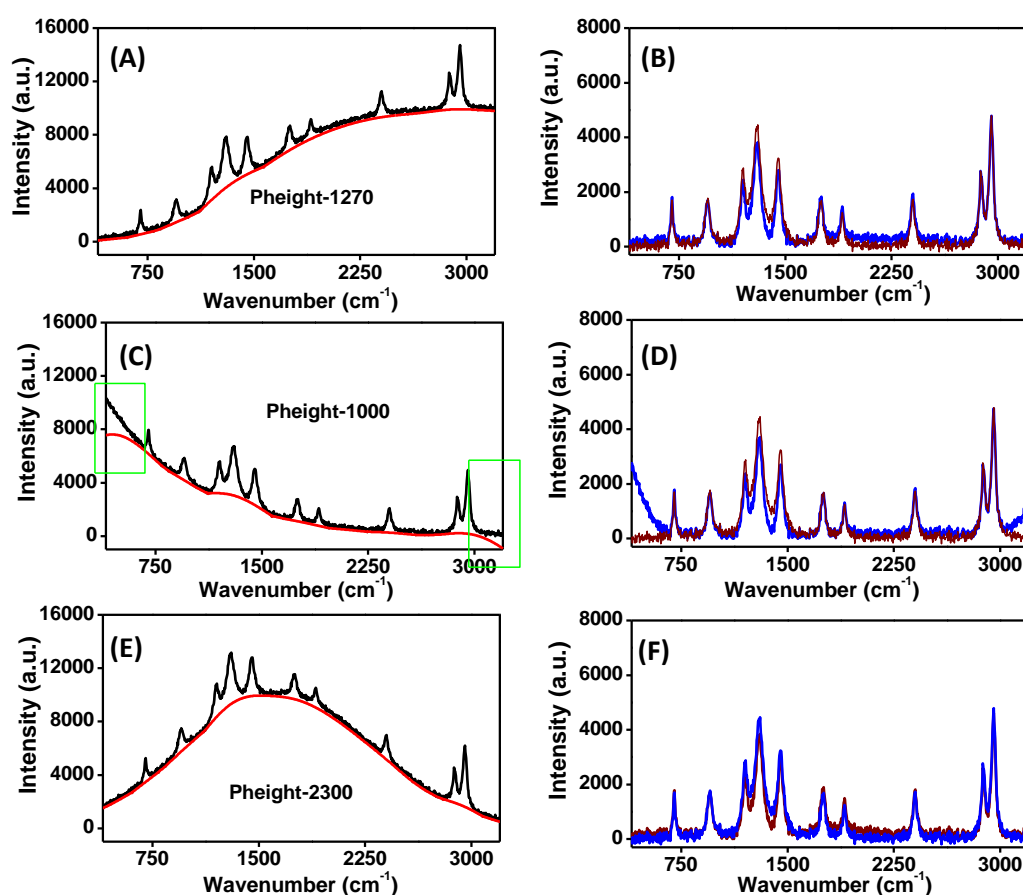


Figure 4.10. (left) Simulated noisy raw data (black) and estimated baseline (red) and (right) extracted Raman spectra (blue) and originally added spectra (wine red); (top) sigmoidal background, (middle) exponential baseline (underestimated baseline is marked in green) and (bottom) Gaussian background using the RIA algorithm.

Table 4.2. R^2 value and recovered peak intensities of the extracted spectra with RIA.

Parameters		Gaussian	Exponential	Sigmoidal
R^2		0.95	0.32	0.96
Recovered peak intensity in %	700 cm^{-1}	98	96	97
	1200 cm^{-1}	88	86	88
	2400 cm^{-1}	99	100	100

(ii). SCARF algorithm

The fitted baseline and the extracted Raman spectra using the SCARF algorithm with input parameters $(n,r,s) = (1,30,40)$ is shown in Figure 4.11.

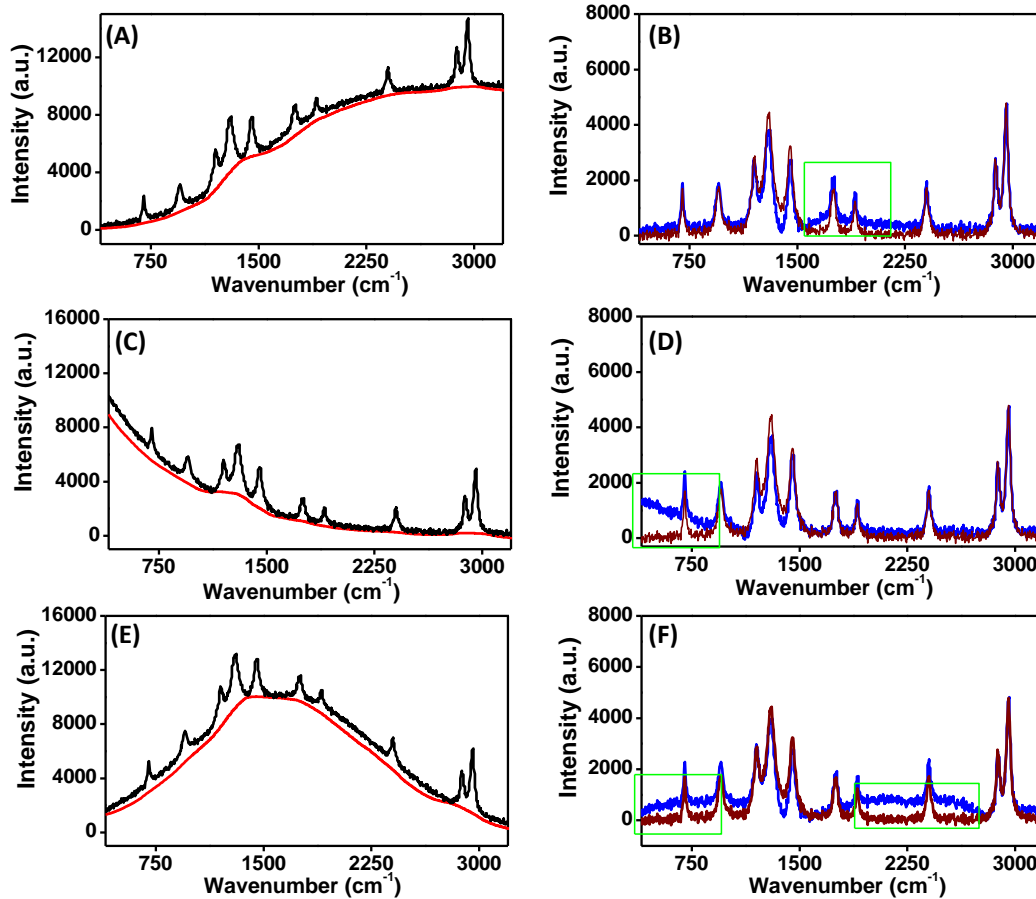


Figure 4.11. (left) Simulated noisy raw data (black) and estimated baseline (red) and (right) extracted Raman spectra (blue) and originally added spectra (wine red); (top) sigmoidal background, (middle) exponential baseline (underestimated baseline is marked in green) and (bottom) Gaussian background using the SCARF algorithm with $(n,r,s)=(1,30,40)$.

In contrast to RIA, the calculated baseline was not smooth, particularly in peak-free regions with a curved background (Figure 4.11 B, D, and F). Reducing r , the radius of the rolling circle, eliminated the uneven baseline to some extent. However, it stripped away Raman peaks (Figure 4.12 A, Table 4.3). Thus the overall quality of the recovered spectra did not improve significantly by reducing the r value ($R^2 \leq 0.85$). With $r = 30$, the optimal value for R^2 and recovered peak intensities were obtained, and hence $r = 30$ was chosen for further analysis. Also, we varied s value from r to $2r$

while keeping $r = 30$ to understand the influence of s on the predicted baseline (Figure 4.12 B). These studies revealed that s had no significant effect on the calculated baseline.

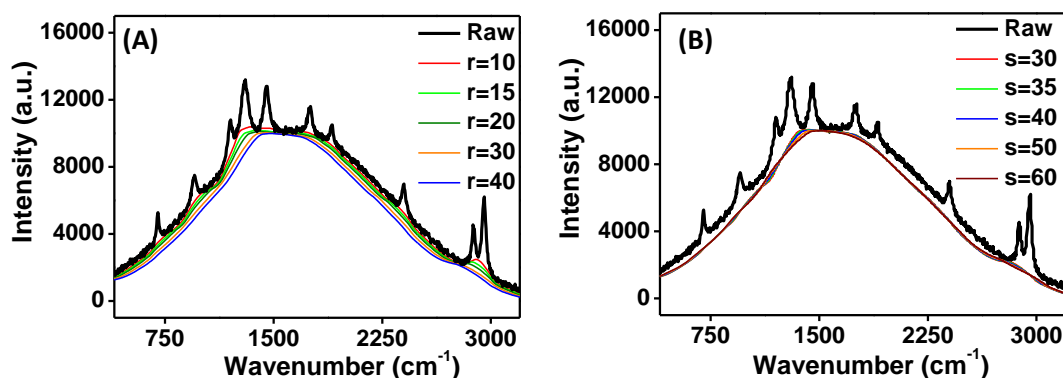


Figure 4.12. SCARF estimated baseline on the simulated spectrum with Gaussian baseline obtained by varying (A) r values and (B) s values at $r = 30$.

Table 4.3. R^2 value and recovered peak intensities of the extracted spectra from Figure 4.12A with different r values in SCARF.

Radius of the rolling circle, 'r'	10	15	20	30	40
Window size, 's'	20	25	30	40	40
R^2	0.80	0.84	0.85	0.83	0.79
Recovered peak intensity in %					
700 cm^{-1}	93	96	97	99	99
1200 cm^{-1}	65	72	78	87	91
2400 cm^{-1}	99	99	99	99	99

The influence of the order of the polynomial function in the S-Golay filter has also been investigated. Various values from $n = 1$ to 7 has been applied to the SCARF keeping r and s constant. As a representative example, Figure 4.13 shows the estimated baseline for spectra with Gaussian background with n varying from 1 to 7, and $(r, s) = (30, 40)$. The results show that the best-fitted baseline was obtained at $n = 1$, with $R^2 = 0.83$, while for higher polynomial orders, the fitting was poor with $R^2 \leq 0.75$. A similar reduction in R^2 value was observed for sigmoidal and exponential baseline. By changing the n from 1 to 7, R^2 value reduced from 0.92 to 0.87 for the

sigmoidal baseline, and it went down to 0.67 from 0.71 for the exponential baseline (Table 4.4). Thus irrespective of the shape of the baseline, a lower value of n works well in recovering the Raman peaks in SCARF algorithm.

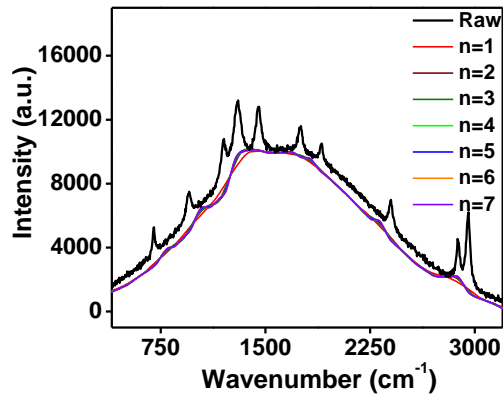


Figure 4.13. SCARF estimated baseline on the simulated spectrum with Gaussian baseline for different values of n .

Table 4.4. R^2 value of the extracted spectra of data with different ' n ' values in SCARF and $(r, s) = (30, 40)$.

Selected polynomial order for the S-Golay filter n	Baseline shape		
	Gaussian	Exponential	Sigmoidal
1	0.83	0.71	0.92
2	0.76	0.68	0.88
3	0.76	0.68	0.88
4	0.74	0.67	0.87
5	0.74	0.67	0.87
6	0.74	0.67	0.87
7	0.74	0.67	0.87

The irregularities in the peak free zone were substantially reduced by a double pass SCARF, (doing a second round of filtering on the recovered spectra from SCARF). As a representative example, Figure 4.14 shows the recovered spectra by single and double pass SCARF performed on spectra with Gaussian baseline, here the R^2 value improved from 0.83 to 0.92 by double filtering. Table 4.5 summarises the results of double RCF filtering performed with the same parameters as single-pass SCARF, i.e $(n, r, s) = (1, 30, 40)$.

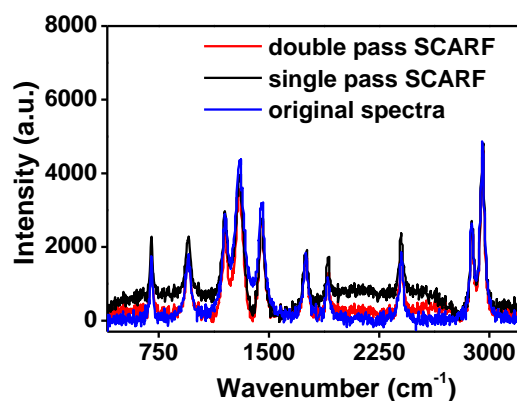


Figure 4.14. Extracted Raman spectrum with a single pass (black), double pass (red) SCARF along with the original spectrum (red).

Table 4.5. R^2 value and recovered peak intensities of the extracted spectra with single-pass and double-pass SCARF.

Parameters		Gaussian		Exponential		Sigmoidal	
		sp*	dp*	sp*	dp*	sp*	dp*
R^2		0.83	0.92	0.71	0.89	0.92	0.92
Recovered peak intensity in %	700 cm^{-1}	99	98	96	99	99	98
	1200 cm^{-1}	87	87	85	78	90	87
	2400 cm^{-1}	99	99	99	96	100	100

*sp: single pass SCARF, dp: double pass SCARF

The results reveal that, unlike RIA, the input parameters (n, r, s) in SCARF is less reliant on the baseline shape, hence baseline correction can be automated. Although irregularities were observed in the recovered spectra in single pass SCARF, double pass SCARF helped to overcome this to a great extent at the expense of peak intensity.

(iii). I-Mod-Poly algorithm

The only user-defined parameter in the I-Mod-Poly algorithm is the polynomial order, n . As a representative example, Figure 4.15 shows the extracted spectra at different polynomial orders for a Gaussian type baseline. The extracted Raman spectra match well with the original spectra at $n = 7$, and increasing beyond 7 doesn't bring any significant difference in the estimated baseline. Therefore, for the current study, $n = 7$ was used for all types of baseline for the optimal recovery for Raman peaks.

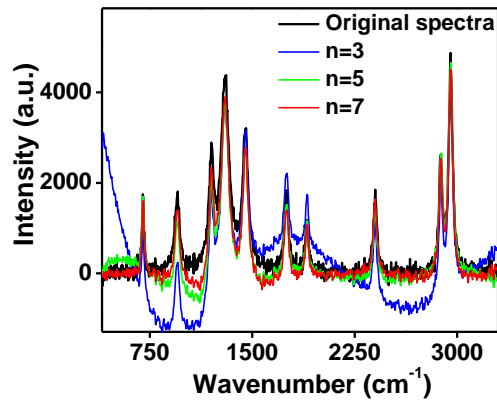


Figure 4.15. Extracted Raman spectrum using I-Mod-Poly algorithm $n = 3$ (blue), $n = 5$ (green), and $n=7$ (red), along with the originally added Raman spectra to the Gaussian baseline.

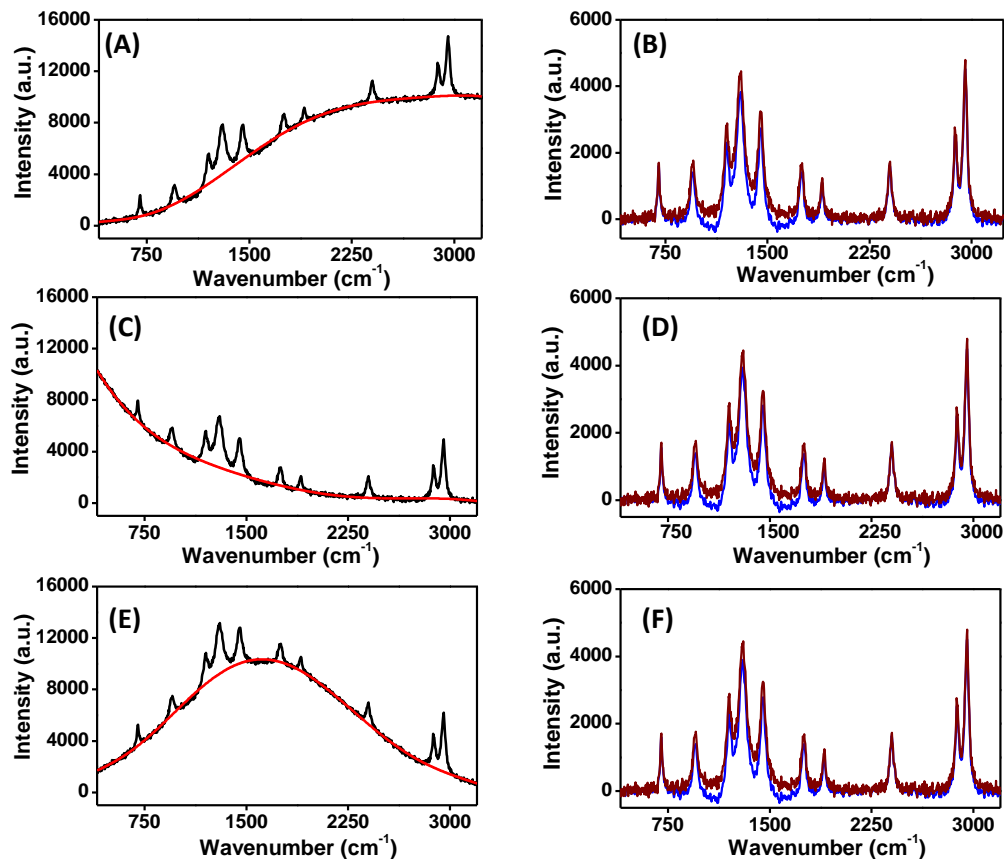


Figure 4.16. (left) Simulated noisy raw data (black) and estimated baseline (red) and (right) extracted Raman spectra (blue) and originally added spectra (wine red); (top) sigmoidal background, (middle) exponential baseline (underestimated baseline is marked in green) and (bottom) Gaussian background using the I-Mod-Poly algorithm.

The fitted baseline and the extracted Raman spectra with $n = 7$ on all simulated spectra are shown in Figure 4.16. Irrespective of the baseline's shape, the I-Mod-Poly

method was able to estimate the baseline peaks close to the contour of the background. Moreover, this method can be fully automated without any user-defined parameters. At least 90% of the peak intensity was recovered after extraction, with maximum similarity ($R^2 \geq 0.96$) with original spectra.

Table 4.6. R^2 value and recovered peak intensities of the extracted spectra with I-Mod-Poly background removal.

		Gaussian	Exponential	Sigmoidal
R^2		0.96	0.97	0.96
Recovered peak intensity in %	700 cm^{-1}	97%	96%	97%
	1200 cm^{-1}	92%	93%	92%
	2400 cm^{-1}	99%	99%	99%

I-Mod-Poly is a better choice for incorporating into the portable Raman spectrometer due to the following reasons (i) it is entirely automated, (ii) almost 92% of the original intensity of all Raman peaks were recovered, and (iii). $R^2 \geq 0.96$, which is better than double pass SCARF (Table 4.6 and Table 4.5). Therefore, I-Mod-Poly was chosen to process the acquired spectra from portable Raman spectrometer and for designing the software.

4.4.2. Processing of Experimental Spectrum

The built portable device was used to analyse the Raman spectra of several substances in order to show the effectiveness of the chosen noise reduction methodology. Figure 4.17 B and C show the raw Raman spectra of two different compounds, cyclohexane and pharmaceutical tablet containing paracetamol, acquired using the developed system at a 5 s integration time. Blank spectra (Figure 4.17 A) were subtracted from raw spectra to remove the influence of fixed noise (red graph). SNR refers to the ratio of the Raman peak's intensity to noise height and is calculated using the equation $\text{SNR} = (\text{signal maximum} - \text{signal minimum}) / (\text{noise maximum} - \text{noise minimum})$.

An S-Golay filter was used to further minimise high-frequency noises. As a representative example Table 4.7 shows SNR improvement in cyclohexane at two separate peaks after filtering. For low-intensity peak, the SNR is relatively lower than the highest peak. The SNR at the lowest intensity peak (1447 cm^{-1}) was 1.37, which increased by almost six times after dark subtraction and further improved to around 25 times of the initial after S-Golay filtering. While in the case of the highest peak, nearly 50 times increment was observed after spectrum processing.

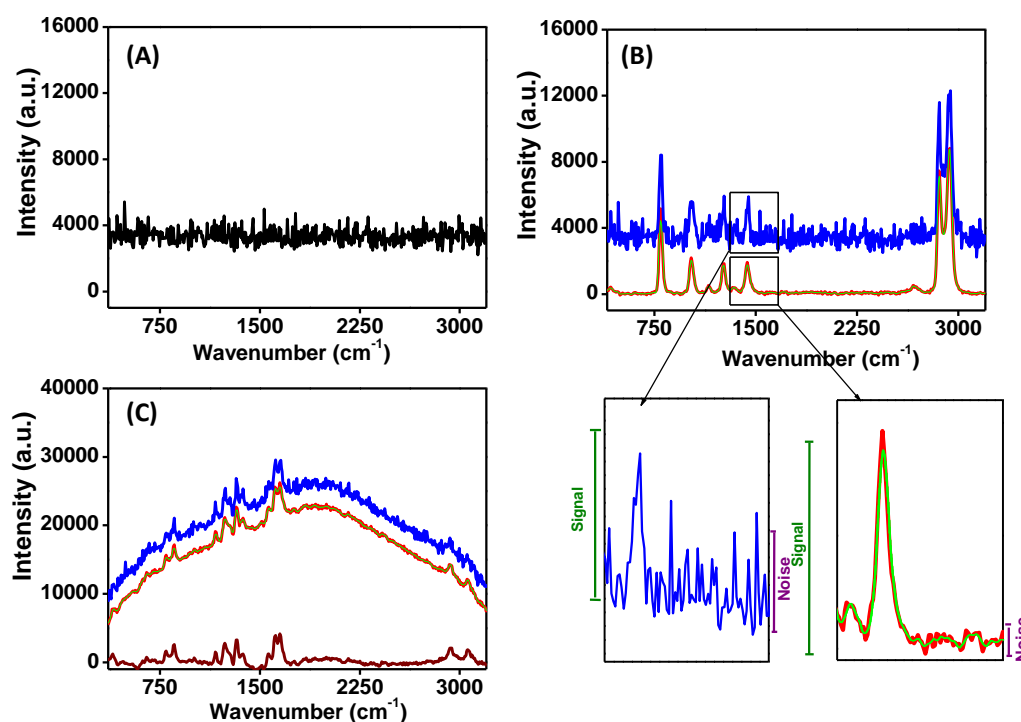


Figure 4.17. (A) Dark spectrum taken at 5 s integration time; raw spectra (blue), blank subtracted spectra (red) and s-Golay filtered spectra (green overlaid) of (B) cyclohexane and (C) paracetamol tablet taken with 5 s integration time. Baseline corrected spectrum (brown) of paracetamol is also shown.

Table 4.7. SNR of experimental spectra before and after noise removal.

Chemical	Measured at peak	SNR		
		Raw	After blank subtraction	After S-Golay filtering
Cyclohexane	1447 cm^{-1}	1.37	7.57	28
	2942 cm^{-1}	3.16	58.87	153

4.4.3. Raman Spectral Library Creation

Database comparison is of paramount importance for the automatic identification of materials through onsite testing. For the identification of unknown materials from its Raman spectra, a library database of 24 samples of commonly used chemicals (listed in Table 4.8) is created. The chemicals include both solid and liquid form.

Table 4.8. List of chemicals selected for spectral database creation.

SI No	Chemical
1	Acetone
2	Acetonitrile
3	Benzene
4	Benzonitrile
5	Butanol
6	Chloroform
7	Cyclohexane
8	Carbon tetra chloride
9	Dichloromethane
10	Di methyl formamide
11	Di methyl sulphoxide
12	Ethanol
13	Ethyl acetate
14	Hexane
15	Water
16	Iso propyl alcohol
17	Methanol
18	Methy metha acrylate
19	Paracetamol
20	Poly dimethyl siloxane
21	Toluene
22	Tetrahydrofuran
23	Tetra ethyl ortho silicate
24	Tetra butanol

The Raman spectra of the above said chemicals are collected using the fabricated spectrometer with ~ 10 mW laser power and 3 s integration time. The high frequency fixed noises, and low-frequency baselines were removed from these spectra, as explained in the previous section. The processed spectra (Figure 4.18) is

saved into the database in the form of an excel spreadsheet, the intensity corresponding to the wavenumber 330 to 3500 cm^{-1} of each spectrum is added to a separate column.

Library matching, a well-established approach, is used to identify unknown compounds through database search in any type of spectroscopic data. This is typically accomplished by cross-correlating the measured spectrum of an unknown material against spectra in the library. The sample spectrum and the reference spectrum should agree on the positions of the peaks, their shape, and their relative heights. The degree of similarity of each possible match is then quantified by measuring the correlation coefficient which is given by equation 4.2.

$$CC = \frac{\sum_{i=1}^n (s_i - \bar{s})(r_i - \bar{r})}{\sqrt{\sum_{i=1}^n (s_i - \bar{s})^2 \sum_{i=1}^n (r_i - \bar{r})^2}} \quad (4.2)$$

CC represents the correlation coefficient between the sample spectra s_i and the library reference r_i . \bar{s} and \bar{r} are the sample's and reference's (in the library) mean spectral intensity values, respectively. The value of CC can be anywhere between -1 and 1, with 1 indicating maximum similarity and 0 indicating no resemblance. The highest CC value will determine the matching index.

The effectiveness of the library search technique was tested using the recently discussed Raman spectrum of paracetamol pill. The CC value was computed in two distinct ways: (i) raw sample spectrum compared with raw spectra in the database, (ii) processed sample spectrum compared with processed spectra in the database. The correlation match results are shown in Table 4.9. The new sample was unambiguously identified as paracetamol in both cases with a matching value lower than the maximum value of 1. However, for raw spectra, the matching index value was only 0.33, showing a poor match even though it predicted correctly as paracetamol. While for the noise removed and baseline-corrected spectra the matching index was 0.83.

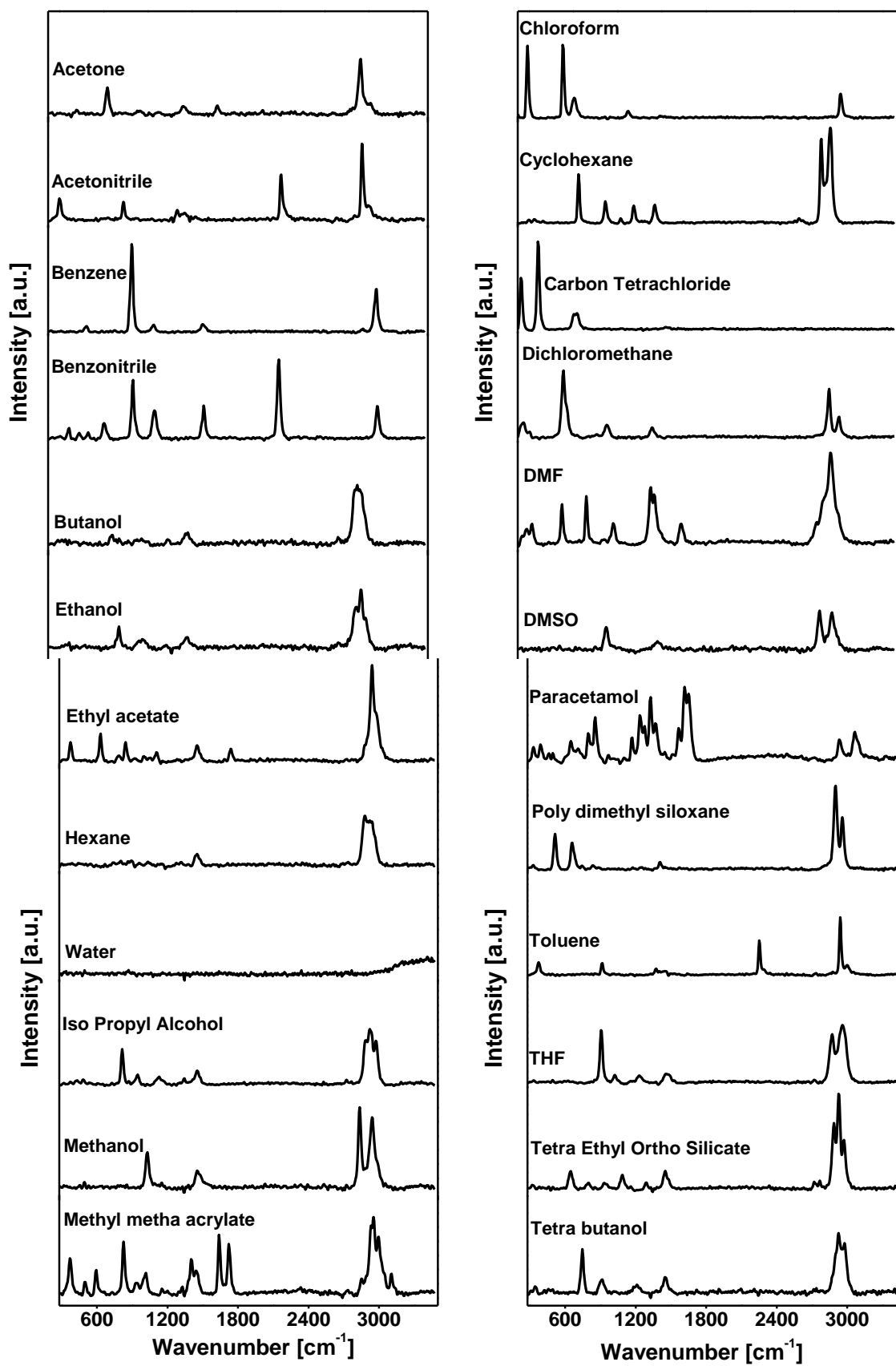


Figure 4.18. Raman spectra of the chemicals after noise removal saved into the database.

Table 4.9. The calculated correlation coefficient for paracetamol sample with library database. The highest correlation coefficient marked in red.

Database spectra	Sample spectra	
	Raw	Baseline corrected
Acetone	-0.04	0.22
Acetonitile	-0.03	0.17
Benzene	-0.08	0.13
Benzonitrile	0.13	0.11
Butanol	-0.17	0.19
Chloroform	-0.27	0.05
Cyclohexane	-0.06	0.23
CCl ₄	-0.22	0.05
Dichloromethane	-0.17	0.16
DMF	-0.12	0.23
DMSO	-0.20	0.12
Ethanol	-0.17	0.19
Ethyl acetate	-0.16	0.24
Water	-0.69	-0.13
Hexane	-0.12	0.20
Iso propyl alcohol	-0.20	0.21
Methanol	-0.19	0.13
Methy metha acrylate	-0.09	0.33
Paracetamol	0.33	0.83
Poly dimethyl silioxane	-0.14	0.17
Toluene	0.03	0.18
THF	-0.04	0.19
Tetra ethyl ortho siliacte	-0.10	0.21
Tetra butanol	-0.20	0.18

The results indicate that baseline correction will improve the prediction accuracy for correlation-based library search.

4.4.4. Standalone Application Development

Together with the spectrum processing techniques and library matching algorithm, the data acquisition module was integrated into the spectrometer in the form of an executable file once they were optimised. The flowchart of the algorithm is given in Figure 4.19. The GUI of the developed software is shown in Figure 4.20 and 4.21.

The spectrometer and laser driver unit are initialised once the software is launched. The user can specify the acquisition parameters such as integration time and laser optical power (marked as 1 and 2 in Figure 4.20). The laser has a maximum power of 40 mW, which corresponds to a current of 300 mA and is continuously variable from 0 to 100% using the given slider option. The CCD spectrometer's integration time is set at 3 seconds by default. Before starting the data acquisition, the user can change these values if necessary. The background set option from the GUI enables to capture the blank spectra at given acquisition settings. The device is now ready for sample spectrum acquisition, and the PC sends commands to the laser driver to switch on the laser and to the spectrometer unit to start the acquisition. The laser will be switched off automatically after the acquisition is finished. The spectrum processing stage follows data acquisition. The obtained spectra will be automatically trimmed to a range of 300-3500 cm^{-1} , baseline corrected, and noise removed. The buttons to disable the baseline correction and blank subtraction is provided in GUI (marked as 2 and 3 in Figure 4.21). The user can save the final processed spectra to the PC as '.txt' file using the save option (marked as 4 in Figure 4.21). The obtained spectra will be automatically examined for possible matches, and the spectra with the greatest CC will be displayed as the match (marked as 5 in Figure 4.21).

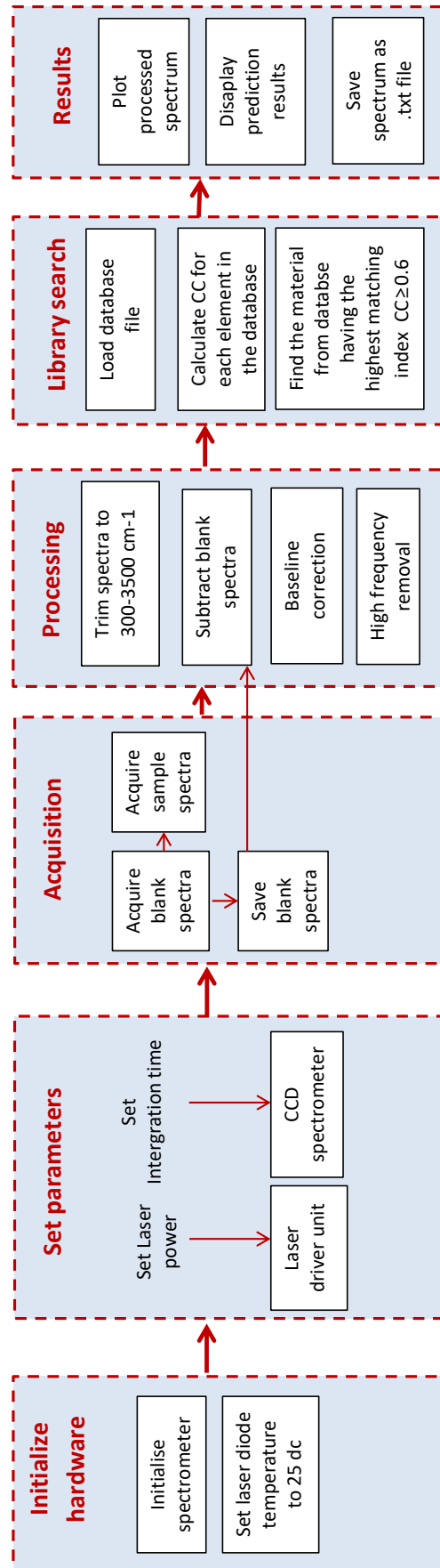


Figure 4.19. Algorithm for the developed software.

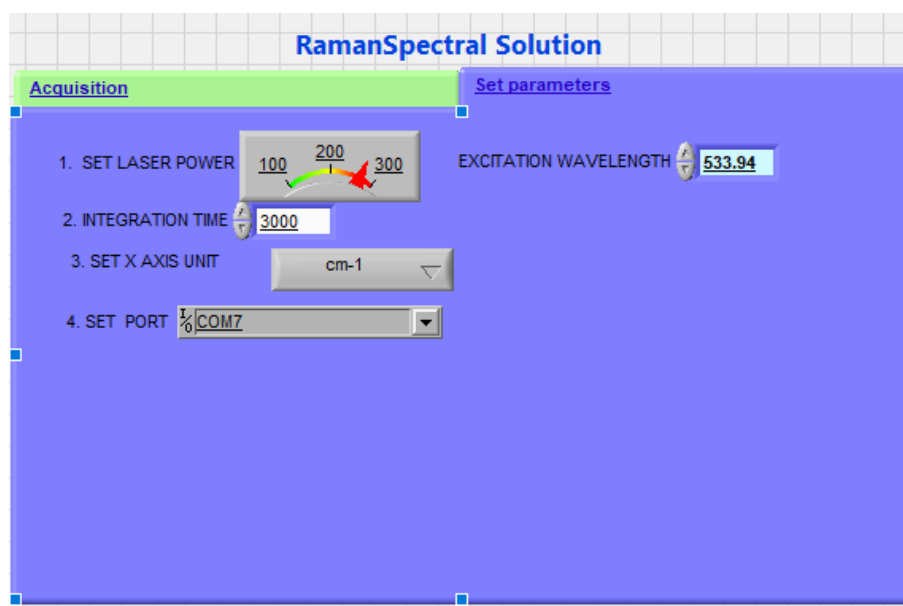


Figure 4.20. Snapshot of the GUI of the developed application showing the 'Set parameters' tab.

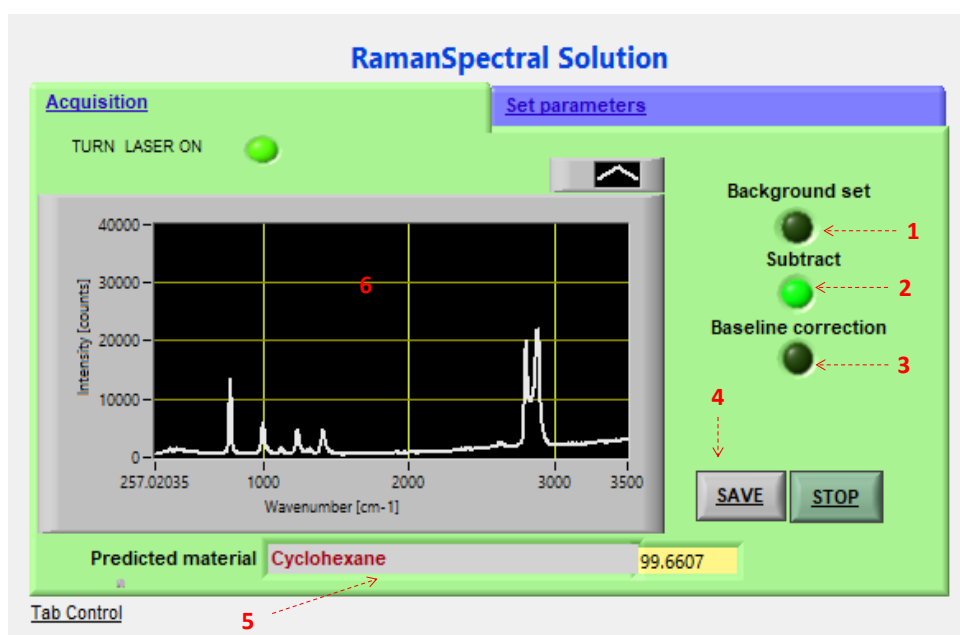


Figure 4.21. Snapshot of the GUI of the developed application showing the 'Acquisition' tab with user interfaces marked as 1. button to acquire bank spectra, 2. button to enable/disable blank subtraction, 3. button to enable/disable baseline correction, 4. button to save the acquired sample spectra in '.txt' form, 5. prediction results based on library search and 6. the acquired spectra after processing.

4.5. Summary and Future Scope

In conclusion, we discussed developing software tools for automatic spectral processing of Raman spectra and thus enabling material identification for onsite analysis. The data

presented herein show that the raw Raman spectra collected using a Raman spectrometer are prone to several noises. Thus, proper spectral processing is necessary to enable onsite analysis, especially when the SNR is low. The blank subtraction itself helped to reduce high-frequency noises leading to a 6 to 7 times improvement in SNR. Further enhancement in SNR is obtainable by enabling digital filters like S-Golay. For removing the low-frequency noise like fluorescence, we studied three distinct baseline correction strategies. For a small spectral range, the RIA approach proved the most effective at reconstructing Raman spectra. However, it is highly dependent on the input parameters, which differ in value depending on the baseline shape. While, regardless of the baseline shape, a double pass SCARF could recover the Raman peaks with at least $R^2 \geq 0.89$ and peak height recovery $\geq 80\%$. However, it required the optimisation of the input parameters like r , s , and n . On the other hand, I-Mod poly was superior in recovered spectra accuracy with $R^2 \geq 0.95$, peak height recovery $\geq 92\%$ and works well for all types of baseline, hence selected for designing the software. Further, to demonstrate the potential of the current system for onsite analysis, a processed Raman spectral library of 24 different chemicals was generated. The device integrated with the developed software could predict the unknown chemical in less than 30 s. Thus, by combining spectral processing along with data acquisition into a single platform, the onsite analysis could be carried out more easily. Being the software was made in LabVIEW, a graphical programming environment, it can be further easily modified for specific POC applications such as disease diagnosis, food or pharmaceutical product analysis. One such example is discussed in the following chapter.

4.6. References

1. Kong, K.; Kendall, C.; Stone, N.; Notingher, I., Raman spectroscopy for medical diagnostics From in-vitro biofluid assays to in-vivo cancer detection.

- Adv. Drug Deliv. Rev.* **2015**, *89*, 121-134.
2. Li, Y.-S.; Church, J. S., Raman spectroscopy in the analysis of food and pharmaceutical nanomaterials. *J. Food Drug Anal.* **2014**, *22* (1), 29-48.
 3. Karacaglar, N. N. Y.; Bulat, T.; Boyaci, I. H.; Topcu, A., Raman spectroscopy coupled with chemometric methods for the discrimination of foreign fats and oils in cream and yogurt. *J. Food Drug Anal.* **2019**, *27* (1), 101-110.
 4. Ong, T. T. X.; Blanch, E. W.; Jones, O. A. H., Surface enhanced Raman spectroscopy in environmental analysis, monitoring and assessment. *Sci. Total Environ.* **2020**, *720*, 137601.
 5. Jones, R. R.; Hooper, D. C.; Zhang, L.; Wolverson, D.; Valev, V. K., Raman techniques: fundamentals and frontiers. *Nanoscale Res. Lett.* **2019**, *14* (1), 231-231.
 6. Lerner., J. M.; Thevenon, A. The optics of spectroscopy.
<https://www.horiba.com/at/scientific/products/optics-tutorial/> (accessed 03/11/2021).
 7. Smulko, J.; Wróbel, M. S.; Barman, I. In *Noise in biological Raman spectroscopy*, 2015 International Conference on Noise and Fluctuations (ICNF), 2-6 June 2015; 2015; pp 1-6.
 8. Foose., D. P.; Sizemore, I. E. P., Vespucci: A Free, Cross-Platform Tool for Spectroscopic Data Analysis and Imaging. *J. Open Source Softw.* **2016**, *e4*, 1-8.
 9. Reisner, L. A.; Cao, A.; Pandya, A. K., An integrated software system for processing, analysing, and classifying Raman spectra. *Chemom. Intell. Lab. Syst.* **2011**, *105* (1), 83-90.
 10. Losq, C. L. *RamPy: Python library for processing spectroscopic data*, GitHub: 2015.
 11. Candeloro, P.; Grande, E.; Raimondo, R.; Di Mascolo, D.; Gentile, F.; Coluccio, M. L.; Perozziello, G.; Malara, N.; Francardi, M.; Di Fabrizio, E., Raman database of amino acids solutions: a critical study of Extended Multiplicative Signal Correction. *The Analyst* **2013**, *138* (24), 7331-7340.
 12. Candeloro, P. Raman Tool Set: Analysis of Raman spectra and spectroscopy data. <https://sourceforge.net/projects/ramantoolset> (accessed 08/03/2020).

13. James, T. M.; Schlösser, M.; Lewis, R. J.; Fischer, S.; Bornschein, B.; Telle, H. H., Automated quantitative spectroscopic analysis combining background subtraction, cosmic ray removal, and peak fitting. *Appl. Spectrosc.* **2013**, *67* (8), 949-59.
14. Rabinowitz, J.; Rezaei, M.; Park, M.-S.; Leong Tan, C.; Ulmer, M.; Mohseni, H., When shot-noise-limited photodetectors disobey Poisson statistics. *Opt. Lett.* **2020**, *45* (11), 3009-3012.
15. McCreery, R. L., Signal-to-Noise in Raman Spectroscopy. In *Raman Spectroscopy for Chemical Analysis* McCreery, J. D. W. a. R. L., Ed. 2000.
16. Fellers., T. J.; Kimberly, M. V.; Michael, W. D. CCD Signal-To-Noise Ratio <https://www.microscopyu.com/tutorials/ccd-signal-to-noise-ratio> (accessed 12/03/2021).
17. Ibsenphotonics Coupling into your spectrometer <https://ibsen.com/technology/spectrometer-tutorial/coupling-into-your-spectrometer/> (accessed 02/03/2021).
18. Chen, H.; Xu, W.; Broderick, N.; Han, J., An adaptive denoising method for Raman spectroscopy based on lifting wavelet transform. *J. Raman Spectrosc.* **2018**, *49* (9), 1529-1539.
19. Barton, S. J.; Ward, T. E.; Hennelly, Bryan M., Algorithm for optimal denoising of Raman spectra. *Anal. Methods* **2018**, *10* (30), 3759-3769.
20. Wei, D.; Chen, S.; Liu, Q., Review of fluorescence suppression techniques in Raman spectroscopy. *Appl. Spectrosc. Rev.* **2015**, *50* (5), 387-406.
21. Shreve, A. P.; Cherepy, N. J.; Mathies, R. A., Effective rejection of fluorescence interference in Raman spectroscopy using a shifted excitation difference technique. *Appl. Spectrosc.* **1992**, *46* (4), 707-711.
22. Baraga, J. J.; Feld, M. S.; Rava, R. P., Rapid near-infrared raman spectroscopy of human tissue with a spectrograph and CCD detector. *Appl. Spectrosc.* **1992**, *46* (2), 187-190.
23. Yaney, P. P., The pulsed laser and gated detection in Raman spectroscopy – a survey of the spectra of common substances including studies of adsorbed benzene. *J. Raman Spectrosc.* **1976**, *5* (3), 219-241.

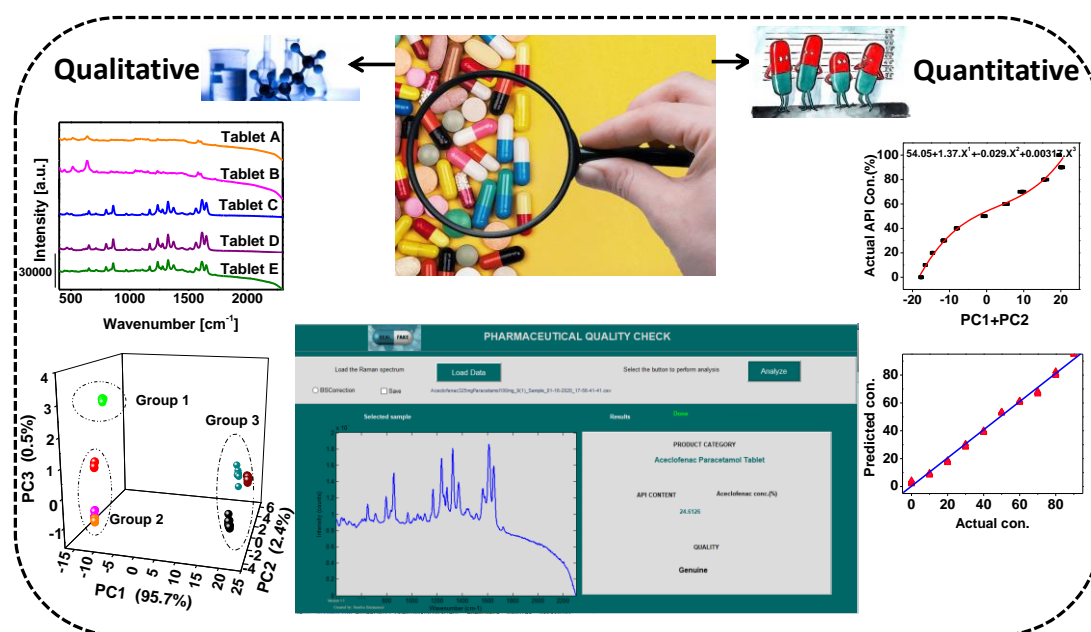
24. Brandt, N.; Brovko, O.; Chikishev, A. Y.; Paraschuk, O., Optimisation of the rolling-circle filter for Raman background subtraction. *Appl. Spectrosc.* **2006**, *60*, 288-93.
25. Chen, K.; Zhang, H.; Wei, H.; Li, Y., Improved Savitzky Golay-method-based fluorescence subtraction algorithm for rapid recovery of Raman spectra. *Appl. Opt.* **2014**, *53* (24), 5559-5569.
26. Xi, Y.; Li, Y.; Duan, Z.; Lu, Y., A Novel Pre-Processing Algorithm Based on the Wavelet Transform for Raman Spectrum. *Appl. Spectrosc.* **2018**, *72* (12), 1752-1763.
27. Mittermayr, C. R.; Nikolov, S. G.; Hutter, H.; Grasserbauer, M., Wavelet denoising of Gaussian peaks: A comparative study. *Chemom. Intell. Lab. Syst.* **1996**, *34* (2), 187-202.
28. Galloway., C. M.; Ru., E. C. L.; Etchegoin, P. G., An iterative algorithm for background removal in spectroscopy by wavelet transform. *Appl. Spectrosc.* **2009**, *63* (12), 1370-1376.
29. Shao, L.; Griffiths, P. R., Automatic baseline correction by wavelet transform for quantitative open-path Fourier transform Infrared spectroscopy. *Environ. Sci. Technol.* **2007**, *41* (20), 7054-7059.
30. Zhi-Min, Z., .; Shan, C.; Yi-Zeng, L., Baseline correction using adaptive iteratively reweighted penalised least squares. *The Analyst* **2010**, *135*, 1138–1146.
31. Park, A.; Baek, S.-J.; Park, J.-Q.; Seo, Y.-G.; Won, Y., Automatic selection of optimal parameter for baseline correction using asymmetrically reweighted penalised least squares. *Journal of the Institute of Electronics and Information Engineers* **2016**, *53* (3), 124-131.
32. Baek, S.-J.; Park, A.; Shen, A.; Hu, J., A background elimination method based on linear programming for Raman spectra. *J. Raman Spectrosc.* **2011**, *42*, 1987-1993.
33. Cadusch, P. J.; Hlaing, M. M.; Wade, S. A.; McArthur, S. L.; Stoddart, P. R., Improved methods for fluorescence background subtraction from Raman spectra. *J. Raman Spectrosc.* **2013**, *44* (11), 1587-1595.

34. Lieber, C.; Mahadevan-Jansen, A., Automated method for subtraction of fluorescence from biological Raman spectra. *Appl. Spectrosc.* **2003**, *57*, 1363-7.
35. Zhao, J.; Lui, H.; McLean, D. I.; Zeng, H., Automated autofluorescence background subtraction algorithm for biomedical Raman spectroscopy. *Appl. Spectrosc.* **2007**, *61* (11), 1225-1232.
36. Claudia C. Soberón-Celedón, J. R. M.-C., Claudio Frausto-Reyes, Juan Carlos; Zenteno-Ruiz, Removal of fluorescence and shot noises in Raman spectra of biological samples using morphological and moving averages filters. *IJETR* **2016**.
37. Schulze, H. G.; Foist, R. B.; Okuda, K.; Ivanov, A.; Turner, R. F. B., A small-window moving average-based fully automated baseline estimation method for Raman spectra. *Appl. Spectrosc.* **2012**, *66* (7), 757-764.
38. Gao, P. F.; Yang, R.; Ji, J.; Guo, H. M.; Hu, Q.; Zhuang, S. L., Locally dynamically moving average algorithm for the fully automated baseline correction of Raman spectrum. *Guang pu xue yu guang pu fen xi = Guang pu* **2015**, *35* (5), 1281-5.
39. Stigler, S. M., Gergonne's 1815 paper on the design and analysis of polynomial regression experiments. *Hist. Math.* **1974**, *1* (4), 431-439.
40. Krishna, H.; Majumder, S. K.; Gupta, P. K., Range-independent background subtraction algorithm for recovery of Raman spectra of biological tissue. *J. Raman Spectrosc.* **2012**, *43* (12), 1884-1894.
41. Mikhailiyuk, I. K.; Razzhivin, A. P., Background subtraction in experimental data arrays illustrated by the example of Raman spectra and fluorescent gel electrophoresis patterns. *Instrum. Exp. Tech.* **2003**, *46* (6), 765-769.
42. James, T. M.; Schlösser, M.; Lewis, R. J.; Fischer, S.; Bornschein, B.; Telle, H. H., Automated quantitative spectroscopic analysis combining background subtraction, cosmic ray removal, and peak fitting. *Appl. Spectrosc.* **2013**, *67* (8), 949-959.
43. Kwiatkowski, A.; Gnyba, M.; Smulko, J.; Wierzba, P., Algorithms of chemicals detection using Raman spectra. *Metrol. Meas. Syst.* **2010**, *17*.
44. Tan, X.; Chen, X.; Song, S., A computational study of spectral matching

algorithms for identifying Raman spectra of polycyclic aromatic hydrocarbons. *J. Raman Spectrosc.* **2017**, *48* (1), 113-118.

45. Zhengmao, Y.; Auner, G. In *Raman spectrum baseline identification and its optimisation using genetic algorithm*, Proceedings of the 2004 IEEE International Symposium on Intelligent Control, 2004., 4-4 Sept. 2004; 2004; pp 489-494.
46. Guevara, E. *Implementation of the Vancouver Raman Algorithm Mathworks*, 2016.

Application of Raman Spectroscopy for Quantification of Aceclofenac from Combinational Tablets Using Chemometric Methods



5.1. Abstract

Due to the increasing number of counterfeit drugs, ensuring the quality of pharmaceutical products is crucial for providing the best quality health care services to the patient. Raman spectroscopy being a non-destructive technique for the fingerprint characterisation of chemicals, can be used for pharmaceutical product quality testing. The potential of Raman spectroscopy for field analysis may be greatly boosted by merging it with sophisticated technologies such as artificial intelligence and machine learning. In this chapter, we attempt to develop a chemometric methodology for API identification and quantification from combinational drugs. PCA was coupled with polynomial regression in the new quantification model, which was

designed using the MATLAB® programming environment. Combinational tablets comprising aceclofenac and paracetamol are used to show the proposed approach. The findings of Raman spectroscopy measurements were compared to those obtained using the usual chemical analysis method, HPLC.

5.2. Introduction

Nowadays, counterfeiting is a severe problem tackled by the pharmaceutical industry.¹ Counterfeiters target almost all types of drugs, including cancer,² cardiovascular,³ erectile dysfunction,⁴ lifestyle diseases,⁵ etc. Very recently, counterfeit covid-19 vaccines reported in the Chinese market contained only mineral water and saline water.^{6,7} Although the severity of drug adulteration is higher in poor and developing countries,^{8,9} developed countries are also not free from this scam.^{10,11} The quality of the counterfeits reaching the patients may vary, and its consumption can lead to severe health issues, including the patient's death.¹² It is estimated that the manufacturing and consumption of pharmaceutical drugs increase annually at a rate of ~ 6%. Around 3,000 pharma companies with a strong network of over 10,500 manufacturing facilities are present in India alone.¹³ As per WHO's report, ~ 1 in 10 tablets available in low and middle-income countries are fake/substandard. Analysing the quality of this large volume of drugs from the market in a limited time is a big challenge. Consequently, quick evaluation tools are required for testing the integrity of the suspected products. Several analytical methods have proved efficient for analysing counterfeit medicines.¹⁴⁻¹⁶ Spectroscopy is one of the most extensively utilised among them.¹⁷ It is non-destructive, reliable, and rapid, and it does not need sample preparation. Especially in the last decade, RS has been the focus of counterfeit detection.^{18,19}

The technological progress in optics and electronics has enabled the development of handheld and portable spectrometers. Handheld Raman spectrometers are currently used in the pharmaceutical industry for testing purposes such as raw material,²⁰ drug stability,²¹ content, and uniformity.^{22,23} Mostly, these are achieved either with the aid of inbuilt library search or Raman barcode-based spectral comparison.²⁴ These help to detect drugs containing wrong or no active pharmaceutical ingredient (API), a major class of counterfeit drugs. However, there is another class of counterfeit drugs that contain all the APIs but in the wrong quantity. These can be two types, (i) drugs that contain API in lower dosage, which doesn't meet the purpose of treatment due to insufficient API, and (ii) drugs with overdosage, which can be harmful to the patient, and a few death incidents have already reported.²⁵

This chapter focuses on developing software methods to identify tablets with the wrong dosage using Raman spectral data. The developed software is essentially based on machine learning techniques, and hence the potential of RS can be enormously improved for pharmaceutical product quality testing. As a representative example, we have chosen a composition of paracetamol (PARA) and aceclofenac (ACE). ACE is a nonsteroidal anti-inflammatory drug²⁶ commonly used to relieve pain and inflammation. In comparison, PARA has analgesic and antipyretic effects.²⁷ These drugs are orally administered in the form of tablets in single or combinational form.

5.3. Experimental Section

5.3.1. Materials and Methods

Chemicals used: The standard references of ACE and 4-Hydroxyacetanilide (PARA) are purchased from TCI chemicals. 11 mixtures of ACE and PARA are prepared by mixing and grinding the pure powders of APIs using a mortar and pestle. The final weight percentage of ACE in the mixture are 0, 10, 20, 30, 40, 50, 60, 70, 80, 90 and 100.

Pharmaceutical samples: For evaluating the developed quantification model, from the local market we collected pharmaceutical tablets of five different brands containing these selected APIs (Table 5.1). Based on their composition, these are primarily classifiable into three categories; tablets containing APIs (i) only ACE, (ii) only PARA and (iii) both the ACE and PARA. As per the manufacturer's description, these tablets also contain other excipients like titanium dioxide (TiO_2) (A and B). However, their presence is not taken into consideration for the present studies, *vide infra*.

Table 5.1. List of pharmaceutical tablets used for the study

Product family	Assigned Name	Appearance	Total weight (mg)	API composition* (mg)	Excipients present*
Class -1	A		398	Aceclofenac- 100	TiO_2
	B		246	Aceclofenac -100	TiO_2
Class -2	C		633	Paracetamol-500	-
	D		838	Paracetamol-650	-
Class -3	E		684	Paracetamol-325 Aceclofenac - 100	

* provided as per the manufacturer

5.3.2. Raman Spectral Measurements

Raman spectra were recorded using a handheld Raman spectrometer (Mira DS, M/s Metrohm) with a ~ 40 mW, 785 nm excitation laser, 400-2300 cm^{-1} spectral range, and 10 cm^{-1} spectral resolution. The optical power was measured using a power meter (843-R, M/s Newport corporation). Analysis was conducted using the universal sample holder (supplied along with the instrument, Part No. 6.07506.010) with a focal distance of 3 mm and the excitation light path is equipped with an orbital raster scan (ORS) system. ORS technology analyses the average spectrum from a larger sample area and minimises inaccuracies from the sample's local inhomogeneity.²⁸ Further to ensure the uniformity of measurements, all the spectra were acquired with the same

acquisition parameters, i.e., 2 s integration time, and the obtained spectra averaged over three accumulations.

Spectra were recorded from 12 different positions of each 16 samples (i.e. 11 laboratory prepared mixtures + 5 tablets), thus generating a total of $12 \times 16 = 192$ spectra. Around 70% of this data was used for training the calibration model and the rest for testing the model. Further validation of the model was performed using an independent data set, and its details are provided in section 5.4.5.

5.3.3. Data Pre-processing

Generally, Raman spectral measurements interfere with (i) intensity fluctuations arising due to the differences in sample placement, laser power variation, and integration time, (ii) both electronic and optical high-frequency noises, (iii) low frequency background, which usually arises from fluorescence, thermal noise of detector and ambient light, and (iv) contribution from cosmic rays. For making the analysis more reliable, the collected raw spectra need a series of pre-processing operations like noise removal, baseline correction, spectral trimming, and normalisation. Data pre-processing and chemometric analysis were performed using the MATLAB® R2013a (MathWorks, USA). The baseline correction was done using a rolling circle spectral filter; the chosen circle's curvature radius was 20 points.²⁹ The major excipient in most commercial tablets is TiO₂, which has strong Raman peaks below 700 cm⁻¹. To avoid the influence of TiO₂, noise removed data were trimmed to the range 810-1750 cm⁻¹. Trimming was followed by intensity normalisation by Standard Normal Variate (SNV) Normalization³⁰ to eliminate intensity fluctuation.

5.3.4. Chemometric Analysis

Pharmaceutical product quality analysis was performed in two stages, (i) identification of API and (ii) quantification of API.

Qualitative analysis: The differentiation of drug samples involves qualitative analysis through principal component analysis (PCA). According to this method, the number of original variables is reduced to retain the relevant spectral characteristics contributing most to its variance.³¹ The optimal number of components which contribute to maximum variance was considered for creating the prediction model.

Quantitative analysis: For quantitative analysis, three different models based on PCA regression (PCR) were conducted on the prepared API mixtures. These are (i) traditional PCR based on multiple linear regression³² using the first 'n' components, explaining 95% of the variance, (ii) a modified PCR model based on non-linear regression using the first component, and (iii) a modified PCR model based on non-linear regression using the first 'n' components explaining 95% of the variance. The predictive capacity of regression models was assessed by the statistical parameters like root mean square error (RMSE), correlation coefficient (R), and receiver operating characteristic (ROC) curve.

RMSE is calculated for all three methods using equation 5.1, where X represents the predicted concentration, Y represents the actual concentration, and n represents the total number of test data. For the best predictive model, this error needs to be minimum.³³

$$RMSE = \sqrt{\frac{\sum(X-Y)^2}{n}} \quad (5.1)$$

Pearson correlation coefficient (R), measures the similarity between two variables. The correlation coefficient values can range from +1 to -1, where a value close to +1, -1, and 0 indicates the perfect positive relationship, ideal negative relationship, and no connection between the variables, respectively. R-value is calculated using equation 5.2, for assessing the extent of correlation between two variables. R-squared (R^2) value was used for evaluating the quality of fit of a model on

data.

$$R = \frac{\Sigma(X-\bar{X})(Y-\bar{Y})}{\sqrt{\Sigma(X-\bar{X})^2 \Sigma(Y-\bar{Y})^2}} \quad (5.2)$$

where \bar{X} and \bar{Y} represents the mean of predicted and actual concentration respectively.

The accuracy of the above three methods in classifying the samples correctly into genuine and fake was later assessed through ROC analysis. ROC illustrates the diagnostic ability of a binary classifier system as its discrimination threshold is varied.³⁴ The best predictive model will be having the highest area under the curve (AUC). ROC is plotted from True positive rate (TPR), and False positive rate (FPR) values at different threshold levels.

$$\text{Sensitivity} = TPR = \frac{TP}{TP+FN} \quad (5.3)$$

$$1\text{-Specificity} = FPR = \frac{FP}{FP+TN} \quad (5.4)$$

Here, True Positive (TP) means genuine drug classified correctly as genuine, False Positive (FP) is fake drug wrongly classified as genuine, False Negative (FN) means genuine drug falsely classified as fake, and True Negative (TN) is fake drug classified correctly as fake.

ROC analysis was performed on the validation data set consisting of commercially available tablets containing 23.5% API, laboratory prepared mixtures equivalent to the commercial tablets with 23.5% API, and fake tablet equivalent prepared mixture with API concentration below and above 23.5%.

5.3.5. Application Development

Once the best prediction model was identified, a graphical user interface (GUI) was made using MATLAB® GUIDE for tablet category determination and API quantification. It

was then compiled using Compiler™ and build into a standalone executable. The standalone application consists of the modules for the following operations (i) spectral pre-processing, (ii) identification of tablet class based on PCA, (iii) quantification of API using the developed PCR model, and (iv) prediction of the type of the drug (genuine or counterfeit). The chemometric models for quantification were created using a separate MATLAB® program and are imported to the primary GUI. The program flowchart is given in Figure 5.1.

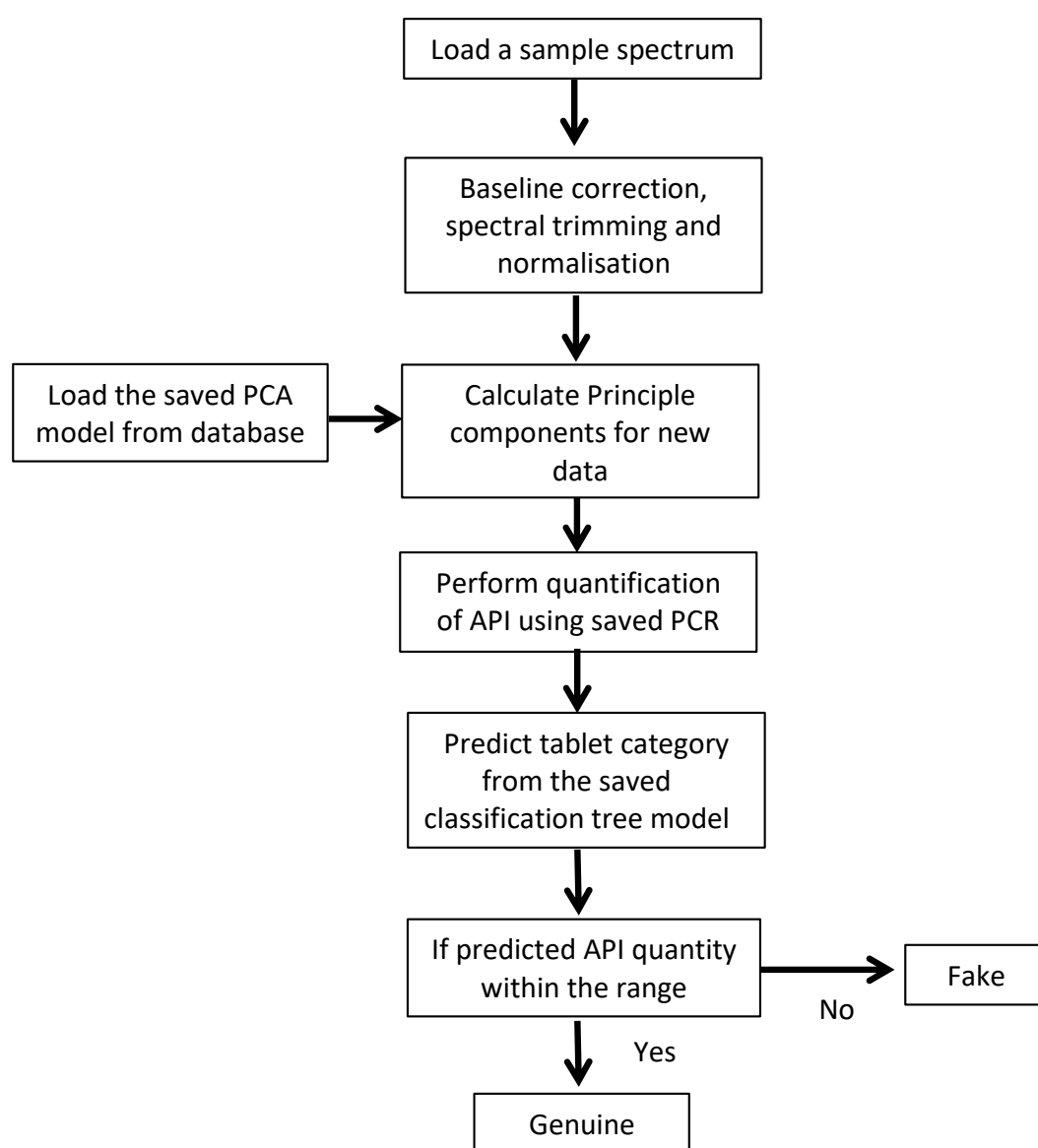


Figure 5.1. Application flowchart

5.3.6. HPLC Analysis

The results obtained from the developed quantification model were compared with those of HPLC analysis. HPLC experiments were performed on a Prominence UFLC system (M/s Shimadzu Corporation, Japan) having LC-20AD pump, Phenomenex Gemini C18 column (250 mm x 4.6 mm, 5 μ m), a column oven (CTO-20A), an autosampler injector (SIL-20AC HT), and a diode array detector (SPD M20A). The mobile phase used was a mixture of 60% acetonitrile and 40% 50 mM NaH_2PO_4 in Milli-Q water. The injection volume was 10 μ L and kept the flow rate at 1 mL/min. The column was maintained at 33 $^\circ\text{C}$, and eluted fractions were monitored at 273 nm. Sample peaks were identified by matching the retention time with that of reference samples, pure APIs. LC Lab software was used for data acquisition and analysis. The

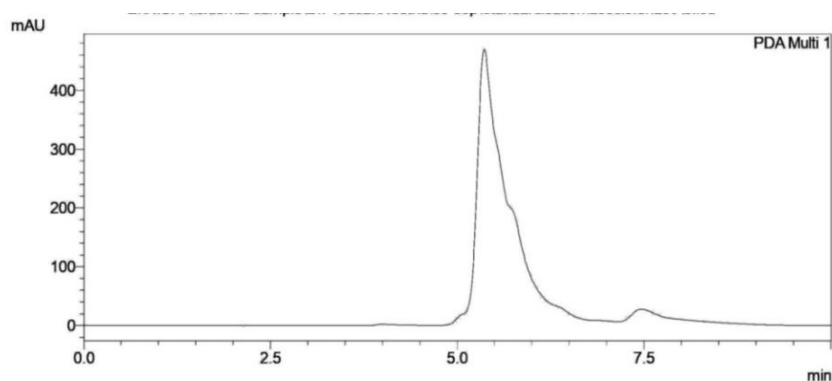


Figure 5.2. Chromatogram of a solution containing 1 mg aceclofenac in 1 mL acetonitrile.

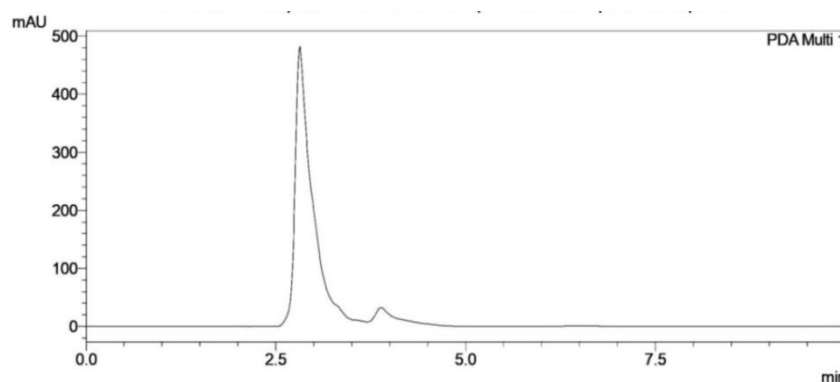


Figure 5.3. Chromatogram of a solution containing 1 mg paracetamol in 1 mL acetonitrile.

stock solutions of APIs (ACE and PARA) were separately dissolved in acetonitrile (1 mg/mL) and filtered through a 0.22 μm PTFE filter. From the chromatogram of these solutions (Figure 5.2 and Figure 5.3), the retention time³⁵ for pure APIs (ACE and PARA) was estimated to be 5.3 min and 2.8 min, respectively.

For quantification, a calibration graph based on the area under the curve vs. concentration was prepared from chromatograms of dilute solutions (62.5, 125, 250, 500, 750, and 1000 $\mu\text{g/mL}$) and is shown in Figure 5.4. To estimate the concentration of API in tablets, each uncoated tablet were crushed and made into a fine powder, then 1 mg of the powdered tablet was accurately weighed and dissolved in 1 mL acetonitrile solution, the undissolved residual was filtered out, and the clean solution was analysed.

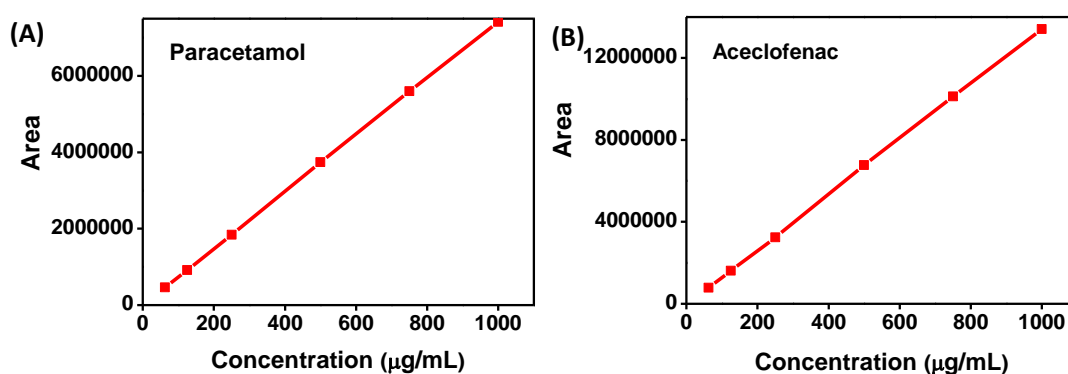


Figure 5.4. Calibration graphs showing area under the curve against the concentration of (A) paracetamol and (B) aceclofenac.

5.4. Results and Discussion

5.4.1. Raman Spectral Analysis

Raw and processed spectra of the PARA and ACE pure API and their chemical structure are presented in Figure 5.5. The Raman peak positions and their associated vibrational modes are listed in Table 5.2.

The Raman spectral data revealed that both ACE and PARA have distinguishable peaks and closely related peaks. For example, ACE and PARA have

peaks positioned around 650 cm^{-1} , 712 cm^{-1} , and 1612 cm^{-1} , corresponding to the phenyl ring deformation, CH_2 wagging and Aryl C-C stretch. On the other hand, vibrational frequencies at 405 cm^{-1} and 767 cm^{-1} , 1580 cm^{-1} , corresponding to C-Cl stretching, C-O-C stretching are found only in ACE, and 1561 cm^{-1} , 1651 cm^{-1} corresponding to the NH bending (amide I), C=O stretching (amide II) is found only in PARA.

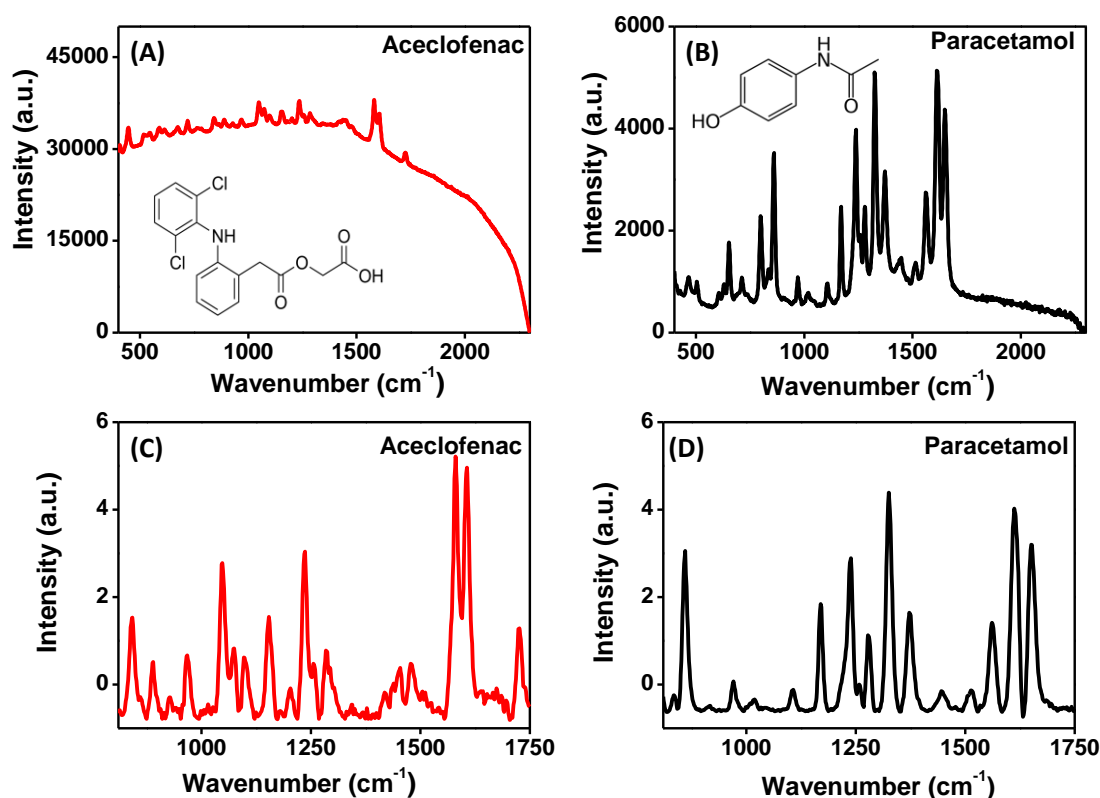


Figure 5.5. (A), (B) Raw Raman spectrum, and (C), (D) processed spectrum of (A, C) ACE, and (B, D) PARA respectively. Inset shows the chemical structure of both APIs.

Figure 5.6 represents the Raman spectra of the five different pharmaceutical tablets. Out of all the five tablets, A and B contains additional excipient TiO_2 . The Raman spectrum of TiO_2 is shown in Figure 5.7. It is evident that TiO_2 has characteristic peaks at 510 cm^{-1} and 635 cm^{-1} . Generally, the collected Raman spectra of the tablets appeared to have contributions from all the ingredients. For example, the Raman spectra of tablets A and B exhibited peaks corresponding to TiO_2 and ACE.

On the other hand, the Raman spectrum of tablets that are declared devoid of any excipients (C and D) matched well with their API, PARA. For the combinational tablet E, the peaks of both ACE and PARA are noticed.

Table 5.2. Important vibrational frequencies of ACE And PARA

Peak position (cm ⁻¹)	Assigned bond vibration
Paracetamol ^{21,36,37}	
652	Deformation of phenyl ring
712	CH ₂ wagging
799	C-C rocking in amide group
860	Ring breathing
1100	CH in-plane bend
1169	C-O-H bending +CH bend aryl
1239	C-N-C stretching
1280	C-N rocking
1325	C-H rocking
1561	NH bending (amide II)
1612	Aryl C-C stretching
1651	C=O stretching (amide I)
Aceclofenac ²¹	
405	C-Cl deformation
447	Ring 2 Out of plane deformation
516	Ring 2+1 Out of plane deformation
545	
659	Deformation of phenyl ring
719	CH ₂ wagging
767	C-Cl stretching
840	CH twist
1047	Ring 2 breathing
1074	Ring 1 breathing
1097	CH wagging+CH bend
1154	Aryl CH in plane bend
1580	C-O asym. stretching
1605	Aryl C-C stretching

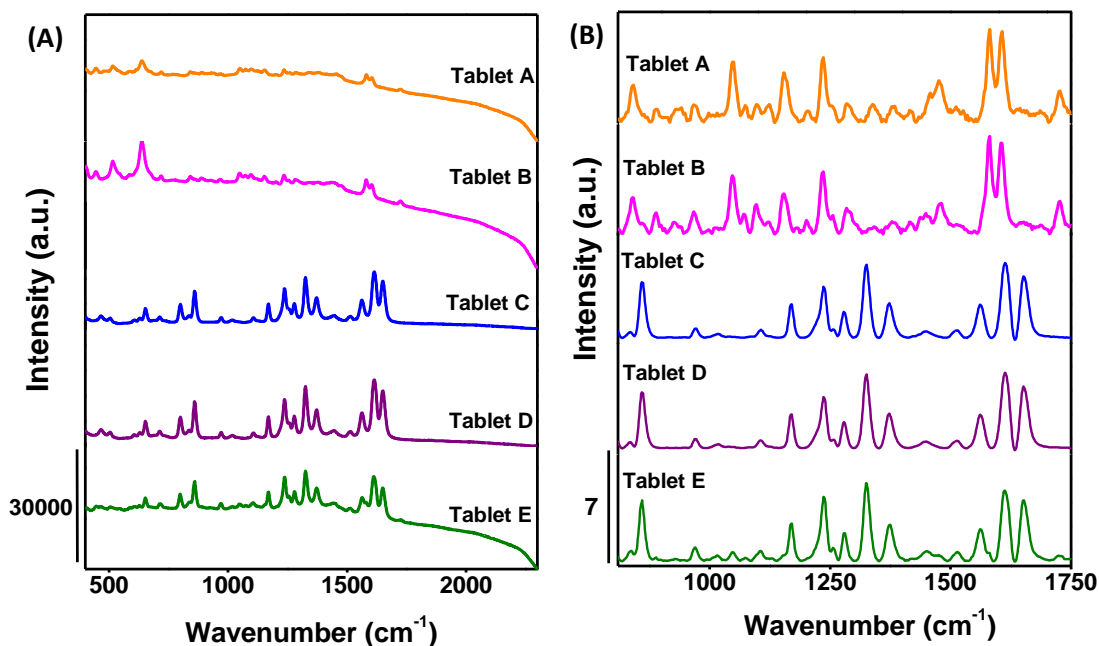


Figure 5.6. (A) Raw and (B) processed Raman spectra of the pharmaceutical tablets under study.

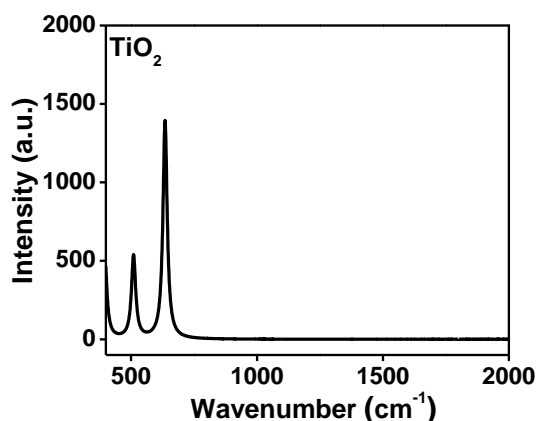


Figure 5.7. Raman spectrum of TiO_2

5.4.2. Qualitative Analysis

The PCA multivariate statistical technique was used to discriminate the drugs based on their API, i.e., drugs containing only PARA, drugs containing only ACE, and combinational drugs. PCA model was created from Raman spectral data after baseline correction, trimming, and intensity normalisation. Figure 5.8 A shows the explained variance by the first ten principal components. It is clear that the first three principal components explained 98.6% of the total variability of the original variables (PC1 = 95.7%, PC2 = 2.4 % and PC3 = 0.5%) and are selected for developing the

classification model. Figure 5.8 B shows the scatter plot of the first three PCs and illustrates the good clustering of ACE, PARA, and combinational drugs. The loading vectors corresponding to the three PCs are also given in Figure 5.9.

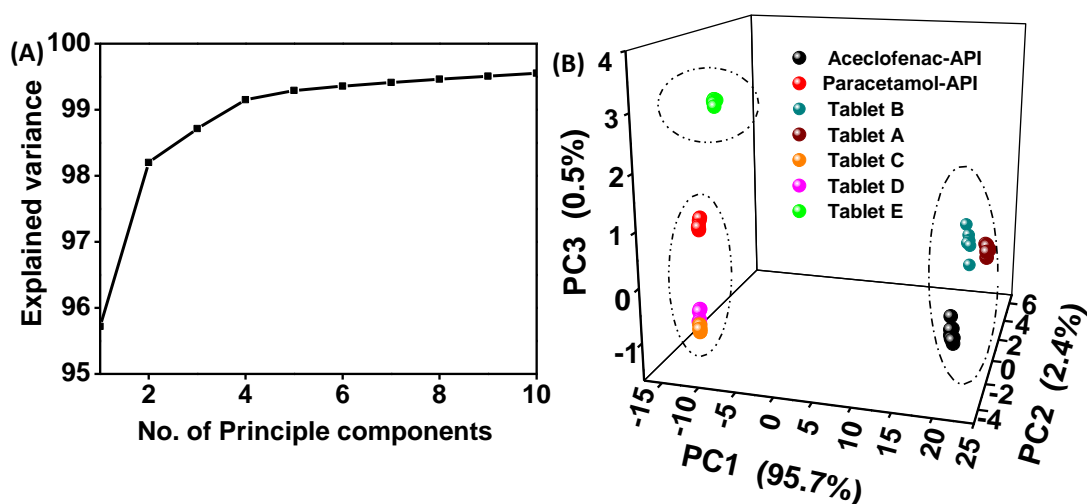


Figure 5.8. (A) Explained variance by the first ten principal components, and (B) PCA score plot showing the clustering of tablets based on their ingredients.

The ACE Raman peaks mainly contribute to PC1 loading and get higher PC1 score values for pure ACE API, tablet A, and tablet B. Although tablet E contains ACE, the presence of PARA (having a negative correlation) makes its PC1 value

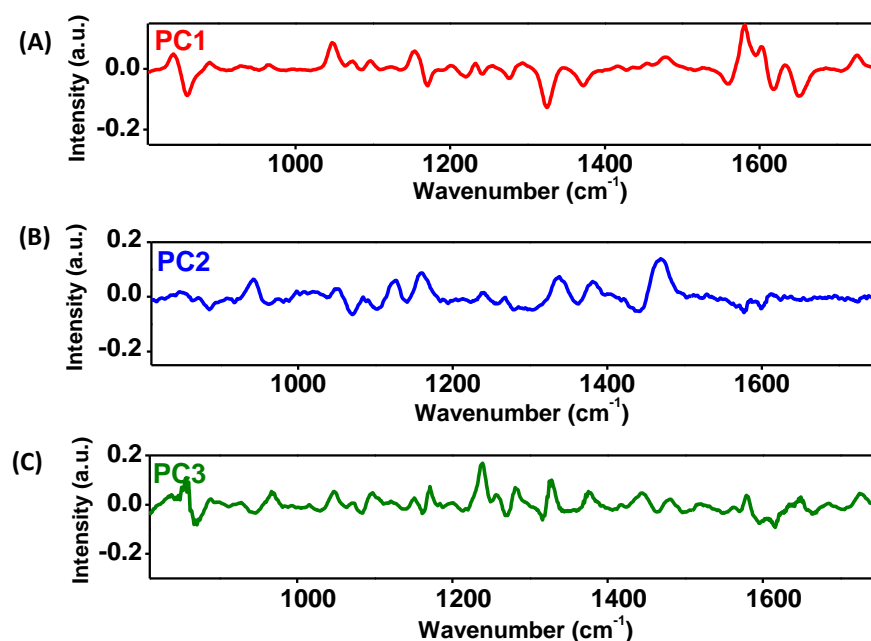


Figure 5.9. PCA loading vectors of (A) 1st (B) 2nd and (C) 3rd principle components

smaller. PC3 is contributed by both ACE and PARA peaks with a positive correlation. Tablets having both these APIs (e.g., E) get higher PC3 value. On the other hand, PC2 is mainly contributed by peaks in the range 1400-1500 cm^{-1} , which is found only in tablet A. Although Raman spectra of A and B have prominent peaks arising from TiO_2 at 519 cm^{-1} and 640 cm^{-1} , their contribution is not reflected in PCA because the trimming operation has removed the spectral information below 810 cm^{-1} . Thus, the created PCA model could classify the tablets into three groups based on the API content. The performance of this model was evaluated on the test data, and all the test samples were correctly classified, see data presented in Figure 5.10.

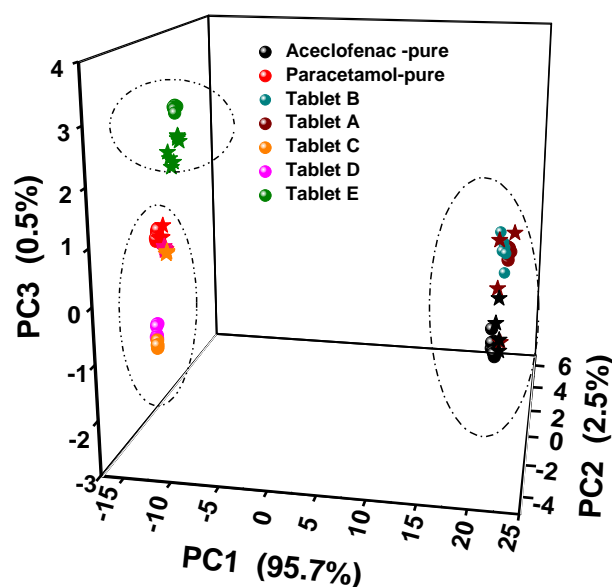


Figure 5.10. Classification of test data using the PCA model, the points marked in star shape corresponds to the test data, and the round shape corresponds to the training data.

5.4.3. Quantitative Analysis

Raman spectra of laboratory prepared ACE-PARA mixtures of varying concentrations (0-100 weight percentage) are shown in Figure 5.11 and used to create the quantification models. For performing quantitative analysis, PCA analysis was first performed on the calibration data set. Results revealed that the first two principal

components explain $\sim 97\%$ of the variance (Figure 5.12 B). The PCA score plot of the first two components and the corresponding loading vectors are shown in Figure 5.12, B, 5.13.

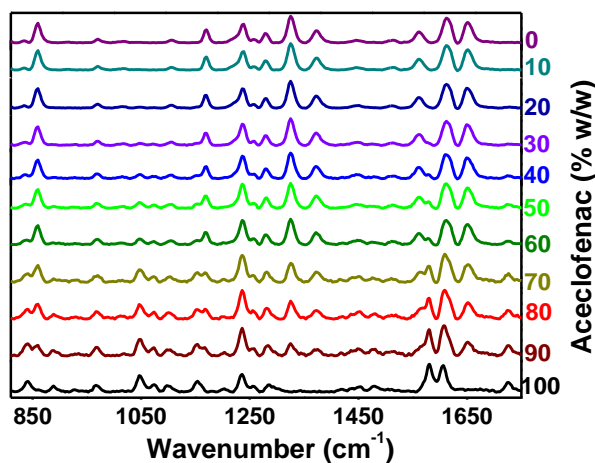


Figure 5.11. Raman spectra of laboratory prepared 0-100 % w/w mixtures of ACE. Data were baseline corrected, trimmed to $810\text{-}1750\text{ cm}^{-1}$, and intensity normalised.

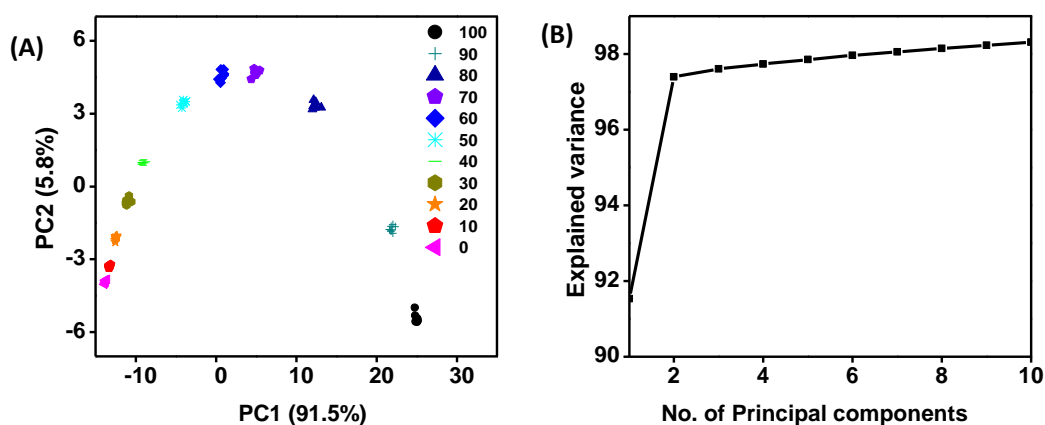


Figure 5.12. (A) PCA score plot, and (B) explained variance of the first 10 principal components.

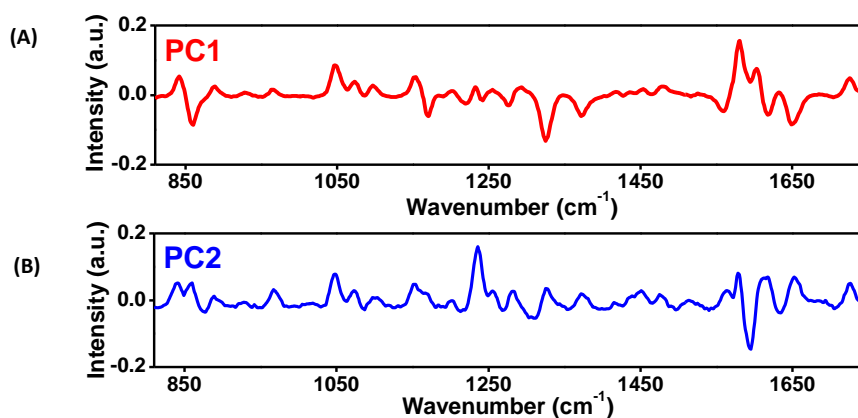


Figure 5.13. (A) PC1 and (B) PC2 loading vectors of the PCA model performed on the quantification calibration model.

Three different quantitative models were analysed based on the above said PCA combined with regression and are described in detail below.

(i). PCR regression

For creating a quantification model, regression of the first two principal components against the API concentration was performed using the multiple linear equations of the form $y=A*x+B*z+C$. The estimated values of the coefficients are shown in equation 5.5. The plot of the estimated API concentration from the multiple linear equation value against the actual API concentration of the training data is shown in Figure 5.14. The resulting R^2 value of the fit is 0.9693.

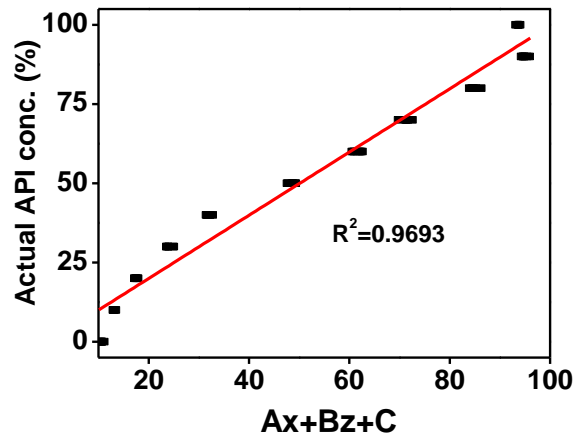


Figure 5.14. Plot showing the relation between PC1 values against the concentration predicted by the multiple linear equations.

$$\text{Predicted}_{Con.}=(2.22*PC_1)+(2.213*PC_2)-1.13*10^{-13}+50 \quad (5.5)$$

From the curve it is obvious that the fitting is poor in the entire concentration range moreover the relation doesn't look linear, providing further scope for improvement in prediction.

(ii). Polynomial PCR regression with PC1 (Mod-PCR 1)

To improve the prediction accuracy of the quantification model, we studied different ways to enhance the R^2 -value of the fitting model. Figure 5.15 represents the plot of 1st principal component against the API concentration of the training data set. The

graph can be best fitted by a 3rd order non-linear relation of the form $Y = A*x + B*x^2 + C*x^3 + D$, and the estimated coefficient values are shown in equation 5.6.

$$\text{Predicted}_{Con.} = (1.828*PC_1) + (-0.108*PC_1^2) + (0.00376*PC_1^3) + 63.24 \quad (5.6)$$

The resulting R^2 value of the fit is 0.983 which is better than the value shown in the PCR regression model.

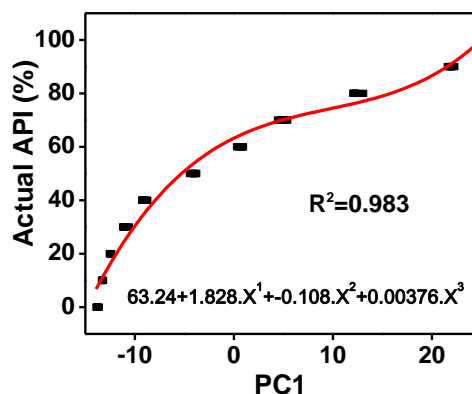


Figure 5.15. Plot showing the relation between PC1 values against API concentration, the red line showing the non-linear fit.

(iii). Polynomial PCR regression with PC1 and PC2 (Mod-PCR2)

It is to be noted that PC1 accommodates only 91.5% of the variance (Figure 5.12 B). One way to improve the prediction accuracy could be by using principal components explaining more of the variance. PC1 and PC2 together accommodate 95% of the variance and thus decided to use both these components in prediction. Figure 5.16 represents the plot of PC1+PC2 against API concentration. This graph is also best fitted by a 3rd order non-linear relation of the form $Y = A*x + B*x^2 + C*x^3 + D$. The resulting R^2 value of the fit is 0.989.

The above described three quantification models i.e. PCR, Mod-PCR1, Mod-PCR2 modelled using the training data was evaluated for predicting the concentration of API from the test data. The details are provided in the next section.

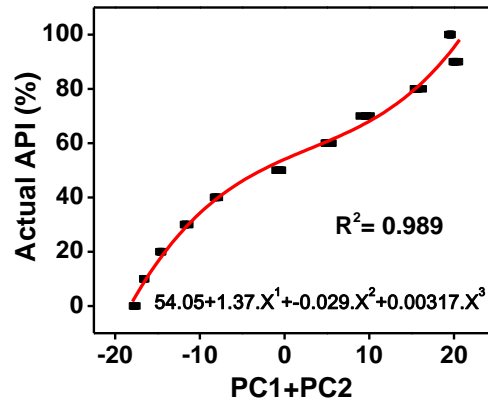


Figure 5.16. Relation between $PC1+PC2$ values against API concentration

5.4.4. Prediction Accuracy of Quantitative Models

30% of the laboratory prepared mixtures was used for testing the quantification models. The ACE, API concentration was predicted from test data set using the three models, is tabulated in Table 5.3. The data were averaged for 4 spectra for each concentration. The calculated RMSE and R^2 -value of the prediction are tabulated in Table 5.4.

Table 5.3. Actual and predicted concentration of API from test data using PCR, Mod-PCR1 and Mod-PCR2 models

Actual API concentration	Predicted API concentration		
	PCR	Mod-PCR1	Mod-PCR2
0	10.03172	9.61993	7.26639
10	13.18034	13.05774	11.13397
20	17.39555	17.42915	16.24976
30	23.90204	24.02954	25.49811
40	31.82306	32.06711	35.37062
50	47.59341	47.78935	53.00515
60	60.63667	60.7905	64.10682
70	71.61022	71.60984	70.29863
80	84.66385	84.58078	76.39846
90	93.87551	93.73863	90.01752
100	93.30101	93.29861	99.9269

Table 5.4. Comparison of RMSE and R^2 value of the quantification models.

Model	RMSE	R^2 value
PCR	5.3	97.1
Mod-PCR1	3.7	98.6
Mod-PCR2	2.8	99.2

The results revealed that the prediction accuracy got improved by using polynomial regression rather than the traditional multiple linear regression. The R^2 value improved from 97.1% to 99.2%, and the RMSE reduced from 5.3 to 2.8. Thus, incorporating more principle components in prediction will help to increase the accuracy of prediction.

5.4.5. Evaluation of the Model in Classifying Genuine and Fake Samples

As the ultimate aim is to determine and quantify the API and predict the genuineness of the tablet from its dosage (overdosage/ under dosage), we carried out further validation of the models through ROC Analysis. An independent validation set consisting of 16 fake equivalents and 16 genuine equivalents, thus a total of 32 data was used for ROC analysis. Tablet E and prepared mixture with 23.5% API is labelled as genuine, and prepared mixture with 10, 20, 30, 40 % API are used as fake. The API concentration was predicted from these samples using the three quantification models, and the results are tabulated in Table 5.5. Further TP, FP, TN, and FN were calculated at nine different threshold levels in the range 23.25-23.75 and 8-45. The calculated values at a selected threshold value are tabulated as a confusion matrix in Table 5.6.

From the confusion matrix, TPR and FPR were calculated using Equations 5.3 and 5.4, and the results are presented in Table 5.7. Later ROC curve is plotted from TPR and FPR values, and the measured AUC is represented in Figure 5.17.

Table 5.5. Actual and predicted concentration of API for genuine and fake equivalent samples

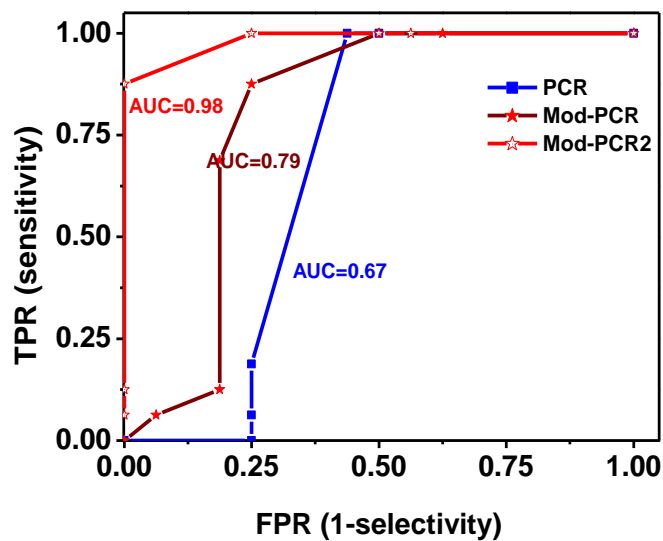
Sample type	Actual ACE (% w/w)	Predicted ACE (% w/w)			
		PCR	Mod-PCR1	Mod-PCR2	
Fake	40	31.61605	35.66937	39.11073	
		31.90643	34.58759	39.43793	
		32.40665	37.03129	39.97945	
		32.69619	36.53701	40.2942	
	10	13.5595	12.03123	10.21133	
		12.77147	10.43517	8.473934	
		13.4393	11.6133	9.950105	
		12.98035	10.86872	8.938966	
	20	17.49387	16.98866	18.22404	
		17.60684	16.70641	18.43989	
		16.91717	15.62802	17.1202	
		17.31146	15.81394	17.8804	
	30	23.79607	24.32191	28.92001	
		23.90456	26.68333	29.5577	
		23.76553	23.83584	28.87741	
		24.00071	24.4303	29.45223	
	Genuine	23.5	18.02124	17.0648	19.21856
			18.61794	18.47514	20.31611
			17.81649	16.63638	19.8363
			18.63029	19.76191	20.33753
17.65975			16.23255	18.54207	
18.63358			19.00833	20.34255	
20.44662			21.24217	23.54196	
21.33882		22.11615	24.04117		
Tablet E		17.6749	17.94622	18.56372	
		18.29217	20.10584	19.70997	
		18.38531	19.70476	19.88376	
		17.90027	19.66195	19.9813	
		18.32947	19.72839	19.78054	
	18.08524	19.35448	19.32866		
	18.48025	20.49474	20.05532		
	19.8631	20.88016	20.7528		

Table 5.6. Confusion matrix for three different methods at a selected threshold

		Actual					
		PCR		Mod-PCR1		Mod-PCR2	
		Genuine	Fake	Genuine	Fake	Genuine	Fake
Predicted	Genuine	TP-3	FP-4	11	3	14	0
	Fake	FN-13	TN-12	5	13	2	16

Table 5.7. Calculated TPR and FPR at different threshold levels

Threshold		PCR		Mod-PCR1		Mod-PCR2	
		TPR	FPR	TPR	FPR	TPR	FPR
T1	[23.25-23.75]	0	0	0	0	6.25	0
T2	[22-24]	0	25	6.25	6.25	6.25	0
T3	[21- 25]	6.25	25	12.5	18.75	12.5	0
T4	[19-26]	18.75	25	68.75	18.75	87.5	0
T5	[17-27]	100	43.75	87.5	25	100	25
T6	[15-28]	100	50	100	50	100	25
T7	[12-35]	100	100	100	62.5	100	50
T8	[10-38]	100	100	100	100	100	56.25
T9	[8-45]	100	100	100	100	100	100

**Figure 5.17.** ROC plot for the three quantification models at nine different threshold levels

The results showed that AUC is highest for Mod-PCR2 (0.98), with Mod-PCR1 second best and PCR the worst. Thus Mod-PCR2 is the best classification model in predicting genuine and fake samples. For implementing the selected model for classifying the samples into genuine and fake effectively, a threshold level needs to be selected in such a way that the classification has the highest sensitivity (TPR) and selectivity (100-FPR). The tabulated data shown in Table 5.7 illustrates that the optimum threshold value is at T4, having a sensitivity and selectivity respectively as 87.5 % and 100%. This indicates that, at this threshold level, the classifier model correctly classifies all the fake samples and 87.5% of the genuine samples. In the current case, the portable Raman spectroscopic system will be used as a screening method for counterfeit detection. It is required that all counterfeit drugs be detected, with no false positives (i.e. fake drug classified as genuine), thus T4 will be the best choice for predicting the quality of the selected drug.

5.4.6. Software Development for Quality Testing

For automatically predicting the API concentration in the pharmaceutical tablets using the developed quantification model, a standalone windows application was developed using MATLAB® guide. The user interface of the developed application is shown in Figure 5.18. The detailed flowchart of the algorithm used for developing the software is shown in Figure 5.19.

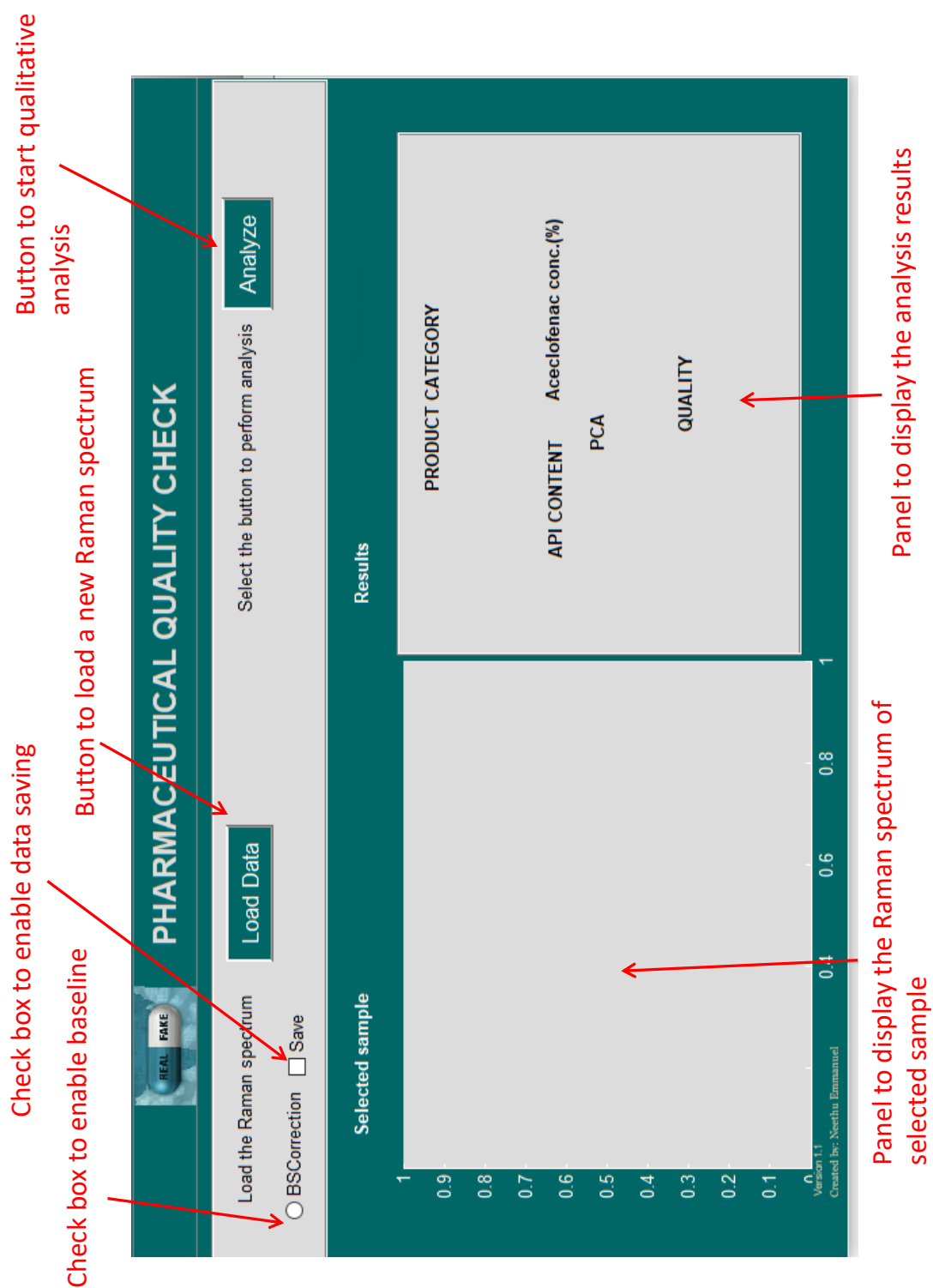


Figure 5.18. Snap-shot showing GUI of the standalone application.

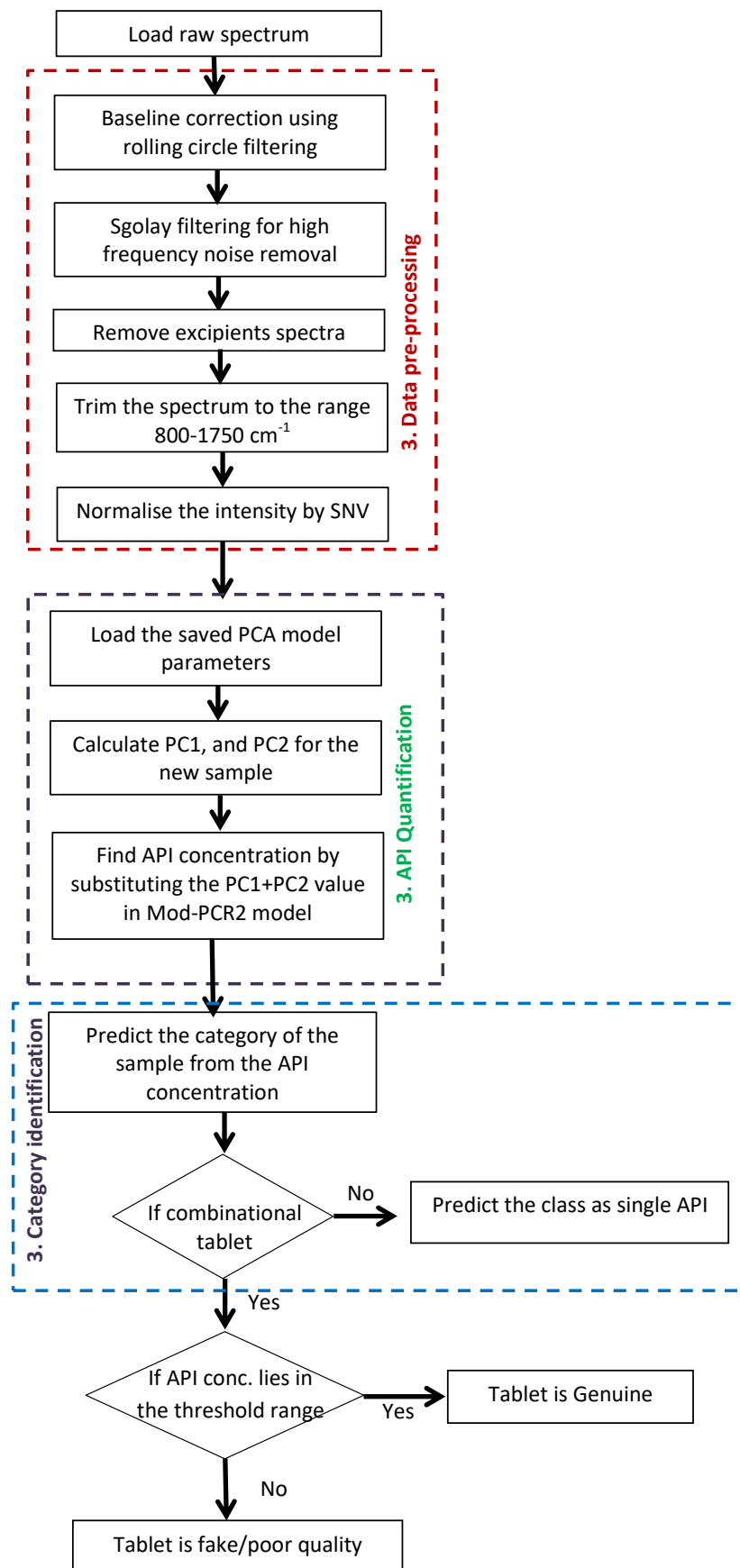


Figure 5.19. Computational algorithm of the developed standalone application for pharmaceutical quality estimation.

Blind Sample Analysis: To evaluate the performance of the developed standalone application in predicting the API concentration, various laboratory prepared mixtures of ACE-PARA and commercial samples were analysed. The obtained results are also compared with HPLC data. The average value of the concentration predicted from 4 repeated experiments is tabulated in Table 5.8. As a representative example, Figure 5.19 shows the snap-shot of the software showing the raw Raman spectrum and predicted API concentration of the sample S4. Figure 5.20 shows the chromatogram of the same. The software estimated concentration is 24.6% while the HPLC analysis of the same yielded concentration is 23.57% (Figure 5.20).

Table 5.8. Comparison of results obtained from HPLC and the developed standalone application

Laboratory prepared mixtures		
Sample	Raman spectrometer (% w/w)	HPLC (% w/w)
S1	10.35	8.55
S2	18.24	16.05
S3	39.44	40.92
S4	24.6	23.57
Pharmaceutical samples		
Sample	Raman spectrometer (% w/w)	HPLC (% w/w)
C1	100	99.09
C2	100	99.58
C3	0	3.85
C4	0	2.5
C5	21.9	22

The results showed that the ACE concentration estimated from Raman spectral studies is in good agreement with the prediction from HPLC data, with a maximum deviation of prediction as +/-4. Raman spectroscopic analysis is very fast, requires no

sample preparation and is non-destructive in comparison with the HPLC analysis. As a result, the demonstrated method could be used as a screening method for analysing pharmaceutical product quality and classify the tablet into genuine and fake based on the API content.

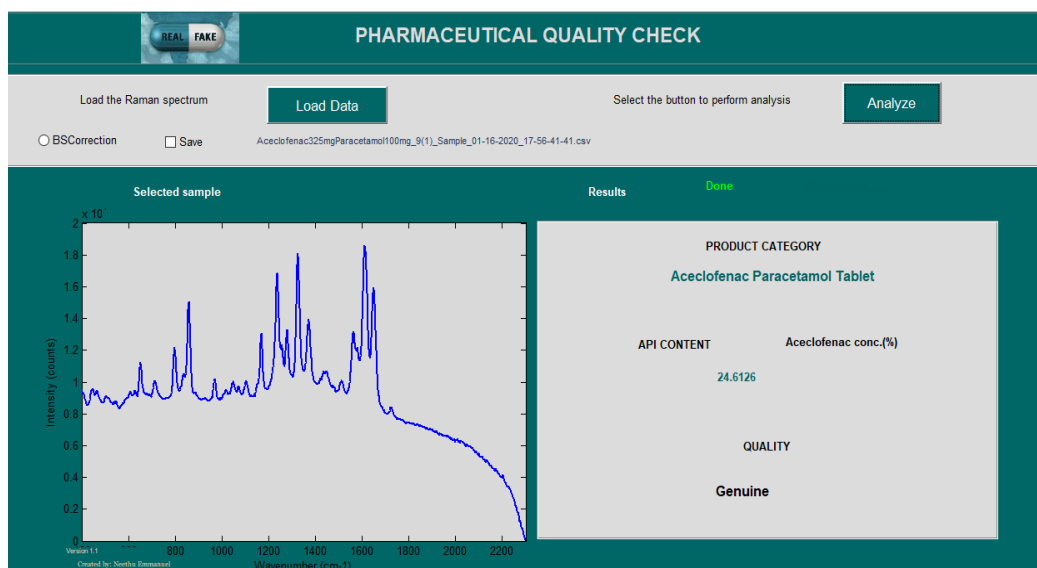


Figure 5.20. Predicted API concentration from the laboratory prepared mixture containing 23.5% ACE.

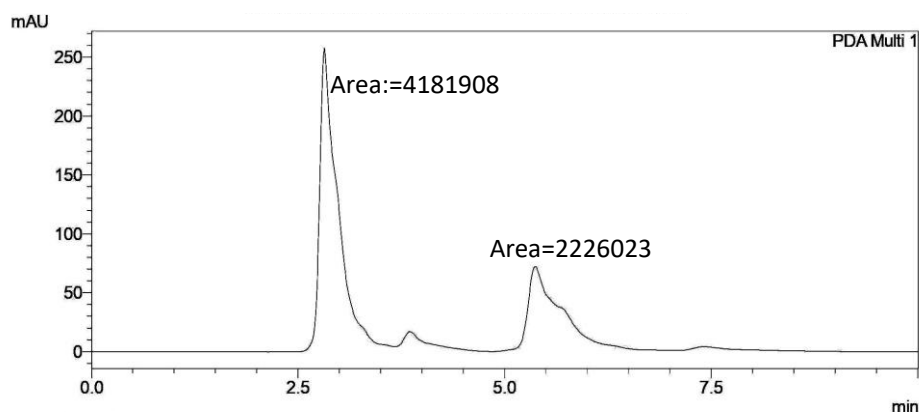


Figure 5.21. HPLC chromatogram of the laboratory prepared mixture containing 23.5% ACE

5.5. Summary and Future Scope

RS is a powerful tool for fast and non-destructive analysis of pharmaceutical products. The flexibility of determination and quantification of ACE from single and

combinational dosage tablet by portable Raman spectrometer in combination with multivariate analysis was investigated in this chapter. PCA with the first 3 components was able to classify the spectra into 3 groups based on the type of API present. Further the quantification of ACE from the tablets was performed using multivariate regression models. Instead of the traditional linear PCR, the polynomial regression based modified PCR model showed superior performance in accurately quantifying the API from tablets. The ability of the PCR models as a binary classifier to categorize the tablets as genuine and fake was evaluated through ROC analysis. The results showed that all the prepared fake samples were correctly classified as fake with 100% selectivity, and correctly classifies 87.5% of the genuine samples. The developed software could be incorporated into a portable spectrometer and thus enables easy determination of pharmaceutical quality. The developed method opens up possibilities for detecting counterfeit drugs even if they contain the right APIs but do not conform to the quantity claimed by the pharmaceutical company.

5.6. References

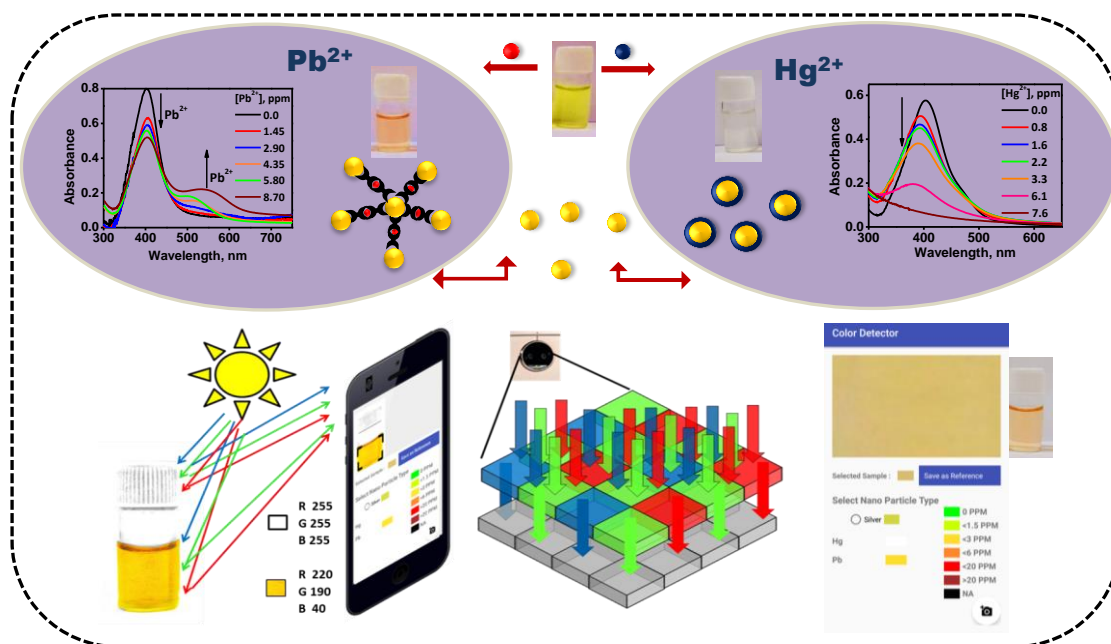
1. Glass, B. D., Counterfeit drugs and medical devices in developing countries. *Res. Rep. Trop. Med.* **2014**, *5*, 11-22.
2. Cuomo, R. E.; Mackey, T. K., An exploration of counterfeit medicine surveillance strategies guided by geospatial analysis: lessons learned from counterfeit Avastin detection in the US drug supply chain. *BMJ Open* **2014**, *4* (12), e006657.
3. Antignac, M.; Bara Diop, I.; Macquart de Terline, D.; Bernard, M.; Do, B.; Ikama, M. S.; N'Guetta, R.; Balde, D. M.; Tchabi, Y.; Aly, A. S.; Toure, I. A.; Zabsonre, P.; F Damorou, J. M.; Takombe, J. L.; Boyer Chatenet, L.; Narayanan, K.; Marijon, E.; Empana, J. P.; Jouven, X., Falsified and substandard cardiovascular drugs in Africa: a need for continued monitoring strategies. *J. Glob. Health* **2019**, *9* (2), 10302.
4. Smith, A., Fake 'Viagra' floods UK clubs and pubs after hitting black market.

- Metro* 2019.
5. Cheng, M. M., Is the drugstore safe? Counterfeit diabetes products on the shelves. *J. Diabetes Sci. Technol.* **2009**, 3 (6), 1516-1520.
 6. Zheng, D., Chinese pharma's history of counterfeits, fakes, and quality issues. *SupChina* 16/03/2021.
 7. <https://www.bbc.com/news/world-asia-china-56080092>, China arrests leader of fake vaccine scam. *BBC News* 12/02/2021.
 8. Stephanie, K.; Stephen E. Hawes, S. N. M.; Emily, M.; Ling, W.; Andy, S., Technologies for Detecting Falsified and Substandard Drugs in Low and Middle-Income Countries. *PloS one* **2014**, 9 (3).
 9. Shah, N. A.; Sattigeri, B. M.; Patel, N. N.; Desai, H. A., Counterfeit drugs in India: significance and impact on pharmacovigilance. *Int. J. Res. Med. Sci.* **2017**, 3 (9), 5.
 10. All 50 states have reported deadly counterfeit pills made with fentanyl. *The Partnership For Safe Medicines* 26/10/2020.
 11. *Janssen Alerts Counterfeit SYMTUZA® (darunavir/ cobicistat/ emtricitabine/ tenofovir alafenamide) is Being Distributed in the United States*; 24/12/2020.
 12. Swaminath, G., Faking it - II: Countering and preventing counterfeiting of drugs. *Indian J. Psychiatry* **2009**, 51 (1), 9-11.
 13. González Peña, O. I.; López Zavala, M.; Cabral Ruelas, H., Pharmaceuticals Market, Consumption Trends and Disease Incidence Are Not Driving the Pharmaceutical Research on Water and Wastewater. *Int. J. Environ. Res. Public Health* **2021**, 18 (5).
 14. Shi, Y.-Q.; Yao, J.; Liu, F.; Hu, C.-Q.; Yuan, J.; Zhang, Q.-M.; Jin, S.-H., Establishment of an HPLC identification system for detection of counterfeit steroidal drugs. *J. Pharm. Biomed. Anal.* **2008**, 46 (4), 663-669.
 15. Rebiere, H.; Kermaïdic, A.; Ghyselink, C.; Brenier, C., Inorganic analysis of falsified medical products using X-ray fluorescence spectroscopy and chemometrics. *Talanta* **2019**, 195, 490-496.
 16. Holzgrabe, U.; Malet-Martino, M., Analytical challenges in drug counterfeiting and falsification-The NMR approach. *J. Pharm. Biomed. Anal.* **2011**, 55 (4), 679-87.
 17. Sacré, P.-Y.; Deconinck, E.; De Beer, T.; Courselle, P.; Vancauwenberghe, R.; Chiap, P.; Crommen, J.; De Beer, J. O., Comparison and combination of

- spectroscopic techniques for the detection of counterfeit medicines. *J. Pharm. Biomed. Anal.* **2010**, *53* (3), 445-453.
18. Visser, B. J.; de Vries, S. G.; Bache, E. B.; Meerveld-Gerrits, J.; Kroon, D.; Boersma, J.; Agnandji, S. T.; van Vugt, M.; Grobusch, M. P., The diagnostic accuracy of the hand-held Raman spectrometer for the identification of anti-malarial drugs. *Malar. J.* **2016**, *15* (1), 160.
 19. Adar, F.; Leary, P.; Kubic, T., Raman Microscopy for Detecting Counterfeit Drugs - A Study of the Tablets Versus the Packaging. *Spectroscopy* **2014**, *29* (6), 10.
 20. Paudel, A.; Rajjada, D.; Rantanen, J., Raman spectroscopy in pharmaceutical product design. *Adv. Drug Deliv. Rev.* **2015**, *89*, 3-20.
 21. Shende, C.; Smith, W.; Brouillette, C.; Farquharson, S., Drug stability analysis by Raman spectroscopy. *Pharmaceutics* **2014**, *6* (4), 651-662.
 22. Hakan, W.; Saly Romero, T.; Sudaratana, W.; Julie Ann, S. W.; Edward R, G.; Taylor, A. L. S., On-line content uniformity determination of tablets using low-resolution Raman spectroscopy. *Appl. Spectrosc.* **2016**, *60* (6), 672-681.
 23. Li., Y.; Benoît, I.; Drennen., J. K.; Anderson., C. A., Method development and validation for pharmaceutical tablets analysis using transmission Raman spectroscopy. *Int. J. Pharm.* **2016**, *498* (1-2), 318-325.
 24. Lawson, L. S.; Rodriguez, J. D., Raman barcode for counterfeit drug product detection. *Anal. Chem.* **2016**, *88* (9), 4706-4713.
 25. MBN: Increase of overdoses involving counterfeit drugs in Pine Belt. *WDAM* 7 2021.
 26. Patel, P. B.; Patel, T. K., Efficacy and safety of aceclofenac in osteoarthritis: A meta-analysis of randomized controlled trials. *Eur. J. Rheumatol.* **2017**, *4* (1), 11-18.
 27. Løkken, P.; Skjelbred, P., Analgesic and anti-inflammatory effects of paracetamol evaluated by bilateral oral surgery. *Br. J. Clin. Pharmacol.* **1980**, *10* (Suppl 2), 253S-260S.
 28. Geravand, A.; Hashemi Nezhad, S. M., Simulation study of the Orbital Raster Scan (ORS) on the Raman spectroscopy. *Optik* **2019**, *178*, 83-89.
 29. Brandt, N. N.; Brovko, O. O.; Chikishev, A. Y.; Paraschuk, O. D., Optimization of the Rolling-Circle Filter for Raman background subtraction. *Appl. Spectrosc.* **2006**, *60* (3), 288-293.

30. Gautam, R.; Vanga, S.; Ariese, F.; Umapathy, S., Review of multidimensional data processing approaches for Raman and infrared spectroscopy. *EPJ. Tech. Instrum.* **2015**, 2 (1), 8.
31. Jolliffe, I. T.; Cadima, J., Principal component analysis: a review and recent developments. *Philos. T R Soc. A* **2016**, 374 (2065), 1-16.
32. Jolliffe, I. T., A note on the use of Principal Components in Regression. *J. R. Stat.Soc. C-Appl.* **1982**, 31 (3), 300-303.
33. Neill, S. P.; Hashemi, M. R., Chapter 8 - Ocean modelling for resource characterization. In *Fundamentals of Ocean Renewable Energy*, Neill, S. P.; Hashemi, M. R., Eds. Academic Press: 2018; pp 193-235.
34. Mehmet, S. A simple and interpretable performance measure for a binary classifier. <https://www.kdnuggets.com/2020/03/interpretable-performance-measure-binary-classifier.html> (accessed 22/03/2021)
35. Dong, M. W., *Separation Science and Technology*. Academic Press: 2005; Vol. 6, p 255-271.
36. Sergey Shashkov, P. D. AFM-Raman characterization of pharmaceutical tablets <https://www.ntmdt-si.com/resources/applications/afm-raman-characterization-of-pharmaceutical-tablets> (accessed 19/03/2021)
37. Nguyen Thi, Y.; Rademann, K.; Emmerling, F., Direct evidence of polyamorphism in paracetamol. *Cryst. Eng. Comm.* **2015**, 17 (47), 9029-9036.

Development of a Smartphone Spectrometer System for Colourimetric Detection of Heavy Metal Ions



6.1. Abstract

One of the leading causes of water pollution is heavy metals like lead and mercury. Currently, its detection relies on specialized analytical techniques that are costly, bulky, and laborious processes. Thus, there exists an unmet need to develop an easy and portable detection technique for water quality testing. Herein, we report a silver nanoparticle (AgNP) based system exhibiting high selectivity and distinct spectrophotometric behaviour towards these metal ions in the aqueous medium. Though many of the metal ions did not influence the characteristic plasmon spectral profile of AgNPs, mercury caused the disappearance of absorbance at ~ 400 nm. Consequently, the

yellow solution became colourless at around 7.6 ppm of Hg^{2+} ions. In contrast, the presence of Pb^{2+} ions induced a decrease in the initial plasmon intensity with the concomitant emergence of a new red-shifted band above 500 nm. As a result, the colour of the solution turned from yellow to red. These colour changes fall well within the spectral responses of R, G, and B filters of the digital camera. Using this, an android mobile application was developed to do further qualitative and quantitative analysis by digitizing the colour values. The estimated concentration value by this method was found to be in good match with those obtained from the absorption spectral measurement. The achieved lower detection limits were ~ 0.8 ppm for Hg^{2+} and ~ 1.5 ppm for Pb^{2+} ions. This illustrates the potential of the proposed combination of smartphone system with AgNPs for easy discrimination and quantification of these two heavy metal ions from the aqueous medium.

6.2. Introduction

Ensuring water quality is essential for sustaining the good health of humans as well as the environment. Mercury and lead are the two heavy metals considered to be the most toxic that pollute aquatic systems and pose a life-threatening danger to living beings.¹⁻⁶ Presently, the estimation of heavy metal ions from water relies on specialized and sophisticated analytical instruments such as mass, atomic absorption and emission spectroscopies.⁷⁻¹¹ They are either bulky, expensive, or involve laborious processes and require trained professionals for operation and thus are unsuitable for onsite field analysis. Therefore, there exists an unmet global need for developing portable and cost-effective devices. Further, the methodologies should be easy to perform, have fast response, high sensitivity and selectivity.

In principle, this can be fulfilled by utilizing smartphone computing technologies. Lately, there is growing attention for portable, low-cost optical

spectroscopic devices integrated with mobile phones. New generation smartphones are equipped with various types of sensors and even advanced technologies like artificial intelligence and machine learning, opening up possibilities for onsite analysis in numerous fields.¹² Some of the recently reported works that specifically utilize the camera for sensing applications are colourimetric detection of pH,¹³ haemoglobin,¹⁴ Bisphenol,¹⁵ and fluorescent lateral flow immunoassay (LFIA) platforms for the point of care detection of Zika virus¹⁶ etc. These were possible by measuring analyte induced variations in either colour or light intensity of the sample upon interaction with a camera. However, the chemical assay's sensitivity and selectivity determine the translation potential of smartphone-based chemical sensors.

Metal nanoparticles exhibit intense colour due to the presence of surface plasmon resonance. In most cases, analytes induce changes to the plasmon spectral profiles resulting in visual colour changes. This has led to the development of several naked eye chemical sensors.¹⁷⁻²² Moreover, to improve the sensing accuracy, people attempted incorporating smartphone cameras for this colourimetric detection.²³⁻²⁵ Major advantage of metal nanoparticles is the simplicity of production. Presently, many procedures are available for the easy synthesis of nanoparticles, including simple room temperature mixing of metal salts with a reductant and a suitable capping ligand.²⁶⁻²⁸

This chapter reports a silver nanoparticle based system that exhibits distinctly different spectrophotometric behaviour towards Pb^{2+} and Hg^{2+} ions from the aqueous medium. Hg^{2+} ions resulted in gradual fading of the yellow colour of the AgNP, while Pb^{2+} induced a drastic colour change to red. However, little spectral changes were noted for other interfering metal ions. Interestingly, the spectral variations induced by Pb^{2+} and Hg^{2+} ions fall well within the spectral response of the R, G, and B colour filters of the digital cameras. By taking advantage of these, we could use a smartphone

and develop a mobile application that can automatically distinguish Pb^{2+} and Hg^{2+} ions from the aqueous medium and quantify them with a detection limit of ~ 1.5 ppm and ~ 0.8 ppm, respectively.

6.3. Experimental Section

6.3.1. Materials and Methods

Nickel(II) acetate ($\text{C}_4\text{H}_6\text{NiO}_4$), Magnesium(II) sulphate (MgSO_4), Zinc(II) sulphate (ZnSO_4), Calcium(II) perchlorate ($\text{Ca}(\text{ClO}_4)_2$), Cadmium(II) chloride (CdCl_2), Mercury(II) acetate ($\text{C}_4\text{H}_6\text{O}_4\text{Hg}$), and Sodium hydroxide (NaOH) were obtained from M/s Sd fine chemicals. Silver nitrate (AgNO_3) and Mercury(II) chloride (HgCl_2) was purchased from M/s Merck. 3,4-dihydroxyhydrocinnamic acid (DHCA) was obtained from M/s Sigma Aldrich Corporation, Lead(II) perchlorate trihydrate ($\text{Pb}(\text{ClO}_4)_2 \cdot 3\text{H}_2\text{O}$) was purchased from M/s Alfa Aesar. All chemicals were used as received. Stock solutions of all the reagents were prepared in doubly distilled water. All the chemicals used herein were of analytical grade. The electronic absorption spectra were recorded on UV-Vis-NIR spectrometer Lambda 950 (M/s PerkinElmer, Inc.). For transmission electron microscopic (TEM) studies, samples were prepared by casting a few drops of their aqueous dispersions on carbon-coated copper grids followed by drying at room temperature and analyzed with FEI 300 kV high resolution transmission electron microscope (FEI-Tecnai G2-30 with EDAX). The hydrodynamic diameter and zeta potential of the nanoparticles were measured by dynamic light scattering (DLS), using a Zetasizer Nano ZS (M/s Malvern Instruments). For FTIR studies, DHCA capped AgNPs was precipitated by centrifugation, dried, mixed with KBr and spectra were acquired in diffused reflectance mode using IRPrestige-21 (M/s Shimadzu corporation).

6.3.2. Synthesis of Silver Nanoparticles (AgNPs)

AgNPs were synthesized through one-step room temperature reduction of AgNO_3 with 3,4-dihydroxyhydrocinnamic acid (commonly called as dihydrocaffeic acid or DHCA) in the presence of sodium hydroxide. Similar to the metal nanoparticle formation by other ligands such as gallic acid, L-DOPA and others²⁹⁻³⁰ herein, DHCA plays the roles of both reducing and capping agents. Mainly, the dihydroxy group acts as the reducing part, and the anchoring of the acid moiety or the carbonyl groups imparts colloidal stability to the nanoparticles.

The synthesis was carried out as follows: 0.74 mM (10 mL) of silver nitrate solution was first mixed with 30 mL of deionized water under stirring. To this, solutions of 60 μL of 10 mM DHCA and NaOH (20 μL , 0.15 M) were added together and stirred at room temperature until it turned yellow.

6.3.3. Interaction of AgNPs with Metal Ions

Initially, to study the sensing capabilities, we prepared stock solutions of metal ions by dissolving their corresponding salts in doubly distilled water (e.g. 7.39 mg of HgCl_2 and 12.95 mg of $\text{Pb}(\text{ClO}_4)_2 \cdot 3\text{H}_2\text{O}$ in 10 mL distilled water each and the final stock solution concentrations were 2.72 mM and 2.81 mM respectively). Titration experiments were conducted by adding an aliquot amount of these stock solutions into 2 mL of the AgNPs. The final metal ion concentrations in nanoparticle solution estimated are $[\text{Hg}^{2+}] = 0 \text{ ppm}, 0.8 \text{ ppm}, 1.6 \text{ ppm}, 2.2 \text{ ppm}, 3.3 \text{ ppm}, 6.05 \text{ ppm}, 7.6 \text{ ppm}$, and $[\text{Pb}^{2+}] = 0 \text{ ppm}, 1.45 \text{ ppm}, 2.9 \text{ ppm}, 4.35 \text{ ppm}, 5.8 \text{ ppm}, 8.7 \text{ ppm}$.

Absorption spectral measurements of AgNPs, after each volume addition of metal ions, were carried out in quartz cuvette (1 cm path length). For smartphone-enabled colourimetric sensing, 2 mL of the AgNP solutions containing varying concentrations of metal ions were transferred into glass vials and photographed using

a mobile camera. To minimize the effect of room light, all the samples were kept in a similar white background and photographed under the same lighting conditions. The R, G, and B values of these photographs were first extracted using ImageJ software. By comparing the variations in their RGB values with the absorbance changes, a correlation is drawn based on which we developed an algorithm for the distinction and quantification of the metal ions.

6.3.4. Mobile Application Development

A mobile application was developed using Android Studio 3.1.4 with Software Development Kit (SDK) Android Nougat, installed on a Laptop with 64 bit Windows 10 operating system. The application was developed in such a way that it can take photographs using a mobile phone's camera, extract R, G, and B values from the selected region of interest (ROI) and, with the help of an algorithm, can distinguish toxic metal ions and predict their concentrations using a linear equation model. The developed android application was tested on a Motorola android smartphone with model No: MotoG5SPlus.

6.4. Results and Discussion

6.4.1. Characterization of AgNPs

In the present case, nanoparticles are prepared by the addition of DHCA and NaOH to AgNO_3 solution. We observed the emergence of a yellow colour in the solution within two minutes of mixing the reagents. (Figure 6.1 A). The corresponding absorption spectral measurements showed a strong absorption band in the range 320 nm – 500 nm with a peak maximum at around 400 nm (Figure 6.1 B). It is known that AgNPs exhibit characteristic plasmon absorption in the 400 - 500 nm, which is size and shape tunable.³¹ Therefore, we attribute the band at 400 nm to plasmon absorption of the

formed AgNPs.

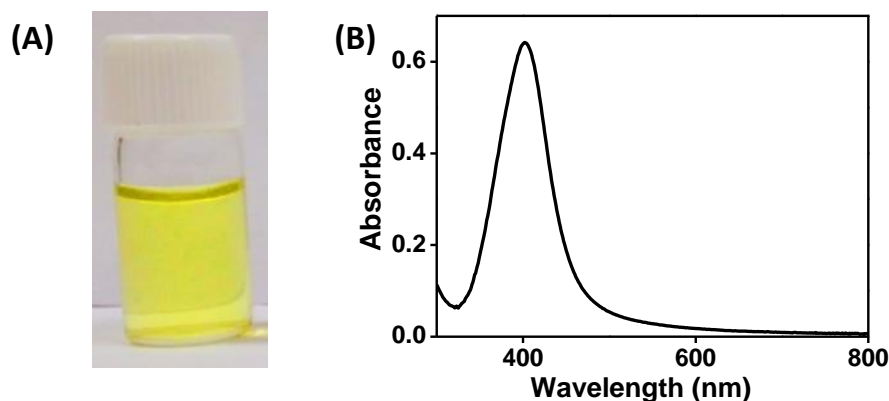


Figure 6.1. (A) Colour photograph and (B) absorption spectra of the AgNP synthesized by addition of 10 mM DHCA to 0.74 mM AgNO_3 in the presence of 0.15 M NaOH.

To have a clear understanding of the nanoparticle's size and shape, we performed detailed DLS and TEM analysis. The DLS curve presented in Figure 6.2 A exhibits a major peak in the range 25-100 nm and a minor in the range 5-10 nm. The representative example of TEM images of AgNPs is shown in Figure 6.2 B. Morphologically the nanoparticles formed are multiply twinned spheres and prisms. Most majority of the particles have a size ~ 60 nm. Nevertheless, a small portion of smaller particles is also visualized in the TEM images and corroborates with the DLS analysis.

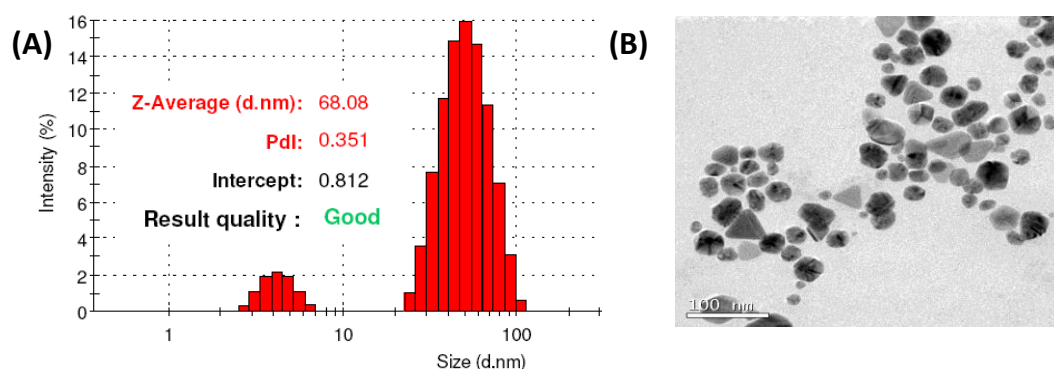


Figure 6.2. (A) DLS curve and (B) TEM image, showing the size distribution of synthesized AgNPs.

In order to estimate the nature of the capping agent, analysis was conducted using FTIR studies. The IR spectrum of the AgNPs displayed significant absorption peaks at

3450 cm^{-1} , 2880 cm^{-1} , 1508 cm^{-1} , and 1068 cm^{-1} corresponding to O-H stretching, C-H stretching, C=C stretching, and O-C stretching respectively. This gives evidence for the presence of H-bonded DHCA on the surface of the AgNPs synthesized herein (Table 6.1 and Figure 6.3).

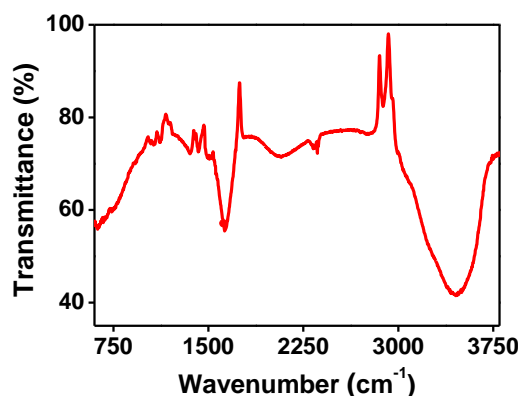


Figure 6.3. FTIR spectrum of the DHCA capped AgNPs.

Table 6.1. Important vibrational frequencies of the DHCA capped AgNPs.

Wavenumber (cm^{-1})	Vibrational bond
3450	O-H stretching
2880	C-H stretching
1508	C=C stretching
1522	C=C stretching (in ring)
1778	C=O stretching
1350	O-H bending (in-plane)
1628	C=C stretching
1420	=C-H bending
1068	O-C stretching
1116	=C-H bending

6.4.2. Interaction of Silver Nanoparticles with Hg^{2+} ions

Figure 6.4 is a representative example of the colour photograph of the nanoparticles solution after the addition of varying amounts of Hg^{2+} ions. The AgNPs exhibited brilliant yellow colour (vide supra). However, the colour of the nanoparticle solution gradually faded as the amount of Hg^{2+} ions is systematically increased and became

completely transparent at ~ 7.6 ppm of Hg^{2+} .

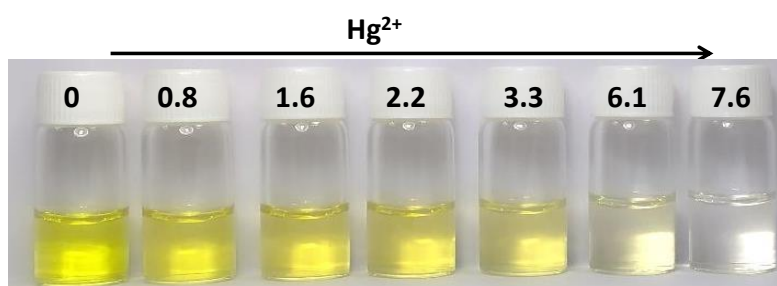


Figure 6.4. Photographs illustrating the colour changes induced to AgNPs by the presence of Hg^{2+} ions at 0 ppm, 0.8 ppm, 1.6 ppm, 2.2 ppm, 3.3 ppm, 6.1 ppm, and 7.6 ppm.

(i) Absorption spectral studies

To investigate the scientific reason behind the Hg^{2+} ion induced colour fading, detailed absorption spectroscopic studies were conducted. Figure 6.5 A shows the absorption spectra of AgNP solution after the addition of varying amounts Hg^{2+} ions. It could be noticed that, with an increase in Hg^{2+} ions concentration, the wavelength of absorption maximum underwent a continuous blue shift. In addition to this, there was a continuous decline in the optical density of the AgNP solution. The optical density got steadily decreased from 0.6 to 0.07 as the Hg^{2+} ions concentration is raised from 0 ppm to 7.6 ppm. This decrease in optical density is the primary reason for the noted colour fading. A plot of the integrated intensity as a function of the metal ion

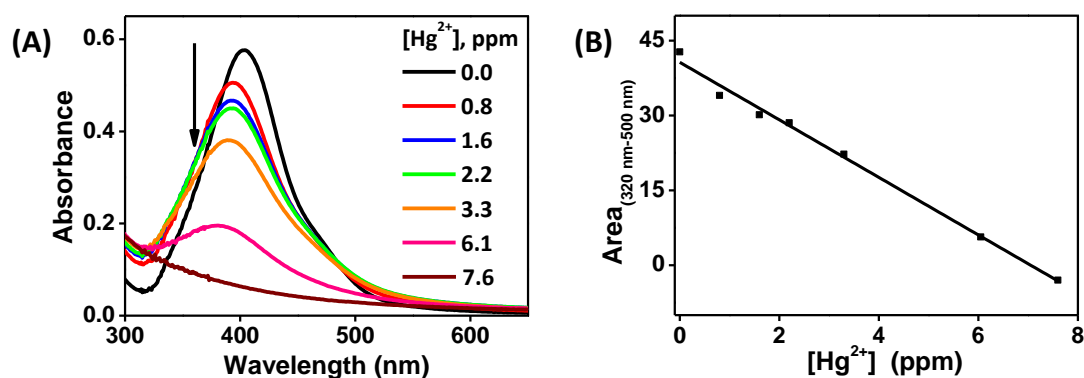


Figure 6.5. (A) Changes in absorption spectra of AgNPs by the presence of varying concentrations of Hg^{2+} ions, and (B) plot of the area under the absorption curve in the range 320-500 nm as a function of Hg^{2+} concentration.

concentration exhibited an excellent linear relationship with an R^2 value of 0.996 within the investigated concentration range (Figure 6.5 B). This illustrates the potential of the current system for the quantitative estimation of Hg^{2+} metal ions from the aqueous medium.

(ii) Mechanism of interaction

The possible reasons for the observed blue shift and dampening of plasmonic features are (i) size reduction of AgNPs by disintegration, (ii) precipitation, or deposition of Hg on the surface of AgNP, (iii) changes in electron density induced by Hg^{2+} ions, or (iv) influence of counterions. From the literature reports, it can be found that the chloride, the counter ion employed in the current studies, may influence the plasmon spectral profile of AgNPs in either way.^{32,33} In some of the reported studies, chloride ion caused aggregation of AgNPs through surface modifications as well as an increase in ionic strengths, thereby reducing electrostatic repulsive interactions. Studies also have brought the disintegration and shape modification through oxidation mediated silver ion dissolution. However, these observations are made at chloride ion concentrations above mM range, which is ~ 100 times higher than present studies. To completely rule out this assumption, experiments were conducted under similar conditions with other metal chloride salts. For example, Figure 6.6 A shows the absorption spectra of AgNP solution in the presence of 0-33 ppm of CdCl_2 solution. We noted no significant change in absorption spectral profiles. Thus, the observed plasmon disappearance and hence the colour fading can solely be attributable to Hg^{2+} ions. This was further reinstated by the observation of plasmon dampening by mercury salt having other counter ions. Figure 6.6 B shows the change in the absorption spectra of AgNP in the presence and absence of mercury acetate. The dampening of plasmon absorption observed was similar to the results obtained by the

addition of HgCl_2 salt (Figure 6.5 A). This confirms that the observed colour fading, as shown in Figure 6.4, is due to the influence of Hg^{2+} ions.

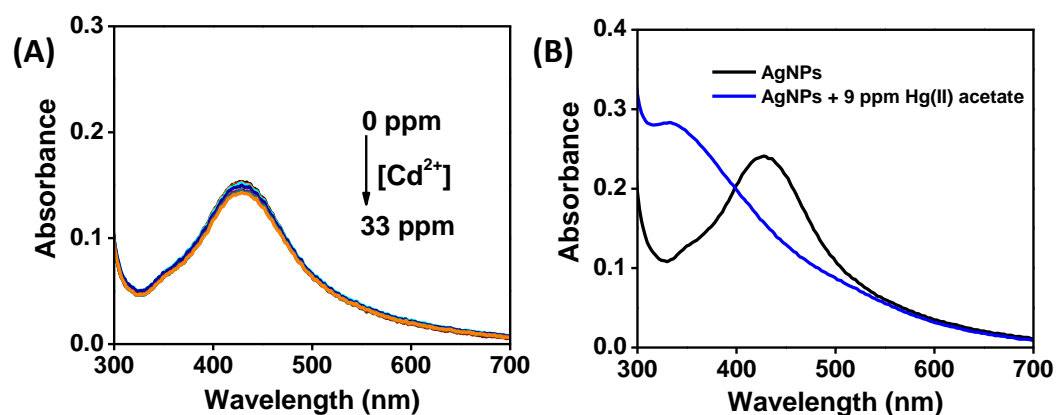


Figure 6.6. Absorption spectra of AgNP solution in the presence of (A) 0-33 ppm cadmium(II) chloride (B) 9 ppm mercury(II) acetate.

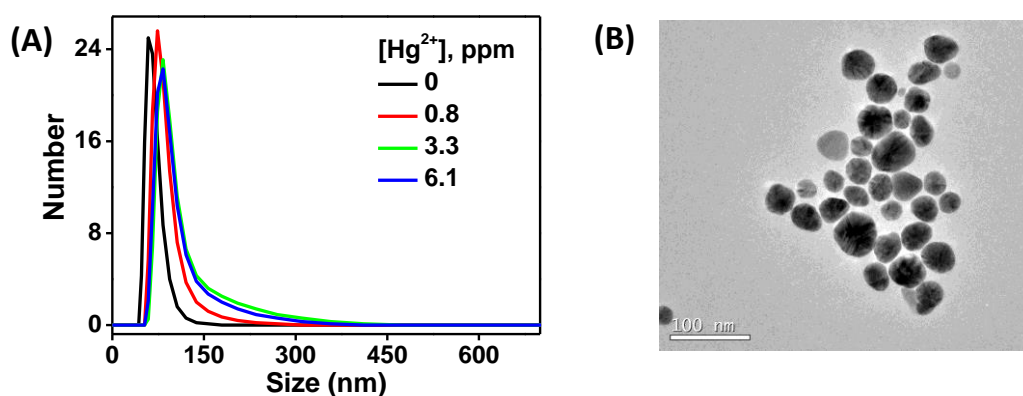


Figure 6.7. (A) DLS curve, and (B) TEM image, showing the size distribution of AgNPs in the presence of Hg^{2+} ions.

Presented in Figure 6.7 are the results of TEM and DLS investigations. The comparison of TEM data with pristine nanoparticles (Figure 6.2 B) revealed no considerable change to the nanoparticle's size (Figure 6.7 B). On the other hand, DLS data showed a slight enlargement of ~ 20 nm in the average particle size with 0 ppm to 3.3 ppm of Hg^{2+} , and no more growth in particle size was observed with further increasing the concentration. The adsorption of Hg atoms on the surface of AgNP may have caused a small increase in particle size at first. Therefore, we argue that the Hg atoms are adsorbed on the surface of the AgNP through amalgam formation.

Amalgam formation was confirmed from the EDX measurements, Figure 6.8 primarily showed the characteristic ‘L α ’ and ‘M α ’ lines of Hg, along with the ‘M α ’ lines of Ag.

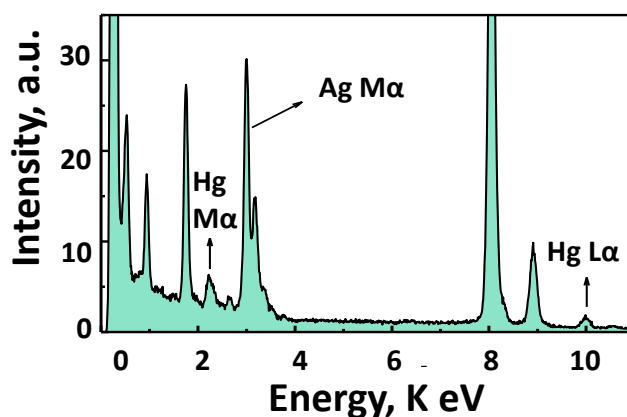


Figure 6.8. Energy dispersive spectrum(EDS) showing the presence of Hg atoms on the surface of AgNPs.

In the electrochemical series, Hg²⁺ occupies slightly lower position compared to Ag⁺ ion ($E_{\text{Ag}^+/\text{Ag}} = 0.8 \text{ V}$ and $E_{\text{Hg}^{2+}/\text{Hg}} = 0.85 \text{ V}$). Thus, when added to the nanoparticle solution, Hg²⁺ ions can easily displace the Ag from nanoparticles (equation 6.1), and this process is thermodynamically feasible.

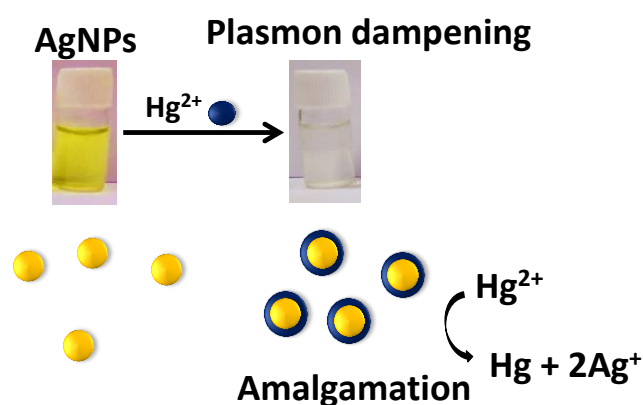
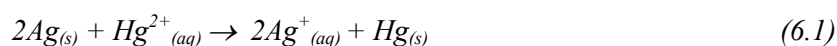


Figure 6.9. Schematic representation of electrochemical displacement of Ag atoms by Hg²⁺ ions and its adsorption onto the nanoparticle surface.

6.4.3. Interaction of Silver Nanoparticles with Pb^{2+} ions

Figure 6.10 is a representative example of the colour photograph of the nanoparticles solution after the addition of varying amounts of Pb^{2+} ions. In contrast to the Hg^{2+} ions, the addition of Pb^{2+} ions induced a drastic colour change to the AgNPs. The colour of the solution got gradually changed to orange and red upon increasing the Pb^{2+} ion concentration to 8.7 ppm.

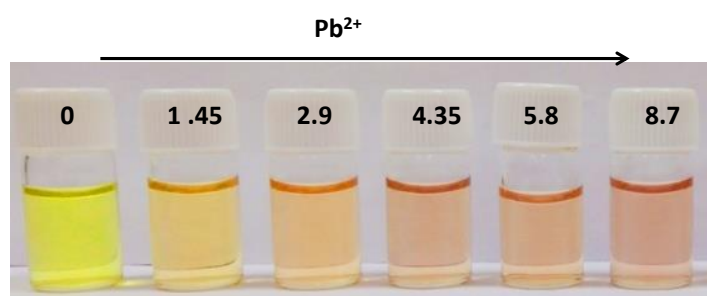


Figure 6.10. Photographs illustrating the colour changes induced to AgNPs by the presence of Pb^{2+} ions (from left to right $[\text{Hg}^{2+}] = 0$ ppm, 1.45 ppm, 2.9 ppm, 4.35 ppm, 5.8 ppm, and 8.7 ppm).

(i). Absorption spectral studies

Figure 6.11 A shows the absorption spectra of AgNP solution after the addition of varying amounts of Pb^{2+} ions. It could be noticed that, with an increase in Pb^{2+} ions concentration, the optical density of the native plasmon absorption continuously

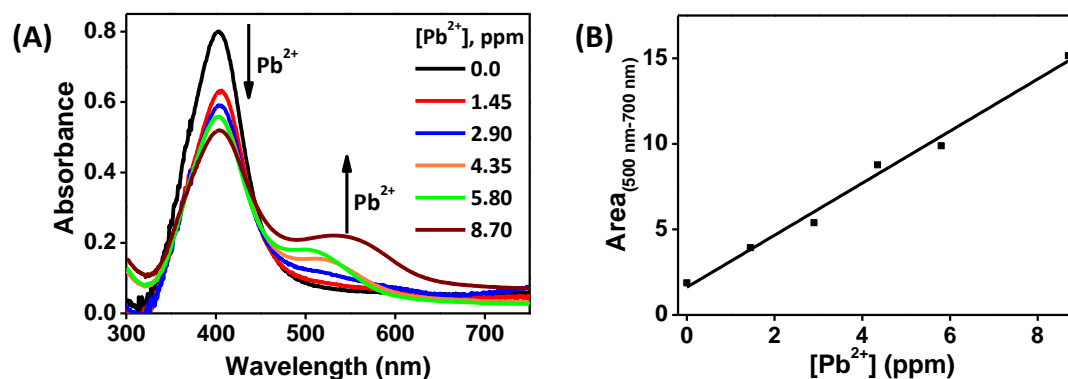


Figure 6.11. (A) Changes in absorption spectra of AgNPs by the presence of varying concentrations of Pb^{2+} ions, and (B) plot of the area under the absorption curve in the range 500-700 nm as a function of Pb^{2+} concentration.

decreased from 0.8 to 0.5. Besides, a new red-shifted peak started forming in the range 500-700 nm. Both the intensity and wavelength of this new band got amplified with increasing concentrations of Pb^{2+} ions. A plot of the integrated intensity of this new band as a function of the metal ion concentration exhibited an excellent linear relationship with an R^2 value of 0.994 within the investigated concentration range (Figure 6.11 B).

(ii) Mechanism of interaction

Several previous studies have established that the absorption maximum of metal nanoparticles undergo a bathochromic shift when nanoparticles are brought too close to each other. In such cases, the individual plasmons undergo interparticle coupling, resulting in new low energy plasmon oscillation. We argue that the possible reason for the appearance of the red-shifted absorption band could be due to the interplasmon coupling facilitated by Pb^{2+} ions through aggregation.

Figure 6.12 shows the results of TEM and DLS investigations. Cluster formation of AgNPs was evident in TEM images. DLS data also supports this, i.e. the size of particles changed from ~ 60 nm to ~ 180 nm with increasing the Pb^{2+} ion concentration from 0 ppm to 8.7 ppm (Figure 6.12). The enlargement in hydrodynamic diameter in the presence of Pb^{2+} ions is a clear indication of aggregate

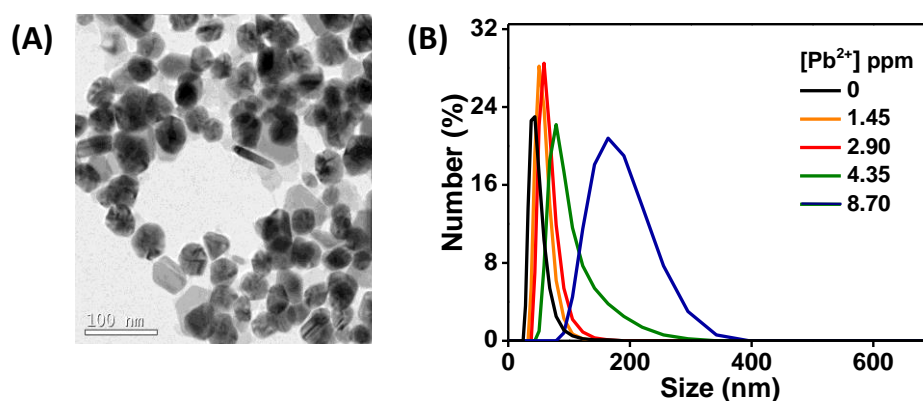


Figure 6.12. (A) TEM image, and (B) DLS data showing the size distribution of AgNPs in the presence of Pb^{2+} ions.

formation.

This suggests that Pb^{2+} ions cause the aggregate formation of AgNPs and is possible through the binding of Pb^{2+} ion with multiple ligands residing on different nanoparticles, thereby bringing them close to each other. The zeta potential measurement of metal nanoparticles indicated a very high surface charge of -40 mV (at around pH 5). This acts as a repulsive force against the agglomeration of nanoparticles imparting high colloidal stability. Thus, only those nanoparticle: analyte interactions capable of overcoming this strong Coulombic repulsion can induce aggregation. Lead is unique in having flexible bond lengths and coordination number. It can simultaneously bond with ligands on the surface of different nanoparticles, thereby bringing AgNPs close to each other thus promoting agglomeration.

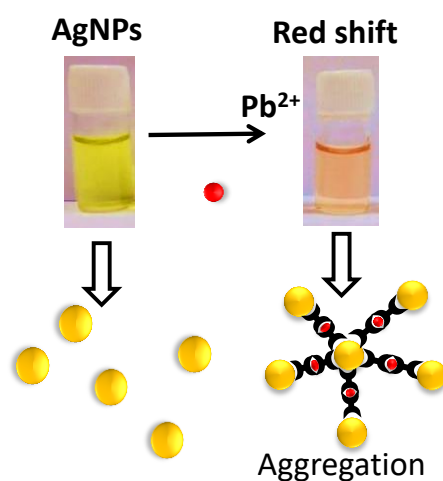


Figure 6.13. Schematic representation of the aggregate formation of AgNP induced by Pb^{2+} ions.

6.4.4. Interaction of Silver Nanoparticles with Other Metal Ions

To establish the selectivity of sensing, we investigated the possible interference by a few other metal ions, including the toxic Cd^{2+} ions. Varying concentrations of the metal ions (Ca^{2+} , Ni^{2+} , Zn^{2+} , Mg^{2+} and Cd^{2+}) in the range ~ 0-30 ppm were added to the AgNP solution. As shown in Figure 6.14 F, only minor changes in optical density

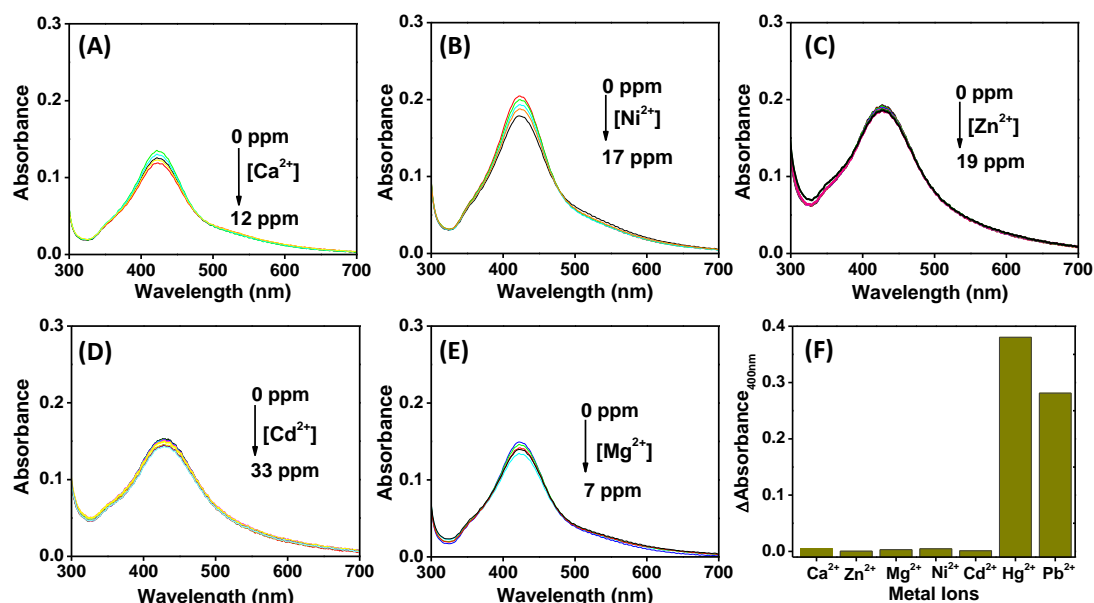


Figure 6.14. Absorption spectra of AgNP solution in presence of (A) 0-12 ppm calcium(II) perchlorate, (B) 0-17 ppm nickel(II) acetate, (C) 0-19 ppm zinc(II) sulphate, (D) 0-33 ppm Cadmium(II) chloride and (E) 0-7 ppm magnesium(II) sulphate and (F) selectivity plot showing the absorbance difference at 400 nm between AgNPs in the absence and presence of different metal ions.

(<0.01) at the plasmon absorption maxima were observed in the presence of these metal ions. Hence we did not observe any characteristic colour change in the AgNP solution. This reveals their inability to induce AgNP agglomeration or any amalgamation under similar experimental conditions.

6.4.5. Colourimetric Analysis Through Photographs

Though the observed distinct and characteristic colour change serves the purpose of naked eye distinction of the metal ions, it has the inherent drawback of quantification since the colour perception is individual dependent. To overcome this, we thought of developing a simple photometric method for distinction and quantification. Presently, smartphones are an inevitable part of everyday life and are commonly equipped with cameras, though of varying capabilities. The camera, in general, consists of a 2D array of photosensory elements called pixels. Each pixel is equipped with a combination of blue (B), green (G), and red (R) filters, which selectively pass a band of wavelengths

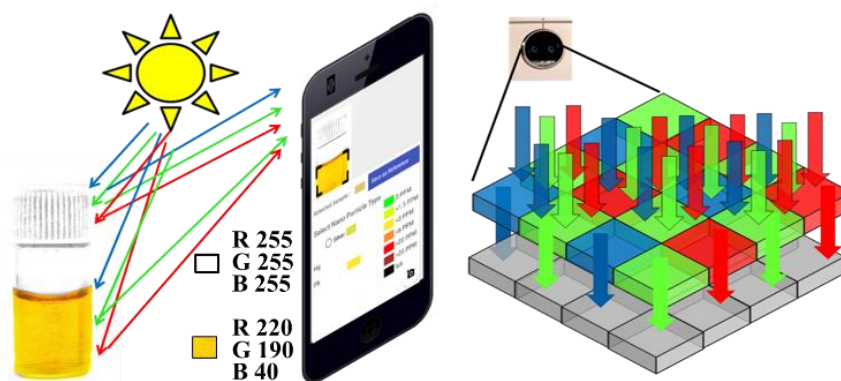


Figure 6.15. Schematic representation illustrating the basic principle of colour photography using a mobile phone camera. The Graphical user interface (GUI) of the developed application for metal ion sensing is also shown.

in the range 400-500 nm, 500-600 nm, and 600-700 nm respectively. The intensities of each of these primary colours are represented on an absolute scale of 0-255. While photographing, the reflected light from the object falls on the sensory elements through these colour filters, generating a photocurrent in the respective pixels and whose magnitude is proportional to the light intensity (Figure 6.15). Then, the actual colour of the materials is identified through their relative values. Another crucial parameter that can be extracted from colour photographs is HSV, a linear colour code.³⁴ In this, H is the angular representation of colour on a scale of 0°-360°. The H values for the three primary colours, red, green, and blue, are respectively 0°, 120° and 240°. The S ranges from 0-100%, which represents the colour content or the saturation value. V varies from 0-100% with the lighting conditions. Pure AgNPs, owing to their bright yellow colour, possess an H value close to 60°. The corresponding R, G, and B values are around 200, 200, and 36 respectively. Herein, the low value of B is attributed to the strong absorption in the 400 nm.

(i). Variation in colour values for the sample containing Hg^{2+} ions

The extracted R, G, B, and HSV values of photographs of the nanoparticle solutions containing different Hg^{2+} metal ion concentrations are provided in Table 6.2.

It is clear from the absorption spectra that with the increase in Hg^{2+} ions concentration, the plasmon peak intensity in the 320-500 nm range decreases linearly (Figure 6.5 B). The sample becomes colourless and transparent at ~ 7.6 ppm of Hg^{2+} ions. Consequently, the percentage of blue component in the reflected light steadily increases and reaches a value of 190, close to the R and G value of pure AgNPs. At the same time, R and G values remain almost unaltered due to the negligible spectral changes above 500 nm (Figure 6.16).

Table 6.2. Variation in RGB and HSV values of photographs of AgNP solutions containing different Hg^{2+} ion concentrations

[Hg^{2+}], ppm	HSV			RGB		
	H($^\circ$)	S(%)	V(%)	R	G	B
0	60	82.0	78.4	200	200	36
0.8	57	63.5	78.4	200	193	73
1.6	56	55.7	78.8	201	194	89
2.2	55	51.0	79.2	202	194	99
3.3	55	40.3	78.8	201	194	120
6.1	54	16.1	78.0	199	196	167
7.6	45	2.1	76.1	194	193	190

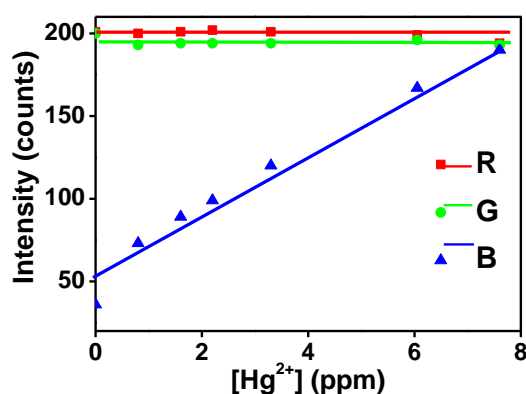


Figure 6.16. Variation in R, G, and B values in nanoparticle's photograph in the presence of varying concentrations of Hg^{2+} .

Also, as the yellow colour fades with increasing Hg^{2+} ion concentration, the corresponding S value decreases (Table 6.2). Thus, the fading of the colour can also be quantified using the S value as it linearly decreases (Figure 6.17 A). Therefore, B

and S are the only parameters varying linearly with Hg^{2+} ion concentration. A plot of this B value against Hg^{2+} ion concentration established a linear relation with an R^2 value of 0.987 (Figure 6.17 A). Thus, the B value at any given concentration of Hg^{2+} ions can be represented by linear equation 6.2. Herein, the Y intercept C_1 is the B value of pure AgNPs. The slope m_1 represents the rate of change of B versus Hg^{2+} ion concentration and is estimated to be ~ 20.13 from Figure 6.17.

$$B=(m_1 \times [\text{Hg}^{2+}]) + C_1 \quad (6.2)$$

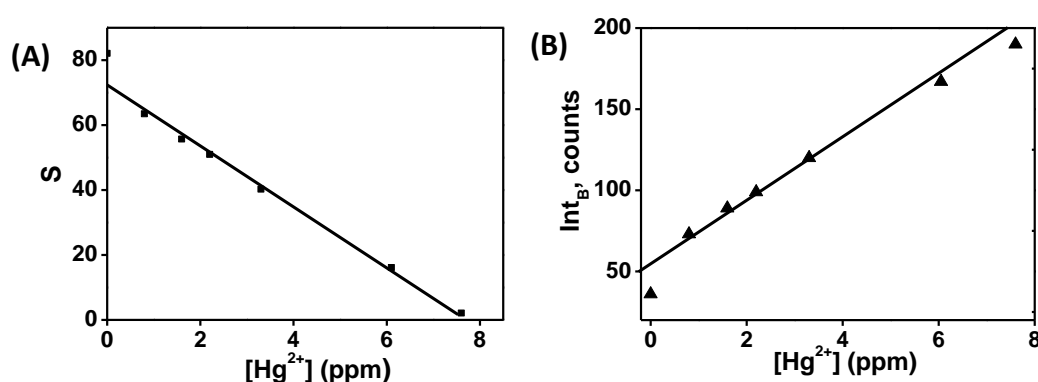


Figure 6.17. Plots showing variation in (A) S value and (B) B value of nanoparticle's photograph in the presence of varying concentrations of Hg^{2+} ions.

(ii). Variation in colour values for sample containing Pb^{2+} ions

The extracted R, G, B, and HSV values of photographs of the nanoparticle's solutions containing Pb^{2+} metal ions at different concentrations are provided in Table 6.3. It is clear that the presence of Pb^{2+} ions altered all the R, G, B colour parameters. Graphical representation of the variation in colour value with increasing Pb^{2+} ion concentration is given in Figure 6.18.

Alteration in all the three colour values are due to the following reasons: (i) A recession in optical density at 400 nm results in a correspondingly intensified value of the blue component in the reflected light and hence the B value. The growth of a new absorption band in the range 500-700 nm diminishes the percentage of both green and

Table 6.3. Variation in RGB and HSV values of photographs of AgNP solutions containing different amounts of Pb^{2+} ions.

[Pb^{2+}] (ppm)	HSV			RGB		
	H (°)	S(%)	V(%)	R	G	B
0	60	70.8	83.1	212	212	62
1.5	45	47.9	85.1	217	191	113
2.9	34	40.5	84.3	215	178	128
4.4	24	33.7	80.4	205	164	136
5.8	22	33.3	80	204	161	136
8.7	15	30.8	77.6	198	152	137

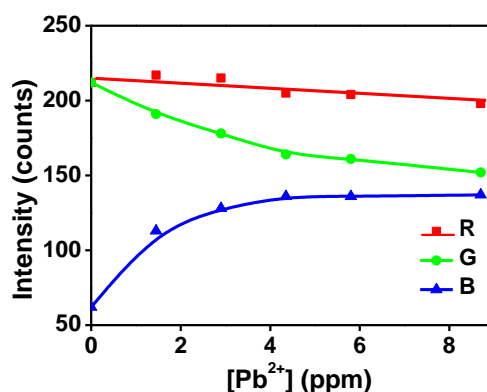


Figure 6.18. Variation in R, G, and B values in nanoparticle's photograph in the presence of varying concentrations of Pb^{2+} .

red components in the reflected light and hence R and G values. Thus, the sum of their values (R+G) will accommodate both these effects. Therefore, plot Pb^{2+} ion concentration vs R+G yielded a linear correlation with R^2 value 0.97 (Figure 6.19 B) and can be represented by equation 6.3. Similarly, the colour variation can also be represented by the H value since its value indicates colour.

$$R+G=(m_2 \times Pb^{2+}) + C_2 \quad (6.3)$$

Herein, the Y intercept C_2 is the R+G value of the pure AgNPs. Also, the slope m_2 is the rate of change of R+G as a function of Pb^{2+} ion concentration. From Figure 6.16 C, its value is extracted to be -8.4. Thus, knowing these parameters and R, G, and B values of the solution containing an analyte of interest, one will be able to quantify

their concentration.

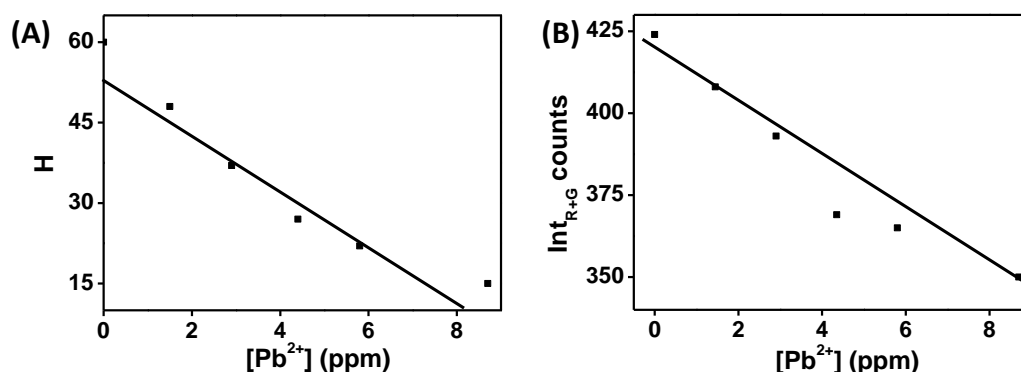


Figure 6.19. (A) Linear variation in H value, and (B) linear variation of $R+G$ value, in nanoparticle's photograph in the presence of varying concentrations of Pb^{2+} .

6.4.6. Android Smart Phone Application Development

To enable smartphone for automatic detection and distinction, these changes in parameters are considered and incorporated into a mobile application using an android development platform. The data flow involved in this process is represented in Figure 6.20 and can be described as follows; (i) the first step involves recording the colour photograph of the pure nanoparticle solution. Subsequently, the user can select the region of interest (ROI), the portion of the picture containing nanoparticles, and the software will automatically estimate its characteristic R_{ref} , G_{ref} , B_{ref} values using equations 6.4, 6.5 and 6.6.

$$R = \frac{\sum_i r}{N} \quad (6.4)$$

$$G = \frac{\sum_i g}{N} \quad (6.5)$$

$$B = \frac{\sum_i b}{N} \quad (6.6)$$

where r , g , b are the red, green and blue intensities of the i^{th} pixel, N is the total number of pixels in the selected region. RGB to HSV conversion is done using an inbuilt function in android, as given below.³⁵

$$\text{Colour.RGBToHSV}(R, G, B, hsv) \quad (6.7)$$

$$\text{val } H = \text{hsv}[0]$$

Primarily, the value of H close to 60° is used to identify the solution as AgNPs, and the extracted values of R , G , B , and HSV will be recorded as the reference. They will also be used to calculate the Y intercepts, C_1 and C_2 . In the next step, the photograph of the solution containing the analyte of the interest can be recorded and define the ROI. The characteristic values of R , G , B , and HSV will be extracted from the ROI in the same way as described above using equations 6.4-6.7. These data are further used for automatic distinction and quantification. As stated before, Hg^{2+} ion induces alteration to only B value while R & G remain negligibly affected. Thus, the condition $B > B_{\text{ref}}$ and $R = R_{\text{ref}}$ and $G = G_{\text{ref}}$ will help to recognize

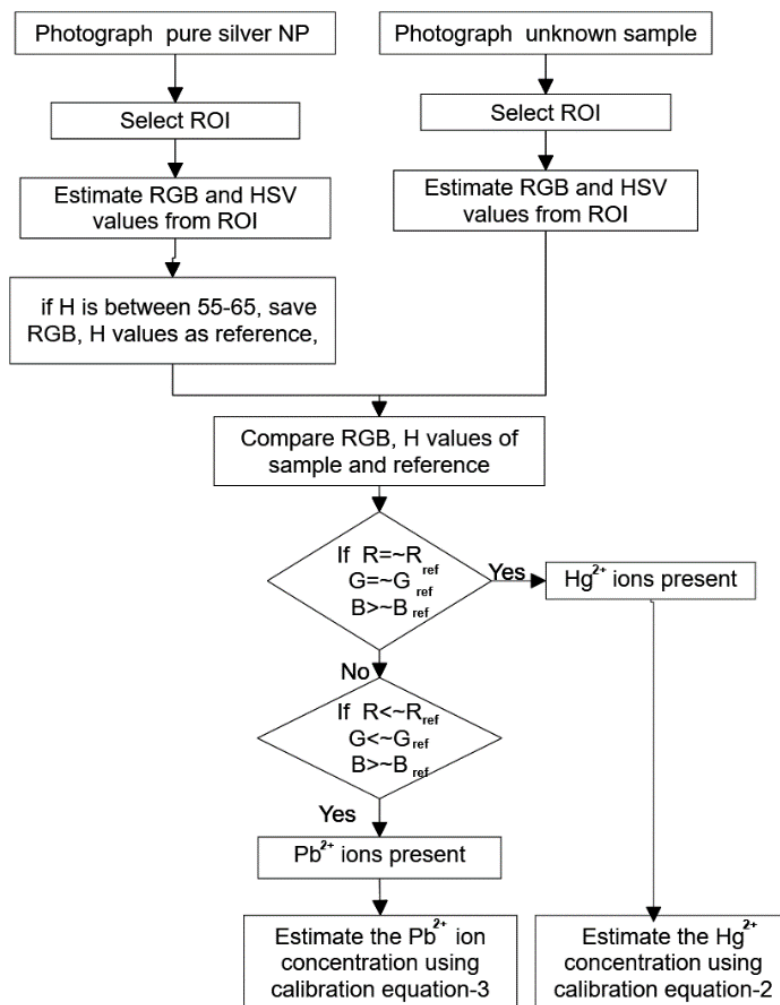


Figure 6.20. Schematic representation of the algorithm developed for metal ion distinction and quantification.

the analyte as Hg^{2+} ions. The android application will report the concentration of the Hg^{2+} ions in the sample by substituting the obtained value of B and C_1 in equation 6.2. On the other hand, the presence of Pb^{2+} ions induces changes to the entire spectral window, a decrease in the band intensity at 400 nm with the concomitant rise of absorption above 500 nm whose intensity as well as wavelength maximum undergoes a steady rise. This resulted in an alteration to all the three R, G, and B values. Thus, the argument $B > B_{\text{ref}}$ along with $G < G_{\text{ref}}$ and $R < R_{\text{ref}}$ can be used to identify the presence of Pb^{2+} ions. From the obtained R+G and C_2 values, the mobile application will automatically quantify Pb^{2+} using equation 6.3. The developed android application was used for determining and quantifying the metal ions from samples. Figure 6.21 shows the GUI of the developed application explaining the user controls. Different steps in operating the android application are illustrated in Figure 6.22.

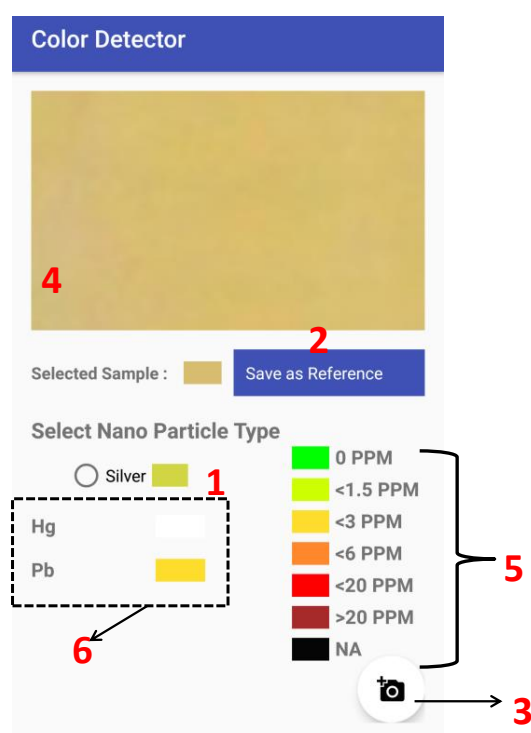


Figure 6.21. Snapshot of the developed android application's GUI showing the user controls marked as 1. colour of the reference sample i.e. pure AgNP already in the database, 2. button for updating the reference, 3.button for loading a new data for analysis 4. colour of the recently selected ROI, 5. panel showing the colour chart based on the concentration for easy interpretation of the results, and 6. panel showing the predicted results.



Figure 6.22. Developed android application screen (i) step 1: loading the reference sample (pure AgNP) data, (ii) step 2: select the ROI from the reference sample's photograph, (iii) step 3: saving the reference sample image into the database, (iv) step 4: updated the reference sample details and load a new sample, (v) step 5: select the ROI, and (vi) step 6: determined and quantified the metal ion present in the sample as lead and quantified as < 3 ppm.

Figure 6.23 represents the comparison of the estimated concentrations of the metal ions through three different modes; (i) absorbance, (ii) manual estimation of RGB values with ImageJ software, and (iii) automatically reported by the mobile application. In general, better concentration prediction accuracy is obtained from absorbance measurement. The R^2 values for concentration estimation through absorption spectral, ImageJ involving manual RGB assessment and mobile application software are respectively 0.995, 0.971 and 0.967. Thus, reasonably good agreement between these independent measurements has been noted.

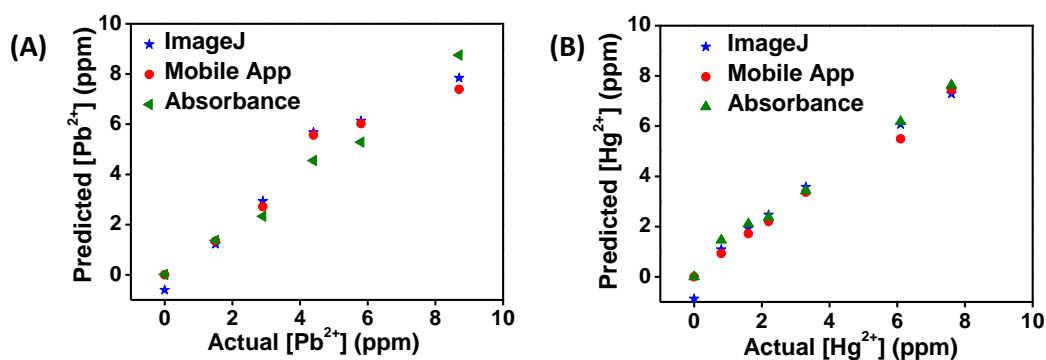


Figure 6.23. Predicted vs actual concentration of (a) Pb^{2+} ions and (b) Hg^{2+} ions using colour values from ImageJ, using the mobile app and from absorbance curve.

6.4.7. Real Sample Analysis

Further, to evaluate the utility of the current methodology for real environmental samples, we attempted to detect mercury from tap water. For that, we have freshly prepared AgNP solution, and the absorption and the colourimetric calibration curve

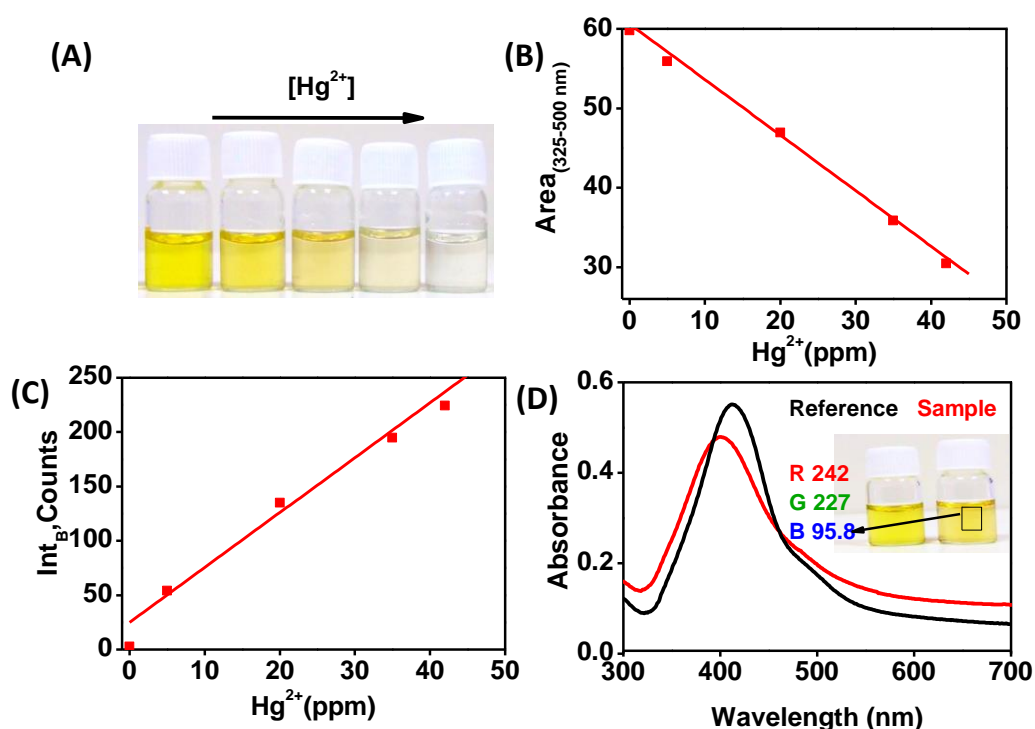


Figure 6.24. Details of calibration data used for quantifying Hg^{2+} ions from tap water (A) colour photograph of the AgNP solutions in the presence of varying concentrations of Hg^{2+} ions (from left to right $[Hg^{2+}] = 0, 2, 26, 35$ and 42 ppm) and corresponding variations in (B) area under the curve 320-500 nm, (C) B values, and (D) absorption spectra of AgNP solutions in the absence and presence tap water spiked with 15 ppm Hg^{2+} ions. Inset shows the corresponding photographs of AgNP solutions.

was prepared as shown in Figure 6.24 B and C. Later, we spiked the tap water available in the laboratory with mercuric chloride such that the final concentration of $[\text{Hg}^{2+}]$ is ~ 15 ppm. The photograph of the real sample, along with the pure AgNP is provided in Figure. 6.24 D. The estimated concentration of Hg^{2+} by smartphone colourimetry and spectral absorption measurements are respectively 14.02 ppm and 13.98 ppm.

6.5. Summary and Future Scope

In conclusion, we demonstrated the potential of the AgNPs synthesized using DHCA for colourimetric detection and discrimination of toxic heavy metal ions in an aqueous medium. The data presented herein evidence that Hg^{2+} and Pb^{2+} ions interact differently with AgNPs causing distinct colour changes. The observed linearity in the absorbance spectral changes of nanoparticle solutions and the RGB values of their photographs opened up possibilities for quantitative estimation of Hg^{2+} and Pb^{2+} ions. We believe that this is possible only due to the ideal match between the spectral regions of metal ion induced absorbance changes and transmissivities of colour filters of the digital camera. Thus, we could diligently combine the specific properties of AgNPs, the characteristic variations in spectral profiles and the technical capabilities of the smartphones for developing an easy methodology for distinction and quantification of toxic metal ions from the aqueous medium. This, together with the wide availability of smartphones and user-friendly mobile applications, can enable the dissemination of the results in terms of point of site analysis. Although, the achieved limit of detection (LOD) with the proposed system is only ~ 0.8 ppm and ~ 1.5 ppm for Hg^{2+} and Pb^{2+} ions, respectively, there still lies further room to enhance the sensitivity. Because parameters such as the concentration of nanoparticles, the surface coverage of the ligand and pH of the medium greatly influence the extent of plasmon

spectral variations. This critically affects the observed sensitivity of the proposed system. However, on the positive side, this leaves further room for improving the LOD through optimizations. Also, herein, the analysis was carried out on photographs taken under normal room light conditions. Equipping the system with a more controlled lighting environment for enhancing the colour contrast would help to improve the sensitivity. It is to be cautioned that the perceived colour and hence the R, G, B values can vary with lighting conditions. This necessitates the need for making calibration curves under each lighting conditions. More studies need to be undertaken to evolve a better strategy that can avoid the effect of room light variations. Thus there exists room to improve the robustness of the proposed system through evolving strategies that minimize the influences of sampling conditions.

6.6. References

1. Clarkson, T. W.; Magos, L.; Myers, G. J., The toxicology of mercury--current exposures and clinical manifestations. *N. Engl. J. Med.* **2003**, *349* (18), 1731-7.
2. Lewis, J. A.; Cohen, S. M., Addressing lead toxicity: complexation of lead(II) with thiopyrone and hydroxypyridinethione O,S mixed chelators. *Inorg. Chem.* **2004**, *43* (21), 6534-6.
3. Gautam, R.; Sharma, S.; Mahiya, S.; Chattopadhyaya, M., *Heavy Metals In Water : Presence, Removal and Safety*. 1st ed.; Royal Society of Chemistry: 2014.
4. Landrigan, P.; Fuller, R.; J R Acosta, N.; Adeyi, O.; Arnold, R.; Nil) Basu, N.; Bibi Baldé, A.; Bertollini, R.; Bose-O'Reilly, S.; Ivey Boufford, J.; N Breyse, P.; Chiles, T.; Mahidol, C.; M Coll-Seck, A.; L Cropper, M.; Fobil, J.; Fuster, V.; Greenstone, M.; Haines, A.; Zhong, M., The Lancet Commission on pollution and health. *Lancet* **2017**, *391*, 462-512.
5. Joselow, M. M., Environmental negligence: the mercury problem. *Am. J. Public Health* **1971**, *61* (9), 1745-1747.
6. Bellinger, D. C.; Bellinger, A. M., Childhood lead poisoning: the torturous path from science to policy. *J. Clin. Invest.* **2006**, *116* (4), 853-857.
7. Narin, İ.; Soylak, M.; Elçi, L.; Doğan, M., Determination of trace metal ions by

- AAS in natural water samples after preconcentration of pyrocatechol violet complexes on an activated carbon column. *Talanta* **2000**, 52 (6), 1041-1046.
8. Lafaye, A.; Junot, C.; Gall, B. R.-L.; Fritsch, P.; Tabet, J.-C.; Ezan, E., Metabolite profiling in rat urine by liquid chromatography/electrospray ion trap mass spectrometry. Application to the study of heavy metal toxicity. *Rapid Commun. Mass Spectrom.* **2003**, 17 (22), 2541-2549.
 9. Dragoie, D.; Spataru, N.; Kawasaki, R.; Manivannan, A.; Spataru, T.; Tryk, D.; Fujishima, A., Detection of trace levels of Pb²⁺ in tap water at boron-doped diamond electrodes with anodic stripping voltammetry. *Electrochim. Acta* **2006**, 51, 2437-2441.
 10. Antler, M.; Maxwell, E. J.; Duford, D. A.; Salin, E. D., Online Standard Additions Calibration of Transient Signals for Inductively Coupled Plasma Mass Spectrometry. *Anal. Chem.* **2007**, 79 (2), 688-694.
 11. Bansod, B.; Kumar, T.; Thakur, R.; Rana, S.; Singh, I., A review on various electrochemical techniques for heavy metal ions detection with different sensing platforms. *Biosens. Bioelectron.* **2017**, 94, 443-455.
 12. Ozcan, A., Mobile phones democratize and cultivate next-generation imaging, diagnostics and measurement tools. *Lab Chip* **2014**, 14 (17), 3187-3194.
 13. Kim, S. D.; Koo, Y.; Yun, Y., A Smartphone-Based Automatic Measurement Method for Colorimetric pH Detection Using a Color Adaptation Algorithm. *Sensors* **2017**, 17 (7), 1604.
 14. Edwards, P.; Zhang, C.; Zhang, B.; Hong, X.; Nagarajan, V. K.; Yu, B.; Liu, Z., Smartphone based optical spectrometer for diffusive reflectance spectroscopic measurement of hemoglobin. *Scientific Reports* **2017**, 7 (1), 12224.
 15. Bayram, A.; Horzum, N.; Metin, A. U.; Kılıç, V.; Solmaz, M. E., Colorimetric Bisphenol-A Detection With a Portable Smartphone-Based Spectrometer. *IEEE Sensors Journal* **2018**, 18 (14), 5948-5955.
 16. Rong, Z.; Wang, Q.; Sun, N.; Jia, X.; Wang, K.; Xiao, R.; Wang, S., Smartphone-based fluorescent lateral flow immunoassay platform for highly sensitive point-of-care detection of Zika virus nonstructural protein 1. *Anal. Chim. Acta* **2019**, 1055, 140-147.
 17. Karami, P.; Khoshsafar, H.; Johari-Ahar, M.; Arduini, F.; Afkhami, A.; Bagheri, H., Colorimetric immunosensor for determination of prostate specific antigen using surface plasmon resonance band of colloidal triangular shape gold

- nanoparticles. *Spectrochim. Acta A Mol. Biomol. Spectrosc.* **2019**, *222*, 117218.
18. Bothra, S.; Upadhyay, Y.; Kumar, R.; Sahoo, S. K., Applications of vitamin B6 cofactor pyridoxal 5'-phosphate and pyridoxal 5'-phosphate crowned gold nanoparticles for optical sensing of metal ions. *Spectrochim. Acta A Mol. Biomol. Spectrosc.* **2017**, *174*, 1-6.
 19. Bothra, S.; Solanki, J. N.; Sahoo, S. K.; Callan, J. F., Anion-driven selective colorimetric detection of Hg^{2+} and Fe^{3+} using functionalized silver nanoparticles. *RSC Adv.* **2014**, *4* (3), 1341-1346.
 20. Bothra, S.; Kumar, R.; Sahoo, S. K., Pyridoxal conjugated gold nanoparticles for distinct colorimetric detection of chromium(iii) and iodide ions in biological and environmental fluids. *New J. Chem.* **2017**, *41* (15), 7339-7346.
 21. Bothra, S.; Kumar, R.; Sahoo, S. K., Pyridoxal derivative functionalized gold nanoparticles for colorimetric determination of zinc(ii) and aluminium(iii). *RSC Adv.* **2015**, *5* (118), 97690-97695.
 22. Bothra, S.; Kumar, R.; Pati, R. K.; Kuwar, A.; Choi, H.-J.; Sahoo, S. K., Virgin silver nanoparticles as colorimetric nanoprobe for simultaneous detection of iodide and bromide ion in aqueous medium. *Spectrochim. Acta A Mol. Biomol. Spectrosc.* **2015**, *149*, 122-126.
 23. Upadhyay, Y.; Bothra, S.; Kumar, R.; Sahoo, S. K., Smartphone-assisted colorimetric detection of Cr^{3+} using vitamin B6 cofactor functionalized gold nanoparticles and its applications in real sample analyses. *ChemistrySelect* **2018**, *3* (24), 6892-6896.
 24. Upadhyay, Y.; Anand, T.; Babu, L. T.; Paira, P.; Kumar Sk, A.; Kumar, R.; Sahoo, S. K., Combined use of spectrophotometer and smartphone for the optical detection of Fe^{3+} using a vitamin B6 cofactor conjugated pyrene derivative and its application in live cells imaging. *J. Photochem. Photobiol. A* **2018**, *361*, 34-40.
 25. Anand, T.; Sahoo, S. K., Cost-effective approach to detect $\text{Cu}(\text{ii})$ and $\text{Hg}(\text{ii})$ by integrating a smartphone with the colorimetric response from a NBD-benzimidazole based dyad. *Phys. Chem. Chem. Phys.* **2019**, *21* (22), 11839-11845.
 26. Karthiga, D.; Anthony, S. P., Selective colorimetric sensing of toxic metal cations by green synthesized silver nanoparticles over a wide pH range. *RSC Adv.* **2013**, *3* (37), 16765-16774.

27. Du, S.; Luo, Y.; Liao, Z.; Zhang, W.; Li, X.; Liang, T.; Zuo, F.; Ding, K., New insights into the formation mechanism of gold nanoparticles using dopamine as a reducing agent. *J. Colloid Interface Sci.* **2018**, *523*, 27-34.
28. Bhattacharjee, Y.; Chakraborty, A., Label-free cysteamine-capped silver nanoparticle-based colorimetric assay for Hg(II) detection in water with subnanomolar exactitude. *ACS Sustain. Chem. Eng.* **2014**, *2* (9), 2149-2154.
29. Ma, Y.-r.; Niu, H.-y.; Zhang, X.-l.; Cai, Y.-q., Colorimetric detection of copper ions in tap water during the synthesis of silver/dopamine nanoparticles. *Chem. Commun.* **2011**, *47* (47), 12643-12645.
30. Ravi, S. S.; Christena, L. R.; SaiSubramanian, N.; Anthony, S. P., Green synthesized silver nanoparticles for selective colorimetric sensing of Hg²⁺ in aqueous solution at wide pH range. *Analyst* **2013**, *138* (15), 4370-4377.
31. Cassar, R. N.; Graham, D.; Larmour, I.; Wark, A. W.; Faulds, K., Synthesis of size tunable monodispersed silver nanoparticles and the effect of size on SERS enhancement. *Vib. Spectrosc.* **2014**, *71*, 41-46.
32. Levard, C.; Mitra, S.; Yang, T.; Jew, A. D.; Badireddy, A. R.; Lowry, G. V.; Brown, G. E., Effect of chloride on the dissolution rate of silver nanoparticles and toxicity to e. Coli. *Environ. Sci. Technol.* **2013**, *47* (11), 5738-5745.
33. Peterson, K. I.; Lipnick, M. E.; Mejia, L. A.; Pullman, D. P., Temperature dependence and mechanism of chloride-induced aggregation of silver nanoparticles. *J. Phys. Chem. C* **2016**, *120* (40), 23268-23275.
34. Poynton, C. A. In *A Guided Tour of Colour Space*, New Foundation for Video Technology: The SMPTE Advanced Television and Electronic Imaging Conference, San Francisco, USA, Feb 11; San Francisco, USA, 1995; pp 167-180.
35. Devolepers, A. Camera API.
<https://developer.android.com/guide/topics/media/camera>
(accessed 22/01/2019).

List of Publications from Thesis

1. **Emmanuel, N.**; Nair, R. B.; Abraham, B.; Yoosaf, K., Fabricating a Low-Cost Raman Spectrometer to Introduce Students to Spectroscopy Basics and Applied Instrument Design. *J. Chem. Educ.* **2021**, **98(6)**, 2109-2116
2. **Emmanuel, N.**; Haridas, R.; Chelakkara, S.; Nair, R. B.; Gopi, A.; Sajitha, M.; Yoosaf, K., Smartphone assisted colourimetric detection and quantification of Pb²⁺ and Hg²⁺ ions using Ag nanoparticles from aqueous medium. *IEEE Sens. J.* **2020**, **20** (15), 8512-8519.
3. **Emmanuel, N.**; Elizabeth J*; Yoosaf, K*., Raman Spectroscopy Based Chemometric method for the Detection and Quantification of Aceclofenac from Combinational Tablets [Manuscript under submission].

Copyrights

1. **Emmanuel, N.**, Yoosaf, K; Software for automatic detection and quantification of API content from Pharmaceutical products, (Submitted)
2. **Emmanuel, N.**, Yoosaf, K., Android mobile application for colourimetric detection of metal ions from aqueous media (Submitted)

List of Publications from Other Related Work

1. Chelakkara,S.; **Emmanuel, N.**; Yoosaf, K*, Estimation of coconut oil adulteration through multivariate analysis of Raman spectrum (Manuscript under preparation).
2. Bini A; **Emmanuel, N.**; Yoosaf, K*, Development of surface-enhanced Raman spectroscopic substrate and machine learning tools for lung cancer studies; (Manuscript under preparation).

Patent

1. Yoosaf, K; Nair, R. B; **Emmanuel, N.**; A Photometric system and methodology for easy Detection and Quantification of components from binary mixtures (Submitted).

List of Posters and Oral Presentations at Conferences

1. Enabling Smartphones for the Colorimetric Detection of Toxic Metal Ions, Oral presentation at *National seminar on neoteric advances in chemical sciences-2018* Kerala University, October 12th 2018.
2. Fast Determination of API content from Bulk Pharmaceutical tablets using Raman spectroscopy, Poster presented at *15th JNC Research conference on Chemistry of Materials*-September 30-Oct 2 2019, Vivanta by Taj, Kovalam.
3. Smartphone Enabled Colorimetric Detection of Toxic Metal Ions from Aqueous Medium, Poster presentation at *14th International conference on ecomaterials*, CSIR-NIIST, Trivandrum, February 5-7 2020.
4. Smartphone Enabled Colorimetric Detection of Toxic Metal Ions from Aqueous Medium, Flash talk at *14th International conference on ecomaterials*, CSIR-NIIST, Trivandrum, February 5-7 2020.
5. Recent Advances in Raman spectroscopy and its applications in food and pharmaceutical Industry- Invited talk at *Webinar series on Photonics research*, June 12th 2020, Electronics department, Govt. Model Engineering college.

Fabricating a Low-Cost Raman Spectrometer to Introduce Students to Spectroscopy Basics and Applied Instrument Design

Neethu Emmanuel, Raji B Nair, Bini Abraham, and Karuvath Yoosaf*



Cite This: <https://doi.org/10.1021/acs.jchemeduc.0c01028>



Read Online

ACCESS |



Metrics & More



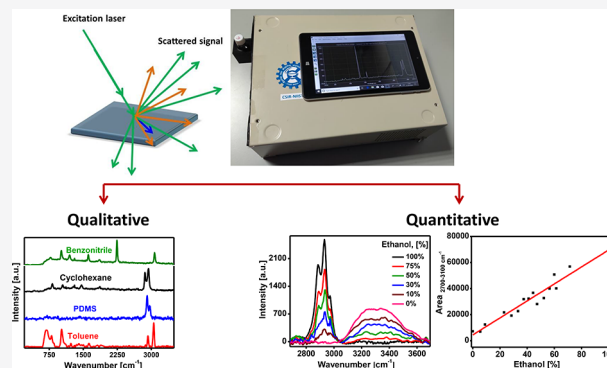
Article Recommendations



Supporting Information

ABSTRACT: Raman spectroscopy has become a popular analytical tool because of its ability to probe nondestructively and provide fingerprint information about materials. The advancements in the field of Raman spectroscopy and the expanding scope of applications warrant the introduction of the topic in the formal education curriculum. The introduction of Raman spectroscopy analysis in the educational curriculum helps the students learn the spectroscopy basics. Furthermore, component-wise familiarization and fabrication training will help the students to evolve their own methodologies to fabricate and customize the instrument for specific applications. Though many Raman spectrometers are commercially available, the high cost makes it unaffordable for most academic institutions. Herein, we describe an easy and cost-effective method to make a fully integrated portable Raman spectrometer and explain a few simple experiments which can be conducted at the classroom level using the fabricated device.

KEYWORDS: Graduate Education/Research, Analytical Chemistry, Demonstrations, Physical Chemistry, Laboratory Equipment/Apparatus, Qualitative Analysis, Quantitative Analysis, Raman Spectroscopy, Spectroscopy



INTRODUCTION

Raman spectroscopy (RS), based on the concept of inelastic scattering invented by C.V. Raman,¹ provides fingerprint vibrational information and serves as a nondestructive technique for the reliable identification of substances. In contrast with absorption-based IR spectroscopy, RS relies on scattering, offering considerable flexibility to both instrumental designs and sample handling. With the advent of new generation lasers and optical components, Raman spectra can currently be acquired even with handheld and battery-operable systems, which have elevated their potential for onsite and point of care applications. Due to minimal interference from water, RS is suitable for studying biological samples even in their native state. RS has evolved as a preferable analytical tool in numerous areas like medical diagnosis,^{2,3} pharmaceutical and food industries,^{4,5} environmental quality testing,⁶ forensics,⁷ homeland security,⁸ anticounterfeiting,⁹ archeology,¹⁰ geology,¹¹ gemstone purity checking,^{12,13} etc., surpassing the limitations of other spectroscopic techniques. This has necessitated introducing RS as an important spectroscopic technique in the formal education curriculum. RS could be introduced to undergraduate students for enhancing their fundamental understanding of spectroscopic techniques through representative examples with various objectives. For example, combining computational chemistry with vibrational spectroscopy experiments is useful for imparting the concepts

of symmetry, polarizability, and selection rules.^{14,15} In the field of practical analytical chemistry, Raman spectrometers are introduced for material identification, mixture analysis,¹⁶ and quantification.¹⁷ In biochemistry, RS helps to characterize cell membranes¹⁸ and demonstrate the potential of multivariate tools for estimating the biomolecular concentrations from complex mixtures.¹⁹ In the emerging fields of nanoscience and nanotechnology,^{20,21} students can characterize and estimate purity and the number of layers of laboratory prepared 2D nanomaterials like graphenes.²² Laboratory experiments can be conducted to teach the concept of surface enhanced Raman spectroscopy (SERS), calculate the enhancement factors, study influences of nanomaterial size and shape,^{20,23} and demonstrate the practical utility of SERS to trace level analyte detection,²⁴ colorants in precious artworks,²⁵ etc. These teaching experiments are augmented by the availability of cost-effective Raman spectrometers at educational institutions easily accessible to students. In addition, knowing the working principles of the instrument and functionalities of each of the

Received: August 5, 2020

Revised: April 11, 2021

Table 1. Synopsis of Significant Contributions in the Literature for Cost-Effective Solutions for Raman Spectrometers

literature source	laser used	probe optics used	detector used	approximate cost, \$U.S.
Gallow et al. ^a	nitrogen laser: 337.2 nm	90°	PMT-based monochromator	not available
Sutherland et al. ^b	He–Ne laser: 9 mW	direct mode	APD-based monochromator	not available
Fitzwater et al. ^c	He–Ne laser: 632.8 nm, 10 mW	90°	PMT-based monochromator	20,000
Bandyopadhyay et al. ^d	argon laser: 514.5 nm, 4 W	backscattering configuration with small-sized mirror as the beam splitter and notch filter	PMT-based monochromator	not available
DeGraff et al. ^e	532 nm, 10 mW	90° probe with notch filter	Ocean Optics S2000	5000
Young et al. ^f	green laser pointer: 532 nm, ~20 mW	backscattering 200 μm core reflection fiber-optic probe and notch filter	Ocean Optics SD2000	3700
Johnson et al. ^g	532 nm, 20 mW	~45° probe optics, notch filter	Ocean Optics HR2000	6500
Mohr et al. ^h	laser pointer: 532 nm, 4 mW	backscattering with a small mirror beam splitter, notch filter	CCD array detector	5000
Somerville et al. ⁱ	laser pointer: 532 nm, 5 mW; He–Ne laser: 633 nm, 30 mW	90° and backscattering, edge filter	Ocean Optics HR4000	3000
Rossi et al. ^j	laser pointer: 532 nm, < 100 mW	transmission mode with Raman edge filter	digital camera 3D printed case	3000
present work	laser pointer: 532 nm	backscattering probe, colored glass long-pass filter	Science Surplus	700 ^k
present work	Thorlabs DJ532–40: 532 nm, ~40 mW	backscattering probe, colored glass long-pass filter	Science-Surplus	970 ^k
present work	laser pointer: 532 nm	backscattering probe, colored glass long-pass filter	home-built spectrometer	940 ^k
present work	laser pointer: 532 nm	backscattering probe, colored glass long pass filter	Ocean Optics USB4000	4000 ^k
present work	laser pointer: 532 nm	backscattering probe, colored glass long-pass filter	Thunder Optics	700 ^k
present work	laser pointer: 532 nm	backscattering probe, colored glass long-pass filter	Thorlabs CCS100	2700 ^k

^aSee ref 26. ^bSee ref 27. ^cSee ref 28. ^dSee ref 29. ^eSee ref 30. ^fSee ref 31. ^gSee ref 32. ^hSee ref 33. ⁱSee ref 34. ^jSee ref 35. ^kSee the Supporting Information for more detail on costs.

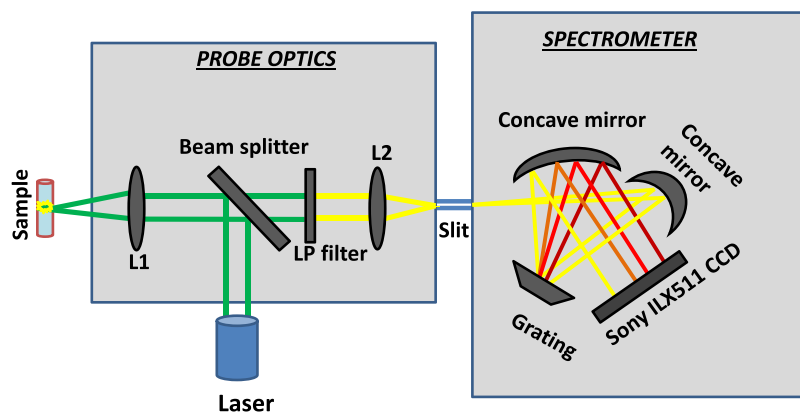


Figure 1. Schematic layout of the portable Raman spectrometer.

components will help the students evolve their own methodologies to fabricate and customize for specific applications.

Commercially available Raman spectrometers cost a minimum of \$12,000 U.S. and are thus unaffordable by most schools and colleges. There have been several efforts to provide cost-effective solutions for RS, and significant contributions are listed in Table 1. Most of these demonstrated configurations provide flexibility in connecting collection optics via optical fiber with any commercial detectors available in the educational institutes. On the other hand, the free-space coupling of the output of the collection optics to the detector may avoid fiber coupling and transmission losses, allowing the detection of less intense signals yielding improved sensitivity. A fully integrated and battery-operable system will also be handier and easy to carry to the point of requirement. Primarily, the availability of such systems will help teaching theory along with

the parallel demonstration of analytical concepts. Herein, we outline a detailed method of constructing a fully integrated and cost-effective portable Raman spectrometer. Furthermore, we describe the functions of different components and how their technical specification can influence the acquired data.

EXPERIMENTAL SECTION

Optical Configuration

Figure 1 displays the adopted optical layout of the device. Herein, we used a JD-851 green laser pointer as the excitation source, probe optics with backscattering configuration, and a Science-Surplus spectrometer as the detector. A power bank (portable mobile charger) is used to supply power for both the laser diode and the spectrograph. The spectral acquisition and display are made on an 8-in. tablet with Windows OS. A

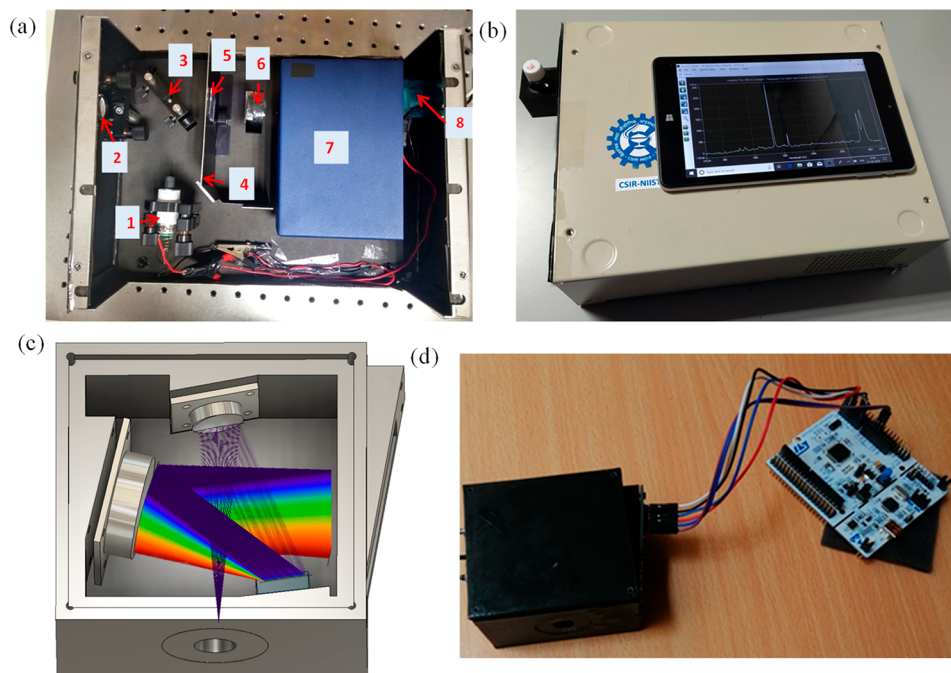


Figure 2. Photographs showing (a) internal components: (1) laser diode, (2) focusing lens, (3) beam splitter, (4) plate to block ambient light and reflected laser entering detector unit, (5) long-pass filter, (6) focusing lens, (7) spectrometer, and (8) RS232 to USB converter to communicate with a Windows tablet. (b) External view of the device showing the 3D printed sample holder and the Windows tablet for spectral acquisition and display, (c) 3D design of the spectrometer, and (d) in-house fabricated spectrometer along with STM32 Nucleo board.

detailed component-wise description and fabrication procedure are explained in the following sections.

Excitation Source

The excitation source's technical specifications, such as wavelength, line width (monochromaticity), optical power, etc., are crucial for obtaining good quality Raman spectra. Typically, the Raman spectrum appears ~ 10 – 200 nm above (Stokes) and below (anti-Stokes) the excitation wavelength. The Raman scattering efficiency varies inversely to the fourth power of the excitation wavelength.³⁶ Thus, lasers with lower excitation wavelength (UV and visible) produce a better Raman signal than the IR light sources. We have used a low-cost and readily available green (~ 532 nm) laser pointer JD-851, a diode pumped solid state laser (DPSS), as the excitation source. The inbuilt Nd:YAG and KTP crystals convert the laser diode's primary emission wavelength, 808 nm, first to 1064 nm and then to 532 nm. Favorably, the laser pointers come with the necessary electronic driver circuit, passive heat dissipater, and collimator lens assembly (see [Supporting Information](#)), eliminating the need for additional components. The laser beam diameter is ~ 2.5 mm, and optical output power is ~ 70 mW, which is sufficient to produce an easily detectable amount of Raman scattered photons. The measured spectral profile indicated that the central wavelength and FWHM are 531.8 nm and ~ 0.78 nm, respectively (see [Supporting Information](#)). From this, the minimum achievable Raman spectral resolution is estimated to be in the range of 20 – 28 cm^{-1} . Corresponding to a 300 – 3000 cm^{-1} Raman shift, the Stokes lines will fall in the range of 540 – 630 nm, and typical silicon detectors exhibit the highest efficiency in this range.³⁷ All these factors contribute to the easy detection of Raman scattered photons with a low-cost CCD detector. Alternatively, one can use commercially available laser diodes like Thorlabs DJ532-40, which also works based on the same principle.

The presence of additional diminished intensity 808 nm lines in the emission profile, generated from the diode within the laser, does not influence the measurement due to the following reasons:

- (i) Its intensity is almost 25 times weaker than the 532 nm.
- (ii) Compared to 532 nm, the 808 nm emission is red-shifted by 276 nm and thus 100 times weaker scattering cross-section.
- (iii) Its Stokes lines appear beyond the sensitive region of the spectrometer.
- (iv) Its anti-Stokes lines appear in the wavelength range 650 – 795 nm, beyond the region of interest.

Probe Optics

The major preferred configurations for probe optics are transmission, 90° , backscattered, and spatially offset. The third is the simplest as it is easy to set up with minimum components and alignment. The primary considerations are to (i) maximize the collection efficiency of the weak Raman radiation and (ii) block the intense Rayleigh radiation from entering into the detection unit. These goals are achieved through focusing lenses, a beam splitter, and a long-pass filter. The collimated light from the laser diode is directed to the sample through a beam splitter and a focusing lens (L1). The purpose of the beam splitter is to separate the excitation light path from the collection path. Instead of specifically designed beam splitters, we used a square cut piece of a microscopic slide (25 mm \times 25 mm \times 1 mm), which, when kept at 45° to the excitation light path, yielded a reflection/transmission ratio of $30:70$ (see [Supporting Information](#)). The backscattered radiation is collected by the same lens (L1), and a portion of this beam directly passes through the beam splitter and is focused on the entrance slit of the spectrophotometer by the second focusing lens (L2). Rayleigh scattered light was blocked

using a long-pass filter with a cutoff wavelength at 550 nm kept in between the beam splitter and L2 lens (see [Supporting Information](#))

Detector

The detector used is a Science-Surplus make having a spectral range of $\sim 450\text{--}700$ nm. However, the present design does not restrict readers from using any other commercially available (e.g., Ocean Optics, Research India, Thunder Optics, etc.) or in-house fabricated spectrometers. The Science-Surplus spectrometer essentially consists of a $50\ \mu\text{m}$ entrance slit, concave mirrors as focusing elements, an 1800 lines/mm diffraction grating, and a Sony ILX511 linear silicon CCD detector. The spectrometer has a resolution of ~ 1 nm, restricting the maximum achievable Raman spectral resolution to $\sim 35\ \text{cm}^{-1}$ at $100\ \text{cm}^{-1}$ and $\sim 25\ \text{cm}^{-1}$ at $3000\ \text{cm}^{-1}$ for a 532 nm excitation. The spectrometer was precalibrated in the factory, and the software module has an inbuilt function for recording the spectra in Raman shift mode. Alternatively, the spectrometer can be calibrated individually, and the detailed procedure is provided in the [Supporting Information](#); however, there was hardly any difference.

As an alternative to the commercial spectrometer, we also attempted the feasibility of building a home-built spectrometer for detecting the Raman signal. Kovarik et al. provides a detailed review of different student-built spectrophotometers.³⁸ Herein, we designed and implemented a dispersive spectrometer in Czerny-Turner configuration using the following components:

- (i) $50\ \mu\text{m}$ entrance slit
- (ii) 1200 lines/mm plane-ruled diffraction grating
- (iii) Two concave mirrors, each with 50 mm focal length
- (iv) Toshiba TCD1304 linear CCD
- (v) home-built CCD driver
- (vi) ST Microelectronics Nucleo-F401RE microcontroller

Firmware and the GUI for data acquisition were adopted from Esben Rossel's work.³⁹ The optical configuration was first optimized on an optical breadboard and then translated into a 3D printed enclosure ([Figure 2C](#) and [D](#); see [Supporting Information](#) for more details).

Elimination of Noises

The prominent noises that interfere with the Raman spectrum are (i) high-frequency noises contributed by electronic circuitry and dark current from the detector and (ii) low-frequency noises from fluorescence and stray light. The effect of the former is minimizable by subtracting a blank spectrum (taken with laser off) from the sample spectrum and of the latter through baseline correction using the moving point average algorithm proposed by Krishna et al.⁴⁰

HAZARDS

The laser is a potential hazard if not properly handled; especially, the 70 mW laser is deeply in the class 3B category. It can cause immediate and irreversible eye damage and skin burning due to the localized heat produced.^{41,42} Directly looking into the laser or from reflected surfaces is to be avoided. It is advisable to remove ornaments such as rings, bangles, watches, etc., which may cause unexpected light reflections. Proper safety procedures such as wearing laser goggles (example LOTG-DYE2/CM Newport, OD ~ 4 at $450\text{--}585$ nm) need to be followed while operating the device. For the alignment, one of the following strategies are

recommended: (i) place a neutral density filter (optical density 2) in front of the laser source, (ii) wear safety goggles having an optical density of 2–3 at 532 nm (e.g., Thorlabs LG14), or (iii) use safety goggles having an optical density of 4 (e.g., LOTG-DYE2/CM, Newport) and follow the beam path using a paper coated with fluorescent material such as rhodamine. Do not allow other personnel to enter the room during the rough stages of alignment. Keep proper beam blocks in place around the instrument, which would protect persons from stray reflections. Gloves and splash goggles should be worn while working with chemicals. Volatile chemicals should be analyzed in capped glass containers. When demonstrating in classrooms, specifically designed sample holders (preferably black colored) should always be used, which confines radiation inside and minimizes reflections. While connecting the electrical cables, always wear gloves. Care must be taken to avoid short-circuiting, overheating, etc.

RESULTS AND DISCUSSION

[Figure 2](#) represents the photographs of the fabricated Raman spectrometer and the home-built detector. The designed mechanical layout, procedures for component integration, and optimization of alignment are detailed in the [Supporting Information](#).

Sample Analysis

Validation of the fabricated device was carried out by analyzing various standard samples and comparing the data with those recorded using a commercial confocal Raman microscope (Model: WITec Alpha300R, M/s WITec Inc. Germany, see [Supporting Information](#) for detailed specifications). As an example, [Figure 3](#) represents the Raman spectrum of various chemicals such as benzonitrile, cyclohexane, polydimethylsiloxane (PDMS), and toluene taken using the fabricated system (see [Supporting Information](#) for data taken using the commercial system). The observed peak positions are

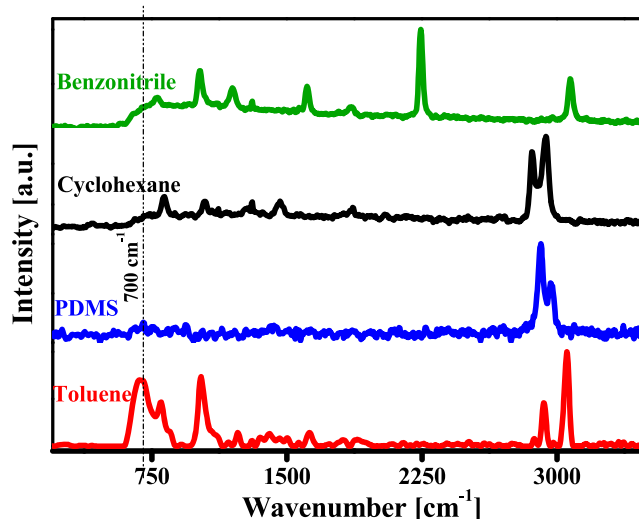


Figure 3. Raman spectra of benzonitrile, cyclohexane, PDMS, and toluene obtained using the fabricated portable system with 10 mW laser power and 5 s integration time. All the spectra are normalized along the y axis. The vertical dotted lines represent the lower cutoff region ($700\ \text{cm}^{-1}$) for the fabricated system imposed by the 550 nm long-pass filter.

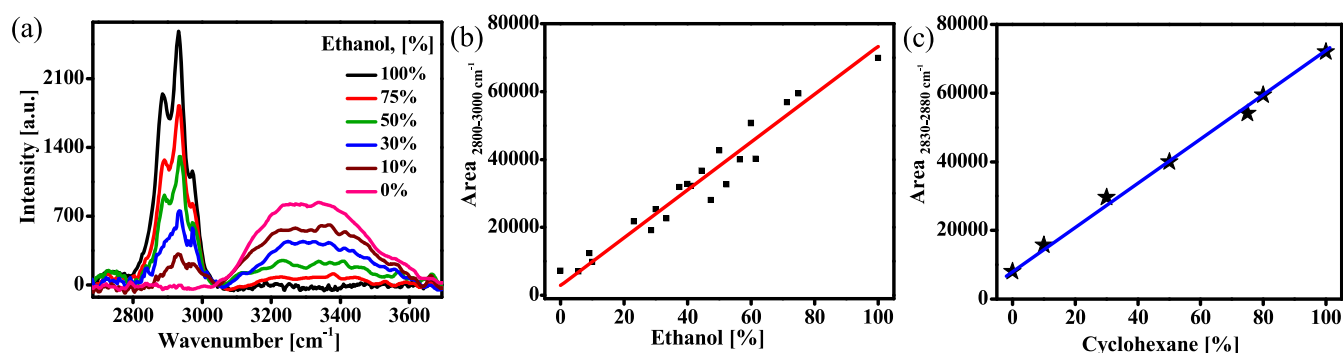


Figure 4. (a) Raman spectra in the range 2700–3700 cm⁻¹ of ethanol–water mixtures of varying compositions collected using the device with 10 mW laser power and 5 s integration time. The spectra were averaged over three accumulations and baseline corrected using a moving point average method.⁴⁰ (b) Variation in integrated peak intensity in the range 2800–3000 cm⁻¹ vs ethanol concentration and (c) variation in integrated peak intensity in the range 2830–2880 cm⁻¹ vs cyclohexane concentration for cyclohexane–toluene mixtures.

tabulated in the [Supporting Information](#) and were assigned to specific bond vibrations from literature references.^{43–46}

In general, for all the compounds investigated, we found good agreements between data obtained from the fabricated device and commercial system in terms of spectral band position and relative intensities. For example, the dominant peaks observed with the fabricated spectrometer system for benzonitrile were 1014 cm⁻¹, 1612 cm⁻¹, 2243 cm⁻¹, and 3075 cm⁻¹ arising from the C–C stretch/ring breath, C=C stretch, C–N stretch, and C–H stretch vibrations, respectively. Our spectrometer's lower spectral acquisition limit is ~ 700 cm⁻¹ because we have employed a 550 nm long-pass filter. The other apparent difference was with the spectral resolution. Very close peaks (751.3 cm⁻¹ and 767.1 cm⁻¹, 1007 cm⁻¹ and 1026.6 cm⁻¹, and 1177.7 cm⁻¹ and 1192.6 cm⁻¹) whose separation was less than 30 cm⁻¹ appeared as single peaks in the Raman spectrum acquired with the currently fabricated system. This is mainly limited by the FWHM of the laser and the resolution of the spectrometer, which resulted in minor variation in the spectral band position with respect to the reported values, see [Supporting Information](#). The other factors contributing to this could be inaccuracies in determining the exact wavelength of the excitation source.

Chemical Mixture Analysis

As the obtained Raman spectral intensities are functions of excitation power, scattering cross-section of the sample, and the material's concentration in the sample, the technique can be used for quantitative analysis. In effect, the observed Raman spectrum will be the algebraic sum of the individual components' contributions. To illustrate the current system's potential for mixture analysis, we studied two model systems: (i) ethanol blended with water and (ii) a cyclohexane–toluene mixture. For the ethanol–water combination, 16 mixtures were created in the concentration range 0–100 volume percentage, and the acquired spectra after baseline correction are presented in [Figure 4a](#). The characteristic Raman peaks for water due to OH stretching appeared in the range 3100–3600 cm⁻¹, while CH₃–CH₂ stretching of ethanol peaked in the range ~2800–3000 cm⁻¹.⁴⁷ The analysis of the data revealed a linear variation in the integrated peak intensities against ethanol concentration. [Figure 4b](#) shows the plot of integrated peak intensity (area under the peak) in the range 2800–3000 cm⁻¹ against the ethanol volume percentage. The linear fit ($y = mx + c$) of this graph yielded a correlation coefficient R^2 value of 0.97. Instead of peak area, one could also employ the peak

intensity for generating a calibration graph; however, there will be a diminished correlation with concentration, as shown in the [Supporting Information](#). In 2001, Sanford et al. attempted to quantify ethanol from alcoholic beverages using a modular Raman system composed of an argon ion laser as the excitation source and Ocean Optics S-2000 CCD detector.¹⁷ Their design also involves using two additional parabolic mirrors, the first one to reflect the transmitted laser light to the sample, thereby increasing the Raman scattering efficiency, and the second to reflect any backscattered signal to the collection optics. As a result, they have obtained a very good R^2 value of 0.9978 for the calibration graph, and the estimated detection limit was 1%.

Similar results obtained for cyclohexane–toluene mixtures are shown in the [Supporting Information](#). The integrated peak intensity in the range 2830–2880 cm⁻¹ (CH₂ stretching of cyclohexane) varied linearly with changes in the composition of mixtures. The R^2 value of the linear fit was estimated to be 0.99.

Effect of Laser Power

We studied the effect of excitation power to identify the minimum required laser intensity for producing a detectable signal with the current Raman spectrometer. Raman spectra of benzonitrile recorded by varying laser power from 5 mW to 55 mW are presented in the [Supporting Information](#). It could be noticed that with the present configuration, the Raman signals were clear and distinguishable at excitation powers as small as 5 mW. Thus, these results indicate adaptability of the current design with lower power laser pointers (<10 mW), as illustrated in some of the prior arts (see [Table 1](#) and refs 31, 33, and 34), which help to improve the safety substantially for classroom demonstration.

Student Learning Outcome

The student learning outcome was assessed on undergraduate and graduate students who visited our laboratory as part of summer programs and those at the early stages of their research program. The students were first introduced to the basic concepts of light-matter interaction, RS, and the spectrometer's operating principles by familiarizing components and their functions. Students were given different sets of samples such as benzonitrile, ethanol, cyclohexane, jewelry containing diamonds, and medicinal paracetamol tablets (contains acetaminophen as the single API) along with a library of reference spectra ([Supporting Information](#)). More than 98% of the students could accurately establish the

unknown samples' identity, and 70% could successfully assign the observed peaks to specific bond vibrations. Research students were provided with the task of configuring the device with collection optics of different numerical apertures (NA) and identifying the effect of NA on the observed Raman spectrum. The students reported almost 4 times higher signal intensity while using an objective lens (Holmarc HO-PA-MO20X) with an NA of 0.4 than with a standard convex lens of focal length 30 mm and aperture 25 mm (see [Supporting Information](#)).

Additionally, we conducted a live demonstration of the spectrometer and lectures of 1 h duration in a few selected colleges. Each of these sessions was attended by more than 40 students.

SUMMARY AND FURTHER WORK

In summary, the design and fabrication of a cost-effective portable Raman spectrometer are presented here. The simplicity of the fabrication procedures detailed herein and the nominal cost of materials make it easily achievable at any educational institution. The design strategy provided in the manuscript offers the flexibility of configuring Raman systems with a different excitation wavelength, and the only modification to be implemented will be the choice of the long-pass filter with the right cutoff wavelength. This helps to explore other capabilities of RS. For example, configuring the system with 405 nm allows study of the well-known resonance Raman effect, which provides a 10^6 signal enhancement with biologically important molecules such as heme and chlorophyll. On the other hand, configuring it with a longer wavelength laser diode (e.g., 650 nm) will help record the Raman spectrum with reduced fluorescence. Yet, another possibility is to explore the demonstration of the concept of SERS with easily preparable metal nanoparticle solutions,^{48–50} which yield enhancement factors as high as 10^{10} .

ASSOCIATED CONTENT

Supporting Information

The Supporting Information is available at <https://pubs.acs.org/doi/10.1021/acs.jchemed.0c01028>.

Details of the optical components; photographs of the stage-wise fabrication procedures; specifications of the confocal Raman microscope; comparison of spectra from confocal Raman microscope and fabricated system; fabrication steps of the home-built Czerny turner spectrometer and its calibration procedure; data of influence of laser power; data of mixture analysis; and student learning outcomes ([PDF](#))

AUTHOR INFORMATION

Corresponding Author

Karuvath Yoosaf – *Photosciences and Photonics Section, Chemical Sciences and Technology Division, CSIR-National Institute for Interdisciplinary Science and Technology, Thiruvananthapuram 695019, Kerala, India; Academy of Scientific and Innovative Research (AcSIR), Ghaziabad 201002, India; orcid.org/0000-0002-8837-4490; Email: yoosafk@niist.res.in*

Authors

Neethu Emmanuel – *Photosciences and Photonics Section, Chemical Sciences and Technology Division, CSIR-National Institute for Interdisciplinary Science and Technology, Thiruvananthapuram 695019, Kerala, India; Academy of Scientific and Innovative Research (AcSIR), Ghaziabad 201002, India; orcid.org/0000-0002-2463-0467*

Raji B Nair – *Photosciences and Photonics Section, Chemical Sciences and Technology Division, CSIR-National Institute for Interdisciplinary Science and Technology, Thiruvananthapuram 695019, Kerala, India; orcid.org/0000-0003-1257-4987*

Bini Abraham – *Photosciences and Photonics Section, Chemical Sciences and Technology Division, CSIR-National Institute for Interdisciplinary Science and Technology, Thiruvananthapuram 695019, Kerala, India; orcid.org/0000-0002-1694-4204*

Complete contact information is available at:

<https://pubs.acs.org/10.1021/acs.jchemed.0c01028>

Notes

The authors declare no competing financial interest.

ACKNOWLEDGMENTS

The authors wish to acknowledge Ms/Vinivish Technologies Pvt. Ltd., Thiruvananthapuram, and KSCSTE for partial funding through the KSCSTE-VINVISH-NIIST PAIR program for this project. Funding was also provided by CSIR-Mission mode (HCP 0012), CSIR-Fast Track Translation (MLP 0039), and DBT (BT/PR22475/NNT/28/1193/2016) projects. This is contribution No. NIIST/2019/Nov/61 from CSIR-National Institute for Interdisciplinary Science and Technology, Thiruvananthapuram.

REFERENCES

- (1) Raman, C. V.; Krishnan, K. S. A new class of spectra due to secondary radiation. *Indian J. Phys.* **1928**, *2*, 379–396.
- (2) Kong, K.; Kendall, C.; Stone, N.; Notingher, I. Raman spectroscopy for medical diagnostics From in-vitro biofluid assays to in-vivo cancer detection. *Adv. Drug Delivery Rev.* **2015**, *89*, 121–134.
- (3) Synytsya, A.; Judexova, M.; Hoskovec, D.; Miskovicova, M.; Petruzalka, L. Raman spectroscopy at different excitation wavelengths (1064, 785 and 532 nm) as a tool for diagnosis of colon cancer. *J. Raman Spectrosc.* **2014**, *45* (10), 903–911.
- (4) Li, Y.; Igne, B.; Drennen, J. K.; Anderson, C. A. Method development and validation for pharmaceutical tablets analysis using transmission Raman spectroscopy. *Int. J. Pharm.* **2016**, *498* (1–2), 318–325.
- (5) Herrero, A. M. Raman spectroscopy a promising technique for quality assessment of meat and fish: A review. *Food Chem.* **2008**, *107* (4), 1642–1651.
- (6) Ong, T. T. X.; Blanch, E. W.; Jones, O. A. H. Surface Enhanced Raman Spectroscopy in environmental analysis, monitoring and assessment. *Sci. Total Environ.* **2020**, *720*, 137601.
- (7) Izake, E. L.; Cletus, B.; Olds, W.; Sundarajoo, S.; Fredericks, P. M.; Jaatinen, E. Deep Raman spectroscopy for the non-invasive standoff detection of concealed chemical threat agents. *Talanta* **2012**, *94*, 342–349.
- (8) Izake, E. L. Forensic and homeland security applications of modern portable Raman spectroscopy. *Forensic Sci. Int.* **2010**, *202* (1–3), 1–8.
- (9) Cui, Y.; Phang, I. Y.; Lee, Y. H.; Lee, M. R.; Zhang, Q.; Ling, X. Y. Multiplex plasmonic anti-counterfeiting security labels based on

surface-enhanced Raman scattering. *Chem. Commun.* **2015**, *51* (25), 5363–5366.

(10) Edwards, H. G. M. Chapter 5 - Raman Spectroscopy in Art and Archaeology: A New Light on Historical Mysteries. In *Frontiers of Molecular Spectroscopy*; Laane, J., Ed.; Elsevier: Amsterdam, 2009; pp 133–173.

(11) Xi, S.; Zhang, X.; Du, Z.; Li, L.; Wang, B. Z.; Luan, Z.; Lian, C.; Yan, J. Y. Laser Raman detection of authigenic carbonates from cold seeps at the Formosa Ridge and east of the Pear River Mouth Basin in the South China Sea. *J. Asian Earth. Sci.* **2018**, *168*, 207–224.

(12) O'Brien, L. C.; Kubicek, R. L.; O'Brien, J. J. Laser Raman Spectroscopy of Diamond. *J. Chem. Educ.* **1994**, *71* (9), 759–760.

(13) Aponick, A.; Marchozzi, E.; Johnston, C. R.; Wigal, C. T. Determining the Authenticity of Gemstones Using Raman Spectroscopy. *J. Chem. Educ.* **1998**, *75* (4), 465–466.

(14) Frey, E. R.; Sygula, A.; Hammer, N. I. Particle in a Disk: A Spectroscopic and Computational Laboratory Exercise Studying the Polycyclic Aromatic Hydrocarbon Corannulene. *J. Chem. Educ.* **2014**, *91* (12), 2186–2190.

(15) Adams, W.; Sonntag, M. D. Vibrational Spectroscopy of Hexynes: A Combined Experimental and Computational Laboratory Experiment. *J. Chem. Educ.* **2018**, *95* (7), 1205–1210.

(16) Nielsen, S. E.; Scaffidi, J. P.; Yeziarski, E. J. Detecting Art Forgeries: A Problem-Based Raman Spectroscopy Lab. *J. Chem. Educ.* **2014**, *91* (3), 446–450.

(17) Sanford, C. L.; Mantooth, B. A.; Jones, B. T. Determination of Ethanol in Alcohol Samples Using a Modular Raman Spectrometer. *J. Chem. Educ.* **2001**, *78* (9), 1221–1225.

(18) Craig, N. C.; Fuchsmann, W. H.; Lacuesta, N. N. Investigation of Model Cell Membranes with Raman Spectroscopy: A Biochemistry Laboratory Experiment. *J. Chem. Educ.* **2003**, *80* (11), 1282–1288.

(19) Wang, L.; Mizaiakoff, B.; Kranz, C. Quantification of Sugar Mixtures with Near-Infrared Raman Spectroscopy and Multivariate Data Analysis. A Quantitative Analysis Laboratory Experiment. *J. Chem. Educ.* **2009**, *86* (11), 1322–1325.

(20) Pavel, I. E.; Alnajjar, K. S.; Monahan, J. L.; Stahler, A.; Hunter, N. E.; Weaver, K. M.; Baker, J. D.; Meyerhoefer, A. J.; Dolson, D. A. Estimating the Analytical and Surface Enhancement Factors in Surface-Enhanced Raman Scattering (SERS): A Novel Physical Chemistry and Nanotechnology Laboratory Experiment. *J. Chem. Educ.* **2012**, *89* (2), 286–290.

(21) Basu-Dutt, S.; Minus, M. L.; Jain, R.; Nepal, D.; Kumar, S. Chemistry of Carbon Nanotubes for Everyone. *J. Chem. Educ.* **2012**, *89* (2), 221–229.

(22) Parobek, D.; Shenoy, G.; Zhou, F.; Peng, Z.; Ward, M.; Liu, H. Synthesizing and Characterizing Graphene via Raman Spectroscopy: An Upper-Level Undergraduate Experiment That Exposes Students to Raman Spectroscopy and a 2D Nanomaterial. *J. Chem. Educ.* **2016**, *93* (10), 1798–1803.

(23) Masson, J.-F.; Yockell-Lelièvre, H. Spectroscopic and Physical Characterization of Functionalized Au Nanoparticles: A Multiweek Experimental Project. *J. Chem. Educ.* **2014**, *91* (10), 1557–1562.

(24) McMillan, B. G. Achieving Very Low Levels of Detection: An Improved Surface-Enhanced Raman Scattering Experiment for the Physical Chemistry Teaching Laboratory. *J. Chem. Educ.* **2016**, *93* (10), 1804–1808.

(25) Mayhew, H. E.; Frano, K. A.; Svoboda, S. A.; Wustholz, K. L. Using Raman Spectroscopy and Surface-Enhanced Raman Scattering To Identify Colorants in Art: An Experiment for an Upper-Division Chemistry Laboratory. *J. Chem. Educ.* **2015**, *92* (1), 148–152.

(26) Galloway, D. B.; Ciolkowski, E. L.; Dallinger, R. F. Raman spectroscopy for the undergraduate physical and analytical laboratories. *J. Chem. Educ.* **1992**, *69* (1), 79.

(27) Sutherland, W. S.; Alarie, J. P.; Stokes, D. L.; Vo-Dinh, T. A Portable Surface-Enhanced Raman Spectrometer. *Instrum. Sci. Technol.* **1994**, *22* (3), 231–239.

(28) Fitzwater, D. A.; Thomasson, K. A.; Glinski, R. J. A Modular Raman Spectroscopy System Using a Helium-Neon Laser That Is

Also Suited for Emission Spectrophotometry Experiments. *J. Chem. Educ.* **1995**, *72* (2), 187.

(29) Bandyopadhyay, A. K.; Dilawar, N.; Vijayakumar, A.; Varandani, D.; Singh, D. A low cost laser-Raman spectrometer. *Bull. Mater. Sci.* **1998**, *21* (5), 433–438.

(30) DeGraff, B. A.; Hennip, M.; Jones, J. M.; Salter, C.; Schaertel, S. A. An Inexpensive Laser Raman Spectrometer Based on CCD Detection. *Chem. Educ.* **2002**, *7* (1), 15–18.

(31) Young, M. A.; Stuart, D. A.; Lyandres, O.; Glucksberg, M. R.; Van Duyne, R. P. Surface-enhanced Raman spectroscopy with a laser pointer light source and miniature spectrometer. *Can. J. Chem.* **2004**, *82* (10), 1435–1441.

(32) Johnson, D.; Larsen, P.; Fluellen, J.; Furton, D.; Schaertel, S. A. A Modular Raman Spectrometer for Solids. *Chem. Educ.* **2008**, *13* (2), 82–86.

(33) Mohr, C.; Spencer, C. L.; Hippler, M. Inexpensive Raman Spectrometer for Undergraduate and Graduate Experiments and Research. *J. Chem. Educ.* **2010**, *87* (3), 326–330.

(34) Somerville, W. R. C.; Le Ru, E. C.; Northcote, P. T.; Etchegoin, P. G. High performance Raman spectroscopy with simple optical components. *Am. J. Phys.* **2010**, *78* (7), 671–677.

(35) Montoya, E. H.; Arbildo, A.; Baltuano, O. R. A Homemade Cost Effective Raman Spectrometer with High Performance. *J. Lab. Chem. Educ.* **2015**, *3* (4), 67–75.

(36) Griffiths, P. R. Introduction to the Theory and Instrumentation for Vibrational Spectroscopy. In *Handbook of Vibrational Spectroscopy*; John Wiley & Sons, Ltd.; 2010.

(37) Spieler, H. Silicon Detectors Many Different Applications, but Built on the Same Basic Physics. IEEE 2012 Nuclear Science Symposium, Medical Imaging Conference, Anaheim, California, 2012.

(38) Kovarik, M. L.; Clapis, J. R.; Romano-Pringle, K. A. Review of Student-Built Spectroscopy Instrumentation Projects. *J. Chem. Educ.* **2020**, *97* (8), 2185–2195.

(39) Rossel, E. TCD1304 PCB. <https://tcd1304.wordpress.com/tcd1304-pcb/> (accessed 3/28/2021).

(40) Krishna, H.; Majumder, S. K.; Gupta, P. K. Range-independent background subtraction algorithm for recovery of Raman spectra of biological tissue. *J. Raman Spectrosc.* **2012**, *43* (12), 1884–1894.

(41) University of Georgia Office of Research. Research Safety: Laser Safety Guidelines. <https://research.uga.edu/safety/laser/safety/> (accessed 3/28/2021).

(42) Laser Institute of America. American National Standards Institute—Z136.5: Safe Use of Lasers in Educational Institutions. <https://www.lia.org/resources/laser-safety-information/laser-safety-standards/ansi-z136-standards/z136-5> (accessed 3/28/2021).

(43) McCreery, R. L. *Raman Spectroscopy for Chemical Analysis*; John Wiley & sons: Canada, 2000.

(44) Cai, D.; Neyer, A.; Kuckuk, R.; Heise, H. M. Raman, mid-infrared, near-infrared and ultraviolet–visible spectroscopy of PDMS silicone rubber for characterization of polymer optical waveguide materials. *J. Mol. Struct.* **2010**, *976* (1), 274–281.

(45) Yadav, R. A.; Singh, I. S. Vibrational spectra and normal coordinate analysis for substituted trifluoromethyl benzenes. *J. Chem. Sci.* **1985**, *95* (5), 471–487.

(46) Borjanovic, V.; Bistričić, L.; Vlasov, I.; Furić, K.; Zamboni, I.; Jaksic, M.; Shenderova, O. Influence of proton irradiation on the structure and stability of poly(dimethylsiloxane) and poly(dimethylsiloxane)-nanodiamond composite. *J. Vac. Sci. Technol.* **2009**, *27* (6), 2396–2403.

(47) Numata, Y.; Iida, Y.; Tanaka, H. Quantitative analysis of alcohol-water binary solutions using Raman spectroscopy. *J. Quant. Spectrosc. Radiat. Transfer* **2011**, *112* (6), 1043–1049.

(48) Emmanuel, N.; Haridas, R.; Chelakkara, S.; Nair, R. B.; Gopi, A.; Sajitha, M.; Yoosaf, K. Smartphone Assisted Colourimetric Detection and Quantification of Pb²⁺ and Hg²⁺ Ions Using Ag Nanoparticles from Aqueous Medium. *IEEE Sens. J.* **2020**, *20* (15), 8512–8519.

(49) Yoosaf, K.; Ipe, B. I.; Suresh, C. H.; Thomas, K. G. In Situ Synthesis of Metal Nanoparticles and Selective Naked-Eye Detection

of Lead Ions from Aqueous Media. *J. Phys. Chem. C* **2007**, *111* (34), 12839–12847.

(50) Sajitha, M.; Vindhyasarumi, A.; Gopi, A.; Yoosaf, K. Shape controlled synthesis of multi-branched gold nanocrystals through a facile one-pot bifunctional biomolecular approach. *RSC Adv.* **2015**, *5* (119), 98318–98324.

Comments and Corrections

Corrections to “Smartphone Assisted Colourimetric Detection and Quantification of Pb^{2+} and Hg^{2+} Ions Using Ag Nanoparticles From Aqueous Medium”

Neethu Emmanuel, Reethu Haridas, Sanoop Chelakkara, Raji B. Nair, Arun Gopi,
Manikantan Sajitha, and Yoosaf Karuvath 

In the above article [1], the authors declare that the affiliation “Neethu Emmanuel, Reethu Haridas, Arun Gopi, Manikantan Sajitha, and Yoosaf Karuvath are with the Academy of Scientific and Innovative Research (AcSIR), New Delhi 110001, India” is to be correctly read as “Neethu Emmanuel, Reethu Haridas, Arun Gopi, Manikantan Sajitha, and Yoosaf Karuvath are with the Academy of Scientific and Innovative Research (AcSIR), Ghaziabad 201002, India.

The authors would like to apologize for any inconvenience caused.

REFERENCES

- [1] N. Emmanuel *et al.*, “Smartphone assisted colourimetric detection and quantification of Pb^{2+} and Hg^{2+} ions using Ag nanoparticles from aqueous medium,” *IEEE Sensors J.*, vol. 20, no. 15, pp. 8512–8519, Aug. 1, 2020.

Manuscript received February 22, 2021; accepted February 22, 2021. Date of current version April 16, 2021. This work was supported in part by the KSCSTE and the VINVISH through PAIR program, in part by the CSIR through its mission mode project HCP0012, and in part by the DBT through the project BT/PR22475/NNT/28/1193/2016. (Corresponding author: Yoosaf Karuvath.)

Neethu Emmanuel, Reethu Haridas, Arun Gopi, Manikantan Sajitha, and Yoosaf Karuvath are with the Photosciences and Photonics Section, Chemical Sciences and Technology Division, CSIR-National Institute for Interdisciplinary Science and Technology, Thiruvananthapuram 695019, India, and also with the Academy of Scientific and Innovative Research (AcSIR), Ghaziabad 201002, India (e-mail: yoosafk@niist.res.in).

Sanoop Chelakkara and Raji B. Nair are with the Photosciences and Photonics Section, Chemical Sciences and Technology Division, CSIR-National Institute for Interdisciplinary Science and Technology, Thiruvananthapuram 695019, India.

Digital Object Identifier 10.1109/JSEN.2021.3062198

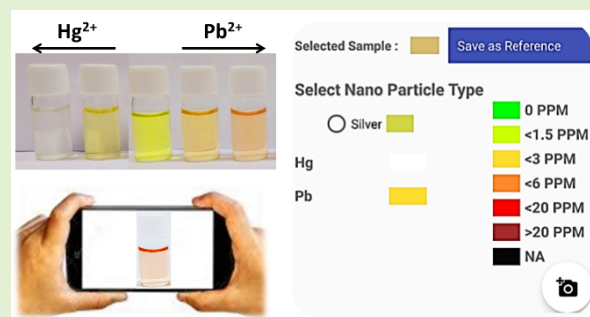
1558-1748 © 2021 IEEE. Personal use is permitted, but republication/redistribution requires IEEE permission.
See <https://www.ieee.org/publications/rights/index.html> for more information.

Smartphone Assisted Colourimetric Detection and Quantification of Pb^{2+} and Hg^{2+} Ions Using Ag Nanoparticles from Aqueous Medium

Neethu Emmanuel, Reethu Haridas, Sanoop Chelakkara, Raji B. Nair, Arun Gopi, Manikantan Sajitha, and Karuvath Yoosaf^{1b}

Abstract—Pollution of aquatic bodies with Lead and Mercury is a serious environmental issue, and there exists an unmet need to develop easy and portable detection techniques. Herein, we report a silver nanoparticle (AgNP) based system exhibiting high selectivity and distinct spectrophotometric behaviour towards these metal ions in the aqueous medium. Though many of the metal ions did not influence the characteristic plasmon spectral profile of AgNPs, Mercury caused the disappearance of absorbance at ~ 400 nm. Consequently, the yellow solution became colourless at around 7.6 ppm of Hg^{2+} ions. While the presence of Pb^{2+} ions induced a decrease in the initial plasmon intensity with the concomitant emergence of a new red-shifted band above 500 nm. As a result, the colour of the solution turned from yellow to red. These colour changes are found to fall well within the spectral responses of R, G and B filters of the digital camera. By making use of this, an android mobile application was developed for digitizing the colour values and for doing further quantitative analysis. The estimated concentration value by this method was found to be in good match with those obtained from absorbance measurement. The achieved lower detection limits were ~ 0.8 ppm for Hg^{2+} and ~ 1.5 ppm for Pb^{2+} ions. This illustrates the potential of the proposed combination of smartphone enabled system with AgNPs for easy discrimination and quantification of these two metal ions from the aqueous medium.

Index Terms—Water pollution, colourimetric detection and distinction, heavy metal ion sensors, mercury, lead, silver nanoparticles, smartphone based sensing, onsite field analysis.



I. INTRODUCTION

ENSURING water quality is essential for sustaining the good health of humans as well as the environment. Mercury and lead are the two heavy metals considered to be the most toxic that pollute aquatic systems and pose a life-threatening danger to living beings[1]–[6]. The sources

Manuscript received September 18, 2019; revised March 2, 2020; accepted March 17, 2020. Date of publication March 31, 2020; date of current version July 6, 2020. This work was supported in part by the KSCSTE and the VINVISH through PAIR program, in part by the CSIR through its mission mode project HCP0012, and in part by the DBT through the project BT/PR22475/NNT/28/1193/2016. The associate editor coordinating the review of this article and approving it for publication was Dr. Anuj K. Sharma. (Corresponding author: Karuvath Yoosaf.)

Neethu Emmanuel, Reethu Haridas, Arun Gopi, Manikantan Sajitha, and Karuvath Yoosaf are with the Photosciences and Photonics Section, Chemical Sciences and Technology Division, CSIR-National Institute for Interdisciplinary Science and Technology, Thiruvananthapuram 695019, India, and also with the Academy of Scientific and Innovative Research (AcSIR), New Delhi 110001, India (e-mail: yoosaf@niist.res.in).

Sanoop Chelakkara and Raji B. Nair are with the Photosciences and Photonics Section, Chemical Sciences and Technology Division, CSIR-National Institute for Interdisciplinary Science and Technology, Thiruvananthapuram 695019, India.

This article has supplementary downloadable material available at <http://ieeexplore.ieee.org>, provided by the authors.

Digital Object Identifier 10.1109/JSEN.2020.2984580

of water contamination are both from humans as well as from natural interventions. Essentially, Lead is one of the components in many consumer products like batteries, paints, pigments, electronics, plastics, cable sheathing, ceramics, etc. which figure in our daily life. Through their unwise disposal and consequent leaching, it reaches water bodies [7]. Due to its wide global abundance and distribution, natural forces like volcanoes and forest fires also accelerate its flow into water bodies [8]. Similarly, apart from the innate degassing of the earth's surface, human activities like gold mining, solid waste incineration, coal-burning power plants, etc., are the major sources of Mercury pollution. The complications arising from the intake of polluted water include malfunctioning of various organs like kidneys, reproductive systems, central nervous system and gastrointestinal tract [9, 10]. It also contributes to physiological stress, hypertension [11], [12] and affects the biological processes like haemoglobin synthesis. Exposure to heavy metals at higher doses by pregnant women may even damage the fetus.

Presently, the estimation of heavy metal ions from water relies on specialized and sophisticated analytical instruments such as mass, atomic absorption and emission

spectroscopies [13]–[17]. They are either bulky, expensive, or laborious and require trained professionals for operation and thus are unsuitable for onsite field analysis. Therefore, there exists an unmet global need for developing portable and cost-effective devices. Further, the methodologies should be easy to perform, have fast response, high sensitivity and selectivity. In principle, this can be fulfilled by utilizing mobile phone based technologies, as they have become an inevitable part of human life. Moreover, new generation smartphones are equipped with even advanced technologies like artificial intelligence and machine learning [18]. Consequently, recent years have witnessed huge drive for using their technical capabilities for many innovative ideas impacting the fields of chemical and biological sensing, healthcare and diagnostics [19]–[21]. Especially, the wide availability of smartphone cameras and image processing techniques would permit the development of low-cost photometric and colourimetric measurement systems for a broad range of chemical analysis [22]–[24]. However, the ease of detection and feasibility of translating mobile devices for onsite quality test are determined by the degree of contrast that an analyte can impart.

Metal nanoparticles of gold and silver exhibit intense colour due to the presence of surface plasmon resonance [25]. They uniquely possess light absorption coefficients a few orders of magnitude higher than the conventional organic chromophores or inorganic materials. Thus, any analyte induced changes in plasmon spectral profiles result in visual colour changes serving as the backbone for many naked-eye detection systems [26]–[42]. By enabling smartphones with algorithms for digitizing the colour variations and analysis, it is possible to derive solutions for easy quantification. Yet, another advantage of metal nanoparticles is the simplicity of production. Presently, the field has grown to a stage where they can be synthesized by simple room temperature mixing of metal salts with a reductant and a suitable capping ligand. All of these factors together have elevated their potential as cost-effective transducers. Some specific examples are the colourimetric Cr³⁺ sensor using vitamin B6 cofactor functionalized gold nanoparticles, [43] and the microfluidic kit for the simultaneous colourimetric detection of arsenic and mercury [44]. Herein, we report a simple silver nanoparticle (AgNP) based system that exhibits distinctly different spectrophotometric behaviour towards Pb²⁺ and Hg²⁺ ions from the aqueous medium. However, negligible spectral changes were noted for other interfering metal ions. Interestingly, the spectral variations induced by Pb²⁺ and Hg²⁺ ions are found to fall well within the individual transmissivity range of R, G and B colour filters of the digital camera. By taking advantage of these, we were able to use a smartphone and develop a mobile application that can automatically distinguish Pb²⁺ and Hg²⁺ ions from the aqueous medium as well as quantify them with a detection limit of ~1.5 ppm and ~0.8 ppm respectively.

II. MATERIALS AND METHODS

A. Chemicals and Instruments Used

Nickel(II) acetate, Magnesium(II) sulphate, Zinc(II) sulphate, Calcium(II) perchlorate, Cadmium(II) chloride,

Mercury(II) acetate and Sodium hydroxide, were obtained from M/s Sd fine chemicals. Silver nitrate (AgNO₃) and Mercury(II) chloride (HgCl₂) was purchased from M/s Merck. 3,4-dihydroxyhydrocinnamic acid (DHCA) was obtained from M/s Sigma Aldrich Corporation, Lead(II) perchlorate trihydrate (Pb(ClO₄)₂·3H₂O) was purchased from M/s Alfa Aesar. All chemicals were used as received. Stock solutions of all the reagents were prepared in doubly distilled water. All the chemicals used herein were of analytical grade. The electronic absorption spectra were recorded on UV-Vis-NIR spectrometer Lambda 950 (M/s PerkinElmer, Inc.). For transmission electron microscopic (TEM) studies, samples were prepared by casting a few drops of their aqueous dispersions on carbon-coated copper grids followed by drying at room temperature and analysed with FEI 300 kV high-resolution transmission electron microscope (FEI-Tecnaï G2–30 with EDAX). The hydrodynamic diameter and zeta potential of the nanoparticles were measured by dynamic light scattering (DLS), using a Zetasizer Nano ZS (M/s Malvern Instruments). For FT-IR studies, DHCA capped AgNPs was precipitated by centrifugation, dried, mixed with KBr and spectra were acquired in diffused reflectance mode using IRPrestige-21 (M/s Shimadzu corporation).

B. Synthesis of Silver Nanoparticles

The synthesis of silver nanoparticles (AgNPs) was carried out as follows: 0.74 mM (10 mL) of silver nitrate solution was first mixed with 30 mL of deionized water under stirring. To this, solutions of 60 μL of 10 mM 3,4-dihydroxyhydrocinnamic acid and NaOH (20 μL, 0.15 M) were added together and stirred at room temperature until it turned yellow.

C. Interaction of AgNPs With Metal Ions

To study the sensing capabilities, initially, stock solutions of metal ions were prepared by dissolving their corresponding salts in 10 mL doubly distilled water each. Titration experiments were conducted by adding an aliquot amount of these stock solutions into 3 mL of the AgNPs. Absorption spectral measurements of these solutions were carried out in quartz cuvette (1 cm path length). For smartphone enabled colourimetric sensing, 2 mL of the AgNP solutions containing varying concentrations of metal ions were transferred into glass vials and photographed using a mobile camera. To minimize the effect of room light, all the samples were kept in a similar white background and photographed under the same lighting conditions. The R, G and B values of these photographs were first extracted using ImageJ software. By comparing the variations in their values with the absorbance changes, a correlation is drawn based on which we developed an algorithm for distinction and quantification of the metal ions.

D. Mobile Application Development

A mobile application was developed using Android Studio 3.1.4 with Software Development Kit (SDK) Android Nougat, installed on a Laptop with 64 bit Windows

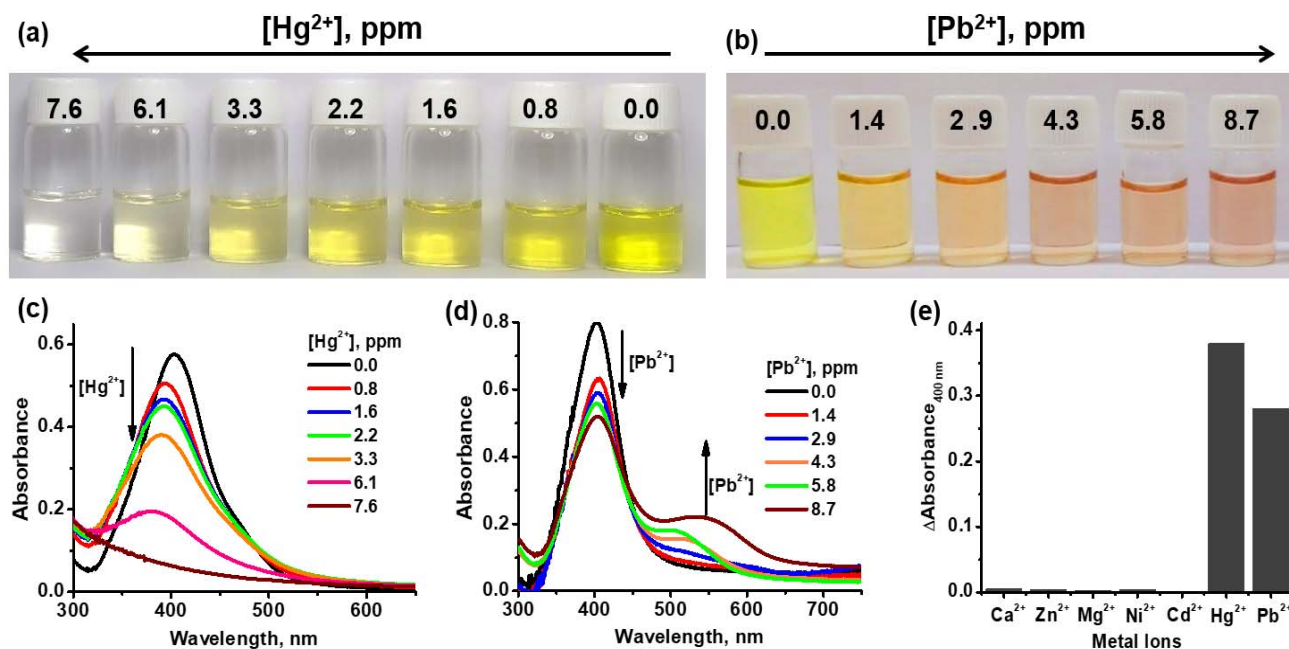


Fig. 1. Photographs illustrating the colour changes induced to **AgNPs** by the presence of varying concentrations of (a) Hg^{2+} ions and (b) Pb^{2+} ions. (c) & (d) represents the corresponding absorption spectral changes. (e) Selectivity plot showing the absorbance difference at 400 nm between **AgNPs** in the absence and presence of different metal ions; $[\text{Ca}^{2+}] = 12$ ppm, $[\text{Zn}^{2+}] = 19$ ppm, $[\text{Mg}^{2+}] = 7$ ppm, $[\text{Ni}^{2+}] = 17$ ppm, $[\text{Cd}^{2+}] = 33$ ppm, $[\text{Hg}^{2+}] = 7.6$ ppm, $[\text{Pb}^{2+}] = 8.7$ ppm.

10 operating system. The application was developed in such a way that it can take photographs using mobile phone's camera, extract R, G and B values from the selected region of interest (ROI) and with the help of algorithm can distinguish toxic metal ions and predict their concentrations using a linear equation model. The developed android application was tested on a Motorola android smartphone with model No: MotoG5SPlus.

III. RESULTS AND DISCUSSION

The chromophore selected for the present studies, **AgNPs**, was synthesized through one-step room temperature reduction of AgNO_3 with 3,4-dihydroxyhydrocinnamic acid (commonly called as dihydrocaffeic acid or DHCA) in the presence of sodium hydroxide. Similar to the metal nanoparticle formation by other ligands such as gallic acid, L-DOPA and others [45], [46], herein DHCA plays the roles of both reducing and capping agents. Mainly, the dihydroxy group acts as the reducing part, and the anchoring of the acid moiety or the carbonyl groups imparts colloidal stability to the nanoparticles. The **AgNP** solution thus obtained exhibited an intense bright yellow colour, and the corresponding absorption spectral measurements revealed the existence of characteristic plasmon absorption at around 400 nm (Fig. S1†) [25]. The average size of these nanoparticles was determined to be ~ 20 nm by using TEM analysis (Fig. S1†). FT-IR spectrum (Fig. S2† and Table S1†) evidenced the presence of H-bonded DHCA on the surface of the **AgNPs** synthesized herein. To study the interaction and hence to probe the possibility of colourimetric sensing, aliquot amounts of each metal ion stock solution were added to a fixed quantity (3 mL) of **AgNPs**. It has been noted that most of the metal ions did not bring any characteristic colour variations. Contrarily, addition of Pb^{2+}

and Hg^{2+} ions resulted in distinctly different colour changes to the **AgNP** solutions, as illustrated in Fig. 1. In the presence of Hg^{2+} ions, the original yellow colour gradually faded and finally became transparent at ~ 7.6 ppm. Whereas, Pb^{2+} ions induced a drastic colour change to red. Thus, this observation served as a method for the preliminary naked-eye detection and distinction of these toxic metal ions from the aqueous medium.

For the quantification of pollutants, first, we investigated the scientific reason behind this through absorption spectroscopic measurements. It was noted that most of the ions did not bring any considerable alterations to the plasmon absorption (Fig. 1e and S3-S6†) and is in accordance with their inability to induce any colour changes, whereas markedly different modifications were evident in the presence of Pb^{2+} and Hg^{2+} ions. Precisely, Hg^{2+} ions triggered a slight blue shift to the plasmon absorption with a continuous decline in its optical density (Fig. 1c) and are the primary reason for the colour fading. On the contrary, the addition of Pb^{2+} ions was always accompanied by a continuous decrease of the initial plasmon absorbance with the concomitant rise of a new red-shifted band (Fig. 1d) and hence the colour drastically turned to red. Both the intensity and wavelength of this new band got augmented with increasing concentrations of Pb^{2+} ions. A plot of the integrated intensity as a function of the metal ion concentration exhibited a very good linear relationship within the investigated range, 0-7.6 ppm for Hg^{2+} and 0-8.7 ppm for Pb^{2+} ions (Fig. S7†). This illustrates the potential of the current system for quantitative estimation of these metal ions from the aqueous medium.

The difference in optical properties suggests independent mechanisms of interaction for the two metal ions with **AgNPs** (Fig. 2). The blue shift and dampening of plasmonic features is

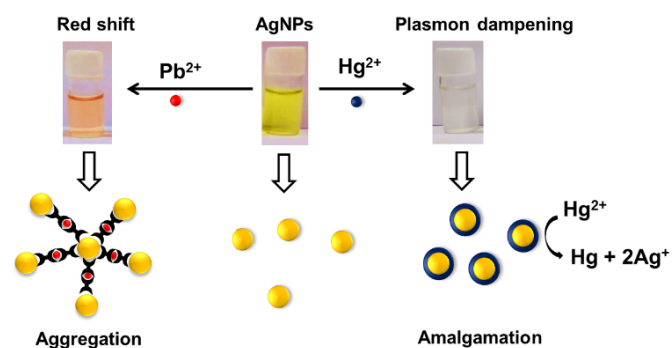


Fig. 2. Pictorial representation of the two different interaction mechanisms of the Hg²⁺ and Pb²⁺ metal ions with AgNPs.

a sign of the disintegration of AgNPs by Hg²⁺ ions. From the literature reports, it can be found that the chloride, the counter ion employed in the current studies, may influence the plasmon spectral profile of AgNPs in either way [47], [48]. In certain instances, chloride ion causes aggregation of AgNPs through surface modifications as well as an increase in ionic strengths, thereby reducing electrostatic repulsive interactions. Studies also have brought the disintegration and shape modification through oxidation mediated silver ion dissolution. However, these observations are made at chloride ion concentrations above mM range, which is ~ 100 times higher than present studies. Notably, in the present work, experiments conducted under similar conditions with other metal chloride salts did not bring any of these changes (Fig. S6[†]). Thus, the observed plasmon disappearance and hence the colour fading can solely be attributable to Hg²⁺ ions. This was further reinstated by the observation of plasmon dampening by mercury salt having other counter ions (e.g. acetate, Fig. S8[†]). In the electrochemical series, Hg²⁺ occupies slightly lower position compared to Ag⁺ ion ($E_{Ag^+/Ag} = 0.8$ V and $E_{Hg^{2+}/Hg} = 0.85$ V) [26] Thus, when added to the nanoparticle solution, Hg²⁺ ions can easily displace the Ag from nanoparticles (eq. 1), and this process is thermodynamically feasible. Both the TEM and DLS investigations did not reveal much change in the nanoparticle's size (Fig. S9[†]). Therefore, we argue that the formed Hg atoms are adsorbed on the surface of AgNPs through the well known process of amalgam formation. This contributes to the continuous dampening of plasmon absorption [49], [50] In fact, Hg 'La' and 'Mα' lines were observed on the EDS spectra [51] of AgNPs recorded in the presence of Hg²⁺ ions (Fig. S10b[†]). On the other hand, the appearance of a red-shifted absorption band implies interparticle plasmon coupling through agglomeration induced by Pb²⁺ ions. Visualization of clusters of nanoparticles in TEM images and the enlargement of the average particle size in the DLS data support this argument (Fig. S11[†]). This is possible through the binding of Pb²⁺ ion with multiple ligands residing on different nanoparticles, thereby bringing them close to each other (Fig. 2). In such instances, it is commonly expected that other metal ions could also bring similar changes often yielding misleading results. To check this, we investigated the potential interference from other metal ions (Ca²⁺, Zn²⁺, Mg²⁺, Ni²⁺, Cd²⁺) in influencing plasmon absorption. However, they remained spectroscopically silent at the concentrations evaluated, reassuring

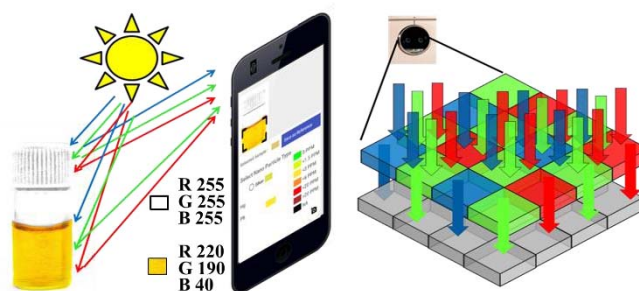
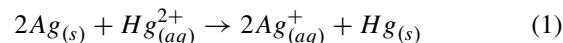


Fig. 3. Schematic representation illustrating the basic principle of colour photography using a mobile phone camera. The Graphical user interface (GUI) of the developed application for metal ion sensing is also shown.

the selectivity in detection. Herein, the metal nanoparticles possess a very high surface charge of -40 mV (at around pH 5). This acts as a repulsive force against agglomeration of nanoparticles imparting high colloidal stability. Thus, only those nanoparticle:analyte interactions capable of overcoming this strong Coulombic repulsion can induce agglomeration. Compared to other metal ions, Lead is unique in having flexible bond lengths and coordination number. Due to this, it can simultaneously bond with ligands on the surface of different nanoparticles, thereby bringing them close to each other and hence promoting agglomeration [27], [28], [52]. Whereas other metal cations are limited by their less coordination number and rigid geometry. Furthermore, the studies conducted with other acetate salts did not produce any spectroscopic variations which nullified contribution from counter ions (Fig. S5[†]).



A. Colourimetric Detection

Though the observed distinct and characteristic colour change serves the purpose of naked-eye distinction of the metal ions, it has the inherent drawback of quantification since the colour perception is individual dependent. To overcome this, we thought of developing a simple photometric method for distinction and quantification. Presently, smartphones are an inevitable part of everyday life and are commonly equipped with cameras, though of varying capabilities. Camera in general consists of a 2D array of photosensory elements called pixels [53]. Each pixel is equipped with a combination of blue (B), green (G) and red (R) filters, which selectively pass a band of wavelengths in the range 400-500 nm, 500-600 nm and 600-700 nm respectively. The intensities of each of these primary colours are represented in an absolute scale of 0-255. While photographing, the reflected light from the object falls on the sensory elements through these colour filters, generating a photocurrent in the respective pixels and whose magnitude is proportional to the light intensity (Fig. 3). Then, the actual colour of the materials is identified through their relative values. Yet, another important parameter that can be extracted from colour photographs is HSV, which is a linear colour code [54]. In this, H is the angular representation of colour on a scale of 0°-360°. The H values for the three primary colours red, green and blue are respectively 0°, 120° and 240°.

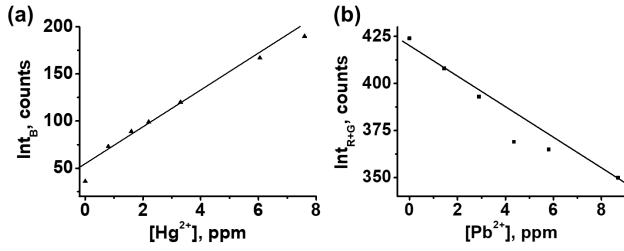


Fig. 4. Plots showing the variations in (a) B and (b) R+G values of nanoparticle's photographs in the presence of varying concentrations of Hg^{2+} and Pb^{2+} ions, respectively.

The value of S ranges from 0-100%, which represents the colour content or the saturation value. V varies from 0-100% with the lighting conditions.

The extracted R, G, B and HSV values of photographs of the nanoparticle's solutions containing different metal ion concentrations are provided in Table I and Table SII†. Pure AgNPs, owing to their bright yellow colour possess an H value close to 60°. The corresponding R, G and B values are around 200, 200 and 36, respectively. Herein, the low value of B is attributed to the strong absorption in the 400 nm region, consequently reducing the percentage of blue component in the reflected light. It is clear from the absorption spectra that with the increase in Hg^{2+} ions concentration, the plasmon peak intensity in the 320-500 nm range decreases linearly (Fig. S7a†). The sample becomes completely colourless and transparent at ~ 7.6 ppm of Hg^{2+} ions. Consequently, the percentage of blue component in the reflected light steadily increases and reaches a value of 190, which is close to the R and G value of pure AgNPs. At the same time, R and G values remain almost unaltered (Fig. S12a†) due to the negligible spectral changes above 500 nm. The fading of the colour can also be quantified using S value as it linearly decreases (Fig. S13a†). Thus, B and S are the only parameters varying linearly with Hg^{2+} ion concentration. A plot of this B value against Hg^{2+} ion concentration established a straight line (Fig. 4a). Thus, the B value at any given concentration of Hg^{2+} ions can be represented by the linear equation 2. Herein, the Y intercept C_1 is the B value of pure AgNPs. The slope m_1 represents the rate of change of B versus Hg^{2+} ion concentration and is estimated to be ~ 20.13 from Fig. 4a.

$$B = (m_1 \times [Hg^{2+}]) + C_1 \quad (2)$$

On the other hand, the presence of Pb^{2+} ions altered all the R, G, B colour parameters (Fig. S12b†). This is due to the following reasons: (i) Recession in optical density at 400 nm results in a correspondingly escalated percentage of blue component in the reflected light and hence the B value. (ii) The growth of new absorption band in the range 500-700 nm diminishes the percentage of both green and red components in the reflected light and hence R and G values. Thus, the sum of their values (R+G) will accommodate this effect giving a linear relation (Fig. 4b) with the Pb^{2+} ion concentration as represented by equation 3. Herein, the Y intercept C_2 is the R+G value of the pure AgNPs. Also, the slope m_2 is the rate of change of R+G as a function of

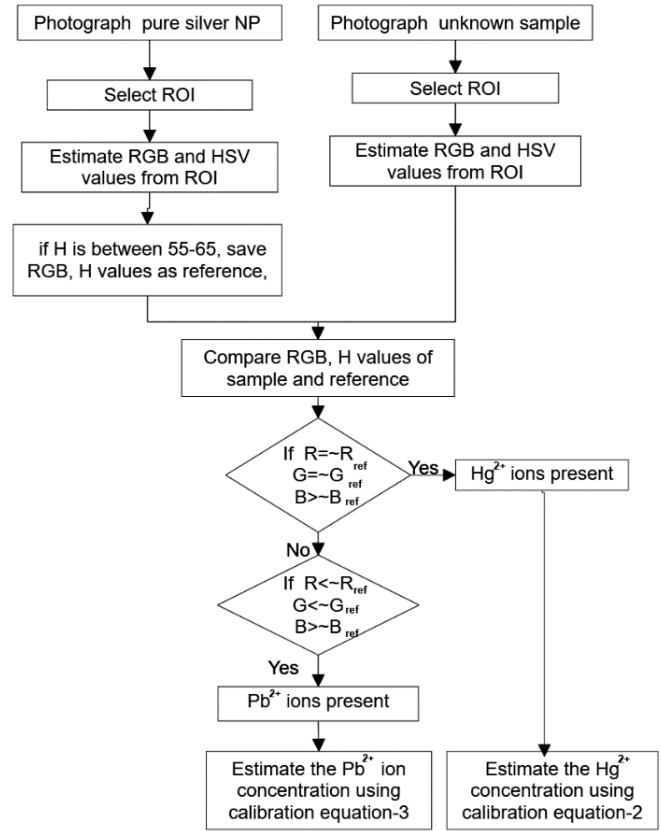


Fig. 5. Schematic representation of the algorithm developed for metal ion distinction and quantification.

Pb^{2+} ion concentration. From Fig. 4b, its value is extracted to be -8.4. Thus, knowing these parameters and R, G, and B values of the solution containing an analyte of interest, one will be able to quantify their concentration.

$$R + G = (m_2 \times [Pb^{2+}]) + C_2 \quad (3)$$

In order to enable smartphone for automatic detection and distinction, these changes in parameters are considered and incorporated into a mobile application, using an android development platform. The data flow involved in this process is represented in Fig. 5 and can be described as follows; (i) in the very first step, colour photograph of the pure nanoparticle solution is recorded. Subsequently, user can select ROI, the portion of the photograph containing nanoparticles, and the software will automatically estimate its characteristic R_{ref} , G_{ref} , B_{ref} values using equations 4, 5 and 6.

$$R = \frac{\sum_i r}{N} \quad (4)$$

$$G = \frac{\sum_i g}{N} \quad (5)$$

$$B = \frac{\sum_i b}{N} \quad (6)$$

where r, g, b are the red, green and blue intensities of the i^{th} pixel, N is the total number of pixels in the selected region.

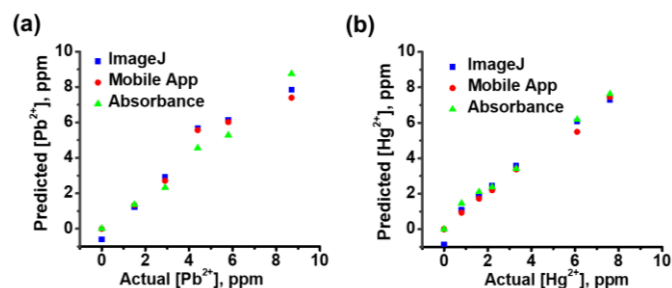


Fig. 6. Predicted concentration Vs Actual concentration of (a) Pb²⁺ ions and (b) Hg²⁺ ions using colour values from ImageJ, using the Mobile app and from absorbance curve.

RGB to HSV conversion is done using an inbuilt function in android as given below[55].

$$\begin{aligned} & \text{Color.RGBToHSV}(R, G, B, hsv) \\ & \text{val H} = hsv[0] \end{aligned} \quad (7)$$

Primarily, the value of H close to 60° is used to identify the solution as AgNPs, and the extracted values of R, G, B and HSV will be recorded as the reference and will also be used to calculate the Y intercepts, C₁ and C₂. In the next step, the photograph of the solution containing the analyte of the interest can be recorded and define ROI. The characteristic values of R, G, B and HSV will be extracted from the ROI in the same way as described above and using equations 4-7. These data are further used for automatic distinction and quantification. As stated before, Hg²⁺ ion induces alteration to only B value while R & G remain negligibly affected. Thus, the condition, B > B_{ref} and R = R_{ref} and G = G_{ref} will help to recognize the analyte as Hg²⁺ ions. The android application will report the concentration of the Hg²⁺ ions in the sample by substituting the obtained value of B and C₁ in equation (2). On the other hand, the presence of Pb²⁺ ions induces changes to the entire spectral window, a decrease in the band intensity at 400 nm with the concomitant rise of absorption above 500 nm whose intensity as well as wavelength maximum undergo a steady increase. This resulted in an alteration to all the three R, G and B values. Thus, the argument B > B_{ref} along with G < G_{ref} and R < R_{ref} can be used to identify the presence of Pb²⁺ ions. From the obtained R+G and C₂ values, the mobile application will automatically quantify Pb²⁺ using equation (3). Fig. 6 represents the comparison of the estimated concentrations of the metal ions through three different modes; (i) absorbance, (ii) manual estimation of RGB values with ImageJ software and (iii) automatically reported by the mobile application. In general, a reasonably good agreement between these independent measurements has been noted.

Further, to evaluate the utility of the current methodology for real environmental samples, we attempted the detection of mercury from tap water. For this, we have spiked the tap water available in the laboratory with mercuric chloride such that the final concentration will be ~ 15 ppm. The photograph and absorption spectra of the real sample, along with the calibration curve used for analysis are provided in Fig. S14† and S15†. The estimated concentration of Hg²⁺ by smartphone colourimetry and absorption spectral measurements are respectively 14.02 ppm and 13.98 ppm.

TABLE I

VARIATION IN RGB AND HSV VALUES OF PHOTOGRAPHS OF AGNP SOLUTIONS CONTAINING DIFFERENT Hg²⁺ ION CONCENTRATIONS

[Hg ²⁺], ppm	HSV			RGB		
	H (°)	S(%)	V(%)	R	G	B
0	60	82.0	78.4	200	200	36
0.8	57	63.5	78.4	200	193	73
1.6	56	55.7	78.8	201	194	89
2.2	55	51.0	79.2	202	194	99
3.3	55	40.3	78.8	201	194	120
6.1	54	16.1	78.0	199	196	167
7.6	45	2.1	76.1	194	193	190

Herein, the achieved limit of detection (LOD) with the proposed system is only ~ 0.8 ppm and ~ 1.5 ppm for Hg²⁺ and Pb²⁺ ions, respectively. The principle of detection is the colour changes induced by the changes to the plasmon absorption by the interaction of respective metal ions. However, parameters such as the concentration of nanoparticles, the surface coverage of the ligand and pH of the medium greatly influence the extent of plasmon spectral variations. This critically affects the observed sensitivity of the proposed system. However, on a positive side, this leaves further room for improving the LOD through optimizations. Also herein, the analysis was carried out on photographs taken under normal room light conditions. Equipping the system with a more controlled lighting environment for enhancing the colour contrast would help to improve the sensitivity. It is to be cautioned that the perceived colour and hence the R, G, B values can vary with lighting conditions. This necessitates the need for making calibration curves under each lighting conditions. More studies need to be undertaken to evolve a better strategy that can avoid the effect of room light variations.

IV. CONCLUSIONS

In conclusion, we demonstrated the potential of the AgNPs synthesized using dihydrocaffeic acid for colourimetric detection and discrimination of toxic heavy metal ions in an aqueous medium. The data presented herein evidence that Hg²⁺ and Pb²⁺ ions interact differently with AgNPs causing distinct colour changes. The observed linearity in the absorbance spectral changes of nanoparticle solutions and the RGB values of their photographs opened up possibilities for quantitative estimation of Hg²⁺ and Pb²⁺ ions. We believe that this is possible only due to the ideal match between the spectral regions of metal ion induced absorbance changes and transmissivities of colour filters of the digital camera. Thus, we could diligently combine the specific properties of AgNPs, the characteristic variations in spectral profiles and technical capabilities of the smartphones, for developing an easy methodology for distinction and quantification of toxic metal ions from the aqueous medium. This, together with the wide availability of smartphones and the user-friendly mobile applications, can enable dissemination of the results in terms of point of site analysis. However, there still lies further room to improve the robustness of the proposed system through evolving strategies that minimize the influences of sampling conditions and enhance the sensitivity.

ACKNOWLEDGMENT

The authors would like to thank Mr. K. Mohan and Mr. R. Philip for helping in Transmission Electron Microscopy studies.

REFERENCES

- [1] T. W. Clarkson, L. Magos, and G. J. Myers, "The toxicology of mercury—Current exposures and clinical manifestations," *New England J. Med.*, vol. 349, no. 18, pp. 1731–1737, Oct. 2003.
- [2] J. A. Lewis and S. M. Cohen, "Addressing lead toxicity: Complexation of Lead(II) with thiopyrone and hydroxypyridinethione O,S mixed chelators," *Inorganic Chem.*, vol. 43, no. 21, pp. 6534–6536, Oct. 2004.
- [3] R. Gautam, S. Sharma, S. Mahiya, and M. Chattopadhyaya, *Heavy Metals In Water: Presence, Removal and Safety*, 1st ed. London, U.K.: Royal Society of Chemistry, 2014.
- [4] P. Landrigan *et al.*, "The Lancet Commission on pollution and health," *Lancet*, vol. 391, pp. 462–512, Feb. 2017.
- [5] M. M. Joselow, "Environmental negligence: The mercury problem," *Amer. J. Public Health*, vol. 61, no. 9, pp. 1745–1747, Sep. 1971.
- [6] D. C. Bellinger, "Childhood lead poisoning: The torturous path from science to policy," *J. Clin. Invest.*, vol. 116, no. 4, pp. 853–857, 2006.
- [7] M. Hanna-Attisha, J. LaChance, R. C. Sadler, and A. C. Schnepf, "Elevated blood lead levels in children associated with the flint drinking water crisis: A spatial analysis of risk and public health response," *Amer. J. Public Health*, vol. 106, no. 2, pp. 283–290, Feb. 2016.
- [8] G. Ignatavičius, G. Sakalauskienė, and V. Oškinis, "Influence of land fires on increase of heavy metal concentrations in river waters of Lithuania," *J. Environ. Eng. Landscape Manage.*, vol. 14, no. 1, pp. 46–51, Mar. 2006.
- [9] S. Hernberg, "Lead poisoning in a historical perspective," *Amer. J. Ind. Med.*, vol. 38, no. 3, pp. 244–254, Sep. 2000.
- [10] D. V. Vassallo *et al.*, "Toxic effects of mercury, lead and gadolinium on vascular reactivity," *Brazilian J. Med. Biol. Res.*, vol. 44, no. 9, pp. 939–946, Sep. 2011.
- [11] S. A. Korrick, D. J. Hunter, A. Rotnitzky, H. Hu, and F. E. Speizer, "Lead and hypertension in a sample of middle-aged women," *Amer. J. Public Health*, vol. 89, no. 3, pp. 330–335, Mar. 1999.
- [12] H. C. Gonick and J. R. Behari, "Is lead exposure the principal cause of essential hypertension?" *Med. Hypotheses*, vol. 59, no. 3, pp. 239–246, Sep. 2002.
- [13] İ. Narin, M. Soylak, L. Elçi, and M. Doğanç, "Determination of trace metal ions by AAS in natural water samples after preconcentration of pyrocatechol violet complexes on an activated carbon column," *Talanta*, vol. 52, no. 6, pp. 1041–1046, Sep. 2000.
- [14] A. Lafaye, C. Junot, B. R.-L. Gall, P. Fritsch, J.-C. Tabet, and E. Ezan, "Metabolite profiling in rat urine by liquid chromatography/electrospray ion trap mass spectrometry. Application to the study of heavy metal toxicity," *Rapid Commun. Mass Spectrometry*, vol. 17, no. 22, pp. 2541–2549, Nov. 2003.
- [15] D. Dragoie *et al.*, "Detection of trace levels of Pb²⁺ in tap water at boron-doped diamond electrodes with anodic stripping voltammetry," *Electrochimica Acta*, vol. 51, no. 12, pp. 2437–2441, Feb. 2006.
- [16] M. Antler, E. J. Maxwell, D. A. Duford, and E. D. Salin, "Online standard additions calibration of transient signals for inductively coupled plasma mass spectrometry," *Anal. Chem.*, vol. 79, no. 2, pp. 688–694, Jan. 2007.
- [17] B. Bansod, T. Kumar, R. Thakur, S. Rana, and I. Singh, "A review on various electrochemical techniques for heavy metal ions detection with different sensing platforms," *Biosensors Bioelectron.*, vol. 94, pp. 443–455, Aug. 2017.
- [18] A. Y. Mutlu, V. Kılıç, G. K. Özdemir, A. Bayram, N. Horzum, and M. E. Solmaz, "Smartphone-based colorimetric detection via machine learning," *Analyst*, vol. 142, no. 13, pp. 2434–2441, 2017.
- [19] A. Ozcan, "Mobile phones democratize and cultivate next-generation imaging, diagnostics and measurement tools," *Lab Chip*, vol. 14, no. 17, pp. 3187–3194, 2014.
- [20] M. Ra, M. S. Muhammad, C. Lim, S. Han, C. Jung, and W.-Y. Kim, "Smartphone-based Point-of-Care Urinalysis under variable illumination," *IEEE J. Transl. Eng. Health Med.*, vol. 6, 2018, Art. no. 2800111.
- [21] H. Nguyen, Y. Sung, K. O'Shaughnessy, X. Shan, and W.-C. Shih, "Smartphone nanocolorimetry for on-demand lead detection and quantitation in drinking water," *Anal. Chem.*, vol. 90, no. 19, pp. 11517–11522, Oct. 2018.
- [22] Y. Upadhyay *et al.*, "Combined use of spectrophotometer and smartphone for the optical detection of Fe³⁺ using a vitamin B6 cofactor conjugated pyrene derivative and its application in live cells imaging," *J. Photochem. Photobiol. A*, vol. 361, pp. 34–40, 2018.
- [23] P. Karami, H. Khoshafar, M. Johari-Ahar, F. Arduini, A. Afkhami, and H. Bagheri, "Colorimetric immunosensor for determination of prostate specific antigen using surface plasmon resonance band of colloidal triangular shape gold nanoparticles," *Spectrochim. Acta A*, vol. 222, p. 117218, 2019.
- [24] T. Anand and S. K. Sahoo, "Cost-effective approach to detect Cu(II) and Hg(II) by integrating a smartphone with the colorimetric response from a NBD-benzimidazole based dyad," *Phys. Chem. Chem. Phys.*, vol. 21, no. 22, pp. 11839–11845, Jun. 2019.
- [25] J. Zhou and B. Tang, "In situ localized surface plasmon resonance spectroscopy for gold and silver nanoparticles," in *In-situ Characterization Techniques for Nanomaterials*. Berlin, Germany: Springer, 2018, pp. 107–157.
- [26] S. S. Ravi, L. R. Christena, N. Saisubramanian, and S. P. Anthony, "Green synthesized silver nanoparticles for selective colorimetric sensing of Hg²⁺ in aqueous solution at wide pH range," *Analyst*, vol. 138, no. 15, p. 4370, 2013.
- [27] K. Yoosaf, B. I. Ipe, C. H. Suresh, and K. G. Thomas, "In situ synthesis of metal nanoparticles and selective naked-eye detection of lead ions from aqueous media," *J. Phys. Chem. C*, vol. 111, no. 34, pp. 12839–12847, Aug. 2007.
- [28] N. Ding *et al.*, "Colorimetric assay for determination of lead (II) based on its incorporation into gold nanoparticles during their synthesis," *Sensors*, vol. 10, no. 12, pp. 11144–11155, 2010.
- [29] Y.-L. Hung, T.-M. Hsiung, Y.-Y. Chen, Y.-F. Huang, and C.-C. Huang, "Colorimetric detection of heavy metal ions using label-free gold nanoparticles and alkanethiols," *J. Phys. Chem. C*, vol. 114, no. 39, pp. 16329–16334, Oct. 2010.
- [30] Y.-R. Ma, H.-Y. Niu, X.-L. Zhang, and Y.-Q. Cai, "Colorimetric detection of copper ions in tap water during the synthesis of silver/dopamine nanoparticles," *Chem. Commun.*, vol. 47, p. 12643, 2011.
- [31] M. Sabela, S. Balme, M. Bechelany, J.-M. Janot, and K. Bissety, "A review of gold and silver nanoparticle-based colorimetric sensing assays," *Adv. Eng. Mater.*, vol. 19, no. 12, Dec. 2017, Art. no. 1700270.
- [32] S. Ye, X. Shi, W. Gu, Y. Zhang, and Y. Xian, "A colorimetric sensor based on catechol-terminated mixed self-assembled monolayers modified gold nanoparticles for ultrasensitive detections of copper ions," *Analyst*, vol. 137, no. 14, p. 3365, 2012.
- [33] D. Karthiga and S. P. Anthony, "Selective colorimetric sensing of toxic metal cations by green synthesized silver nanoparticles over a wide pH range," *RSC Adv.*, vol. 3, no. 37, p. 16765, 2013.
- [34] P. Nalawade and S. Kapoor, "Gold nanoflowers based colorimetric detection of Hg²⁺ and Pb²⁺ ions," *Spectrochim. Acta A*, vol. 116, pp. 132–135, 2013.
- [35] P. Kumar, K.-H. Kim, V. Bansal, T. Lazarides, and N. Kumar, "Progress in the sensing techniques for heavy metal ions using nanomaterials," *J. Ind. Eng. Chem.*, vol. 54, pp. 30–43, Oct. 2017.
- [36] S. Bothra, Y. Upadhyay, R. Kumar, and S. K. Sahoo, "Applications of vitamin B6 cofactor pyridoxal 5'-phosphate and pyridoxal 5'-phosphate crowned gold nanoparticles for optical sensing of metal ions," *Spectrochim. Acta A*, vol. 174, pp. 1–6, Mar. 2017.
- [37] S. Bothra, J. N. Solanki, S. K. Sahoo, and J. F. Callan, "Anion-driven selective colorimetric detection of Hg²⁺ and Fe³⁺ using functionalized silver nanoparticles," *RSC Adv.*, vol. 4, no. 3, pp. 1341–1346, 2014.
- [38] S. Bothra, J. N. Solanki, and S. K. Sahoo, "Functionalized silver nanoparticles as chemosensor for pH, Hg²⁺ and Fe³⁺ in aqueous medium," *Sens. Actuators B, Chem.*, vol. 188, pp. 937–943, Nov. 2013.
- [39] S. Bothra, R. Kumar, and S. K. Sahoo, "Pyridoxal conjugated gold nanoparticles for distinct colorimetric detection of chromium(III) and iodide ions in biological and environmental fluids," *New J. Chem.*, vol. 41, no. 15, pp. 7339–7346, 2017.
- [40] S. Bothra, R. Kumar, and S. K. Sahoo, "Pyridoxal derivative functionalized gold nanoparticles for colorimetric determination of zinc(II) and aluminium(III)," *RSC Adv.*, vol. 5, no. 118, pp. 97690–97695, 2015.
- [41] S. Bothra, R. Kumar, R. K. Pati, A. Kuwar, H.-J. Choi, and S. K. Sahoo, "Virgin silver nanoparticles as colorimetric nanoprobe for simultaneous detection of iodide and bromide ion in aqueous medium," *Spectrochim. Acta A*, vol. 149, pp. 122–126, Oct. 2015.
- [42] S. Bothra, R. Kumar, A. Kuwar, N. Singh, and S. K. Sahoo, "Cu²⁺-driven selective colorimetric sensing of iodide ions and AND logic gate using citrate-capped AgNPs," *Mater. Lett.*, vol. 145, pp. 34–36, Apr. 2015.

- [43] Y. Upadhyay, S. Bothra, R. Kumar, and S. K. Sahoo, "Smartphone-assisted colorimetric detection of Cr³⁺ using vitamin B₆ cofactor functionalized gold nanoparticles and its applications in real sample analyses," *ChemistrySelect*, vol. 3, no. 24, pp. 6892–6896, Jun. 2018.
- [44] A. Motalebizadeh, H. Bagheri, S. Asiaei, N. Fekrat, and A. Afkhami, "New portable smartphone-based PDMS microfluidic kit for the simultaneous colorimetric detection of arsenic and mercury," *RSC Adv.*, vol. 8, no. 48, pp. 27091–27100, 2018.
- [45] K.-W. Huang, C.-J. Yu, and W.-L. Tseng, "Sensitivity enhancement in the colorimetric detection of lead(II) ion using gallic acid–capped gold nanoparticles: Improving size distribution and minimizing inter-particle repulsion," *Biosensors Bioelectron.*, vol. 25, no. 5, pp. 984–989, Jan. 2010.
- [46] S. Du *et al.*, "New insights into the formation mechanism of gold nanoparticles using dopamine as a reducing agent," *J. Colloid Interface Sci.*, vol. 523, pp. 27–34, Aug. 2018.
- [47] C. Levard *et al.*, "Effect of chloride on the dissolution rate of silver nanoparticles and toxicity to *E. Coli*," *Environ. Sci. Technol.*, vol. 47, no. 11, pp. 5738–5745, Jun. 2013.
- [48] K. I. Peterson, M. E. Lipnick, L. A. Mejia, and D. P. Pullman, "Temperature dependence and mechanism of chloride-induced aggregation of silver nanoparticles," *J. Phys. Chem. C*, vol. 120, no. 40, pp. 23268–23275, Oct. 2016.
- [49] Y. Bhattacharjee and A. Chakraborty, "Label-free cysteamine-capped silver nanoparticle-based colorimetric assay for Hg(II) detection in water with subnanomolar exactitude," *ACS Sustain. Chem. Eng.*, vol. 2, no. 9, pp. 2149–2154, Sep. 2014.
- [50] L. Deng *et al.*, "Exploiting the higher specificity of silver amalgamation: Selective detection of Mercury(II) by forming Ag/Hg amalgam," *Anal. Chem.*, vol. 85, no. 18, pp. 8594–8600, Sep. 2013.
- [51] J. C. Russ, "Energy dispersive spectrometers," in *Fundamentals Energy Dispersive X-Ray Analysis*, vol. 1, J. C. Russ, Ed. Oxford, U.K.: Butterworth-Heinemann, 1984, pp. 17–41.
- [52] K.-C. Noh, Y.-S. Nam, H.-J. Lee, and K.-B. Lee, "A colorimetric probe to determine Pb²⁺ using functionalized silver nanoparticles," *Analyst*, vol. 140, pp. 8209–8216, 2015.
- [53] J. Seymour, "Color measurement with an RGB camera," presented at the TAGA, 2009.
- [54] C. A. Poynton, "A guided tour of colour space," in *Proc. New Found. Video Technology: SMPTE Adv. Telev. Electron. Imag. Conf.*, San Francisco, CA, USA, Feb. 1995, pp. 167–180.
- [55] A. Devolepers. (Jan. 22, 2019). *Camera API*. [Online]. Available: <https://developer.android.com/guide/topics/media/camera>



Sanoop Chelakkara received the B.Sc. degree in chemistry from Calicut University and the M.Sc. degree in chemistry from Mahatma Gandhi University. He is currently pursuing the Ph.D. degree at CSIR-NIIST, Thiruvananthapuram. His areas of research interest are Raman spectroscopy and analysis methodologies for the detection of food adulterations and disease biomarkers.



Raji B. Nair received the B.Tech. degree in electronics and communication engineering from CUSAT in 2015 and the M.Tech. degree in electronics and communication (optoelectronics and optical communication) from Kerala University. She is presently working as a Project Assistant III with CSIR-NIIST, Thiruvananthapuram. Her current interests are in the design and instrumentation of opto-electronic devices, particularly in Raman spectrometers.



Arun Gopi received the B.Sc. and M.Sc. degrees in chemistry from Mahatma Gandhi University and the Ph.D. degree in chemistry from AcSIR in 2018. He was a Research Scholar with CSIR-NIIST, Thiruvananthapuram. He is currently working as an Assistant Professor with the School of Marine Sciences, CUSAT. His current research interests are the design of nanomaterials for wastewater treatment and sensing toxic metal contamination in water.



Neethu Emmanuel received the B.Tech. degree in electronics and biomedical engineering and the M.Tech. degree in opto-electronics and communication engineering from the Govt. Model Engineering College. She is currently pursuing the Ph.D. degree in optical spectroscopy for sensing and diagnostic applications with AcSIR, CSIR-NIIST, Thiruvananthapuram. She worked at the Central Imaging and Flow Cytometry Facility, NCBS, Bangalore, for one year in the field of high end optical microscopy. Later, she worked

as an Optical Engineer at Vinvish Technologies Pvt. Ltd., Thiruvananthapuram. Her research interest includes miniature spectroscopic device development, light sheet microscopy, spectroscopic data processing, machine learning, and software application development.



Manikantan Sajitha received the B.Sc. degree in chemistry and the M.Sc. degree in analytical chemistry, the B.Ed. degree from the University of Kerala, and the Ph.D. degree in science from AcSIR in 2020. She was a Research Scholar with CSIR-NIIST, Thiruvananthapuram. Her current research interests include the development of nanomaterials for sensing and biomedical applications.



Reethu Haridas received the B.Sc. degree in chemistry from Kannur University, the M.Sc. degree in hydrochemistry, and the M.Phil. degree in chemical oceanography from the Cochin University of Science and Technology (CUSAT). She is currently pursuing the Ph.D. degree in chemistry with AcSIR, CSIR-NIIST, Thiruvananthapuram. Her current research interests are synthesis nanomaterials and organic chromophores, optical spectroscopy, and energy harvesting devices.



Karuvath Yoosaf was born in Nilambur, Kerala, India, in 1979. He received the B.Sc. degree in chemistry from the University of Calicut, the M.Sc. degree in applied chemistry from CUSAT, and the Ph.D. degree from the faculty of science, CUSAT. He worked as a Research Scholar at CSIR-NIIST, Thiruvananthapuram. Later, he was a Postdoctoral Fellow and a Researcher level-III with the Molecular Photo-science Group, ISOF-CNR, Bologna, Italy. In 2011, he joined back CSIR-NIIST. He is currently

a Senior Scientist with CSIR-NIIST and an Assistant Professor with AcSIR. His current research interests include the development of nanomaterials, organic chromophores and opto-electronic devices for energy harvesting, sensing, and biomedical applications.